

Charge-Modulated Extended Gate Organic  
Field Effect Transistor for Biosensing  
Applications

Ahmed Ben Khaial

Doctor of Philosophy

University of York

Electronic Engineering

December 2017

## Abstract

The interest in organic field effect transistors (OFETs) employed as a biosensing platform has grown in recent years, driven largely by the potential to create inexpensive, sensitive analytical devices with a wide range of chemical and biological sensing applications. A particularly promising architecture for these type of devices is the Charge-Modulated Organic Field-Effect Transistor (CM-OFET). In the CM-OFET, a control gate electrode is capacitively coupled to a floating gate and used to bias the OFET, eliminating the need for an additional, often macroscale, reference electrode. In addition, charge accumulated in a designated sensing region of the floating gate modulates the transistor's output source drain current, providing sensing activity that is spatially separated from the organic semiconductor layer.

Here, a CM-OFET based on solution processed Tips-pentacene as the organic semiconductor that is both low cost and very simple to fabricate is reported. The thesis includes a detailed description of the CM-OFET fabrication alongside a detailed discussion of the principle of operation, both as OFET and as analytical for monitoring pH and protein detection.

The thesis focusses primarily on the characteristics of CM-OFET devices based on the Si/SiO<sub>2</sub> substrate. The fabrication of Si/SiO<sub>2</sub> CM-OFETs was very simple, requiring only a single evaporation stage. Despite the simplicity, the CM-OFETs reliably displayed electrical characteristics typical of OFETs. However, the responses of the devices when tested for pH sensing and protein detection, were inconsistent and with large error. Further analysis of the CM-OFET architecture revealed limitations associated with the geometrical layout of the Si/SiO<sub>2</sub> CM-OFET device may have caused the sensing response deficiency.

A modified CM-OFET employing Al/Al<sub>2</sub>O<sub>3</sub> was designed in which the geometry was optimized to maximise sensitivity. Developed Al-based CM-OFETs were found to exhibit typical OFET behaviour, albeit with relatively lower source drain current compared to Si/SiO<sub>2</sub> CM-OFET devices. Due to limited time, the sensitivity of the Al-based CM-OFET was not fully characterized. Further work regarding the enhancement of the device's charge carrier mobility and particularly, experimental investigation of the Al/Al<sub>2</sub>O<sub>3</sub> CM-OFET for sensing applications is needed.

# Table of Contents

Abstract .....	ii
Table of Contents.....	iv
List of Tables .....	ix
List of Figures .....	x
List of Abbreviations .....	xxiv
Acknowledgments .....	xxvii
Declaration .....	xxix
<b>Chapter 1: Introduction .....</b>	<b>1</b>
1.1 Biosensors.....	1
1.1.1 Exemplar Biosensors: ELISA and SPR-based biosensors.....	4
1.1.1.1 Enzyme-linked immunosorbent assay.....	4
1.1.1.2 Surface plasmon resonance based biosensors.....	5
1.1.1.2.1 Label-free biosensors for real-time measurements of biomolecular interactions.....	7
1.1.2 Next generation biosensors .....	11
1.2 Organic Electronic Devices.....	12
1.3 Conductivity in organic materials.....	14
1.3.1 Intra-molecular charge transport.....	15
1.3.1.1 Band gap, conjugation and semiconducting behaviour .....	18
1.3.2 Inter-molecular charge transport in organic semiconductor films.....	19
1.3.3 Approaches to improve intermolecular charge transport.....	21
1.4 OTFT Operation and fundamental Layers.....	22
1.5 Organic thin film transistors for chemical and biological sensing.....	24

1.5.1 Types of OTFTs used for biosensing.....	24
1.5.1.1 The Dual Gate OFET (DG-OFET) biosensor.....	28
1.5.1.2 Extended Gate OFET biosensor.....	28
1.6 Summary and thesis outline.....	30
1.7 References.....	32
<b>Chapter 2: Materials and fabrication of the CM-OFET .....</b>	<b>45</b>
2.1 Substrate, Gate electrode and Gate Dielectric .....	45
2.1.1 Si/SiO <sub>2</sub> approach .....	46
2.1.2 Al/Al <sub>2</sub> O <sub>3</sub> approach .....	48
2.1.3: Effective sensitivity ( $\Delta I_D/\Delta V_{TH}$ ) of the Al/Al <sub>2</sub> O <sub>3</sub> and Si/SiO <sub>2</sub> devices .....	49
2.2 Source/Drain S/D contacts .....	50
2.3 Organic Semiconductor OSC .....	51
2.4 Sensing area functionalization (with 3-aminopropyltri-ethoxysilane APTES) .....	53
2.5 Polydimethylsiloxane (PDMS) microfluidic chamber .....	55
2.6 OFET-Sensor Fabrication.....	57
2.6.1 Si/SiO <sub>2</sub> Devices .....	57
2.6.1.1 Substrate Preparation and Cleaning .....	57
2.6.1.2 Sensing area fabrication .....	58
2.6.1.3 Fabrication of source, drain and control gate electrodes .....	59
2.6.1.4 OSC deposition .....	60
2.6.1.5 Functionalizing the surface of the sensing region and microfluidic integration .....	62
2.6.1.6 PDMS microfluidic chamber fabrication .....	64
2.6.2 Al/Al <sub>2</sub> O <sub>3</sub> Devices .....	65
2.6.2.1 Substrate Preparation and Cleaning .....	65

2.6.2.2 Al gate deposition .....	66
2.6.2.3 Al <sub>2</sub> O <sub>3</sub> gate dielectric deposition.....	68
2.6.2.4 Contact fabrication .....	70
2.6.2.5 OSC deposition .....	71
2.6.2.6 Fabrication of the sensing area .....	71
2.6.2.7 Sensing area functionalizing and Microfluidic integration.....	72
2.7 References .....	74
<b>Chapter 3: Electrical characterization of the CM-OFET device .....</b>	<b>82</b>
3.1 Electrical characterization of the fabricated devices .....	82
3.1.1 Electrical measurement setup .....	83
3.1.2 Electrical characterization of the OFET devices .....	84
3.1.3 Electrical characterization of the CM-OFET devices .....	90
3.2 Quantification of the CM-OFET sensing response .....	94
3.2.1 Maximum source drain current I <sub>SD</sub> Max .....	94
3.3 Environmental considerations .....	96
3.3.1 Electrical noise .....	96
3.3.2 Temperature .....	97
3.3.2.1 Self device heating .....	97
3.3.3 Light .....	99
3.4 Conclusions .....	105
3.5 References .....	107
<b>Chapter 4: CM-OFET Device as pH sensor .....</b>	<b>110</b>
4.1 Architecture of the pH CM-OFET charge sensor .....	110
4.2 Surface chemistry and surface engineering for pH sensitivity .....	111
4.2.1 Combined pH sensitivity of a NH <sub>2</sub> and Si – OH terminated silicon surface....	113

4.2.2 The CM-OFET pH sensor containing both NH <sub>2</sub> and Si-OH surface groups....	115
4.3 APTES surface analysis .....	116
4.3.1 APTES SAM XPS Spectra .....	116
4.3.1.1 XPS: Experimental Procedure .....	117
4.3.1.2 Detailed spectra of Si XPS peaks .....	119
4.3.1.3 Detailed spectra N 1s XPS peaks .....	120
4.3.1.4 Detailed spectra C 1s Peaks .....	121
4.4 pH CM-OFET: Results and discussion .....	123
4.4.1 Surface modification of Si floating gate using APTES and its effect on the OSC layer .....	123
4.4.2 Experimental consideration for CM-OFET testing; the influence of light.....	128
4.4.3 pH sensing using the CM-OFET .....	132
4.4.3.1 pH sensing using the CM-OFET: Transfer characteristics .....	133
4.4.3.2 CM-OFET pH sensor: Time domain measurements .....	145
4.5 Conclusion .....	150
4.6 References .....	151
<b>Chapter 5: Protein Detection Using the CM-OFET Device.....</b>	<b>156</b>
5.1 Biotin, Avidin and their interaction.....	156
5.1.1 Biotin .....	156
5.1.2 Avidin .....	157
5.1.3 Biotin-Avidin interactions for surface functionalization .....	158
5.1.3.1 Biotin-Avidin stacking on Si .....	159
5.1.3.2 Biotin-Avidin immobilizing protocol on Si .....	152
5.2 Quartz Crystal Microbalance with Dissipation Monitoring (QCM-D) .....	163
5.3 Results and discussion .....	167

5.3.1	QCM-D results .....	167
5.3.1.1	Experimental protocol .....	167
5.3.1.2	QCM-D measurement .....	168
5.3.2	CM-OFET results .....	173
5.3.2.1	Specific binding of avidin to biotinylated CM-OFET devices .....	174
5.3.2.2	Nonspecific avidin binding test using CM-OFET devices .....	181
5.4	Discussion of the Si/SiO <sub>2</sub> CM-OFET biosensor .....	185
5.5	Gating by the control gate; the effect of device geometry .....	186
5.6	Device geometry and sensitivity .....	195
5.7	The trade-offs of the design .....	196
5.8	The modified Al/Al <sub>2</sub> O <sub>3</sub> CM-OFET device behaviour as a transistor .....	196
5.9	Conclusions .....	198
5.10	References .....	200
<b>Chapter 6: Conclusions and Future Works .....</b>		<b>205</b>
6.1	Conclusions .....	205
6.2	Future Works .....	208
Appendix A.....		211
Appendix B.....		220
Appendix C.....		223
Appendix D.....		230
Appendix E.....		233

## List of Tables

<b>Table 1.1:</b> The main differences between organic and inorganic semiconductors.....	14
<b>Table 1.2:</b> Electrons distribution on carbon's atomic orbitals.....	15
<b>Table 3.1:</b> Average estimated values of figures of merit for characterized OFET devices...	90
<b>Table 4.1:</b> the extracted values of $\tau$ and $\beta$ from the fitting of equation 4.6 to $I_{SD}$ decay for six CM-OFET devices.....	129
<b>Table 4.2:</b> The percentage change in the measured maximum source drain current, $I_{SDMax}$ , during a 7 hours period in the dark compare to $I_{SDMax}$ in light.....	130
<b>Table 4.3:</b> Mixing table for making 50ml of citric and Mcilvaine buffer solutions and the measured pH of prepared buffer solutions compare to the targeted pH.....	133
<b>Table 5.1:</b> Summary of QCM-D experiment stages.....	168
<b>Table 5.2:</b> Estimated avidin mass adsorbed to each of the 4 investigated sensors.....	172
<b>Table 5.3:</b> Average percentage change in maximum source drain current after avidin deposition relative to the maximum source drain current before avidin deposition for nine, biotinylated CM-OFET devices. ....	180
<b>Table 5.4:</b> Average percentage change in maximum source drain current after avidin deposition relative to the maximum source drain current before avidin deposition for the non-biotinylated, silanized CM-OFET biosensors. ....	184

## List of Figures

<b>Figure 1.1:</b> The generic biosensor model .....	2
<b>Figure 1.2:</b> The four different combinations of antigen capture and detection used commonly in ELISA. ....	5
<b>Figure 1.3:</b> (a) A setup of the SPR detection techniques using the Kretschmann configuration, (b) the detected reflectivity response and (c) how the angular shift is translated in a sensorgram [48]. ....	7
<b>Figure 1.4:</b> Typical SPR sensorgram showing the four phases: association phase, steady state or equilibrium phase, dissociation phase, and regeneration phase [49].....	8
<b>Figure 1.5:</b> (a) An example of SPR sensorgrams generated by challenging a surface functionalized with a specific bio-recognition element with a range of solutions of differing analyte concentrations, (b) SPR response at equilibrium from all sensorgrams from (a) plotted against analyte concentration [55]. ....	10
<b>Figure 1.6:</b> cost vs performance comparison of silicon based devices and OEDs [61].....	12
<b>Figure 1.7:</b> Types of the orbitals hybridization in the carbon atom [75].....	16
<b>Figure 1.8:</b> Bonds and orbitals overlap in the ethane, C <sub>2</sub> H <sub>6</sub> , 7 $\sigma$ bonds; one C–C $\sigma$ bond results from overlap of $sp^3$ hybrid orbitals in the two carbon atoms and six C–H $\sigma$ bonds result from the overlap between the C atoms $sp^3$ orbitals with s orbitals on the hydrogen atoms [76].....	16
<b>Figure 1.9:</b> Bonds and orbitals overlap in the ethene, C <sub>2</sub> H <sub>4</sub> , (a) five $\sigma$ bonds; one C–C $\sigma$ bond results from overlap of $sp^2$ hybrid orbitals in the two carbon atoms. Four C–H bonds result from the overlap between the C atoms' $sp^2$ orbitals with s orbitals on the hydrogen atoms. (b) The $\pi$ bond is formed by the side-by-side overlap of the two unhybridized p orbitals in the two carbon atoms. The two lobes of the $\pi$ bond are above and below the plane of the $\sigma$ system [77]. ....	17
<b>Figure 1.10:</b> Bonds and orbitals overlap in acetylene, C <sub>2</sub> H <sub>2</sub> , (a) there are 3 $\sigma$ bonds; two C–H $\sigma$ bonds and one C–C $\sigma$ bond and two C–C $\pi$ bonds. The dashed lines, each connecting two lobes, indicate the side-by-side overlap of the four unhybridized p orbitals. (b) the	

overall outline of the bonds in  $C_2H_2$ . The two lobes of each of the  $\pi$  bonds are positioned across from each other around the line of the C–C  $\sigma$  bond [77].....17

**Figure 1.11:** Schematic of energy-level in alkenes with increasing conjugation length, highlighting the energy gap between HOMO to LUMO. The bandgap of polyacetylene depends on the number of monomers  $n$  in the polymer. Arrows represent spin-paired electrons [84]. .....19

**Figure 1.12:** Typical architectures of OTFTs (a) Bottom contact, (b) Top contact, (c) Top gate-Bottom contact and (d) Top gate-Top contact. S: Source, D: Drain, G: Gate, and OSC: organic semiconductor. ....23

**Figure 1.13:** The schematic structure of a typical (a) organic field effect transistor (OFET) biosensor and (b) organic electrochemical transistor (OECT) biosensor.....25

**Figure 1.14:** Schematic diagram of the ion-sensitive organic field effect transistors (ISOFET).....26

**Figure 1.15:** Schematic diagram of the electrical double layers formed in the electrolyte-gated organic field effect transistor (EGOFET). ....27

**Figure 1.16:** schematic structure of (a) DG-OFET, and (b) the DG-OFET configured as a biosensor. ....28

**Figure 1.17:** OFET with Extended Gate, Charge Modulated OFET (CM-OFET).....30

**Figure 2.1:** Illustrate the effect of 1V gate shift on the current-voltage response for low and high operating voltage range (simulated data for two devices with same mobility and electrode dimensions but different gate dielectric layers).....47

**Figure 2.2:** Delamination of the Al layer during anodization process.....48

**Figure 2.3:** Energy barrier between Metal work function and HOMO / LUMO of OSC.  $h^+$  and  $e^-$  are holes and electrons respectively. ....50

**Figure 2.4:** Chemical structure of (a) Pentacene (b) Tips-pentacene.....51

**Figure 2.5:** Schematic diagram showing the three phases of Tips-pentacene/P $\alpha$ MS after separation. ....53

<b>Figure 2.6:</b> APTES chemical structure and Optimal APTES Silanization process on Si substrate [54].	54
<b>Figure 2.7:</b> Polymerization of PDMS when mixing oligomer base (1) and curing agent (2) [64].	56
<b>Figure 2.8:</b> PDMS oxygen plasma surface treatment and bonding to silica substrate [69,74]	57
<b>Figure 2.9:</b> Clean Si/SiO <sub>2</sub> substrate (a) Top view (b) Cross section	58
<b>Figure 2.10:</b> etched SiO <sub>2</sub> sensing region of Si/SiO <sub>2</sub> substrate (a) Top view (b) Cross section.	59
<b>Figure 2.11:</b> Deposition of device contacts on Si/SiO <sub>2</sub> substrate (a) Top view (b) Cross section.	60
<b>Figure 2.12:</b> OSC deposition on S/D contacts of the device (a) Top view (b) Cross section.	61
<b>Figure 2.13:</b> Optical microscope image of the source/drain electrodes (a) before and (b) after Tips-pentacene deposition. Images were captured using a 5x objective lens	62
<b>Figure 2.14:</b> Complete Si/SiO <sub>2</sub> CM-OFET sensor (a) Top view (b) Cross section	64
<b>Figure 2.15:</b> Making of a PDMS replica mold.	65
<b>Figure 2.16:</b> PDMS Microfluidic chamber with an inlet and an outlet	65
<b>Figure 2.17:</b> Clean Si/SiO <sub>2</sub> substrate (a) Top view (b) Cross section	66
<b>Figure 2.18:</b> Deposition of Al gate layer on the entire substrate (a) Top view (b) Cross section, and pattern Al gate layer (c) Top view (d) Cross section	67
<b>Figure 2.19:</b> PE-ALD cycle for Al <sub>2</sub> O <sub>3</sub> deposition [78]	69
<b>Figure 2.20:</b> ALD Al <sub>2</sub> O <sub>3</sub> layer deposition on Al gate (a) Top view (b) Cross section	70
<b>Figure 2.21:</b> Deposition of device contacts on top of Al <sub>2</sub> O <sub>3</sub> layer (a) Top view (b) Cross section	70
<b>Figure 2.22:</b> OSC deposition on S/D contacts of the device (a) Top view (b) Cross section	71

<b>Figure 2.23:</b> Etched Al <sub>2</sub> O <sub>3</sub> sensing region of Al/Al <sub>2</sub> O <sub>3</sub> bilayer (a) Top view (b) Cross section.....	72
<b>Figure 2.24:</b> Complete Al/Al <sub>2</sub> O <sub>3</sub> CM-OFET sensor (a) Top view (b) Cross section.....	73
<b>Figure 3.1:</b> Electrical characterization measurement setup. ....	84
<b>Figure 3.2:</b> A photograph of four OFETs fabricated on a Si/SiO <sub>2</sub> substrate. Here, the gold source and drain electrodes were fabricated by photolithography before Tips-pentacene was drop cast over the substrate surface. Contact to the degenerately doped Si gate was achieved by mechanical removal of the 300 nm thick SiO <sub>2</sub> gate dielectric .....	85
<b>Figure 3.3:</b> Measured output characteristics of one of the fabricated OFETs, the channel length of the device is 60 μm and the thermally grown SiO <sub>2</sub> gate dielectric has a thickness of 300 nm. ....	86
<b>Figure 3.4:</b> Measured transfer characteristics of one of the fabricated OFETs at V <sub>SD</sub> = -40V, the channel length of the device is 60μm and the thermally grown SiO <sub>2</sub> gate dielectric has a thickness of 300nm. ....	86
<b>Figure 3.5:</b> Optical microscope image of the formation of Tips-pentacene crystals that assemble on and between source and drain following drop casting. Images were captured using a 5x objective lens. (a) Situation where crystals bridge the S/D contacts and (b) no crystals in the channel between the S/D contacts. ....	87
<b>Figure 3.6</b> Transfer characteristics for four nominally identical OFETs (T1 – 4) fabricated on the same Si/ SiO <sub>2</sub> substrate at V <sub>SD</sub> = -40 V. Here, the channel length (spacing between source and drain electrodes) is 60 μm and the thermally grown SiO <sub>2</sub> gate dielectric has a thickness of 300 nm. ....	88
<b>Figure 3.7:</b> The range of maximum source drain current, I <sub>SD</sub> Max, for all working OFET devices (total = 131). Here I <sub>SD</sub> Max is defined as the source drain current flowing between source and drain contacts at V <sub>SD</sub> = -40 V and V <sub>G</sub> = -40 V. ....	89
<b>Figure 3.8:</b> The range of ON/OFF ratio for all working OFET devices (total = 131). ....	89
<b>Figure 3.9:</b> A photograph of four CM-OFETs fabricated on a Si/SiO <sub>2</sub> substrate. Here, the gold source, drain and control gate electrodes were fabricated by shadow masking before	

Tips-pentacene was drop cast over the substrate surface. The gate dielectric layer SiO <sub>2</sub> thickness is 300 nm thick. ....	91
<b>Figure 3.10:</b> Measured output characteristics of one of the fabricated CM-OFETs, the channel length of the device is 60 μm and the thermally grown SiO <sub>2</sub> gate dielectric has a thickness of 300 nm. ....	92
<b>Figure 3.11:</b> Measured transfer characteristics of one of the fabricated CM-OFETs at V <sub>SD</sub> = -40V, the channel length of the device is 60μm and the thermally grown SiO <sub>2</sub> gate dielectric has a thickness of 300nm. ....	93
<b>Figure 3.12:</b> The range of maximum source drain current, I <sub>SDMax</sub> , for characterized CM-OFET devices (total = 27). Here I <sub>SDMax</sub> is defined as the source drain current flowing between source and drain contacts at V <sub>SD</sub> = -40 V and V <sub>G</sub> = -40 V. ....	94
<b>Figure 3.13:</b> Effect of ±1V gate voltage range shift on the I <sub>SD</sub> of a transfer characteristic, (inset) shows the difference between I <sub>SDMax</sub> . (simulated curves for Si/SiO <sub>2</sub> CM-OFET device with W = 0.1 cm, L = 60 X 10 <sup>-4</sup> cm, C <sub>i</sub> = 11.51nF/cm <sup>2</sup> and μ = 1 X 10 <sup>-3</sup> cm <sup>2</sup> V <sup>-1</sup> S <sup>-1</sup> ). ....	96
<b>Figure 3.14:</b> Power consumed during a transfer characteristics measurement of one CM-OFET device.....	99
<b>Figure 3.15:</b> spectrum of laboratory fluorescent light measured at the position of the tested CM-OFET devices. ....	100
<b>Figure 3.16:</b> The change in I <sub>SDMax</sub> periodically measured for 5 CM-OFET under light and dark conditions. ....	101
<b>Figure 3.17:</b> The change in I <sub>SD</sub> periodically measured for a CM-OFET under light and dark conditions at V <sub>G</sub> = -10, -20, -30 and -40V. ....	102
<b>Figure 4.1:</b> Schematic diagram of the CM-OFET sensor showing the two key components of the device; the OFET and the sensing region which can be exposed to an analyte through a PDMS microfluidic manifold. Coupling between the two components is achieved via the floating gate. The control gate, C <sub>g</sub> , is used to bias the OFET without the need for applying a potential directly to the floating gate. Here, the schematic shows a CM-OFET responsive to pH where the pH sensitivity arises from amine groups introduced on the surface of the sensing region by the APTES self-assembled monolayer. ....	111

<b>Figure 4.2:</b> ionization states of silanol groups at the interface between the native silica formed on silicon substrate and an aqueous electrolyte as a function of solution pH [4].	112
<b>Figure 4.3:</b> Schematic plot of the Henderson-Hasselbalch relationship of the amine group	114
<b>Figure 4.4:</b> A representative XPS survey scan showing the elemental composition of the surfaces of (a) APTES modified Si substrate, (b) reference Si substrate. The APTES modified Si sample spectrum has a reduced intensity compared to the reference sample. This is because a smaller aperture was used to reduce artefacts associated with photoelectrons generate from the sample plate.	118
<b>Figure 4.5:</b> Experimental XPS spectra for Si (2s & 2p) peaks for the (a and c) APTES modified Si substrate and (b and d) for the unmodified reference Si substrate.	119
<b>Figure 4.6:</b> XPS spectra for N (1s) on (a) APTES modified Si substrate, and (b) reference Si substrate.	120
<b>Figure 4.7:</b> Detailed XPS spectra for N (1s) peaks for APTES modified Si substrate. Peak fitting reveals two peaks associated with the neutral (NH <sub>2</sub> ) and protonated (NH <sub>3</sub> <sup>+</sup> ) binding energies. All deconvoluted fitted peaks are Gaussian functions	121
<b>Figure 4.8:</b> Detailed XPS spectra for C (1s) peaks on (a) APTES modified Si substrate and (b) reference Si substrate.	122
<b>Figure 4.9:</b> Detailed XPS spectra for C (1s) peaks for (a) APTES modified Si substrate and (b) reference Si substrate. Peak fitting reveals three peaks associated with binding energies of C – C ~284.4 eV (peak 1), C – N ~286.2 eV (peak 2) and C = O ~288 eV (peak 3). All deconvoluted fitted peaks are Gaussian functions.	123
<b>Figure 4.10:</b> The two fabrication sequences implemented for fabricating the CM-OFET devices.	124
<b>Figure 4.11:</b> Transfer characteristics of a CM-OFET before and after functionalization of the Si sensing region with 5% APTES in IPA. Here, V <sub>SD</sub> = -40 V.	125
<b>Figure 4.12:</b> Transfer characteristics of a device before and after APTES functionalization using approach 2 and after exposing the device to APTES vapour (V <sub>SD</sub> =-40V).	126

**Figure 4.13:** Effect of immersion in (APTES-Toluene) and (APTES-IPA) solutions on PDMS chamber, (a) before (b) after immersion in (APTES-Toluene) solution, (c) before (d) after immersion in (APTES-IPA) solution. ....127

**Figure 4.14:** Time dependence of the maximum source drain current for a CM-OFET device due to shielding from ambient light. Here, the Tips-pentacene layer is covered by black tape and the transfer characteristics were measured every 25 minutes for 7 hours and  $I_{SD}$  is the maximum source drain current recorded at  $V_G = -40$  V. ....129

**Figure 4.15:** The percentage of change in the measured maximum source drain current  $I_{SDMax}$  for six CM-OFETs. .... 131

**Figure 4.16:** comparison of the RSD between recorded  $I_{SDMax}$  at different periods of the experiment for six CM-OFETs. ....131

**Figure 4.17:** Experimental results of pH sensing using CM-OFET device 1. (a) Percentage change in  $I_{SDMax}$  for three independent measurements over the full pH range. Here, the transfer characteristics were measured 25 mins after introduction of the test pH solution. (b) The average change in  $I_{SDMax}$  for the three independent measurements (25min measurement). (c) Percentage change in  $I_{SDMax}$  for two independent measurements over the full pH range. Here, the transfer characteristics were measured immediately after introduction of the test pH solution. (d) The average change in  $I_{SDMax}$  for the two independent measurements (immediate measurement). Error bars are  $\pm SD$  .....136

**Figure 4.18:** Experimental results of pH sensing using CM-OFET device 2. (a) Percentage change in  $I_{SDMax}$  for three independent measurements over the full pH range. Here, the transfer characteristics were measured 25 mins after introduction of the test pH solution. (b) The average change in  $I_{SDMax}$  for the three independent measurements (25min measurement). (c) Percentage change in  $I_{SDMax}$  for two independent measurements over the full pH range. Here, the transfer characteristics were measured immediately after introduction of the test pH solution. (d) The average change in  $I_{SDMax}$  for the two independent measurements (immediate measurement). Error bars are  $\pm SD$  .....137

**Figure 4.19:** Experimental results of pH sensing using CM-OFET device 3. (a) Percentage change in  $I_{SDMax}$  for three independent measurements over the full pH range. Here, the transfer characteristics were measured 25 mins after introduction of the test pH solution.

(b) The average change in  $I_{SDMax}$  for the three independent measurements (25min measurement). (c) Percentage change in  $I_{SDMax}$  for two independent measurements over the full pH range. Here, the transfer characteristics were measured immediately after introduction of the test pH solution. (d) The average change in  $I_{SDMax}$  for the two independent measurements (immediate measurement). Error bars are  $\pm SD$  .....138

**Figure 4.20:** Experimental results of pH sensing using CM-OFET device 4. (a) Percentage change in  $I_{SDMax}$  for three independent measurements over the full pH range. Here, the transfer characteristics were measured 25 mins after introduction of the test pH solution. (b) The average change in  $I_{SDMax}$  for the three independent measurements (25min measurement). (c) Percentage change in  $I_{SDMax}$  for two independent measurements over the full pH range. Here, the transfer characteristics were measured immediately after introduction of the test pH solution. (d) The average change in  $I_{SDMax}$  for the two independent measurements (immediate measurement). Error bars are  $\pm SD$  .....139

**Figure 4.21:** Experimental results of pH sensing using CM-OFET device 5. (a) Percentage change in  $I_{SDMax}$  for three independent measurements over the full pH range. Here, the transfer characteristics were measured 25 mins after introduction of the test pH solution. (b) The average change in  $I_{SDMax}$  for the three independent measurements (25min measurement). (c) Percentage change in  $I_{SDMax}$  for two independent measurements over the full pH range. Here, the transfer characteristics were measured immediately after introduction of the test pH solution. (d) The average change in  $I_{SDMax}$  for the two independent measurements (immediate measurement). Error bars are  $\pm SD$  .....140

**Figure 4.22:** Experimental results of pH sensing using CM-OFET device 6. (a) Percentage change in  $I_{SDMax}$  for three independent measurements over the full pH range. Here, the transfer characteristics were measured 25 mins after introduction of the test pH solution. (b) The average change in  $I_{SDMax}$  for the three independent measurements (25min measurement). (c) Percentage change in  $I_{SDMax}$  for two independent measurements over the full pH range. Here, the transfer characteristics were measured immediately after introduction of the test pH solution. (d) The average change in  $I_{SDMax}$  for the two independent measurements (immediate measurement). Error bars are  $\pm SD$  .....141

**Figure 4.23:** Experimental results of pH sensing using CM-OFET device 7. (a) Percentage change in  $I_{SDMax}$  for three independent measurements over the full pH range. Here, the

transfer characteristics were measured 25 mins after introduction of the test pH solution. (b) The average change in  $I_{SDMax}$  for the three independent measurements (25min measurement). (c) Percentage change in  $I_{SDMax}$  for two independent measurements over the full pH range. Here, the transfer characteristics were measured immediately after introduction of the test pH solution. (d) The average change in  $I_{SDMax}$  for the two independent measurements (immediate measurement). Error bars are  $\pm SD$  .....142

**Figure 4.24:** Experimental results of pH sensing using CM-OFET device 8. (a) Percentage change in  $I_{SDMax}$  for three independent measurements over the full pH range. Here, the transfer characteristics were measured 25 mins after introduction of the test pH solution. (b) The average change in  $I_{SDMax}$  for the three independent measurements (25min measurement). (c) Percentage change in  $I_{SDMax}$  for two independent measurements over the full pH range. Here, the transfer characteristics were measured immediately after introduction of the test pH solution. (d) The average change in  $I_{SDMax}$  for the two independent measurements (immediate measurement). Error bars are  $\pm SD$  .....143

**Figure 4.25:** The average of  $[(I_{SDMax}(pH) - I_{SDMax}(citric)) / I_{SDMax}(citric)] \%$  change for each investigated pH level across all tested CM-OFET devices (25min measurement). Error bars are  $\pm SD$  .....145

**Figure 4.26:** Source drain current decay over time due to bias stress effect for a CM-OFET device. ....146

**Figure 4.27:** Normalized real time source drain current as a function of solution pH for CM-OFET device 1. The data has been smoothed using a 200s averaging period. Here, air was injected into the PDMS chamber prior to the injection of each buffer. ....147

**Figure 4.28:** Normalized real time source drain current as a function of solution pH for CM-OFET device 2. The data has been smoothed using a 200s averaging period. Here, air was injected into the PDMS chamber prior to the injection of each buffer. ....147

**Figure 4.29:** Normalized real time source drain current as a function of solution pH for CM-OFET device 3. The data has been smoothed using a 200s averaging period. Here, air was injected into the PDMS chamber prior to the injection of each buffer. ....148

**Figure 4.30:** Normalized real time source drain current as a function of solution pH for CM-OFET device 4. The data has been smoothed using a 200s averaging period. Here, air was

injected into the PDMS chamber prior to the injection of each buffer. ....	148
<b>Figure 4.31:</b> Normalized real time source drain current as a function of solution pH for CM-OFET device 5. The data has been smoothed using a 200s averaging period. ....	148
<b>Figure 4.32:</b> Normalized real time source drain current as a function of solution pH for CM-OFET device 6. The data has been smoothed using a 200s averaging period. ....	149
<b>Figure 4.33:</b> Normalized real time source drain current as a function of solution pH for CM-OFET device 7. The data has been smoothed using a 200s averaging period. ....	149
<b>Figure 5.1:</b> Chemical structure of biotin molecule. ....	157
<b>Figure 5.2:</b> A ribbon representation of the avidin tetrameric arrangement [12]. ....	158
<b>Figure 5.3:</b> Schematic representation of the two methods utilizing biotin-avidin conjugation to bind targeted biomolecules to sensor surface. In a) the surface is first chemically modified for conjugation to biotin. In contrast, the approach shown schematically in b) employs physisorption of avidin to the solid support. ....	159
<b>Figure 5.4:</b> Si surface functionalization, biotinylation and Avidin binding process, from left to right, a hydroxylated Si surface was first silanized with APTES, then biotinylated and finally avidin binds to the biotinylated surface [19]. ....	160
<b>Figure 5.5:</b> Schematic diagram of (a) QCM quartz crystal sensor with drive electrodes, (b) initial geometry of the crystal before applying the AC drive voltage and (c) oscillation of the crystal upon applying AC voltage. ....	163
<b>Figure 5.6:</b> Representation of the fundamental resonant frequency ( $n=1$ ) and the first two harmonics ( $n=2$ and $3$ ) produced by crystal oscillation [30]. ....	164
<b>Figure 5.7:</b> Illustration of the difference in frequency and dissipation response in a QCM-D system for rigid and soft films [36]. ....	166
<b>Figure 5.8:</b> QCM-D $\Delta f$ and $D$ vs time response for the 3 <sup>rd</sup> overtone to the layer by layer adsorption on the SiO <sub>2</sub> coated crystal for sensor 1. ....	169
<b>Figure 5.9:</b> QCM-D $\Delta f$ and $D$ vs time response for the 3 <sup>rd</sup> overtone to the layer by layer adsorption on the SiO <sub>2</sub> coated crystal for a non-biotinylated surface (sensor 3). ....	170
<b>Figure 5.10:</b> QCM-D $\Delta f$ vs time response for the 3 <sup>rd</sup> overtone to the layer by layer adsorption on the 4 crystal sensors. ....	171

<b>Figure 5.11:</b> QCM-D D vs time response for the 3 <sup>rd</sup> overtone to the layer by layer adsorption on the 4 crystal sensors. ....	171
<b>Figure 5.12:</b> Estimated avidin mass adsorbed to each of the 4 investigated sensors and the effect of 1 hour rinse in SPB solution. ....	172
<b>Figure 5.13:</b> The average calculated final avidin mass adsorbed in the carried-out measurement for specific and nonspecific binding to the QCM-D sensors. Error bars are $\pm$ SD .....	173
<b>Figure 5.14:</b> The raw data of the three measurements after biotinylation of the sensing region of one CM-OFET device and three measurements after avidin binding. ....	175
<b>Figure 5.15:</b> The average measured $I_{SDMax}$ for CM-OFET device 1 for (a) The three measured transfer characteristics with SPB pH8 solution on the biotinylated sensing surface and (b) The three measured transfer characteristics with SPB pH8 solution on the avidin covered sensing surface. Error bars are $\pm$ SD .....	175
<b>Figure 5.16:</b> The average measured $I_{SDMax}$ for CM-OFET device 2 for (a) The three measured transfer characteristics with SPB pH8 solution on the biotinylated sensing surface and (b) The three measured transfer characteristics with SPB pH8 solution on the avidin covered sensing surface. Error bars are $\pm$ SD .....	176
<b>Figure 5.17:</b> The average measured $I_{SDMax}$ for CM-OFET device 3 for (a) The three measured transfer characteristics with SPB pH8 solution on the biotinylated sensing surface and (b) The three measured transfer characteristics with SPB pH8 solution on the avidin covered sensing surface. Error bars are $\pm$ SD .....	176
<b>Figure 5.18:</b> The average measured $I_{SDMax}$ for CM-OFET device 4 for (a) The three measured transfer characteristics with SPB pH8 solution on the biotinylated sensing surface and (b) The three measured transfer characteristics with SPB pH8 solution on the avidin covered sensing surface. Error bars are $\pm$ SD .....	177
<b>Figure 5.19:</b> The average measured $I_{SDMax}$ for CM-OFET device 5 for (a) The three measured transfer characteristics with SPB pH8 solution on the biotinylated sensing surface and (b) The three measured transfer characteristics with SPB pH8 solution on the avidin covered sensing surface. Error bars are $\pm$ SD .....	177

**Figure 5.20:** The average measured  $I_{SDMax}$  for CM-OFET device 6 for (a) Three measured transfer characteristics with SPB pH8 solution on the biotinylated sensing surface and (b) The three measured transfer characteristics with SPB pH8 solution on the avidin covered sensing surface. Error bars are  $\pm SD$  .....178

**Figure 5.21:** The average measured  $I_{SDMax}$  for CM-OFET device 7 for (a) The single measured transfer characteristics with SPB pH8 solution on the biotinylated sensing surface and (b) The three measured transfer characteristics with SPB pH8 solution on the avidin covered sensing surface. Error bars are  $\pm SD$  .....178

**Figure 5.22:** The average measured  $I_{SDMax}$  for CM-OFET device 8 for (a) The single measured transfer characteristics with SPB pH8 solution on the biotinylated sensing surface and (b) The three measured transfer characteristics with SPB pH8 solution on the avidin covered sensing surface. Error bars are  $\pm SD$  .....179

**Figure 5.23:** The average measured  $I_{SDMax}$  for CM-OFET device 9 for (a) The single measured transfer characteristics with SPB pH8 solution on the biotinylated sensing surface and (b) The three measured transfer characteristics with SPB pH8 solution on the avidin covered sensing surface. Error bars are  $\pm SD$  .....179

**Figure 5.24:** Comparison of average percentage change in  $I_{SDMax}$  after avidin deposition  $I_{SDMax}$  (Av) relative to the  $I_{SDMax}$  (Biotin) before avidin deposition for the nine biotinylated CM-OFET devices. ....181

**Figure 5.25:** The average measured  $I_{SDMax}$  for CM-OFET device 1 for (a) The last three transfer characteristics recorded with SPB solution on silanized sensing surface, (b) The three measured transfer characteristics with SPB pH8 solution on nonspecific avidin covered sensing surface. Error bars are  $\pm SD$  .....182

**Figure 5.26:** The average measured  $I_{SDMax}$  for CM-OFET device 2 for (a) The last three transfer characteristics recorded with SPB solution on silanized sensing surface, (b) The three measured transfer characteristics with SPB pH8 solution on nonspecific avidin covered sensing surface. Error bars are  $\pm SD$  .....182

**Figure 5.27:** The average measured  $I_{SDMax}$  for CM-OFET device 3 for (a) The last three transfer characteristics recorded with SPB solution on silanized sensing surface, (b) The

three measured transfer characteristics with SPB pH8 solution on nonspecific avidin covered sensing surface. Error bars are $\pm$ SD .....	183
<b>Figure 5.28:</b> The average measured $I_{SDMax}$ for CM-OFET device 4 for (a) The last three transfer characteristics recorded with SPB solution on silanized sensing surface, (b) The three measured transfer characteristics with SPB pH8 solution on nonspecific avidin covered sensing surface. Error bars are $\pm$ SD .....	183
<b>Figure 5.29:</b> Average percentage change in $I_{SDMax}$ after avidin deposition $I_{SDMax}$ ( $A_V$ ) relative to $I_{SDMax}$ before avidin deposition for the non-biotinylated, silanized CM-OFET biosensors. Error bars are $\pm$ SD .....	184
<b>Figure 5.30:</b> (a) Cross section of CM-OFET device proposed by Lai et.al [43]; the employed materials are reported in the palette; (b) the layout of the device. ....	186
<b>Figure 5.31:</b> Capacitive coupling in the CM-OFET device and simplified equivalent circuit considering only capacitive contributions. ....	187
<b>Figure 5.32:</b> Charge distribution and charge conservation in floating gate. ....	188
<b>Figure 5.33:</b> Electrodes geometrical dimensions and the Si/SiO <sub>2</sub> CM-OFET device general layout. ....	189
<b>Figure 5.34:</b> The relationship between the control gate and drain area ratio and the contribution of each one in biasing the floating gate. ....	190
<b>Figure 5.35:</b> Al/Al <sub>2</sub> O <sub>3</sub> CM-OFET device with modified electrodes' layout. ....	190
<b>Figure 5.36:</b> An example of an output characteristics of a Si/SiO <sub>2</sub> CM-OFET device. ....	192
<b>Figure 5.37:</b> An example of an output characteristics of an Al/Al <sub>2</sub> O <sub>3</sub> CM-OFET device. ....	192
<b>Figure 5.38:</b> An example of a transfer characteristics of a Si/SiO <sub>2</sub> CM-OFET device (transistor on from start). ....	193
<b>Figure 5.39:</b> An example of a transfer characteristics of a Si/SiO <sub>2</sub> CM-OFET device (transistor turn on in the positive gate voltage region). ....	194
<b>Figure 5.40:</b> An example of a transfer characteristics of an Al/Al <sub>2</sub> O <sub>3</sub> CM-OFET device. ....	194

**Figure 5.41:** Comparison between the effective S/D areas  $A_S/A_D$  in the CM-OFET Si/SiO<sub>2</sub> and Al/Al<sub>2</sub>O<sub>3</sub> devices ( $W=1\text{mm}$  and  $L_S=L_D=10.5\text{mm}$  for Si/SiO<sub>2</sub> devices and  $W=1\text{mm}$  and  $L_S=L_D=1.5\text{mm}$  for Al/Al<sub>2</sub>O<sub>3</sub> devices). .....197

**Figure 6.1:** Experimental results of pH sensing using an Al/Al<sub>2</sub>O<sub>3</sub> CM-OFET device, the figure shows the percentage change in  $I_{SD\text{Max}}$  for three independent measurements (at 3 different pH levels). Here, the transfer characteristics of the device were measured 25 mins after introduction of the test pH solution. ....208

**Figure 6.2:** Theoretical effect of mobility on maximum source drain current change per unit gate voltage shift for Al/Al<sub>2</sub>O<sub>3</sub> CM-OFET (Al<sub>2</sub>O<sub>3</sub> 40nm). ....209

## List of abbreviations

$\pi$ bond	Pi bond
$\sigma$ bond	Sigma bond
a-Si:H	Hydrogenated amorphous silicon
ALD	Atomic layer deposition
APTES	3-aminopropyltriethoxysilane
BGD	Bässler's Gaussian disorder model
CM-OFET	Charge Modulated-organic field effect transistor
D	Drain electrode
DG-OFET	Dual Gate-organic field effect transistor
DNA	Deoxyribonucleic acid
EDL	Electrical Double Layers
EGOFET	Electrolyte-gated organic field effect transistor
ELISA	Enzyme-linked immunosorbent assay
G	Gate electrode
GOx	Glucose Oxidase
HOMO	Highest occupied molecular orbital
IPA	Isopropyl alcohol
ISOFET	Ion-Sensitive Organic Field Effect Transistor
LCAO	Linear Combination of Atomic Orbitals
LCD	Liquid-crystal display
LOC	Lab-on-chip
LOD	Limit of detection
LUMO	Lowest unoccupied molecular orbital

MTR	Multiple trap and release
NHS	N-hydroxysulfosuccinimide
OE	Organic electronic
OECT	Organic Electrochemical Transistor
OED	Organic electronic device
OFET	Organic field effect transistor
OLED	Organic Light-Emitting Diode
OPV	Organic Photovoltaic Devices
OSC	Organic semiconductor
OTFT	Organic thin film transistor
OTS	Octadecyltrichlorosilane
PDMS	Polydimethylsiloxane
PE-ALD	Plasma enhanced- Atomic layer deposition
PER	Percolation model
P $\alpha$ MS	Poly( $\alpha$ -methyl styrene)
QCM	Quartz crystal microbalance
QCM-D	Quartz crystal microbalance with dissipation
RFID	Radio frequency identification
RNA	Ribonucleic acid
rpm	Revolutions per minute
S	Source/Sub-threshold slope
SAM	Self-assembled monolayer
SMU	Source-measurement unit
SPB	Sodium phosphate buffer
SPR	Surface plasmon resonance

Tips-pentacene	6,13-Bis(triisopropylsilylethynyl)-pentacene
TMA	Trimethyl Aluminium
UV	Ultraviolet
VRH	Variable range hopping
XPS	x-ray photoelectron spectroscopy

# Acknowledgements

First and foremost, I praise Allah the Almighty for giving me the power, patience and strength of mind to complete this thesis.

“He who does not thank people, does not thank Allah”, so for that, I would like to take this opportunity to extend my thanks to all the people whom have contributed to the completion of my thesis.

I would like to express my gratitude to my supervisor Dr. Steven Johnson for his scientific support, help and patience throughout this doctorate research, thank you for all your insightful feedbacks.

My heartfelt gratitude to Professor Mohamed El Gomati for all his valuable advices and my thanks extends to his family whom have been all but supportive for me and my wife during our study years.

Thank you to Dr. Alison Parkin for her discussion and thoughts on the research.

I would like to thank all the present and past group members of the Bio-inspired Lab, special thanks to Pepe for his generous help and encouragement throughout the PhD years. My thanks also to Elena for her assistance during the research work.

Huge thanks goes to Louis Fry-Bouriaux for his generous time to perform the ALD deposition, I really enjoyed the fruitful conversations we had every time I come over to Leeds.

I should not forget to thank the experimental officers for their support to my research activities, particularly, late Jonathan Creamer, sadly we could not celebrate my degree together. Thank you to Ian and Charan as well.

Thanks to Camilla and Helen in the postgraduate office for taking care of all the administrative support and services.

A big thank you to all the department personnel whom helped to complete this project in any shape or form.

I cannot thank enough my lovely wife, who has stood by me through all the ups and downs of my research. You were an exceptional companion, without your help, support, sacrifices and presence this thesis would not have been completed.

Deep thank you to my family, Dad, stepmother, brother and my sister and her family for their encouragement and passionate support all the way.

My sincere gratitude goes out to all my in-law family uncle Monsef, aunt Halima, Mohammed, Marwan, Osama and Yosef, your prayers, concerns and encouragement was priceless.

My big thanks to all the Libyan families in York whom we had share good times with.

## Declaration

I declare that the work presented in this thesis, if not otherwise stated, is my own. Some of the material presented within this thesis has previously been published in the following conference:

Ben Khaial, A. and Johnson, S. (2017), Charge-modulated field-effect transistor biosensors based on solution processed TIPS-pentacene, Biodetection & Biosensors Conference, Cambridge, UK

# Chapter 1: Introduction

## 1.1 Biosensors

From identifying contaminants and toxins to ensure food product safety, to detecting biomarkers of disease and monitoring pollutants in the environment, technologies for detection and quantification of chemical and biological molecules are today an integral part of the modern world. A broad range of technologies, generally known as *biosensors*, have been demonstrated to meet these analytical challenges, and the innovation of novel biosensors with improved sensitivity, speed and applicability remains a significant research activity. For example, in 2018 alone, a total of 1,570 articles were published containing the word biosensor in the title (data from Google scholar).

The term “biosensor” is believed to have been coined by Cammann in 1977 [1-2], however, it is widely accepted that the first biosensor can be traced back to 1962 to the work of Leyland C. Clark, the inventor of Clark Oxygen Electrode [3-6]. His concept, which earned him the title of the father of the biosensor, involved electrochemical reduction of oxygen as a method of quantifying dissolved oxygen content. This approach laid the foundation for one of the most commercially important biosensors; the electrochemical glucose biosensor which provides an approach for the diagnosis and management of diabetes through the detection and quantification of glucose using glucose oxidase (GOx) enzyme immobilized on an electrode [3,5,7]. Today, biosensor technologies have become a multi-billion dollars market [8-10] and the development of novel biosensors continues to be a major research activity that spans the scientific disciplines and impacts on a wide range of application areas including clinical and medical diagnosis, food safety, environmental monitoring, precision agricultural, industrial monitoring, homeland security and defence [3-6,11-13].

Generally, biosensors are analytical devices that combine a biological or biologically derived recognition element with a physicochemical detector element commonly referred to as “transducer” [3-4,11-12]. The role of the transducer is to convert a specific interaction between the recognition element and a target analyte into a measurable signal that can be

quantified to provide a measure of analyte concentration [3-5,12]. Specificity to the required analyte is provided by the biological recognition element.

Although multiple recognition elements and transducer mechanisms have been demonstrated, the fundamentals of a biosensor remain the same and can be modelled by a four components system as illustrated in figure 1.1. The first component of the generic biosensor is the analyte. This is the target chemical or biological substance that is to be detected and is often dissolved in a complex aqueous matrix. For example, in clinical diagnostics the target analyte is often a protein biomarker indicative of disease that needs to be detected in a complex clinical sample, such as plasma or urine. The second component is the bio-recognition element which is able to interact with the target analyte specifically and with high affinity, in order to recognise the target analyte despite the complex sample background. The third entity of the biosensor is the transducer which translates the interaction between the bioanalyte and bio-recognition into a quantifiable response. The final part of the system is the instrumentation that processes the signal from the transducer and presents it to the user in a user-friendly format. This unit often comprises electronic circuitry, that may amplify, filter and perform computation in order to quantify the detected signal, integrated with a display unit used to feed information back to the user [6,9,11-12].

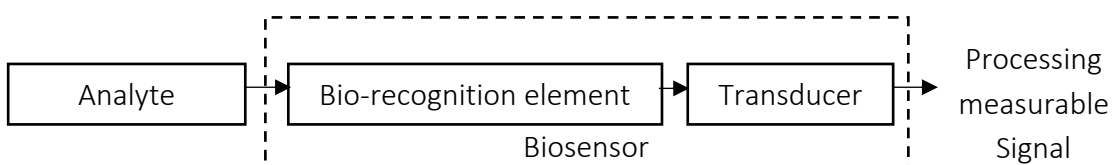


**Figure 1.1:** The generic biosensor model.

It is widely accepted that the term biosensor refers to the integrated ensemble of the bio-recognition element and transducer, however due to the essential role of the processing unit, some consider the biosensor as a three-element system [4,8]

A range of bio-recognition elements have been implemented in biosensors, including enzymes, nucleic acids (RNA and DNA), antibodies and antibody mimetics, antigens, living cells or tissues. The choice of bio-recognition element depends, to a large degree, on the targeted analyte. For example, bio-recognition elements based on oligonucleotides are

best suited for the detection of DNA and RNA biomarkers while the selectivity and specificity of antibodies are ideally suited to the detection of protein biomarkers [12,15-16]. Similarly, a wide range of transduction elements have been demonstrated each sensitive to a different physiochemical change that occur following the specific interaction between the target analyte and its associated bio-recognition element. These include transducers sensitive to a change in electric current/potential, conductance, refractive index, mass, viscosity or temperature [3,5-6,11,14]. The choice of transducer is often based on the physiochemical parameter(s) that change as a result of the interaction between the targeted analyte and the bio-recognition element.

A key consideration for biosensor engineering is the method of integrating the bio-recognition element with the transducer, a process often referred to as “immobilization”. The process of immobilization is critical to ensure the functionality of the bio-recognition element is preserved following integration and that the transducer remains sensitive to interactions between the analyte and bio-recognition element [5-6,17-18]. The most common immobilization methods are physical adsorption [19], covalent binding [20], matrix entrapment [21], cross-linking [22] and encapsulation [23].

The analytical performance of a biosensor is typically quantified through a number of attributes or figures of merit. For example, biosensor linearity quantifies the accuracy with which the measured response shifts proportionally, i.e. linearly, with analyte concentration. [17-24]. Perhaps the most important figure of merit is biosensor sensitivity, also known as the limit of detection (LOD), which quantifies the minimum concentration of target analyte that can be detected with statistical confidence [25-28]. In addition to technical attributes, a biosensor should ideally also meet a number of more performance related requirements. For example, repeatability or reproducibility is a measure of the ability of a biosensor to yield identical responses in duplicate assays i.e. provide the same measure of analyte concentration when challenged with identical samples [24]. Repeatability is a basic requirement for biosensors whether the sample investigated is simple (i.e. contains only the target analyte) or the target analyte is dissolved in a complex sample matrix. In complex sample matrices where the target analyte is present within a background of other molecular species, it is crucial that the sensor only interacts with the analyte of interest. This ability to detect a specific analyte within a complex sample matrix

is known as specificity [17-24]. High specificity is a major challenge to biosensors, particularly those used in clinical applications where a clinical sample (such as serum) is a highly complex mixture of biological molecules. Here, complete specificity is often unachievable as the transducer is often also sensitive to interference and non-specific interactions from other substances in the sample matrix, complicating the biosensor response. Typically, a compromise is often sought, where interference and non-specific interactions are minimized and sensitivity to the targeted analyte in the sample is maximized; this is known as selectivity [11,24-25,29]. It should be noted that this distinction between the selectivity and specificity is not always considered and the two terms are more often used interchangeably. For biosensor commercialisation, a range of other attributes need also to be considered, which often relate to the specific application, including response time, size, durability, amenability for mass manufacturing and cost [3,5-6,30].

### **1.1.1 Exemplar Biosensors: ELISA and SPR-based biosensors**

Two of the most commercial successful stories of biosensor that have been applied widely to detect numerous biomolecules are the enzyme-linked immunosorbent assay (ELISA) and biosensors based on surface plasmon resonance (SPR) technology.

#### **1.1.1.1 Enzyme-linked immunosorbent assay**

In the simplest format of ELISA, an antigen is detected using its associated antibody which is linked to a reporter molecule, typically an enzyme hence the name ELISA, that is capable of producing a colorimetric response. Typical ELISA assays are performed in microwell plates and the basic process comprises two phases; the capture phase, where the target antigen is captured and immobilized to the plate, followed by the detection phase where the captured antigen is labelled via a specific antibody to enable detection (see figure 1.2). The capture phase can either be direct or indirect (also referred to as a “sandwich” assay). In direct capturing, the target antigen is directly immobilized to the assay plate. In contrast, indirect capturing employs an antibody specific to the target antigen that is first coated to the surface of the microwell plate. Subsequent binding of the target antigen to the immobilised antibody allows the antigen to be tethered to the surface. Once immobilised, detection and quantification of the target analyte is achieved using an enzyme-labelled, analyte-specific antibody. Again, the detection phase can be direct or indirect. In direct detection, the captured antigen is complexed with an antibody that is linked to an enzyme,

while in indirect detection the captured antigen is first complexed with an unconjugated antibody (referred to as primary detection antibody), which subsequently binds to a secondary detection antibody that is conjugated with an enzyme. For both detection methods, once the enzyme-conjugated antibody is bound and the unbound antibodies are washed away, a substrate for the enzyme is added, and catalysis by the enzyme leads to a change in colour either chromogenically or by means of chemifluorescence or chemiluminescence indicating the presence of the antigen [31-32].

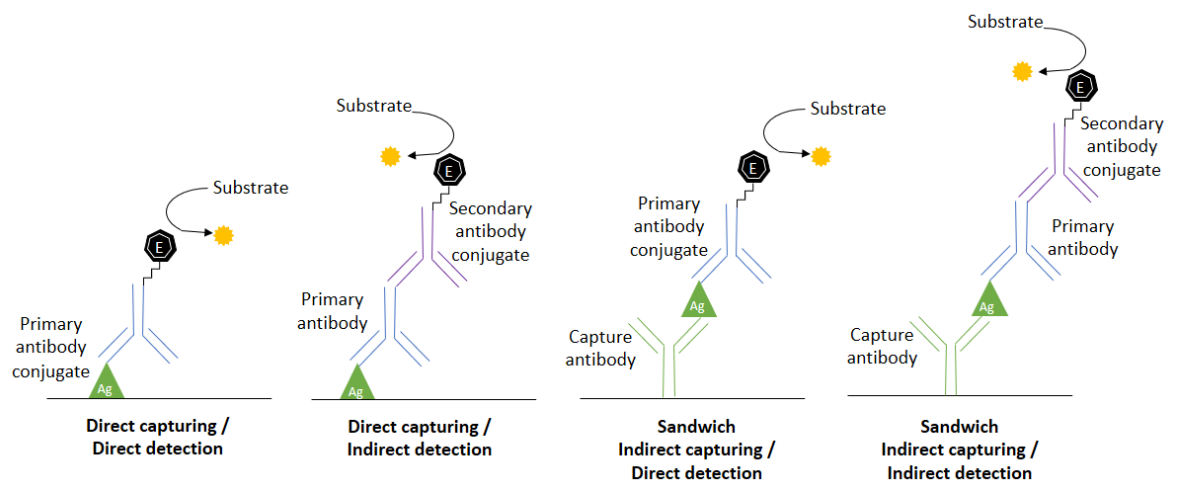


**Figure 1.2:** The four different combinations of antigen capture and detection used commonly in ELISA.

The most widely used ELISA methodology is indirect capture with indirect detection. This is because antigen detection is effectively performed twice to increase specificity; first using a pre-immobilized capture antibody and second with the primary detection antibody. Furthermore, in indirect detection, the primary detection antibody can bind multiple secondary detection antibodies. As each secondary antibody is conjugated with a reporter enzyme, the final signal when the substrate is added is amplified. This signal can be further amplified by conjugating the primary antibody with multiple reporter enzymes, for example using the multivalent biotin–avidin interaction (the biotin – avidin interaction will be discussed further in chapter 5) [31,33-34].

### 1.1.1.2 Surface plasmon resonance based biosensors

ELISA belongs to a class of biosensor known as labelled biosensors. These biosensors rely on the addition of a label, typically fluorescent dyes, radioactive isotopes or redox-active

labels (conjugated enzymes), to quantify detection [11,35]. Although generally considered robust, label-based biosensors have fundamental shortcomings. The labelling process itself can impede the antibody-antigen interaction, for example through changes in molecular conformation, a reduction in the bioactivity and mobility of labelled molecules, blocking of active binding sites and an increase in steric hindrance. The labelling process is also costly and can take a considerable amount of time, making real-time measurement impractical [36-39]. Label-free biosensors on the other hand essentially eliminate complexity, time, and cost associated with labelling techniques. Label-free biosensors detection requires the use of a transducer that is sensitive to changes in physicochemical properties that occur inherently following biochemical binding [9,36-38,40]. For example, surface plasmon resonance (SPR) detects local changes in refractive index that occur following binding of an analyte to a surface-immobilized bio-recognition element.

SPR is an optical phenomenon that can occur when light is reflected from a conducting film at the interface between two media having different refractive indices. In SPR, light is focused through a glass prism onto a conducting film covering a glass substrate. Above a critical angle of incidence, total internal reflection occurs and the reflected light is detected on the reflection side of the prism. Under total internal reflection conditions, the interaction of the incident light with the sea of free electrons in the conducting film creates a plasmonic wave on the metal surface (surface plasmons). The evanescent electrical field of this plasmonic wave extends hundreds of nanometers into the medium adjacent to gold surface. At a certain angle of incidence (known as resonance angle), the plasmons resonate with the incident light, resulting in absorption of light at that angle. This creates a dark region in the reflected beam. A change in the refractive index of the medium above the surface of the metal film, for example due to analyte binding to the surface, results in a shift in the critical angle which can be detected and quantified to provide a label-free measure of analyte binding [41-44].

The SPR sensor, often a glass substrate coated with thin metallic film, is typically functionalized with the bio-recognition element. This sensor is integrated into an optical detection system, commonly using the kretschmann configuration (see figure 1.3a), where the sensor is mounted on top of a prism. Here, binding between the bio-recognition element and its associated analyte will result in a local change in refractive index which

leads, in turn, to a shift in the resonance angle [41-42,45-47]. The local change in refractive index and consequently the resonance angular shift is observed by the shift in the characteristic reflectivity curve measured at the light detector (see figure 1.3b). The magnitude of the angular shift provides information regarding the surface concentration of analyte, while monitoring the reflectivity curve as a function of time during the course of the interaction provides information regarding the kinetics of a biomolecular binding event, as shown schematically in figure 1.3c.

#### 1.1.1.2.1 Label-free biosensors for real-time measurements of biomolecular interactions

The change in SPR reflectivity can be plotted as a function of time to produce a sensorgram that provides information regarding the kinetics of a biomolecular interaction and allows the different stages of a binding event to be visualized and evaluated. A typical sensorgram is displayed in figure 1.4 it comprises of an association phase, equilibrium phase, dissociation phase and finally a regeneration phase.

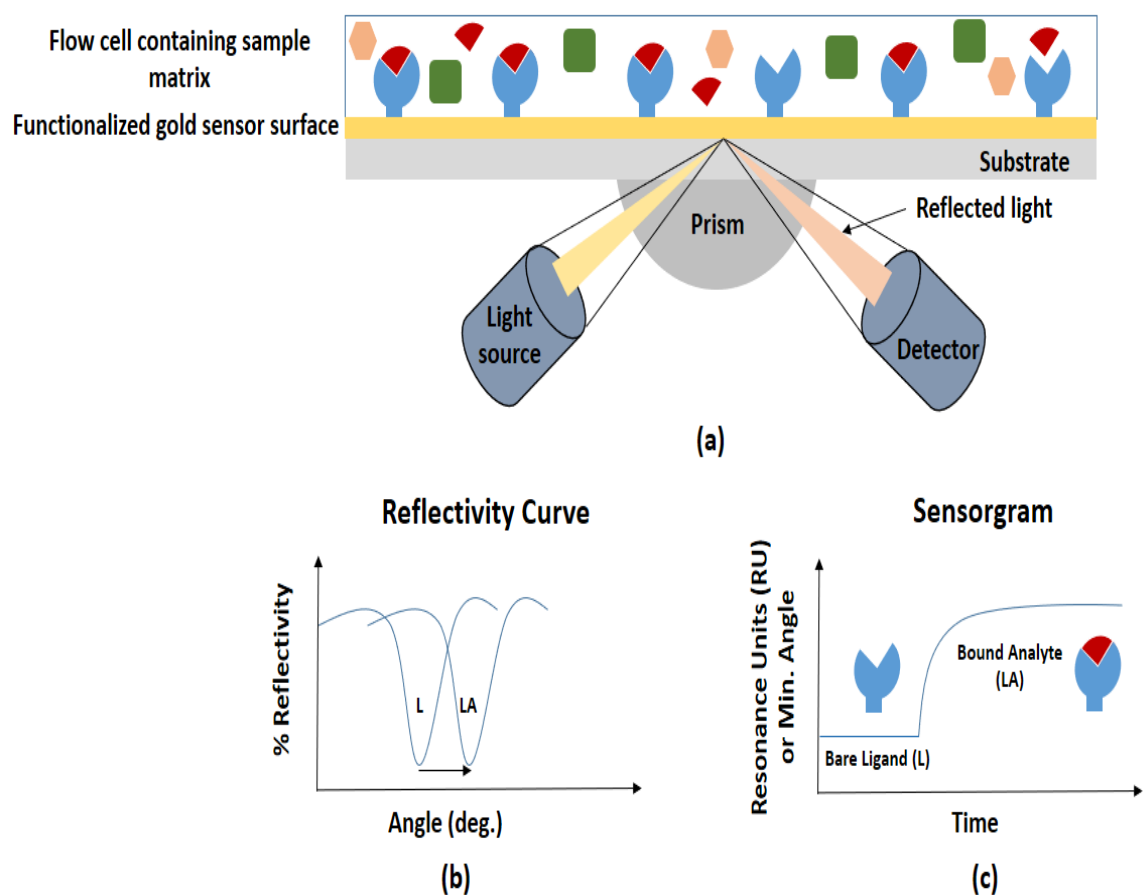


**Figure 1.3:** (a) A setup of the SPR detection techniques using the Kretschmann configuration, (b) the detected reflectivity response and (c) how the angular shift is translated in a sensorgram [48].

The association phase which occurs immediately after sample injection, is associated with binding of molecules from solution to surface immobilised bio-receptors. After a certain time, the rate of binding and dissociation are in equilibrium and a steady state is reached. The magnitude of the biosensor response at steady state is dependent on the concentration of analyte in solution. When the analyte injection is stopped, and an analyte-free buffer is injected to the system, dissociation dominates the sensorgram leading to a decrease in biosensor response. With sufficient time, the response will ideally return to the initial condition however, depending on the dissociation rate, a regeneration step maybe necessary to remove all bound analyte molecules.

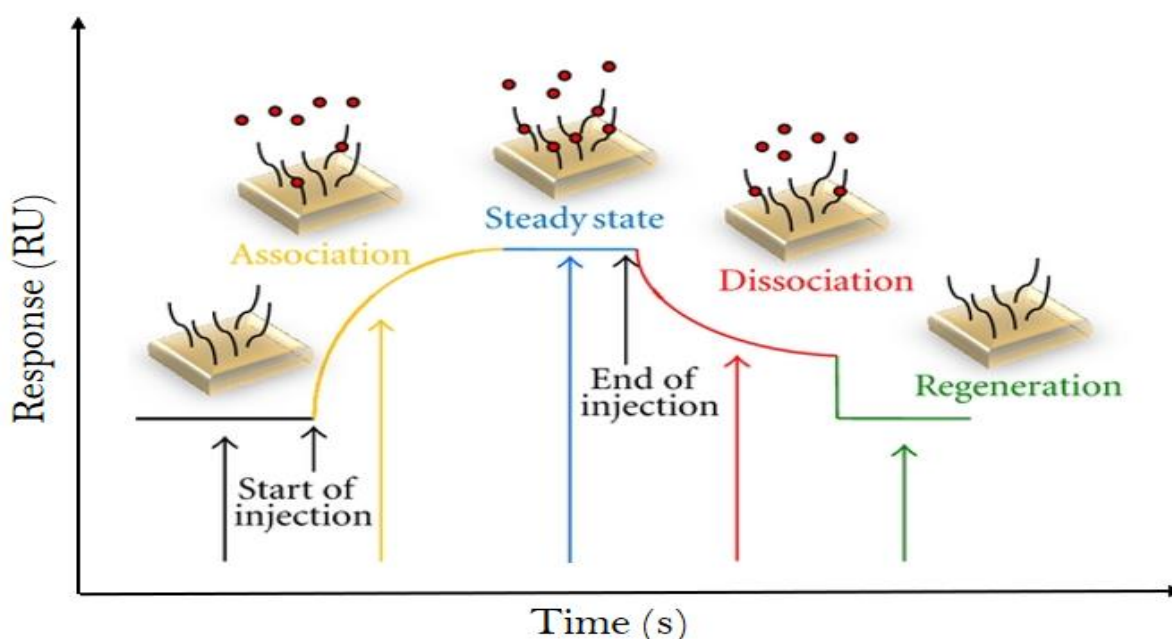
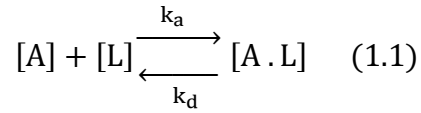


**Figure 1.4:** Typical SPR sensorgram showing the four phases: association phase, steady state or equilibrium phase, dissociation phase, and regeneration phase [49].

The sensorgram can give a detailed picture of a biomolecular interaction and valuable information can be extracted from it, including the association and dissociation rates and binding affinity. The simplest and one of the most widely used kinetic binding model to describe molecular interactions is the so-called Langmuir model (also termed 1:1 interaction model or 1:1 Langmuir model). This model was developed by Irving Langmuir in 1916 to describe the adsorption of gas onto a solid surface [41, 50-51]. This model describes a reversible biomolecular interaction between an analyte, A, at a concentration of [A] and an immobilized ligand, L, at a concentration [L]:



In equation (1.1),  $k_a$  and  $k_d$  are the association and dissociation rate constants, respectively [A] is the concentration of analyte, [L] is the concentration of immobilized ligand and [A.L] is the concentration of the analyte-ligand complex. This model assumes that all binding sites are equivalent, that binding events are independent i.e. one ligand molecule interacts with one analyte molecule with no lateral interaction between the adsorbed analyte molecules, and only a monolayer is formed at maximum adsorption [52-53].

Combining the dynamic equilibrium equation with the sensorgram response provide estimates of both association and dissociation rate constants ( $k_a$  and  $k_d$ ). This is usually done from the net rate equation of the complex formation which is expressed as:

$$\frac{d[A \cdot L]}{dt} = k_a \cdot [A] \cdot [L] - k_d \cdot [A \cdot L] \quad (1.2)$$

In a label-free biosensor, such as one based on SPR, the response, R, is proportional to the concentration of the analyte-ligand complex, [A.L]. The relationship of equation (1.2) can then be rewritten as:

$$\frac{dR}{dt} = k_a \cdot C \cdot (R_{max} - R) - k_d \cdot R \quad (1.3)$$

Where R is the label-free biosensor response at time t which is proportional to [A.L],  $R_{max}$  is the maximum response and C is the concentration of the analyte in solution, [A]. Here, [L] is expressed as  $(R_{max} - R)$  because at any time the concentration of free ligand equals the concentration of maximum analyte binding capacity ( $R_{max}$ ) minus the concentration of the complex formed R [41, 53-54].

Solving this equation at the association and dissociation phases of the sensorgram gives values of the association and dissociation rate constants,  $k_a$  and  $k_d$ . From these rate constants it is then possible to calculate the equilibrium association and dissociation constants,  $K_A$  and  $K_D$  respectively, which are defined as:

$$K_A = \frac{k_a}{k_d}, K_D = \frac{k_d}{k_a}$$

These two equilibrium constants are the characteristic of the affinity between two biomolecules i.e. the strength of the interaction. More detail will be provided in chapter 5.

This approach to quantifying biomolecular interactions is commonly referred to as kinetic analysis where the kinetics of the interaction can be measured. For time-independent measurements, such as those performed in ELISA, an alternative approach known as equilibrium analysis can be implemented. In equilibrium analysis, a Langmuir binding isotherm can be generated by challenging the biosensor with a series of solution of differing analyte concentration and plotting the corresponding equilibrium response (or steady-state response as in figure 1.4) against analyte concentration, as shown in figure 1.5.

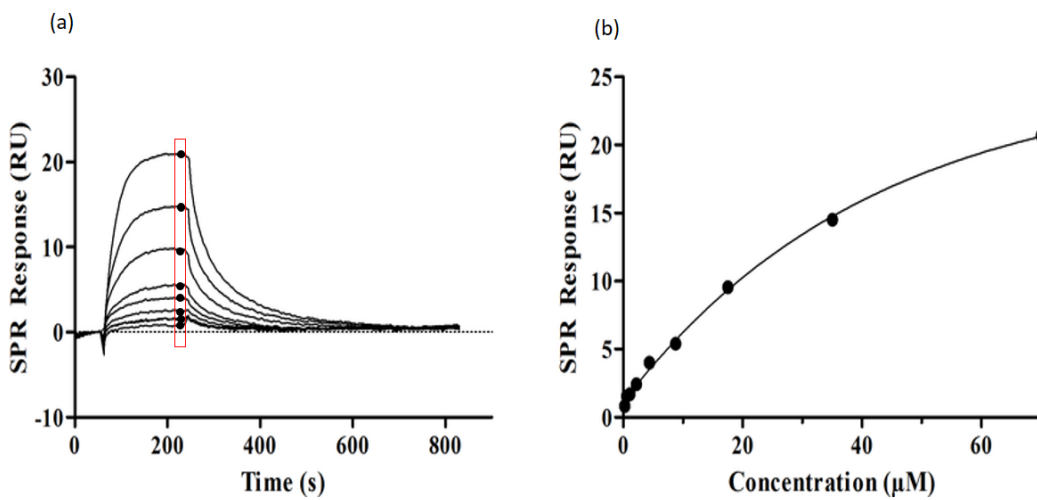


**Figure 1.5:** (a) An example of SPR sensorgrams generated by challenging a surface functionalized with a specific bio-recognition element with a range of solutions of differing analyte concentrations, (b) SPR response at equilibrium from all sensorgrams from (a) plotted against analyte concentration [55].

At equilibrium, the net rate of the complex formation,  $dR/dt = 0$ . Equation (1.3) thus becomes:

$$0 = k_a \cdot C \cdot (R_{max} - R) - k_d \cdot R \quad (1.4)$$

By rearranging this equation and defining the response,  $R$ , as the equilibrium response,  $R_{eq}$  (i.e.  $R = R_{eq}$ ), a new equation can be formed to estimate the equilibrium dissociation constant,  $K_D$ , between the analyte and the ligand as follows:

$$R_{eq} = \frac{C R_{max}}{K_D + C} \quad (1.5)$$

It can be seen that in this equation when the concentration of the analyte is equal to  $K_D$  ( $C = K_D$ ), then  $R_{eq}/R_{max} = 1/2$ . Therefore, the  $K_D$  value can be easily estimated from a plot of equilibrium response against analyte concentration ( $R_{eq}$  vs  $C$ ), as the concentration that yields half the maximum response.

### **1.1.2 Next generation biosensors**

The label-free nature of SPR provides significant advantages to traditional labelled approaches such as ELISA. These include a reduction in laborious sample processing steps, lower reagent costs and reduced sample volumes. Moreover, the ability to monitor biomolecular interactions in real time allows the determination of binding kinetics and not just binding affinity as in ELISA. Despite these advantages, SPR equipment is significantly more costly than the equipment required for ELISA. For example, commercial SPR instruments such as Biacore models costs hundreds of thousands of dollars, moreover, they require consumable sensor chips which each cost tens of dollars. ELISA and SPR also require trained personnel to perform the assay. There is thus significant interest in alternative, label-free biosensor technologies that reduce the complexity and cost of existing, commercial biosensors.

Many new technologies are being explored and exploited for the development of each component of the biosensing system, from the bio-recognition element and associated transducer to the processing part with the aim of identifying innovative solutions to current limitations in the field of biosensing. However, despite significant research effort into innovative label-free biosensors, it is striking that so few have penetrated the commercial market. Much of this can be explained by the challenges associated with manufacturing biosensors in a cost-effective way. [8,56-57].

Printing technology and microfluidics among others are at the forefront of technologies that are shaping and advancing the modern biosensor field and that have the potential to reduce manufacturing costs [8,58]. Printing technology enables mass production and microfluidics integration allows the use of low sample and reagent volumes and lower power consumption offering significant cost reduction [4,12]. One of the devices that can be made using printing technologies and can be integrated with microfluidic technologies

is organic electronic devices (OEDs). The next section provides a general overview of OEDs before proceeding to discuss a specific family of OEDs, namely organic thin film transistors, and their application in biosensing.

## 1.2 Organic Electronic Devices

Organic electronic devices (OEDs) are electronic devices that have one or more of its fundamental layers (semiconducting, conducting or insulating) made of organic materials [59]. Although organic materials have been used in the electronic industry for many years either as an insulator or a sacrificial layer, e.g. photoresist [60-61], the discovery of organic materials that exhibit electrical conductivity, transformed the role of organic materials in the fabrication of electronic devices. Early organic electronic (OE) materials exhibited very low electrical conductivity and, as a result, much of the early work into OEDs was limited to academic research. Since then, improvements in the electronic properties of OE materials have led to the demonstration of many OEDs, from both industry and academia alike [61-62]. While the performance of OEDs remained below that of more traditional, inorganic electronics (largely dominated by silicon), industrial interest in OEDs was motivated by the possibility of manufacturing devices at significantly lower costs, as explained schematically in figure 1.6.

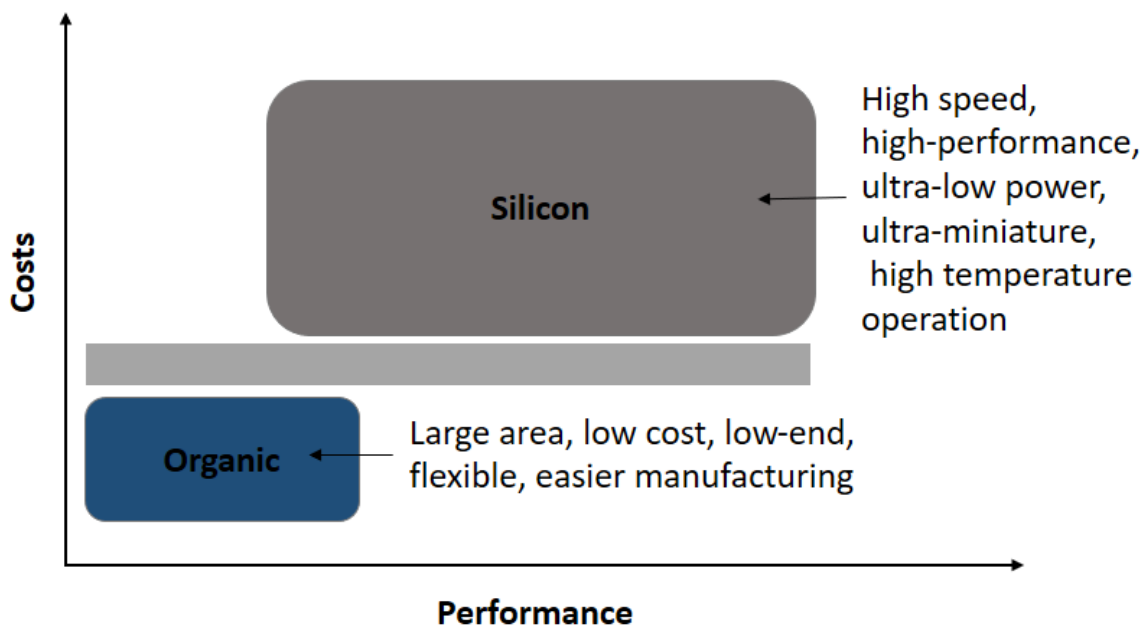


**Figure 1.6:** cost vs performance comparison of silicon-based devices and OEDs [61].

Currently OEDs have found widespread use in the low resolution, low speed, mass production electronics market such as for smart cards and labels, flat, flexible and large displays, logic for radio-frequency identification (RFID) tags and sensors [61,63-65].

From a solid-state perspective, organic semiconductors (OSCs) are very different to their inorganic counterparts. This is because they are formed from organic molecules which are bound together by relatively weak van der Waals interactions, in contrast to the covalent bonding between atoms observed in inorganic semiconductors. Consequently, the band structure and charge transport mechanisms are fundamentally different. Specifically, the weak intermolecular electronic coupling in OSC, typically results in movement of charge carriers via an inefficient process of 'hopping' between molecules. This leads to a reduction in the electron and hole mobility compared to that observed in inorganic semiconductors, where the periodic structure associated with covalent bonding results in an energy band where charge carriers can diffuse freely with limited scattering, hence feature relatively high mobility [60,66-68].

From the manufacturing and commercial perspectives, organic semiconductors offer some very appealing advantages over inorganic semiconductors. Unlike inorganic semiconductors, which are highly crystalline and require extremely high purity and rigorous processing under highly controlled conditions, organic semiconductors are generally much less expensive, and their synthesis involve inexpensive reactants and reaction conditions. Manufacturing of electronic devices based on inorganic semiconductor requires high-temperature, high-vacuum deposition, and costly patterning procedures. In contrast, processing temperatures for organic semiconductors are typically low (generally less < 100 °C), enabling the fabrication of electronic devices on plastic and flexible substrates. Moreover, many organic semiconductors are soluble in common solvents which allows processing directly from solution using low cost technologies such as roll-to-roll and inkjet printing. This allows the production of OEDs on large scales and at a fraction of the cost. It is worth noting that fabrication processes for inorganic semiconductor-based devices are standardized which is of great importance from the manufacturing point of view. At least for now, such standardization has not been applied to organic semiconductor-based devices. Finally, advances in synthetic chemistry make it possible to tailor the electronic and optical properties of organic semiconductors such that they can be engineered for a

specific application. [69-70]. Table 1.1 summarizes some of the main differences between organic and inorganic semiconductors.

**Table 1.1:** The main differences between organic and inorganic semiconductors.

	<b>Organic semiconductors</b>	<b>Inorganic semiconductors</b>
Bonding	van der Waals interaction between molecules	covalent
Charge transport	Hopping transport	Band transport
Charge carrier mobility	low	high
Mechanically	Flexible	Inflexible
Fabrication and processing	Simple and cheap	Complicated and expensive (but standardize)

The main active OEDs that have seen significant investigation and investment are. 1) Organic Light-Emitting Diodes (OLEDs) which are now sufficiently advanced that they are widely used in the electronics market. 2) Organic Photovoltaic Devices, (OPVs), which, despite having efficiencies lower than their inorganic counterpart, are constantly improving, and with the advantage of low cost materials and processes, soon the balance of efficiency and cost may shift towards OPVs especially for large solar panels [66,71]. 3) Organic Thin-Film Transistors (OTFTs) which exhibit performances competing with that of transistors based on amorphous silicon (a-Si:H), making them a competitive replacement in liquid crystal displays and similar applications [61,66].

Another application for low-cost OTFTs that has recently gained attention, is the use of OTFTs in chemical and biological sensing applications. Here, the relatively low charge carrier mobility associated with organic semiconductors is not critical, as detection can take place over tens or even hundreds of seconds [72]. Before discussing the merits of OTFT based sensors, it is worth appreciating the interesting conduction mechanisms of organic materials which make their conductivity distinct from the conventional inorganic counterpart.

### **1.3 Conductivity in organic materials**

The bulk conductivity of organic materials arises from two charge transport mechanisms; *intra-chain* where charge transport occurs within a single molecule or chain and *inter-chain* which describes charge transport between molecules or chains.

### 1.3.1 Intra-molecular charge transport

Intra-molecular charge transport originates from the ability of carbon atoms, the fundamental building block of organic molecules, to form hybrid orbitals. On the atomic level, carbon has six electrons, two core electrons and four valence electrons. In the ground state, the electrons in a carbon atom are distributed over its atomic orbitals in a  $1s^2 2s^2 2p^2$  configuration as in table 1.2.

**Table 1.2:** Electrons distribution on carbon's atomic orbitals.

Orbital	1s	2s	2p <sub>x</sub>	2p <sub>y</sub>	2p <sub>z</sub>
No. of electrons	2	2	1	1	

Without hybridization, the structure of a carbon molecule, such as methane (CH<sub>4</sub>), would be defined by the geometric orientation of the atomic orbitals. However, mixing of the atomic orbitals of carbon can occur in order to form energetically favourable molecular orbitals which differ in energy and orientation from the atomic orbitals. This process is known as orbital hybridization, or simply hybridization. In carbon molecules, an electron from the 2s carbon orbital can be promoted to the 2p<sub>z</sub> orbitals (see figure 1.7) to yield four orbitals each occupied by a single electron. In order to minimise energy, the resulting singly occupied s-orbital mixes with one (or more) of the p-orbitals to create a new hybrid orbital known as sp-orbital. Three hybridization possibilities can occur depending on the number of p-orbitals contributing in the hybridization, namely sp, sp<sup>2</sup> or sp<sup>3</sup> [73-75].

In sp<sup>3</sup> hybridization, the s-orbital mixes with each of the three p-orbitals to create four singly occupied sp<sup>3</sup>-orbitals. The angle between sp<sup>3</sup>-orbitals is 109.5°, which results in the tetrahedral crystal structure of crystal. An example of a molecule containing sp<sup>3</sup> hybridization is ethane C<sub>2</sub>H<sub>6</sub> (see figure 1.8). Here, both carbon atoms are sp<sup>3</sup> hybridized. Three sp<sup>3</sup>-orbitals from each atom form σ-bonds (direct orbital overlap) with the s-orbital of three H atoms. The remaining sp<sup>3</sup>-orbitals overlap head-on to create a σ-bond between the C atoms which lies along the plane of the molecule.

sp<sup>2</sup> hybridization arises from a combination of one s-orbital and two p-orbitals. This results in three sp<sup>2</sup>-orbitals that lie in the same plane, separated by 120°, plus one non-hybridized

p-orbital perpendicular to the  $sp^2$ -orbitals. Graphite is a notable example of a carbon crystal formed from  $sp^2$ -orbitals. Here, the carbon atoms are arranged in single layers, bound together by  $\sigma$ -bonds from overlapping  $sp^2$ -orbitals with the remaining p-orbitals forming  $\pi$ -bonds (partial orbital overlap). A similar structure is also observed in simple molecules, such as ethene, shown in figure 1.9. As a result of the reduced orbital overlap compared to  $\sigma$  bond and the relatively large spatial distance from the atom, the  $\pi$  bond is weaker. This results in a double bond between the two carbon atoms. The electron in the  $\pi$  bond, also called  $\pi$ -electron, is “delocalized” between the two carbon neighbouring atoms and lies above and below the molecular axis. The delocalization of  $\pi$ -electrons can extend over an entire molecule giving rise to intra-molecular charge transport [73-75].

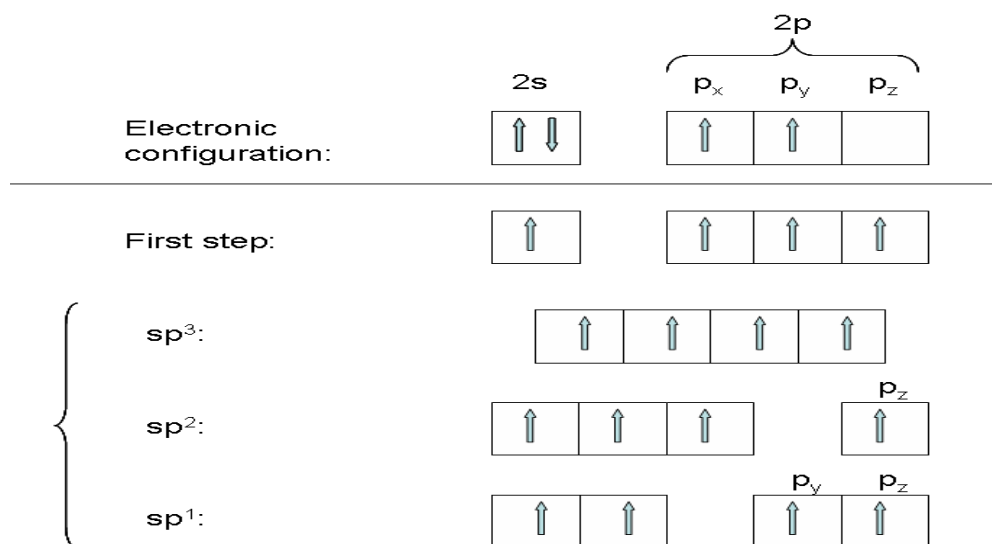


**Figure 1.7:** Types of the orbitals hybridization in the carbon atom [75].

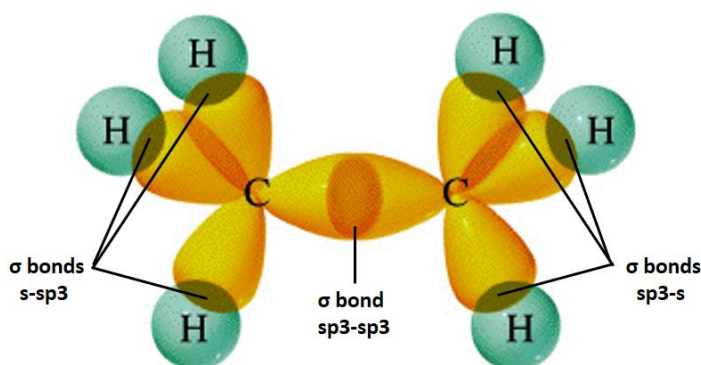


**Figure 1.8:** Bonds and orbitals overlap in the ethane, C<sub>2</sub>H<sub>6</sub>, 7  $\sigma$  bonds; one C–C  $\sigma$  bond results from overlap of  $sp^3$  hybrid orbitals in the two carbon atoms and six C–H  $\sigma$  bonds result from the overlap between the C atoms  $sp^3$  orbitals with s orbitals on the hydrogen atoms [76].

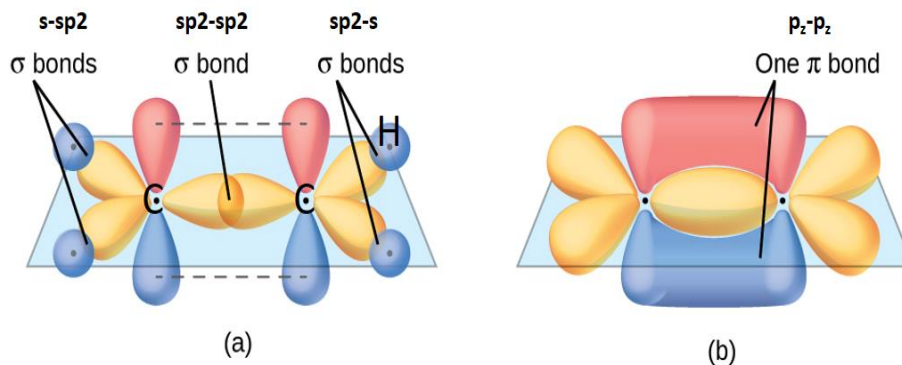


**Figure 1.9:** Bonds and orbitals overlap in the ethene,  $C_2H_4$ , (a) five  $\sigma$  bonds; one C–C  $\sigma$  bond results from overlap of  $sp^2$  hybrid orbitals in the two carbon atoms. Four C–H bonds result from the overlap between the C atoms'  $sp^2$  orbitals with  $s$  orbitals on the hydrogen atoms. (b) The  $\pi$  bond is formed by the side-by-side overlap of the two unhybridized  $p$  orbitals in the two carbon atoms. The two lobes of the  $\pi$  bond are above and below the plane of the  $\sigma$  system [77].

Finally, in  $sp^1$  hybridization, one  $s$ -orbital and one  $p$ -orbital mix to produce two  $sp$ -orbitals with a characteristic angle of  $180^\circ$  and two unhybridized  $p$ -orbitals. In acetylene, shown in figure 1.10, the two C atoms are bound together by a strong  $\sigma$ -bond formed by overlapping of  $sp^1$ -orbitals, while the remaining  $p$ -orbitals overlap above and below the plane of the molecule to form  $\pi$ -bonds, leading to a triple bond between C atoms. Again, since  $sp^1$  hybridization leads to  $\pi$  bonding, electron delocalization occurs and accordingly, intra-molecular charge transportation is expected in molecule with  $sp^1$  hybridization [73-75].

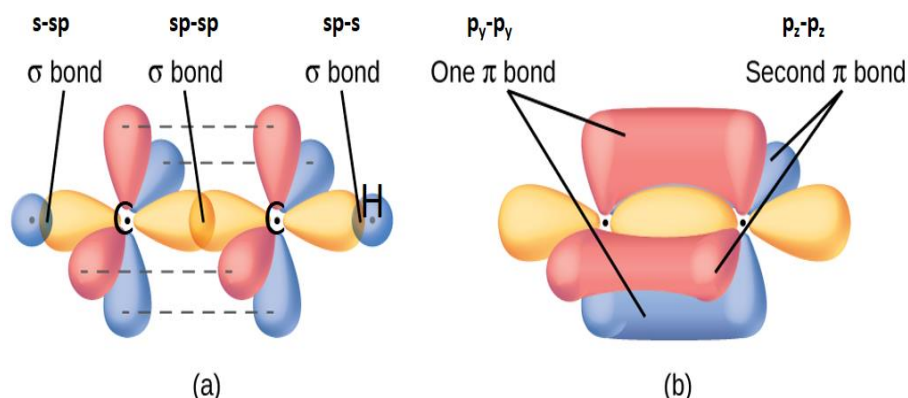


**Figure 1.10:** Bonds and orbitals overlap in acetylene,  $C_2H_2$ , (a) there are 3  $\sigma$  bonds; two C–H  $\sigma$  bonds and one C–C  $\sigma$  bond and two C–C  $\pi$  bonds. The dashed lines, each connecting two lobes, indicate the side-by-side overlap of the four unhybridized  $p$  orbitals. (b) the overall outline of the bonds in  $C_2H_2$ . The two lobes of each of the  $\pi$  bonds are positioned across from each other around the line of the C–C  $\sigma$  bond [77].

### 1.3.1.1 Band gap, conjugation and semiconducting behaviour

According to molecular orbital (MO) theory, when two atoms are bound together, their atomic orbitals with similar energy will split creating two molecular orbitals; one that is lower in energy than the initial atomic orbital (called bonding orbital) and one with a higher energy than the initial atomic orbital (called anti-bonding orbital). The difference in energy between the bonding and anti-bonding orbitals, reflects the energy of the original atomic orbitals prior to the splitting and the nature of the bond. For example, the direct overlap of atomic orbitals that occurs in the  $\sigma$  bond, will result in greater energy splitting between the  $\sigma$  bond and anti  $\sigma$ -bond ( $\sigma^*$ ) compared to splitting between the  $\pi$ -bond and anti  $\pi$ -bond ( $\pi^*$ ). The new molecular orbitals are populated with electrons according to their energy from low to high, obeying Hund's rule and Pauli exclusion principle. The last molecular orbital to be occupied with electrons is referred to as highest occupied molecular orbital, or HOMO, while the first unoccupied molecular orbital is referred to as lowest unoccupied molecular orbital, or LUMO. The distinct HOMO and LUMO orbitals are also called frontier orbitals and they determine the optical and electrical properties of a molecule. As the energy difference between the bonding and antibonding molecular orbitals is smaller for the  $\pi$ - $\pi^*$  case than for the  $\sigma$ - $\sigma^*$ , for molecules that contain  $\pi$ - $\pi^*$  molecular orbitals, the HOMO and LUMO levels will be of  $\pi$ - $\pi^*$  orbitals.

The energy difference between the HOMO and LUMO is analogous to the forbidden energy gap, or band gap, observed in the energy band structure of solids [73-75]. In organic molecules, the size of the band gap depends on the delocalisation of  $\pi$  electrons. Electron delocalization is observed in large organic molecules containing alternating single and multiple (double or triple) bonds between carbon atoms i.e. in molecules in which the bonding alternates between  $\sigma$  and ( $\sigma + \pi$ ) bonds. In these molecules, the overlap of p-orbitals leads to the formation of  $\pi$ -conjugate systems which extend over the whole molecule leading to electron delocalization along the backbone of the molecule [73-75,78-79]. This alternation in bonding is referred to as conjugation and molecules that have this structure are referred to as conjugated molecules. As illustrated in figure 1.11, as the conjugation of a molecule increases, the  $\pi$  electrons become more delocalized and the band gap decreases leading to a semiconducting behaviour of the conjugated molecule.

Since the gap between occupied ( $\pi$ ) and empty ( $\pi^*$ ) orbitals in delocalized  $\pi$ -systems become smaller with increasing delocalization, it implies that in molecules with extended delocalization (e.g. infinitely long conjugated polymer), the band gap could be diminished, leading to an organic conductor. However, the complete elimination of bandgap in a one-dimensional  $\pi$ -system and thus, the development of organic conductors, is inhibited by the so called *Peierls' distortion*. This structural distortion happens spontaneously to reduce the energy of the system, and leads to alternating pairs of carbon atoms to move closer to each other breaking the symmetry of the bond length in the alternating carbon bonds [80-82]. This bond dimerization opens up a small gap between fully occupied ( $\pi$ ) and empty ( $\pi^*$ ) orbitals. Organic conjugated molecules are thus classified as *organic semiconductors* and metallic behaviour can only be achieved in some polymers by chemical "doping". Here, doping of organic semiconductors refers to a redox process where electrons are either removed from the full  $\pi$ -orbitals (oxidation) or added to the empty  $\pi^*$  orbitals (reduction) using an oxidizing or reducing agent [80,83].

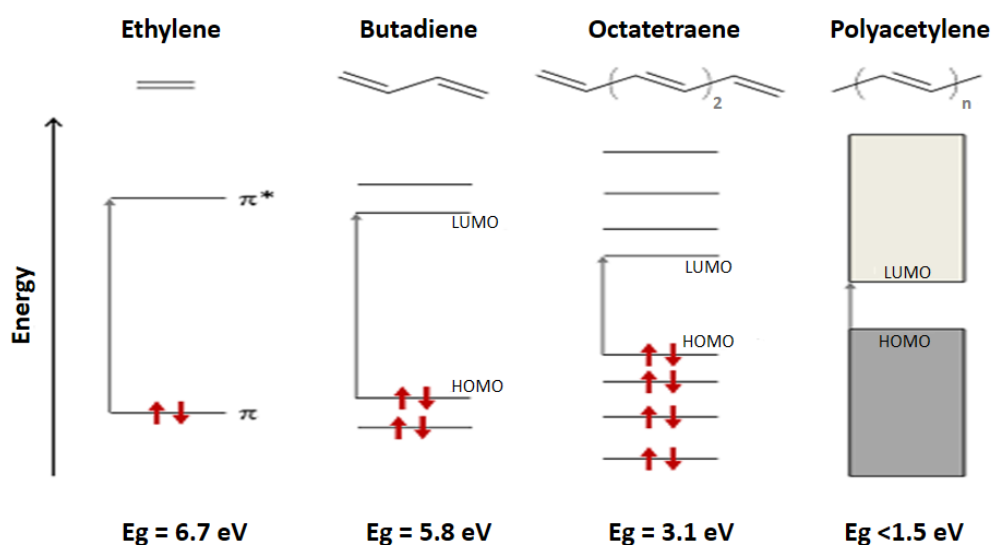


**Figure 1.11:** Schematic of energy-level in alkenes with increasing conjugation length, highlighting the energy gap between HOMO to LUMO. The bandgap of polyacetylene depends on the number of monomers  $n$  in the polymer. Arrows represent spin-paired electrons [84].

### 1.3.2 Inter-molecular charge transport in organic semiconductor films

In OEDs, the organic semiconductor (OSC) materials are typically deposited as molecular films. This OSC films are typically disordered both spatially and energetically. Critically,

localized states can be generated within the band gap at the grain boundaries between molecules, which act to trap the delocalized, mobile charge carriers. For a charge to transport from one molecule to another, it is thus necessary to excite charge carriers from the trap states typically through a thermally activated process known as hopping [85-90].

Many models have been proposed to describe the microscopic motion of charge carriers in organic semiconductor materials. Since the microstructure of the organic material plays a significant role in charge hopping, transport models will vary depending on the degree of disorder in the OSC film. In highly ordered, molecular single crystals, charge transport can be considered to occur through a band-like transport mechanism. On the other hand, for amorphous films, the variable range hopping (VRH) model is the widely used to describe charge transport. Other models, such as Bässler's Gaussian disorder (BGD) model and the percolation (PER) model have also been proposed for amorphous and highly disordered semiconductors [91].

Polycrystalline organic semiconductors, such as the OSC chosen for this PhD research, lie between these two extremes (i.e. single crystal and amorphous films). Charge transport in these materials is widely considered to be properly described by the multiple trapping and release (MTR) model. This model considers two conducting mediums; crystalline ordered grains which are separated from each other by disordered amorphous grain boundaries. Inside the grains, carriers are delocalized while at the grain boundaries, carriers become trapped in localized states and they require thermal assistance to transport to another delocalized region [89,92-93]. The main assumption of the MTR model is that charge carriers arriving at grain boundary are trapped instantaneously with a probability close to 1. The release of trapped carriers is controlled by a thermally-activated process. The key parameters that govern the charge transport through these OSC films are thus the density of trap states and the energy levels of those traps. The effective mobility,  $\mu_{eff}$ , can be related to the delocalized band mobility,  $\mu_0$ , by the following mobility – temperature, T, relationship:

$$\mu_{eff} = \mu_0 \alpha \exp\left[-\frac{E_T}{k_B T}\right] \quad (1.6)$$

where  $\mu_0$  is the mobility at the band edge (delocalized mobility inside grain),  $\alpha$  is the ratio between the effective density of states at the transport band edge and the density of traps, and  $E_T$  is the energy of the trap state [94].

### **1.3.3 Approaches to improve intermolecular charge transport**

Due to the complex nature of intermolecular charge transport in OSC, a lot of effort has been put into regulating and modifying the environment surrounding the OSC material to enhance intermolecular charge transport conditions. In an extensive review on charge transport in organic semiconductors, Coropceanu et.al [95] discussed 8 factors that influence charge mobility namely molecular packing, disorder, temperature, electric field, impurities, pressure, charge-carrier density and size/molecular weight [95-96]. In general, the fundamental concept is to increase the organization and arrangement of OSC molecules, in order to minimize the density of traps generated at grain boundaries between the OSC molecules [97-98]. Two key factors are normally considered. Firstly, controlling the OSC chemical structure and processing conditions during the material deposition. For example, during synthesis, the molecular weight, side chain chemistry and regioregularity of the OSC can be controlled alongside regulation of the film thickness and deposition method. In the case of material deposited from solution, this includes consideration of the solvent selection and subsequent thermal annealing temperature and deposition environment [61]. The purity of the OSC material can also impact the charge transport due to additional traps associated with impurities [97,99].

The second main factor is control over the surface on which the OSC will assemble. In the OTFT context for example, whatever the arrangement of the transistor (presented in section 1.4), the OSC will always make two interfaces; one with source and drain contacts and the second with the gate dielectric surface. The first interface determines charge injection to the OSC while the second dictates charge transport [61]. A common technique used to improve molecular ordering of the OSC at the OSC/gate dielectric interface is the use of self-assembled monolayers SAMs (silane SAMs in particular). Modifying the interface with a SAM provides a uniform and controllable intermediate layer that promotes alignment of the OSC molecules by dictating the nucleation and growth of the OSC films [61, 100-101].

It is worth noting that high mobility is of particular concern to those developing high performance devices. While high mobility is advantageous for sensor applications, the stability of the OSC is of higher significance for sensor performance.

#### **1.4 OTFT Operation and fundamental Layers**

A thin film transistor (TFT) consists of thin film fundamental layers deposited on a supporting substrate. The organic TFT (OTFT), first proposed by A. Tsumura, H. Koezuka and T. Ando in 1986 is a special case where the semiconductor layer is an organic film, although since then OTFTs with both OSC and organic dielectric films and an all organic based OTFTs have also been reported [102-109]. OTFTs are commonly field effect transistors, FETs, and their basic operation can be described by the modulation of a conducting channel inside an OSC layer assembled between two contacts, known as the source, S, and drain, D, electrodes by an electric-field generated at a third contact, the gate electrode, G. It also can be modelled as a parallel plate capacitor, where one plate is the gate electrode and the other plate is the S/OSC/D assembly, separated by the gate dielectric. OTFTs have been demonstrated in various architectures, depending on the arrangement of the gate, source and drain contacts with respect to the organic semiconductor OSC layer [61,106]. The most common device architectures are presented in figure 1.12. Regardless of the OTFT structure, three fundamental layers and the interfaces between these layers determine the OTFT performance; the active OSC layer, S/D contacts and gate dielectric layer. Specifically, the interface between the OSC and gate dielectric strongly influence the field effect mobility,  $\mu_{\text{FET}}$ , (or simply mobility,  $\mu$ ) while the contact resistance,  $R_c$ , is regulated by the OSC layer and source and drain interface [61,106,110].

OFETs normally operate in accumulation mode where charge accumulates in the OSC upon application of an electric field, creating a conducting channel between S and D. Typically, the source contact is held at ground potential and the accumulation channel is controlled by the bias applied to the drain and gate contact. With no gate voltage, the flow of charge carriers between S and D is dominated by the intrinsic conductivity of the OSC, which is typically low in organic films due to the high density of trap states from grain boundaries. This is the OFF state of the transistor. Upon application of a voltage to the gate electrode,

a potential gradient is generated in the capacitor structure and at a certain threshold voltage when all the traps are occupied, the transistor is turned ON. As the gate voltage increases, charges inside the OSC with the opposite sign to the gate voltage will be attracted to the OSC/gate dielectric interface. By simultaneously applying a drain voltage of the same sign to the gate, the accumulated charges at the OSC/gate dielectric interface drift towards the drain leading to a net current flow [61,111-114].

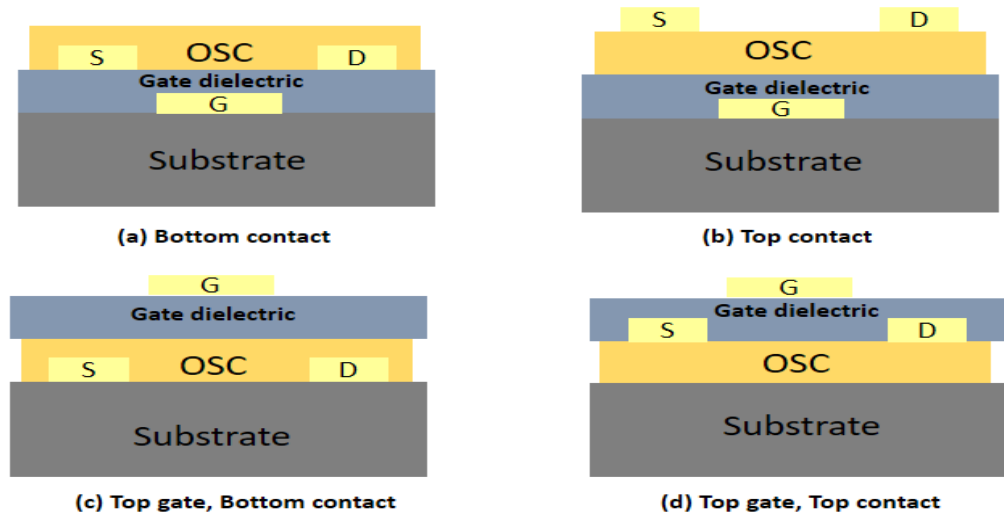


**Figure 1.12:** Typical architectures of OTFTs (a) Bottom contact, (b) Top contact, (c) Top gate-Bottom contact and (d) Top gate-Top contact. S: Source, D: Drain, G: Gate, and OSC: organic semiconductor.

The current voltage relationship between the source drain current,  $I_{SD}$ , and the applied voltages, namely the source drain voltage,  $V_{SD}$ , and gate voltage,  $V_G$ , is given by equation 1.7 [111,115]:

$$I_{SD} = \frac{W\mu C_i}{L} \left[ (V_G - V_{TH}) - \frac{V_{SD}}{2} \right] V_{SD} \quad (1.7)$$

Where  $W$  is the transistor channel width,  $L$  is the transistor channel length,  $\mu$  is the field-effect mobility,  $V_{TH}$  is the threshold voltage and  $C_i$  is the capacitance per unit area of the gate insulator.

From the general equation (1.7), the OFET can be seen to operate in two regimes. When  $V_{SD} \ll (V_G - V_{TH})$ , the term  $\frac{V_{SD}}{2}$  becomes negligible and equation (1.7) is simplified to (1.8) where the current flowing through the OSC between the source and drain contacts,  $I_{SD}$ , is linearly related to the source drain voltage,  $V_{SD}$ . This is known as the linear regime.

$$I_{SD} = \frac{W\mu C_i}{L} (V_G - V_{TH}) V_{SD} \quad (1.8)$$

In the second regime  $V_{SD} > (V_G - V_{TH})$ . Here,  $V_D$  becomes comparable to  $V_G$  creating a depletion region near the drain electrode (due to the absence of potential difference) leading to saturation of  $I_{SD}$ . In this regime equation (1.7) is approximated to (1.9).

$$I_{SD} = \frac{W\mu C_i}{2L} (V_G - V_{TH})^2 \quad (1.9)$$

These equations, particularly equation (1.9) are used estimate the mobility of the OSC and the threshold,  $V_{TH}$ , of the OFET device, which are two important features in describing the characteristic behaviour of the OFET device. When used in sensing applications, the change in  $I_{SD}$  can be related to changes in the sensing region, as will be explain in later chapters.

## 1.5 Organic thin film transistors for chemical and biological sensing

Chemical and biological sensors based on OTFTs can potentially benefit from the distinguishing features of organic semiconductor materials. Firstly, the powerful transistor-based sensor which have inherent signal amplification can be made at low cost and can be exploited to create commercially viable, single use sensors. Being carbon based, OSCs are compatible with the integration of selective biological recognition elements. For example, a recent review by Feron et.al [116] demonstrated the ability to culture cells on various OSC layers in cell-based OTFT biosensors. Furthermore, the synthetic freedom of organic chemistry can be exploited to modify OSCs, for example by adding functional groups (in the form of side chains) to the organic semiconductor backbone for directly integrating bio-recognition elements. In addition, the low temperature processing conditions used in the fabrication of OTFTs is compatible with biological molecules, such as enzymes which denature at the high temperatures associated with processing of traditional electronic materials. Finally, the mechanical flexibility of OSCs make them good candidates for fabricating implantable or wearable sensors [117-123].

### 1.5.1 Types of OTFTs used for biosensing

The two main classes of OTFTs used for biosensing applications are organic electrochemical transistors (OECT) and organic field effect transistors (OFET). These are shown in Figure 1.13. The main difference between these two devices is that the OECT does not contain a

thin gate dielectric layer between the gate electrode and OSC. Thus, unlike conventional field effect devices, the OECT does not operate by capacitive coupling. Instead, OECTs employ conducting polymers (CP) as their active layer as opposed to OSCs in OFET devices, which is in direct contact with the surrounding electrolyte. The most widely used CP is poly(3,4-ethylenedioxythiophene) doped with poly(styrene sulfonate) (PEDOT:PSS) which is a p-type CP, where the negative charge of PSS is compensated by a hole in the PEDOT backbone. The operation mechanism of the OECT is explained by migration of ions between the CP and adjacent electrolyte causing electrochemical doping/de-doping that alters the polymer conductivity [121,124-125]. Specifically, a positive voltage applied to the gate electrode leads to diffusion of hydrated cations from the electrolyte into the CP channel, leading to de-doping and a reduction in source drain current. Since the doping/de-doping process is reversible, the conducting channel can be switched between different doping levels by the gate voltage and/or a sensing event in the sensor [126-127].

In the OFET biosensor, the behaviour is similar to the typical OFET, where the insulating layer acts as a dielectric spacer between the OSC and the gate electrode and the electric field generated by a bias applied to the gate electrode causes charge carriers to accumulate at the OSC/insulator interface, however, as shown in figure 1.13 (a), the active OSC layer can be exposed to either liquids or gases containing analytes which can further modulate charge accumulation in the OSC.[121,124-125].

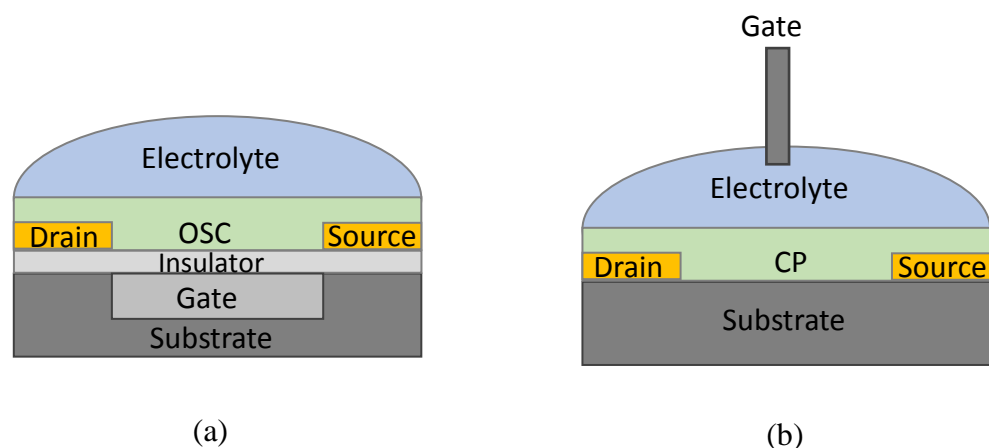


**Figure 1.13:** The schematic structure of a typical (a) organic field effect transistor (OFET) biosensor and (b) organic electrochemical transistor (OECT) biosensor.

A more commonly used OFET structure in sensing application is the ion-sensitive organic field effect transistors (ISOFET). In the ISOFET (see figure 1.14) the OSC and electrolyte solution are separated by a dielectric layer and the transistor response is highly dependent on the sensitivity of this dielectric layer [72,121]. A change in charge concentration at the electrolyte/dielectric layer interface, for example due to a sensing event occurring at the interface, will result in modulation of the charge concentration in the OSC channel.

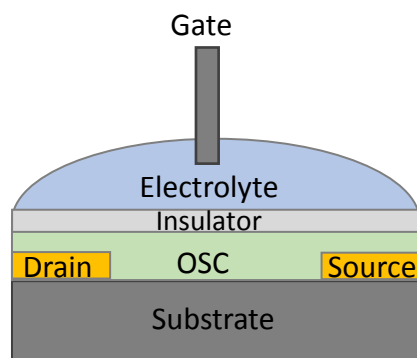


**Figure 1.14:** Schematic diagram of the ion-sensitive organic field effect transistors (ISOFET).

Another more recently developed OFET structure is the electrolyte-gated organic field effect transistor (EGOFET), is displayed in figure 1.15. The structure is very similar to the OECT sensor (figure 1.13 (b)) but employs an OSC as the active layer rather than a CP in the OECT. In the EGOFET, cations/anions from the electrolyte accumulate at the gate electrode in response to a small bias voltage applied to the gate electrode. As a result, an electrical double layers (EDL) is created at both the gate/electrolyte interface and at the electrolyte/OSC interface. In this scenario, both double layers are formed from a layer of hydrated ions and a layer of electronic charge separated by (few Å), leading to a very high capacitance [120,122,125,128-129].

The OECT biosensor is distinguished from the EGOFET in that the whole volume of the CP layer participates in the conduction of the transistor channel compared to field effect gating in a thin OSC layer in the EDL of EGOFET, this yield a higher current in OECT compare to EGOFET [120,125]. It must be noted that, it is not always firmly verified that only the field effect mechanism dominates channel modulation in the EGOFET channel modulation

and it is possible that both field effect and electrochemical modulation can occur simultaneously [122,125,130-131].

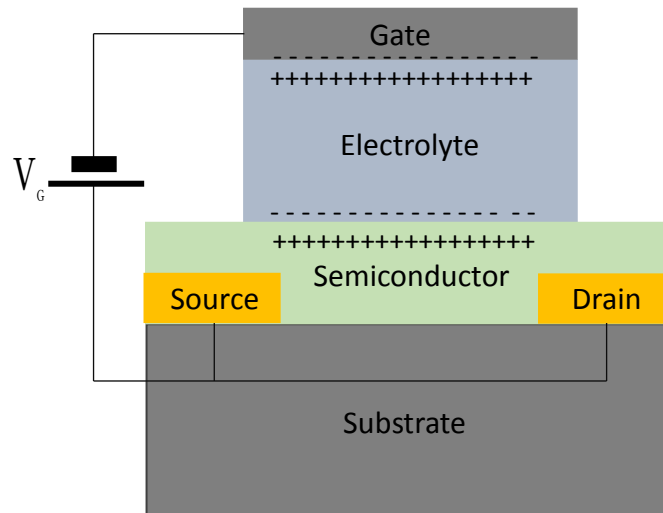


**Figure 1.15:** Schematic diagram of the electrical double layers formed in the electrolyte-gated organic field effect transistor (EGOFET).

In both the OEFT and EGOFET, the absence of the gate dielectric layer means they require reduced operation voltages; normally 1V or less. This is a significant advantage when using aqueous electrolytes as at these voltages electrolysis/ hydrolysis are suppressed [120,125,130].

Apart from the ISOFET, in all other configuration of OFET biosensors, the OSC is in direct contact with the electrolyte. While this direct interaction increases the sensitivity of the sensor, there are some undesirable consequences. Firstly, it limits the number of the OSCs that can be used, especially when aqueous solutions are used due to the instability of some OSCs in both air and water [132]. Moreover, in some cases the effect of the sensing activity on the morphology of the active layer cannot be easily reversed. Also, apart from the OFET transistor the other types suffer from the presence of a large, macro gate electrode which restricts the feasibility of miniaturization [132-133]. To overcome these limitations, two more architectures have recently been investigated; the dual gate OFET concept and extended gate OFET.

### 1.5.1.1 The Dual Gate OFET (DG-OFET) biosensor

In the DG-OFET (figure 1.16), one gate electrode is used to bias the transistor and any change of the potential on the second gate electrode (normally top) is then observed by a change in the transistor characteristics. When configured as a biosensor, the second gate electrode is replaced by a layer of bio-recognition elements attached to the second gate dielectric. Any change in this layer of bio-recognition elements, for example a change in charge due to analyte binding, effectively lead to a change in the performance of the transistor.

Although the DG-OFET concept can provide a solution to some of the limitations that other OFET devices can encounter, careful consideration has to be given to the thickness of both the OSC and the second dielectric layer as the physics of the device will vary depending on their thicknesses. This actually depends on whether two independent spatially separated conducting channels are formed in the OSC at each dielectric interface or a crossover interference (mutual channel) is taking place [134-136]. Also, it is challenging to deposit a uniform dielectric layer on top of the OSC.

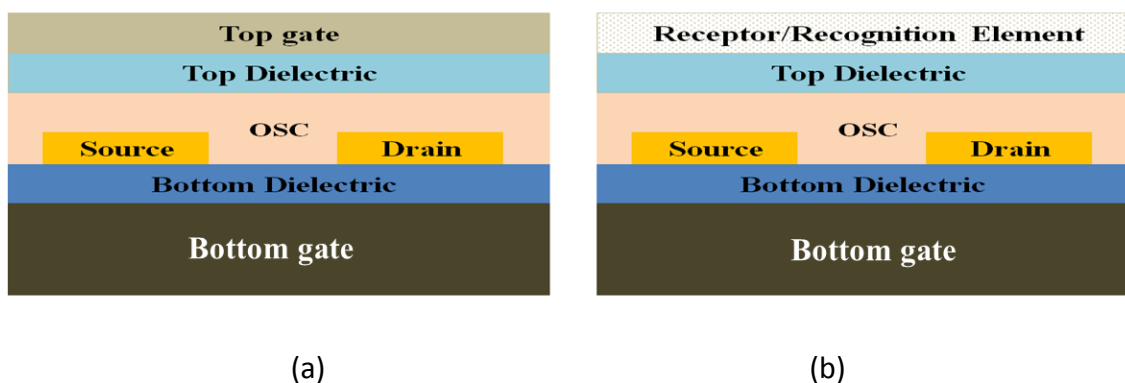


**Figure 1.16:** schematic structure of (a) DG-OFET, and (b) the DG-OFET configured as a biosensor.

### 1.5.1.2 Extended Gate OFET biosensor

Another attempt to overcome the challenges of the instability of some OSCs in aqueous solution is the extended gate biosensor. Here, the gate electrode extends beyond the transistor region. In this way, the sensing area is spatially separated from the transistor, hence, the detection mechanism does not rely on the properties of the OSC. An

electrochemical change in the sensing area, for example due to binding of an analyte to bio-recognition molecules immobilised in the sensing area, is coupled to the OFET through the extended gate. This causes a shift in the threshold voltage of the transistor, that can be used to quantify the specific analyte [133,137-139].

The extended gate concept has been used to make OFET biosensor for pH sensing, nitrate and immunoglobulin G (IgG) detection [140-142]. While this approach overcomes the instability of many OSCs in aqueous solutions, a macro-scale reference electrode was used in order to bias the transistor. This makes the microfabrication of extended gate biosensor arrays challenging. Recently, a group from the Department of Electrical and Electronic Engineering, University of Cagliari has taken the concept further, and developed an innovative design that not only protects the OSC from the sensing activity, but also operates without the need of an external macro reference electrode.

The concept, called the Charge Modulated OFET (CM-OFET), employs two gates; an extended gate and a control gate, as shown in figure 1.17. As above, the extended gate extends beyond the transistor region in order to separate the OFET from solution. The extended gate is functionalized at a specific region, known as the sensing region, with a layer of bio-recognition elements. The control gate is separated from the extended floating gate by the dielectric layer of the transistor. This control gate is also isolated from solution and can thus be used to bias the transistor by capacitive coupling, removing the need for a reference electrode. The conducting channel in the OSC is biased using the control gate and the charge variation resulting from sensing activity occurring on a selected portion of the extended floating gate, modulates this conduction channel. The first demonstration of the concept was achieved using an inorganic FET [143], but later the group developed the organic version and demonstrated the concept for sensing of local pH [144]. The concept has since been applied for the detection of DNA hybridization [145], electrophysiological monitoring of excitable cells [146] and as a pressure sensor [147].

It is noteworthy, that even though there is no direct contact between the OSC and the analyte in either of the DG-OFET and extended gate devices, the sensing mechanism results in a shift in the threshold voltage,  $V_{TH}$ , which according to equation (1.9), changes quadratically with the saturated current,  $I_{SD}$ , so can still provide a pronounced effect on the transistor behaviour.

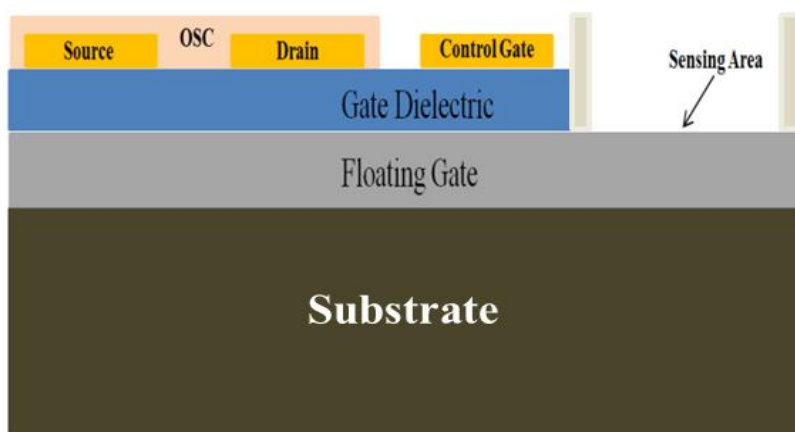


**Figure 1.17:** OFET with Extended Gate, Charge Modulated OFET (CM-OFET).

Given isolation of the OSC from solution, the lack of reference electrode and the possibility of fabricating the device through a very simple, cost effective process, it was decided that the CM-OFET was the most attractive version of OFET-based biosensor to take forward for further research in this thesis.

## 1.6 Summary and thesis outline

This chapter has provided a general overview of biosensors for healthcare, environmental and security applications and the need for innovative biosensing methods and technologies to overcome some of the limitations in existing technologies, particularly cost and usability limitations. Biosensors based on organic electronic device are emerging as a technology with the potential to meet these technological needs. The main organic electronic devices being developed for biosensing applications is the organic field effect transistors OFETs. While a number of OFET-based biosensor architectures have been demonstrated, the recently developed charge modulated organic field effect transistor CM-OFET shows particular promise.

In chapter 2, a thorough description for the fabrication process of two CM-OFET designs based on Si/SiO<sub>2</sub> and Al/Al<sub>2</sub>O<sub>3</sub> as gate and gate dielectric layers respectively is provided, accompanied with a discussion on the material choice for the two designs.

In chapter 3, the experimental setup for device testing, experimental considerations and methods for characterization of the CM-OFET device is discussed.

Chapter 4 presents an investigation into the Si/SiO<sub>2</sub> CM-OFET biosensor for pH sensing. The chapter includes discussion on the sensing mechanism including surface functionalization of the floating gate to improve sensitivity as well as surface analysis of the functionalized sensing surface. The chapter is concluded with electrical characterization of the fabricated CM-OFET devices.

Chapter 5 looks at the use of the Si/SiO<sub>2</sub> based CM-OFET device for protein detection, here exploiting the well-defined avidin-biotin interaction. The chapter presents results of a quartz crystal microbalance with dissipation study to verify the surface biotinylation protocol for avidin binding. Experimental results and investigation of the CM-OFET for the detection of avidin binding to a biotinylated extended gate are discussed and analysed. Finally, major shortcomings in the Si/SiO<sub>2</sub> CM-OFET device are highlighted and a new modified CM-OFET device based on a new design with Al/Al<sub>2</sub>O<sub>3</sub> as gate and gate dielectric layers respectively is introduced.

Finally, chapter 6 concludes with final remarks on the research programme and suggests some future work to optimize the device performance.

## 1.7 References

- [1] Mehrotra, P. (2016). Biosensors and their applications—A review. *Journal of oral biology and craniofacial research*, 6(2), 153-159.
- [2] Cammann, K. (1977). Bio-sensors based on ion-selective electrodes. *Fresenius' Zeitschrift für Analytische Chemie*, 287(1), 1-9.
- [3] Yasmin, J., Ahmed, M. R., & Cho, B. K. (2016). Biosensors and their Applications in Food Safety: A Review. *Journal of Biosystems Engineering*, 41(3), 240-254.
- [4] Perumal, V., & Hashim, U. (2014). Advances in biosensors: Principle, architecture and applications. *Journal of Applied Biomedicine*, 12(1), 1-15.
- [5] Monošík, R., Stredánský, M., & Šturdík, E. (2012). Biosensors-classification, characterization and new trends. *Acta Chimica Slovaca*, 5(1), 109-120.
- [6] Ali J, Najeeb J, Ali MA, Aslam MF, Raza A (2017) Biosensors: Their Fundamentals, Designs, Types and Most Recent Impactful Applications: A Review. *J Biosens Bioelectron* 8: 235. doi: 10.4172/2155-6210.1000235
- [7] Clark, L. C., & Lyons, C. (1962). Electrode systems for continuous monitoring in cardiovascular surgery. *Annals of the New York Academy of sciences*, 102(1), 29-45.
- [8] Goode, J. A., Rushworth, J. V. H., & Millner, P. A. (2014). Biosensor regeneration: a review of common techniques and outcomes. *Langmuir*, 31(23), 6267-6276.
- [9] Li, H., Liu, X., Li, L., Mu, X., Genov, R., & Mason, A. J. (2016). CMOS Electrochemical Instrumentation for Biosensor Microsystems: A Review. *Sensors*, 17(1), 74.
- [10] Turner, A. P. (2013). Biosensors: sense and sensibility. *Chemical Society Reviews*, 42(8), 3184-3196.
- [11] Sang, S., Zhang, W., & Zhao, Y. (2013). Review on the design art of biosensors. In *State of the Art in Biosensors-General Aspects*. InTech.
- [12] Luka, G., Ahmadi, A., Najjaran, H., Alocilja, E., DeRosa, M., Wolthers, K., Malki, A, Aziz, H, Althani, A & Hoorfar, M. (2015). Microfluidics integrated biosensors: a leading technology towards lab-on-a-chip and sensing applications. *Sensors*, 15(12), 30011-30031.

- [13] Luong, J. H., Male, K. B., & Glennon, J. D. (2008). Biosensor technology: technology push versus market pull. *Biotechnology advances*, 26(5), 492-500.
- [14] Mohanty, S. P., & Kougiyanos, E. (2006). Biosensors: a tutorial review. *IEEE Potentials*, 25(2), 35-40.
- [15] Geddes, C. & Lakowicz, J. (2006), Glucose Sensing. Springer. DOI 10.1007/0-387-33015-1
- [16] Economou, A., del Campo, J., Reddy, S. M., Lunte, S., Thompson, M., Kranz, C., & JinLee, H. (2015). *Electrochemical strategies in detection science*. Royal Society of Chemistry.
- [17] Lee, Y. H., & Mutharasan, R. (2005). Biosensors. *Sensor Technology Handbook*, 161-180
- [18] Touhami, A. (2014). Biosensors and Nanobiosensors: Design and Applications. *Nanomedicine*, 374-400.
- [19] Nanduri, V., Sorokulova, I. B., Samoylov, A. M., Simonian, A. L., Petrenko, V. A., & Vodyanoy, V. (2007). Phage as a molecular recognition element in biosensors immobilized by physical adsorption. *Biosensors and Bioelectronics*, 22(6), 986-992.
- [20] Schuhmann, W., Lammert, R., Uhe, B., & Schmidt, H. L. (1990). Polypyrrole, a new possibility for covalent binding of oxidoreductases to electrode surfaces as a base for stable biosensors. *Sensors and Actuators B: Chemical*, 1(1-6), 537-541.
- [21] Gupta, R., & Chaudhury, N. K. (2007). Entrapment of biomolecules in sol-gel matrix for applications in biosensors: Problems and future prospects. *Biosensors and Bioelectronics*, 22(11), 2387-2399.
- [22] Nenkova, R., Ivanova, D., Vladimirova, J., & Godjevargova, T. (2010). New amperometric glucose biosensor based on cross-linking of glucose oxidase on silica gel/multiwalled carbon nanotubes/polyacrylonitrile nanocomposite film. *Sensors and Actuators B: Chemical*, 148(1), 59-65.
- [23] Iso, M., Shirahase, T., Hanamura, S. I., Urushiyama, S., & Omi, S. (1989). Immobilization of enzyme by microencapsulation and application of the encapsulated enzyme in the catalysis. *Journal of microencapsulation*, 6(2), 165-176.
- [24] Cahn, T. M. (1993). *Biosensors* (Vol. 1). Springer Science & Business Media.

- [25] Bhalla, N., Jolly, P., Formisano, N., & Estrela, P. (2016). Introduction to biosensors. *Essays in biochemistry*, 60(1), 1-8.
- [26] Rajan, N. K., Brower, K., Duan, X., & Reed, M. A. (2014). Limit of detection of field effect transistor biosensors: Effects of surface modification and size dependence. *Applied Physics Letters*, 104(8), 084106.
- [27] O'Hare, D. (2014). Biosensors and Sensor Systems. In *Body Sensor Networks* (pp. 55-115). Springer London.
- [28] PerkinElmer. (2011). Sensitivity Versus Detection Limit. Available at: <https://www.perkinelmer.com/lab-solutions/resources/docs/AASensitivityvsDetectionLimitTechNote.pdf> [Accessed 30/07/17]
- [29] Vessman, J. (1996). Selectivity or specificity? Validation of analytical methods from the perspective of an analytical chemist in the pharmaceutical industry. *Journal of pharmaceutical and biomedical analysis*, 14(8-10), 867-869.
- [30] Arugula, M. A., & Simonian, A. (2014). Novel trends in affinity biosensors: current challenges and perspectives. *Measurement Science and Technology*, 25(3), 032001.
- [31] Scientific, T. (2010). Elisa technical guide and protocols. *Manual*, 747, 815.
- [32] Sakamoto, S., Putalun, W., Vimolmangkang, S., Phoolcharoen, W., Shoyama, Y., Tanaka, H., & Morimoto, S. (2018). Enzyme-linked immunosorbent assay for the quantitative/qualitative analysis of plant secondary metabolites. *Journal of natural medicines*, 72(1), 32-42.
- [33] Bio-Rad, (2018), Introduction to ELISA, URL: <https://www.bio-rad-antibodies.com/elisa-types-direct-indirect-sandwich-competition-elisa-formats.html> [last access 20/02/2019]
- [34] Ferri, G. L., Gaudio, R. M., Castello, F. I., Tirolo, C., & Chiolerio, F. (1999). Multiple biotin-avidin amplification for multiple immunostaining. *Applied Immunohistochemistry & Molecular Morphology*, 7(1), 73-80.
- [35] Thorp, H. H. (1998). Cutting out the middleman: DNA biosensors based on electrochemical oxidation. *Trends in Biotechnology*, 16(3), 117-121.

- [36] Cooper, M. A. (Ed.). (2009). *Label-free biosensors: techniques and applications*. Cambridge University Press.
- [37] Cunningham, B. T., & Laing, L. (2006). Microplate-based, label-free detection of biomolecular interactions: applications in proteomics. *Expert review of proteomics*, 3(3), 271-281.
- [38] Berggren, C., Bjarnason, B., & Johansson, G. (2001). Capacitive biosensors. *Electroanalysis*, 13(3), 173-180.
- [39] Ramachandran, N., Larson, D. N., Stark, P. R., Hainsworth, E., & LaBaer, J. (2005). Emerging tools for real-time label-free detection of interactions on functional protein microarrays. *The FEBS journal*, 272(21), 5412-5425.
- [40] Hitt, E. (2004). Label-free methods are not problem free. *Drug Discov. Devel*, 7(9), 34-42.
- [41] Hodnik, V., & Anderluh, G. (2013). Surface plasmon resonance for measuring interactions of proteins with lipid membranes. In *Lipid-Protein Interactions* (pp. 23-36). Humana Press, Totowa, NJ.
- [42] GE Healthcare Life Sciences, (2019), Surface plasmon resonance, URL: <https://www.gelifesciences.com/ja/jp/solutions/protein-research/knowledge-center/surface-plasmon-resonance/surface-plasmon-resonance> [Last access: 09/03/19]
- [43] Tang, Y., Zeng, X., & Liang, J. (2010). Surface plasmon resonance: an introduction to a surface spectroscopy technique. *Journal of chemical education*, 87(7), 742-746.
- [44] Drescher, D. G., Selvakumar, D., & Drescher, M. J. (2018). Analysis of protein interactions by surface plasmon resonance. In *Advances in protein chemistry and structural biology* (Vol. 110, pp. 1-30). Academic Press.
- [45] Nguyen, H., Park, J., Kang, S., & Kim, M. (2015). Surface plasmon resonance: a versatile technique for biosensor applications. *Sensors*, 15(5), 10481-10510.
- [46] Van Der Merwe, P. A. (2001). Surface plasmon resonance. *Protein-ligand interactions: hydrodynamics and calorimetry*, 1, 137-170.
- [47] Heinrich, L., Tissot, N., Hartmann, D. J., & Cohen, R. (2010). Comparison of the results obtained by ELISA and surface plasmon resonance for the determination of antibody affinity. *Journal of immunological methods*, 352(1-2), 13-22.
- [48] Cheng Research Lab, The University of California, (2016), Surface Plasmon Resonance Spectroscopy and Imaging, URL: <https://chenglab.ucr.edu/spr.html> [last access 10/03/19]

- [49] Ritzefeld, M., & Sewald, N. (2012). Real-time analysis of specific protein-DNA interactions with surface plasmon resonance. *Journal of amino acids*, 2012.
- [50] Langmuir, I. (1916). The constitution and fundamental properties of solids and liquids. Part I. Solids. *Journal of the American chemical society*, 38(11), 2221-2295.
- [51] Langmuir, I. (1918). The adsorption of gases on plane surfaces of glass, mica and platinum. *Journal of the American Chemical society*, 40(9), 1361-1403.
- [52] Leontiou, C., Lightowers, R., Lakey, J. H., & Austin, C. A. (2003). Kinetic analysis of human topoisomerase II $\alpha$  and  $\beta$  DNA binding by surface plasmon resonance. *FEBS letters*, 554(1-2), 206-210.
- [53] GE Healthcare, (2019) Basic theory of kinetics, URL: [https://www.biacore.com/lifesciences/help/basic\\_theory\\_of\\_kinetics/index.html](https://www.biacore.com/lifesciences/help/basic_theory_of_kinetics/index.html) [Last access: 09/03/19]
- [54] Sahu, A., Soulika, A. M., Morikis, D., Spruce, L., Moore, W. T., & Lambris, J. D. (2000). Binding kinetics, structure-activity relationship, and biotransformation of the complement inhibitor compstatin. *The Journal of Immunology*, 165(5), 2491-2499.
- [55] Memczak, H., Lauster, D., Kar, P., Di Lella, S., Volkmer, R., Knecht, V., ... & Stöcklein, W. F. (2016). Anti-hemagglutinin antibody derived lead peptides for inhibitors of influenza virus binding. *PLoS one*, 11(7), e0159074.
- [56] Kissinger, P. T. (2005). Biosensors—a perspective. *Biosensors and Bioelectronics*, 20(12), 2512-2516.
- [57] Lee, T. M. H. (2008). Over-the-counter biosensors: Past, present, and future. *Sensors*, 8(9), 5535-5559.
- [58] Arduini, F., Cinti, S., Scognamiglio, V., Moscone, D., & Palleschi, G. (2017). How cutting-edge technologies impact the design of electrochemical (bio) sensors for environmental analysis. A review. *Analytica Chimica Acta*.
- [59] DeFranco, J. A., Schmidt, B. S., Lipson, M., & Malliaras, G. G., "Photolithographic patterning of organic electronic materials". *Organic Electronics*, 7(1), 2006, 22-28.
- [60] Shaw, J. M., & Seidler, P. F. , "Organic electronics: introduction". *IBM Journal of Research and Development*, 45(1), 2001, 3-9.
- [61] Li, F., Nathan, A., Wu, Y., & Ong, B. S., *Organic Thin Film Transistor Integration: A Hybrid Approach*. 2013. John Wiley & Sons.

- [62] Facchetti, A., *“Organic Electronics”, Materials, Manufacturing and Applications*. Edited by Hagen Klauk, *Angewandte Chemie*, 46( 9), 2007, 1367–1368.
- [63] Lim, S. C., Kim, S. H., Chu, H. Y., Lee, J. H., Lee, J. I., Oh, J. Y., ... & Zyung, T., “New Method of Driving an OLED with an OTFT”. *Synthetic metals*, 151(3), 2005, 197-201.
- [64] Jang, J., & Han, S. H., “High-performance OTFT and its application”. *Current Applied Physics*, 6, 2006, e17-e21.
- [65] Shinar, R., & Shinar, J., *Organic electronics in sensors and biotechnology*. 2009. McGraw-Hill, Inc.
- [66] Jain, S. C., Willander, M., & Kumar, V., *Conducting organic materials and devices* (Vol. 81). 2011. Newnes.
- [67] Tarver, J., & Loo, Y. (2010). Organic Electronic Devices with Water-Dispersible Conducting Polymers. *Handbook of Nanoscale Optics and Electronics*, 107.
- [68] Solanki, C. S. (2015). *Solar photovoltaics: fundamentals, technologies and applications*. PHI Learning Pvt. Ltd..
- [69] Schöll, A., & Schreiber, F. (2018). Thin Films of Organic Molecules: Interfaces and Epitaxial Growth. In *Molecular Beam Epitaxy* (pp. 551-570). Elsevier.
- [70] Zhao, X., Chaudhry, S. T., & Mei, J. (2017). Heterocyclic Building Blocks for Organic Semiconductors. In *Advances in Heterocyclic Chemistry* (Vol. 121, pp. 133-171). Academic Press.
- [71] Zang, Ling, *Energy Efficiency and Renewable Energy through Nanotechnology*. Berlin: Springer, 2011.
- [72] Elkington, D., Cooling, N., Belcher, W., Dastoor, P. C., & Zhou, X. “Organic Thin-Film Transistor (OTFT)-Based Sensors”. *Electronics*, 3(2), 2014, 234-254.
- [73] Majewski, L. (2011), *supplementary teaching material*, Organic Electronics, Nano Electronics, University of Manchester.
- [74] Menke, T., “Molecular Doping of Organic Semiconductors: A Conductivity and Seebeck Study”, 2013.
- [75] Stella, M., *Study of Organic Semiconductors for Device Applications*, doctoral thesis, University of De Barcelona. 2010.

- [76] Lower, S, (2018), The Hybrid Orbital Model II, URL: <https://bit.ly/2TCmET8> [last access 10/03/19]
- [77] OpenStax, Chemistry. OpenStax CNX. Jun 20, 2016  
<http://cnx.org/contents/85abf193-2bd2-4908-8563-90b8a7ac8df6@9.311>.
- [78] Shinar, R., & Shinar, J. *Organic electronics in sensors and biotechnology*. McGraw-Hill, Inc. 2009.
- [79] Brédas, J. L., Calbert, J. P., da Silva Filho, D. A., & Cornil, J., "Organic semiconductors: A theoretical characterization of the basic parameters governing charge transport". *Proceedings of the National Academy of Sciences*, 99(9), 2002. 5804-5809.
- [80] Majewski, L. A. (2006). *Alternative Gate Insulators for Organic Field-Effect Transistors* (Doctoral dissertation, University of Sheffield, Department of Physics and Astronomy).
- [81] Bäessler, H., & Köhler, A. (2011). Charge transport in organic semiconductors. In *Unimolecular and supramolecular electronics I* (pp. 1-65). Springer, Berlin, Heidelberg.
- [82] Chen, C. H., & Shih, I. (2006). Hybrid organic on inorganic semiconductor heterojunction. *Journal of Materials Science: Materials in Electronics*, 17(12), 1047-1053.
- [83] Malhotra, B. D. (2017). *Biosensors: Fundamentals and Applications*. Smithers Rapra.
- [84] University of Cambridge,(2019), Optoelectronics, Organic Semiconductors, URL: <https://www.oe.phy.cam.ac.uk/research/materials/osemiconductors> [last access 10/03/19]
- [85] Bäessler, H., & Köhler, A., "Charge transport in organic semiconductors". In *Unimolecular and Supramolecular Electronics I* Springer Berlin Heidelberg. 2012, 1-65.
- [86] Li, L., Meller, G., & Kosina, H., "Temperature and field-dependence of hopping conduction in organic semiconductors", *Microelectronics journal*, 38(1), 2007,47-51.
- [87] Li, L., Meller, G., & Kosina, H., "Influence of traps on charge transport in organic semiconductors". *Solid-state electronics*, 51(3), 2007, 445-448.
- [88] Locci, S., *Modeling of physical and electrical characteristics of organic thin film transistors*. 2009

- [89] Guo, D., Miyadera, T., Ikeda, S., Shimada, T., & Saiki, K., "Analysis of charge transport in a polycrystalline pentacene thin film transistor by temperature and gate bias dependent mobility and conductance". *Journal of Applied Physics*, 102(2), 2007, 023706.
- [90] Fishchuk, I. I., Kadashchuk, A., Hoffmann, S. T., Athanasopoulos, S., Genoe, J., Bässler, H., & Köhler, A., "Analytic model of hopping transport in organic semiconductors including both energetic disorder and polaronic contributions". In *15th International Conference on Transport in Interacting Disordered Systems (Tids15)* 1610 (1), 2014, August, 47-52. Aip Publishing.
- [91] Liu, C., Huang, K., Park, W. T., Li, M., Yang, T., Liu, X., & Noh, Y. Y. (2017). *A unified understanding of charge transport in organic semiconductors: the importance of attenuated delocalization for the carriers*. *Materials Horizons*.
- [92] Olivier, Y., Lemaire, V., Brédas, J. L., & Cornil, J., "Charge hopping in organic semiconductors: Influence of molecular parameters on macroscopic mobilities in model one-dimensional stacks". *The Journal of Physical Chemistry A*, 110(19), 2006, 6356-6364.
- [93] Jouili, A., Mansouri, S., Al-Ghamdi, A. A., El Mir, L., Farooq, W. A., & Yakuphanoglu, F. (2017). Characterization and Modeling of Nano-organic Thin Film Phototransistors Based on 6, 13 (Triisopropylsilylethynyl)-Pentacene: Photovoltaic Effect. *Journal of Electronic Materials*, 46(4), 2221-2231.
- [94] Bao, Z., & Locklin, J. (Eds.). (2007). *Organic field-effect transistors*. CRC press.
- [95] Coropceanu, V., Cornil, J., da Silva Filho, D. A., Olivier, Y., Silbey, R., & Brédas, J. L. "Charge transport in organic semiconductors." *Chemical reviews*, 107(4), 2007, 926-952..
- [96] Yoann Olivier, *Charge Transport in Organic Conjugated Materials: From the Molecular Picture to the Macroscopic Properties*, Université de Mons-Hainaut Faculté des Sciences, Laboratoire de Chimie des Matériaux Nouveaux, 2008.
- [97] Wang, C., Dong, H., Hu, W., Liu, Y., & Zhu, D., "Semiconducting  $\pi$ -conjugated systems in field-effect transistors: a material odyssey of organic electronics.", *Chemical reviews*, 112(4), 2011, 2208-2267.
- [98] Botiz, I., & Stingelin, N., "Influence of Molecular Conformations and Microstructure on the Optoelectronic Properties of Conjugated Polymers." *Materials*, 7(3), 2014, 2273-2300.

- [99] Kaake, L. G., Barbara, P. F., & Zhu, X. Y, "Intrinsic charge trapping in organic and polymeric semiconductors: a physical chemistry perspective." *The Journal of Physical Chemistry Letters*, 1(3), 2010, 628-635.
- [100] Goldmann, C., Krellner, C., Pernstich, K. P., Haas, S., Gundlach, D. J., & Batlogg, B., "Determination of the interface trap density of rubrene single-crystal field-effect transistors and comparison to the bulk trap density." *Journal of applied physics*, 99(3), 2006, 034507.
- [101] Bao, Z., "Organic materials for thin film transistors.", *Material Matters*, 2(3), 2007, 4-6.
- [102] Tomas G. Ba"cklund, et al., ,*Towards all-polymer field-effect transistors with solution processable materials*, *Synthetic Metals* 148, 2005, 87–91, Elsevier.
- [103] Myung Sub Lee, et al., *Flexible all-polymer field effect transistors with optical transparency using electrically conducting polymers*, *Thin Solid Films* 477 (2005), 169– 173, Elsevier.
- [104] Henning Rost, et al., *Air-stable all-polymer field-effect transistors with organic electrodes*, *Synthetic Metals* 145, (2004), 83–85, Elsevier.
- [105] Hamadani, B., *Electronic Charge Injection and Transport in Organic Field-Effect Transistors*, Houston, Texas. (January 2007),
- [106] Gordon Yip, *Development of Al<sub>2</sub>O<sub>3</sub> Gate Dielectrics for Organic Thin-film Transistors*, University of Toronto, 2008.
- [107] Mang Mang Ling and Zhenan Bao, ,*Thin Film Deposition, Patterning, and Printing in Organic Thin Film Transistors*, *Chem. Mater.*, 16 (23), (2004), 4824-4840, American Chemical Society.
- [108] Globerman, O., *Lateral and Vertical Organic Thin Film Transistors*, the Senate of the Technion-Israel Institute of technology. April 2006
- [109] A. Tsumura, H. Koezuka and T. Ando, *Macromolecular electronic device: Fieldeffect transistor with a polythiophene thin film*. *Appl. Phys. Lett.* 49, (1986), 1210
- [110] Chung-Chen Kuo, *High Performance Small-Molecule Organic Thin Film Transistors*, the Pennsylvania State University. December 2005.

- [111] Katz, Howard E., and Jia Huang. "Thin-film organic electronic devices." *Annual Review of Materials Research* 39 ,2009, 71-92.
- [112] DiBenedetto, Sara A., Antonio Facchetti, Mark A. Ratner, and Tobin J. Marks. "Molecular Self-Assembled Monolayers and Multilayers for Organic and Unconventional Inorganic Thin-Film Transistor Applications." *Advanced materials* 21(14-15), 2009, 1407-1433.
- [113] Facchetti, Antonio, M-H. Yoon, and Tobin J. Marks. "Gate dielectrics for organic field-effect transistors: new opportunities for organic electronics." *Advanced Materials* 17( 14 ), 2005, 1705-1725.
- [114] Perkinson, Joy C. "Organic field-effect transistors, 2007." Available at: <http://web.mit.edu/joyp/Public/OFET%20Term%20Paper.pdf> [Last access 27/11/14]
- [115] Newman, Christopher R., C. Daniel Frisbie, Demetrio A. da Silva Filho, Jean-Luc Brédas, Paul C. Ewbank, and Kent R. Mann. "Introduction to organic thin film transistors and design of n-channel organic semiconductors." *Chemistry of materials* 16( 23 ) ,2004, 4436-4451.
- [116] Feron, K., Lim, R., Sherwood, C., Keynes, A., Brichta, A., & Dastoor, P. (2018). Organic Bioelectronics: Materials and Biocompatibility. *International journal of molecular sciences*, 19(8), 2382.
- [117] Logothetidis, S., "Flexible organic electronic devices: Materials, process and applications". *Materials Science and Engineering: B*, 152(1), 2008, 96-104.
- [118] Nam, S., Jang, J., Park, J. J., Kim, S. W., Park, C. E., & Kim, J. M. "High-performance low-voltage organic field-effect transistors prepared on electro-polished aluminum wires". *ACS applied materials & interfaces*, 4(1), 2011, 6-10.
- [119] Richter, S., Ploetner, M., Fischer, W. J., Schneider, M., Nguyen, P. T., Plieth, W., ... & Adler, H. J., "Development of organic thin film transistors based on flexible substrates". *Thin solid films*, 477(1), 2005, 140-147.
- [120] Cramer, T., Campana, A., Leonardi, F., Casalini, S., Kyndiah, A., Murgia, M., & Biscarini, F. "Water-gated organic field effect transistors—opportunities for biochemical sensing and extracellular signal transduction". *Journal of Materials Chemistry B*, 1(31), 2013, 3728-3741.

- [121] Mabeck, J. T., & Malliaras, G. G., "Chemical and biological sensors based on organic thin-film transistors". *Analytical and bioanalytical chemistry*, 384(2), 2006, 343-353.
- [122] Kergoat, L., Piro, B., Berggren, M., Horowitz, G., & Pham, M. C. , "Advances in organic transistor-based biosensors: from organic electrochemical transistors to electrolyte-gated organic field-effect transistors". *Analytical and bioanalytical chemistry*, 402(5), (2012), 1813-1826.
- [123] Roberts, M. E., Mannsfeld, S. C., Queraltó, N., Reese, C., Locklin, J., Knoll, W., & Bao, Z. "Water-stable organic transistors and their application in chemical and biological sensors". *Proceedings of the National Academy of Sciences*, 105(34), 2008, 12134-12139.
- [124] Lin, P., & Yan, F. "Organic Thin-Film Transistors for Chemical and Biological Sensing". *Advanced materials*, 24(1), 2012, 34-51
- [125] Caizhi Liao & Feng Yan, "Organic Semiconductors in Organic Thin-Film Transistor-Based Chemical and Biological Sensors", *Polymer Reviews*, 53(3), 2013, 352-406.
- [126] Yeung, S. Y., Gu, X., Tsang, C. M., Tsao, S. W., & Hsing, I. M. (2019). Engineering organic electrochemical transistor (OECT) to be sensitive cell-based biosensor through tuning of channel area. *Sensors and Actuators A: Physical*, 287, 185-193.
- [127] Strakosas, X., Bongo, M., & Owens, R. M. (2015). The organic electrochemical transistor for biological applications. *Journal of Applied Polymer Science*, 132(15).
- [128] H. Sinno, S. Fabiano, X. Crispin, M. Berggren, and I. Engquist, "Bias stress effect in polyelectrolyte-gated organic field-effect transistors", *Appl. Phys. Lett.*, 2013, 102, 113306.
- [129] Loïg Kergoat, Lars Herlogsson, Benoit Piro, Minh Chau Pham, Gilles Horowitz, Xavier Crispin, and Magnus Berggren, "Tuning the threshold voltage in electrolyte-gated organic field-effect transistors", *PNAS*, , 109(22), 2012, 8394–8399.
- [130] Peter Andersson Ersman, David Nilsson, Jun Kawahara, Goran Gustafsson and Magnus Berggren, "Fast-switching all-printed organic electrochemical transistors", *Organic electronics*, 14(5), 2013, 1276-1280.
- [131] Loig Kergoat, Lars Herlogsson, Daniele Braga, Benoit Piro, Minh-Chau Pham, Xavier Crispin, Magnus Berggren, and Gilles Horowitz, "A Water-Gate Organic Field-Effect Transistor", *Adv. Mater.*, 22, 2010, 2565–2569.

- [132] Torres, T., & Bottari, G. *Organic nanomaterials: synthesis, characterization, and device applications*. John Wiley & Sons. 2013
- [133] Lai, S., Demelas, M., Casula, G., Cosseddu, P., Barbaro, M., & Bonfiglio, A. "Ultralow Voltage, OTFT-Based Sensor for Label-Free DNA Detection" *Advanced Materials*, 25(1), 2013, 103-107.
- [134] Brondijk, J. J., Spijkman, M., Torricelli, F., Blom, P. W. M., & De Leeuw, D. M. "Charge transport in dual-gate organic field-effect transistors". *Applied Physics Letters*, 100(2), 2012, 023308.
- [135] Maddalena, F. *Organic Field-effect Transistors for Sensing Applications*. Doctoral dissertation, University of Groningen, The Zernike Institute for Advanced Materials. 2011
- [136] Göllner, M. *Double-Gate Pentacene Thin Film Transistors for Biosensing*, Doctoral dissertation, der Ludwig–Maximilians–Universität at München. 2012
- [137] Caboni, A., Cambarau, W., Orgiu, E., Barbaro, M., & Bonfiglio, A. "A flexible floating-gate organic thin-film transistor for detection of chemical species". *In Sensors, IEEE 2008*, 859-862.
- [138] Caboni, A., Orgiu, E., Barbaro, M., & Bonfiglio, A. "Flexible organic Thin-Film transistors for pH monitoring". *Sensors Journal, IEEE*, 9(12), 2009, 1963-1970.
- [139] Demelas, M., Lai, S., Casula, G., Scavetta, E., Barbaro, M., & Bonfiglio, A. "An organic, charge-modulated field effect transistor for DNA detection" *Sensors and Actuators B: Chemical*, 171, 2012, 198-203.
- [140] Nguyen, T. N. T., Seol, Y. G., & Lee, N. E. (2011). Organic field-effect transistor with extended indium tin oxide gate structure for selective pH sensing. *Organic Electronics*, 12(11), 1815-1821.
- [141] Minamiki, T., Minami, T., Kurita, R., Niwa, O., Wakida, S. I., Fukuda, K., ... & Tokito, S. (2014). A label-free immunosensor for IgG based on an extended-gate type organic field effect transistor. *Materials*, 7(9), 6843-6852.
- [142] Minami, T., Sasaki, Y., Minamiki, T., Wakida, S. I., Kurita, R., Niwa, O., & Tokito, S. (2016). Selective nitrate detection by an enzymatic sensor based on an extended-gate type organic field-effect transistor. *Biosensors and Bioelectronics*, 81, 87-91.

[143] Barbaro, M., Bonfiglio, A., & Raffo, L. (2006). A charge-modulated FET for detection of biomolecular processes: conception, modeling, and simulation. *IEEE Transactions on Electron Devices*, 53(1), 158-166.

[144] Alessandra Caboni, Emanuele Orgiu, Massimo Barbaro, Member, IEEE, and Annalisa Bonfiglio, Flexible Organic Thin-Film Transistors for pH Monitoring, *Sensors Journal*, IEEE (Volume:9 , Issue: 12 ), 1963 – 1970 (2009)

[145] Demelas, M., Lai, S., Barbaro, M., & Bonfiglio, A. (2011, October). DNA hybridization detection based on an Organic charge modulated Field Effect Transistor. In *Sensors, 2011 IEEE* (pp. 1917-1920). IEEE

[146] Spanu, A., Lai, S., Cosseddu, P., Tedesco, M., Martinoia, S., & Bonfiglio, A. (2015). An organic transistor-based system for reference-less electrophysiological monitoring of excitable cells. *Scientific reports*, 5.

[147] Lai, S., Cosseddu, P., Bonfiglio, A., & Barbaro, M. (2013). Ultralow voltage pressure sensors based on organic FETs and compressible capacitors. *IEEE Electron Device Letters*, 34(6), 801-803.

# Chapter 2

## Materials and fabrication of the CM-OFET

After introducing the concept of a sensor based on the CM-OFET concept in chapter 1, this chapter will introduce the structure and fabrication of the CM-OFET. The first part of the chapter will discuss the material choice for each layer of the device, while the second part will discuss the fabrication steps followed to build the CM-OFET device.

### 2.1 Substrate, Gate electrode and Gate Dielectric

The main requirement for gate electrode selection is to be conductive to produce an effective electric field to attract charge carriers to the transistor conducting channel, secondary to that, is the compatibility with the layer in contact (i.e. gate dielectric). In a bottom gate configuration, the morphology of the gate electrode surface also needs to be considered as this impacts the quality of the subsequent layers [1].

As for the gate dielectric material, the requirements to be fulfilled are, first, the layer should be free of pinholes to minimize (ideally completely prevent) leakage current. Secondly, because of the low intrinsic conductivity/mobility of OSC, a relatively high gate voltage (compared to devices based on inorganic SC) is often required to gate the device sufficiently, hence the gate dielectric has to have a high breakdown voltage [1-4]. Metal oxides and organic materials are commonly used as gate dielectrics providing they fulfil the above-mentioned conditions. The choice typically depends on the application and the device requirements. For example, in flexible displays when plastic substrates are used, organic gate dielectric layer are preferable due to the thermal expansion matching [5-6].

Two material systems were adopted for the substrate, gate electrode and gate dielectric materials for the CM-OFET. The first approach, based on Si/SiO<sub>2</sub> materials, provides a reliable, simple and inexpensive approach to device fabrication. The second approach based on Al/Al<sub>2</sub>O<sub>3</sub>, requires relatively more complex fabrication processes but offers lower

power consumption and increases in what can be referred to as the effective sensitivity of the CM-OFET sensor (to be discussed in Section 2.1.3).

### 2.1.1 Si/SiO<sub>2</sub> approach

The combination of Si/SiO<sub>2</sub> is a conventional choice for bottom-gate architecture OFET devices (as employed in the CM-OFET) that has been used for the fabrication of transistors for decades. Because silicon technology is so well established, Si wafers with thermally grown silicon dioxide are widely available in high quality which contributes to reproducible device fabrication and performance [7-9]. Furthermore, the manufacture of OFETs on Si/SiO<sub>2</sub> is very simple requiring only two stages of fabrication; contact formation and OSC deposition.

In the Si/SiO<sub>2</sub> architecture, the Si substrate plays a dual role; mechanical support for the whole device and a conductive substrate that acts as the gate electrode. In order for the Si to act as an efficient gate, it is typical to use a substrate that is degenerately doped such that it acts like a metal [7-8]. The silicon dioxide layer produced by direct thermal oxidation of Si wafers acts as the gate dielectric layer and provides effective electrical insulation between the gate electrode and OSC layer with low leakage. The oxide surface is also smooth providing a favourable base for the deposition of subsequent layers [7,9].

Although this approach is simple and reliable, Si/SiO<sub>2</sub> OFETs suffer from a fundamental shortcoming associated with the large operating voltage required to operate the device. This requirement for large operating voltages has two consequences. First, is the high power consumption which is normally perceived as a major disadvantage for any electronic device. However, the fact that the sensing measurement is normally completed in a short time, may make this problem less of an issue for the CM-OFET. The second consequence of the large operating voltage is related to the sensing response of the device. Based on the working principle of our device, the sensing activity results in an effective shift in the threshold voltage,  $V_{TH}$ . This shift is translated into a change in the source-drain current,  $I_{SD}$ , which is reflected in the current-voltage relationship curve. The ratio of the change in source-drain current,  $\Delta I_{SD}$ , to the shift in threshold voltage change,  $\Delta V_{TH}$ , is what was referred to as the effective sensitivity ( $\Delta I_{SD}/\Delta V_{TH}$ ).

The impact of a given sensing activity (i.e. threshold voltage shift) on the current-voltage relationship curve of a measurement is not equal for two devices working in two operating range/window. Providing the OSC layer is similar (i.e.  $\approx$  Mobility), the rate of  $I_{SD}$  current change per  $V_G$  unit will be different for different operating range/window. The  $I_{SD}$  current change will be more rapid if the operating voltage range is lower. Figure 2.1 illustrate the difference between the two cases, it shows that a 1V gate shift produces a more significant  $I_{SD}$  change if the operating voltage is lower.

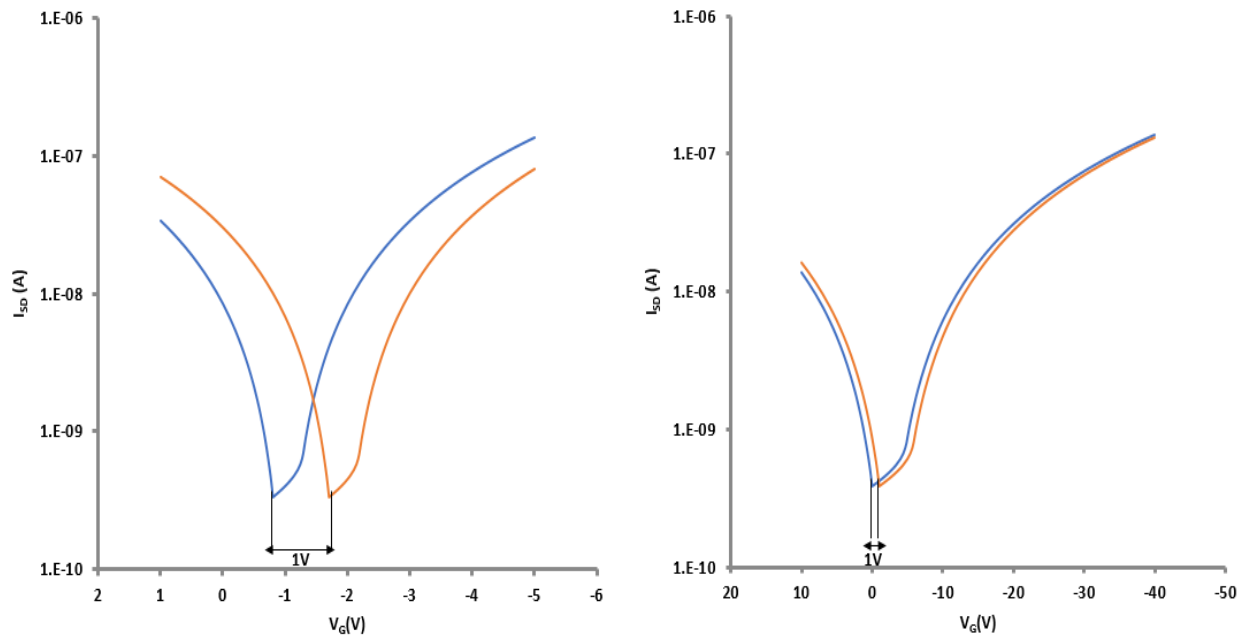


**Figure 2.1:** Illustrate the effect of 1V gate shift on the current-voltage response for low and high operating voltage range (simulated data for two devices with same mobility and electrode dimensions but different gate dielectric layers).

The large operating voltage needed to operate Si/SiO<sub>2</sub> devices stems from the relatively low dielectric constant of SiO<sub>2</sub> ( $k = 3.9$ ) and the need to have thick layers in order to reduce the density of pinholes. So in order to make a device that can operate at reduced operating voltages, both the dielectric constant and thickness of the gate dielectric need to be addressed.

According to equations (1.8) and (1.9) the source drain current  $I_{SD}$  is proportional to the capacitance per unit area of the gate dielectric layer,  $C_i$ , where:

$$C_i = k\epsilon_0 / t \quad (2.1)$$

$\epsilon_0$  is the free space permittivity,  $k$  is the dielectric constant and  $t$  is the dielectric layer thickness.

Thus, a reduction in operating voltage while maintaining high source-drain current can be practically achieved either by using gate dielectric materials of high  $k$  or by reducing the thickness of the gate dielectric layer or both. One should bear in mind when reducing the gate dielectric thickness not to breach the condition of a pinhole free layer [1-4].

### 2.1.2 Al/Al<sub>2</sub>O<sub>3</sub> approach

In this approach, the Si/SiO<sub>2</sub> wafer was used only as a substrate to provide mechanical support and polished surface for CM-OFET fabrication. A thin layer of Al deposited on top of a Si/SiO<sub>2</sub> wafer acted as the gate electrode. The Al electrode was subsequently coated with a thin layer of Al<sub>2</sub>O<sub>3</sub> which acts as the gate dielectric. A number of approaches are available for deposition of Al<sub>2</sub>O<sub>3</sub>. An inexpensive approach is to grow Al<sub>2</sub>O<sub>3</sub> by anodization, as proposed by Majweski et al [10]. Here, Al is anodized using citric acid as an electrolyte in an electrolytic cell enabling the production of pin hole free Al<sub>2</sub>O<sub>3</sub> films of 6.5nm thick. While anodizing of Al evaporated layers was attempted, it was found that delamination of the Al layer occurs at much lower voltage than the maximum voltage needed for anodization (see figure 2.2). While this approach remains attractive in terms of ease of fabrication and low cost, anodization was not investigated further and our attention was shifted towards depositing Al<sub>2</sub>O<sub>3</sub> layer by another method.



**Figure 2.2:** Delamination of the Al layer during anodization process.

The alternative method chosen for depositing the Al<sub>2</sub>O<sub>3</sub> gate dielectric layer was Atomic Layer Deposition ALD. Precise control of Al<sub>2</sub>O<sub>3</sub> film thickness can be produced by ALD and the film is highly conformal and predominantly defect-free, making it ideal as gate dielectric [11-13].

From the source drain current equation 2.2, for two nominally identical devices in terms of geometry and charge mobility, the capacitance per unit area of the gate dielectric layer,  $C_i$ , determines the operating voltage of the device.

$$I_{DS} = \frac{W\mu C_i}{2L} (V_G - V_T)^2 \quad (2.2)$$

Thus,  $C_i$  for an  $\text{Al}_2\text{O}_3$  gate dielectric will be 2.5 times higher than the capacitance of a  $\text{SiO}_2$  dielectric (assuming a constant thickness) owing to the dielectric constant of 9-10 for  $\text{Al}_2\text{O}_3$  compared to 3.9 for  $\text{SiO}_2$ .

As the ALD deposited layer is almost defect free, this enables the deposition of very thin gate dielectric layer, thus enabled us to reduced the thickness of the  $\text{Al}_2\text{O}_3$  gate dielectric layer to only 40nm compared to 300nm for  $\text{SiO}_2$ . This in principle should reduce the operating voltage as the source drain current is enhanced by a factor of 7.5, which makes the combined effect of higher  $\text{Al}_2\text{O}_3$  dielectric constant and reduced gate dielectric thickness nearly a factor of 15.

This simplification is however far from accurate, and as will explained (in chapter 5 section 5.8) that another factor (surface energy of the gate dielectric layer) plays a vital role in determining the drain current and hence the operating voltage required. Nevertheless, lower operating voltage compare to Si/ $\text{SiO}_2$  devices was achieved.

### 2.1.3: Effective sensitivity ( $\Delta I_D/\Delta V_{TH}$ ) of the Al/ $\text{Al}_2\text{O}_3$ and Si/ $\text{SiO}_2$ devices

In principle  $\Delta I_D/\Delta V_{TH}$  should be higher for Al/ $\text{Al}_2\text{O}_3$  based devices compare to Si/ $\text{SiO}_2$  based on the following valid assumptions:

- 1- For the same given sensing event, the charge accumulated in the sensing area for both devices should be the same. The resulting shift in threshold voltage,  $\Delta V_{TH}$ , will thus be the same for both devices.
- 2- For the same OSC (i.e. same mobility) and identical geometry, a similar  $I_{SD}$  transfer characteristic curve can be drawn by smaller gate voltage range for Al/ $\text{Al}_2\text{O}_3$  device compare to Si/ $\text{SiO}_2$ . This in turns means that for the same gate voltage change the corresponding change in the magnitude of  $I_{SD}$  will be different as follows:

$$\Delta V_G (\text{Al}/\text{Al}_2\text{O}_3) = \Delta V_G (\text{Si}/\text{SiO}_2) \text{ then}$$

$$\Delta I_D (\text{Al}/\text{Al}_2\text{O}_3) > \Delta I_D (\text{Si}/\text{SiO}_2)$$

So any change in  $V_G$  value and thus  $V_{TH}$  will be more significant in Al/ $Al_2O_3$  devices.

## 2.2 Source/Drain S/D contacts

Since the S/D contacts are in direct contact with the OSC and are required to inject charge into the organic layer, conductivity alone is not a sufficient criterion for contact material selection. The energy levels of the S/D contacts and OSC material (see figure 2.3) also has to be considered for material selection. It is well understood that one of the major factors that affects the efficiency of carrier (holes/electrons) injection is the alignment of the S/D metal contact work function,  $\Phi_m$ , to either the HOMO or LUMO levels of the OSC active layer (depending on whether the OSC is p or n type material respectively) [14-16].

The best choice to enhance carrier injection and hence reduce the contact resistance is to select a metal contact with a work function matching the HOMO or LUMO level of the OSC material or at least lowering the height of the hole/electron barrier created by the offset between the metal work function or the Fermi energy level and OSC HOMO/LUMO level [14,17].

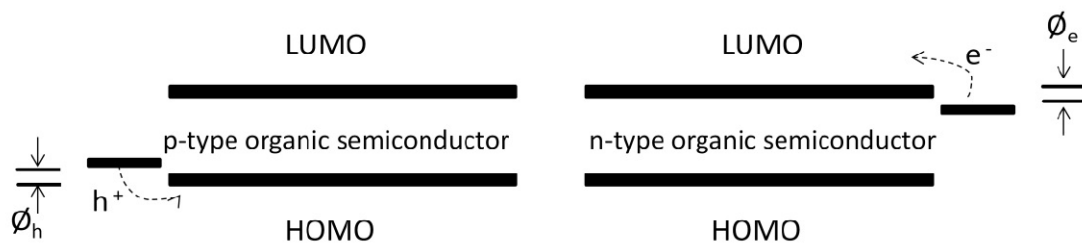


**Figure 2.3:** Energy barrier between Metal work function and HOMO / LUMO of OSC.  $h^+$  and  $e^-$  are holes and electrons respectively.

For p-type OSCs, which have HOMO level in the range of  $-5.1 \pm 0.3$  eV, a metal like Au is commonly used and sometimes Pt and Pd. For n-type OSCs, which have LUMO level around -4 eV, Ca, Mg and Al electrodes are normally used [1,18].

Because of the higher availability and superior mobility of the p-type OSCs, they are used more widely in organic electronics devices than n-type materials even though they require contacts fabricated from relatively expensive metals. It is worth noting that cheaper alternative metals coupled with simple modification have been demonstrated as an

inexpensive replacement for coinage metal contacts [16]. For example, a simple Self-Assembled Monolayer (SAM) treatment using thiol-SAMs that assemble spontaneously on metals like Ag, was found to reduce the band energy offset with an OSC, here Tips-pentacene [16]. It is believed that SAM modification introduces an intermediate dipole moment that alters the work function of metals [2,19-23].

Contact engineering was not the scope for this project, so based on the HOMO level of the p-type OSC chosen for this project (Tips-pentacene and discussed in section 2.3), gold was chosen for the S/D contact material. The work function of Au is  $\sim 5.1\text{eV}$  which is in close alignment to the HOMO level of Tips-pentacene  $\sim 5.2\text{eV}$  [1,24-26].

### 2.3 Organic Semiconductor OSC

Ultimately, high charge carrier mobility is what is required in an OSC, many aspects of how improved mobility/conductivity in OSC can be achieved was discussed in section 1.3.3. Here the focus will only be on the OSC selected for this project, namely 6,13-bis(triisopropylsilylethynyl) pentacene, a small organic molecule commonly known as Tips-pentacene. Tips-Pentacene is a soluble derivative of the insoluble OSC precursor Pentacene, modified to include triisopropylsilylethynyl chains at the 6 and 13 carbon terminal positions (see Figure 2.4).

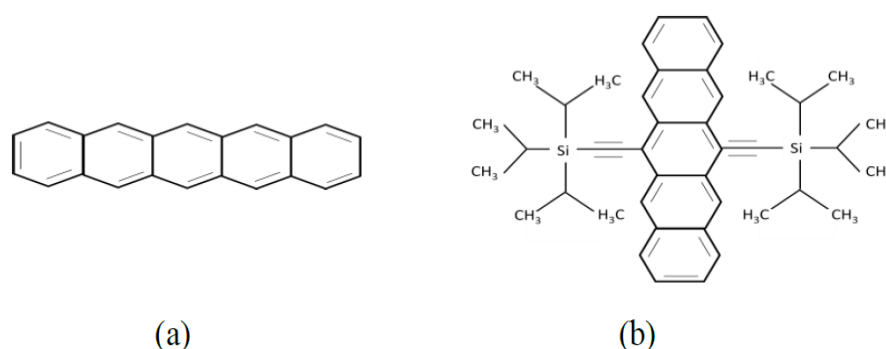


**Figure 2.4:** Chemical structure of (a) Pentacene (b) Tips-pentacene

Pentacene is one of the earliest known organic semiconductors that has been investigated widely as an active, semiconducting layer for OTFTs applications [27-28]. “It is a cyclic

aromatic hydrocarbon that forms a well-ordered polycrystalline material in the thin film phase" [29]. Using evaporated pentacene, field effect mobility as high as  $7\text{cm}^2/\text{V}\cdot\text{s}$  have been reported [30]. This high level of mobility arises from the high degree of order found in pentacene films produced by evaporation. Although evaporated pentacene forms well-ordered films with high mobility, the need for expensive vacuum equipment for evaporation increases the cost and complexity of the whole fabrication process compared to low cost solution based processes [27,30-31]. In order to process pentacene from solution, many efforts have been made to increase its solubility [29,31-33]. It has been shown that attaching a functionalizing group to pentacene improves its solubility, the most notable example being Tips-pentacene in which solubility of the pentacene precursor is increase through attachment of triisopropylsilylethynyl.

As Tips-Pentacene is soluble in most common organic solvents, it can be deposited by various simple deposition methods such as spin coating [34], drop casting [35], dip coating [36] and ink-jet printing [37]. The performance of devices based on Tips-Pentacene is highly dependent on the order and morphology of the Tips-Pentacene film, which in turn depend on the deposition method, the solvent used and any post processing treatment [31,38-39].

In terms of solvent choice, unless a special method is applied for Tips-Pentacene deposition [40], solvents with high boiling point typically provide films with a higher degree of crystallinity due to slow solvent evaporation rate [30,41-43]. Similarly, the presence of a saturated solvent environment surrounding the OFET sample also reduces the rate of solvent evaporation, further extending the time required for crystallization [44-45].

There is no golden rule regarding the post treatment process apart from being a method to remove solvent excess and enhance the molecular ordering of OSC layer [46-48].

To further enhance the crystal formation of OSC films, a customary approach where the OSC can be blended with an insulating polymer was chosen. The use of such a molecular composition is known to improve the interfacial packing and morphology of OSCs. This approach was first proposed by T. Ohe *et al.* [49] and it was found that a mixture of Tips-pentacene and poly $\alpha$ -methylstyrene (P $\alpha$ MS) enables the assembly of a uniform, thermally stable and reproducible layer [49-51]. It is believed that once settled, the mixture phase separate into three layers; a well-ordered, semiconducting Tips-pentacene film at the interface with the S/D contacts, a mixed layer of Tips-pentacene and P $\alpha$ MS in the middle

that provides extra protection for the active Tips–pentacene layer and finally a second Tips–pentacene layer at the surface. This layer does not contact the S/D electrodes and thus not does contribute to the operation of the device [49-51]. This is shown schematically in figure 2.5.

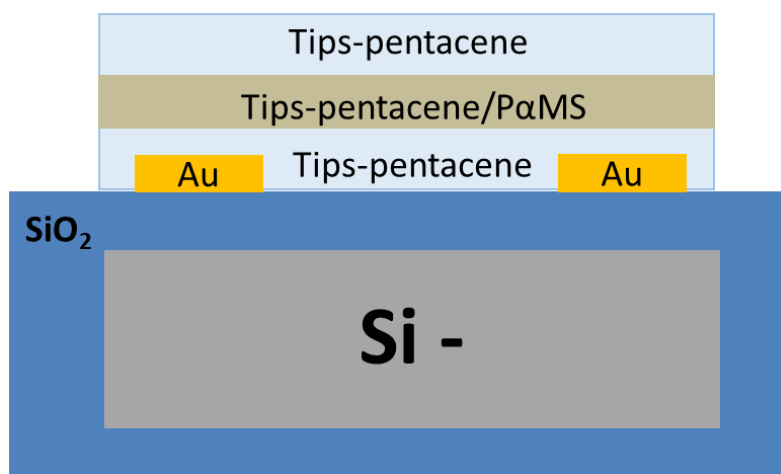


**Figure 2.5:** Schematic diagram showing the three phases of Tips-pentacene/PαMS after separation.

The materials discussed above are the materials for the fundamental components of an organic transistor. Two further materials are needed to transform the transistor to a CM-OFET sensor; the first concerns the functionalization of a portion of the gate electrode surface to make it sensitive to the analyte of interest, the second is the material used to form a fluidic chamber incorporated to the transistor for analyte solution delivery.

#### **2.4 Sensing area functionalization (with 3-aminopropyltri-ethoxysilane APTES)**

The formation of organosilane (derivatives of silane with at least one carbon-silicon bond in their structure) monolayers on a substrate surface is typically referred to as silanization [52-53]. Silanization is commonly achieved via self-assembly of the organosilane either from the vapor or liquid phase [53-54]. In the process, shown in figure 2.6, the presence of moisture or water traces catalyses the hydrolysis of alkoxy groups in the organosilane molecule to form silanol groups (Si–O–H) which reacts with free hydroxyl groups (OH) on

the surface, leading to the formation of a covalent Si-O-Si which tethers the organosilane molecules to the surface [52,55-56]. Once immobilized by the head group of the organosilane self-assembled monolayer, the opposite end of the SAMs molecules, the tail group, will be the new dominant surface chemical species [53-54,57].

One of the most common uses of surfaces modified with organosilane monolayers is to be used as an intermediate layer in biosensors for subsequent protein and biomolecule immobilization. Among the most frequently used organosilane SAMs for this application is 3-aminopropyltri-ethoxysilane (APTES) [55-56,58], in which the tail group is the chemically reactive amine group that can be used subsequently for attaching biomolecules.

In the CM-OFET device, the sensing region was modified with APTES where in principle the immobilizing mechanism should be that the three ethoxy groups in the APTES hydrolysis to react with hydroxyl groups (OH) on the Si or Al surfaces to form (Si-O-Si) and (Si-O-Al) bonds respectively to assemble on the surface, leaving the amine group (NH<sub>2</sub>) on the other end of the APTES SAM to be the new electroactive surface of the region.

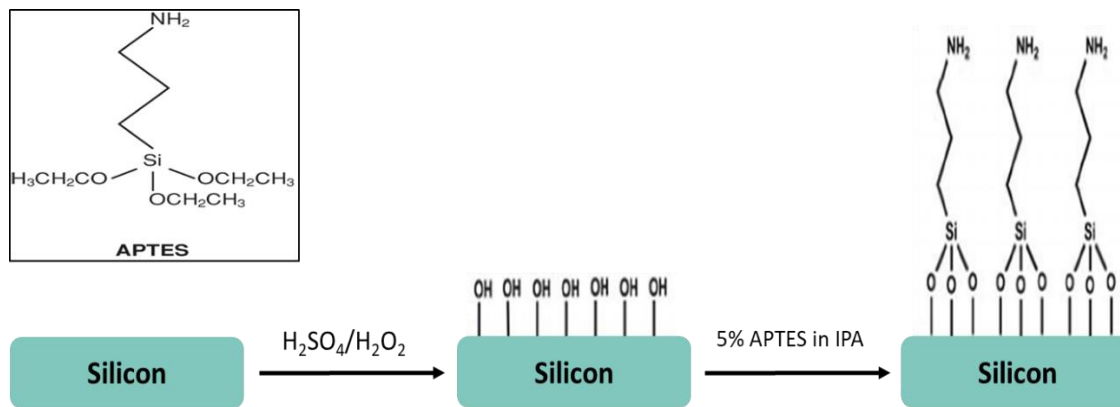


Figure 2.6: APTES chemical structure and Optimal APTES Silanization process on Si substrate, adapted with permission from [54]. Copyright 2012.

The functional amine group terminal was utilized for two fundamental roles in the CM-OFET at two different phases in the project.

- 1- To examine the working principle of the device as a pH sensor. Here, the sensitivity of the amine group to the local concentration of H<sup>+</sup> was exploited to modify the

response of the CM-OFET to different pH solutions where the amine group undergo de/protonation based on the pH level of the analyte solution (discussed in chapter 4).

- 2- The amine group was employed as an anchoring site for subsequent biomolecule attachment via a biotinylation process (discussed in chapter 5).

## 2.5 Polydimethylsiloxane (PDMS) microfluidic chamber

Polydimethylsiloxane (PDMS) is a malleable organosilicon polymer [59]. PDMS can be readily manipulated to form variety of passive and active components of a microfluidic system, making it very much the material of choice for most microfluidic based platform applications as it can be handy in making various microfluidic prototypes [60].

As well as being simple to use, easy to process and commercially available at low cost [61-62], PDMS offers a number of favourable physical and chemical properties that make it a favourable material for microfluidics. On the physical side, PDMS has relatively low viscosity enabling it to diffuse through small patterns of a master template (down to microscale features) [63]. Another key physical property, is that the polymerization (process of cross-linking shown in figure 2.7) of liquid (un-cured) PDMS can be performed at low to moderate temperatures, making it compatible with other various fabrication processes [63].

Commercial PDMS comes in a kit of two liquid bottles, one for the oligomer base and one for curing agent. The crosslinked PDMS elastomer is produced by mixing the two components at a specific ratio. The chemistry of the crosslinking process is explained in detail in [64]. Briefly, as can be seen in figure 2.7, crosslinking occurs through a hydrosilylation process, where in the presence of platinum catalyst, hydrosilanes (Si-H) in the curing agent **2** reacts with vinyl groups (CH=CH<sub>2</sub>) in the oligomer base **1**. In the reaction, hydrosilation of the double bonds occurs and Si-CH<sub>2</sub>-CH<sub>2</sub>-Si linkages are formed [64-67].

Typically making microfluidics using PDMS is realized by soft-lithography techniques. The fabrication of PDMS microfluidic devices using soft-lithography is simply achieved by pouring un-cured PDMS on a master template before the PDMS is cured by curing process normally involve heating. Once cured, the PDMS will contain a replica imprint structure of

the master template [68-69]. Master templates are typically made of silicon substrates patterned with SU8 photoresist features, however, other materials can also be used, including 3D printed thermoplastics, as used in this project.

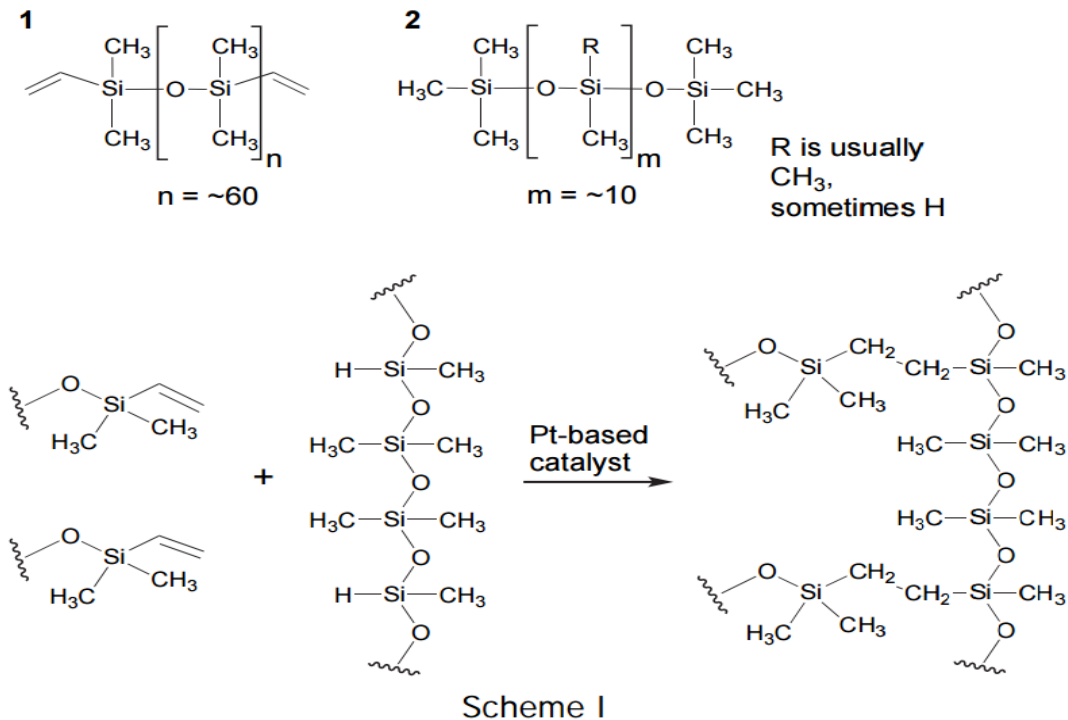


**Figure 2.7:** Polymerization of PDMS when mixing oligomer base (1) and curing agent (2), reprinted with permission from [64]. Copyright 1999.

Cured PDMS produced from soft lithography and other fabrication methods also has a distinct mechanical property; which is that the structure of pure PDMS deforms reversibly, however, PDMS can be doped with other materials to tune its elasticity [70].

Besides the unique PDMS physical properties utilized in the fabrication of microfluidics, PDMS has advantageous chemical properties that are of particular importance for use in medical and biological applications, similar to our project. PDMS is biocompatible, nontoxic and chemically inert [61,71-73]; enabling it to be used safely in virtually any biological applications with little interference with an analyte passing through it.

Another convenient advantage for PDMS that is a plus in the fabrication of PDMS microfluidic systems, is that upon exposure to oxygen plasma, silanol groups (Si-O-H) are

formed on the PDMS surface which allows it to irreversibly seal to hydroxylated surfaces such as Si and glass when brought to conformal contact; by forming a strong (Si-O-Si) bond, bounding the PDMS to the surface [63,69,74] as shown in figure 2.8.

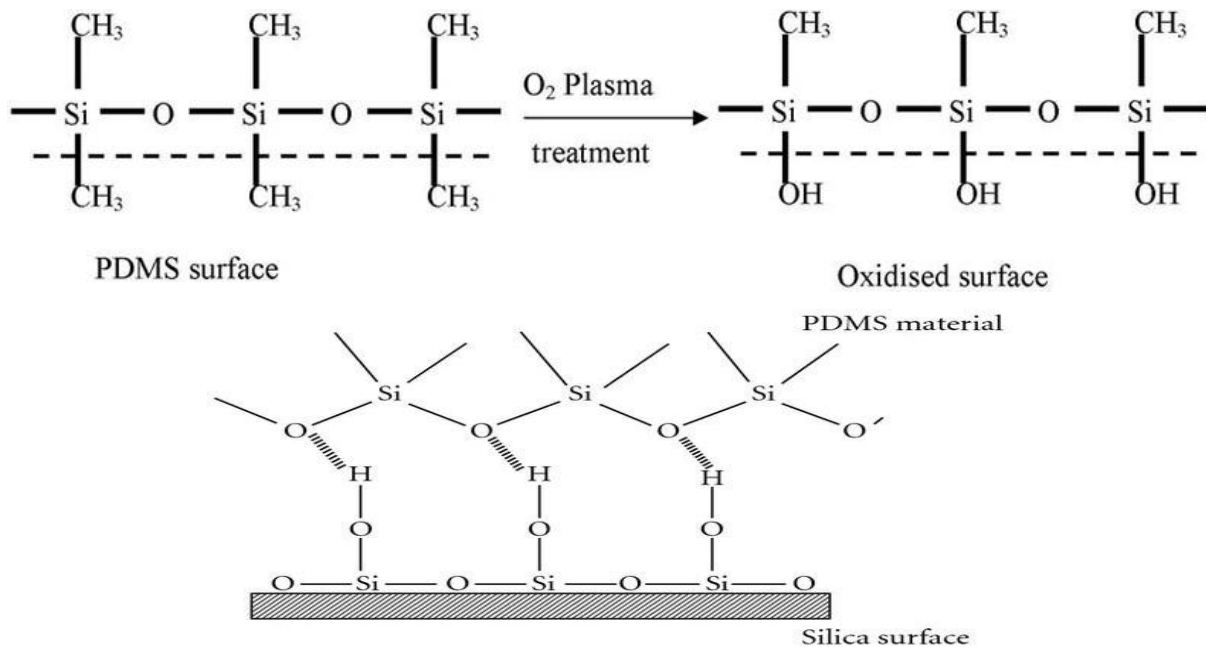


**Figure 2.8:** PDMS oxygen plasma surface treatment and bonding to silica substrate [69,74].

## 2.6 OFET-Sensor Fabrication

### 2.6.1 Si/SiO<sub>2</sub> Devices

#### 2.6.1.1 Substrate Preparation and Cleaning

Substrates used for device fabrication are Si wafers covered with a 300nm thick layer of SiO<sub>2</sub>. 3" or 4" wafers were purchased from IDB Technologies Ltd. The Si (100) substrate was heavily doped (0.001-0.005 Ω/cm) n-type to serve as gate electrode, and the covering thermally grown SiO<sub>2</sub> serves as gate dielectric.

Wafers were cleaved into individual samples of approximately 1.2 X 3 cm. At this size, multiple transistors and the sensing area could be fabricated on a single die. After dicing, the samples were first blown with nitrogen gun to remove debris, and then sonicated in a beaker of acetone in an ultra-sonication bath for 3 minutes. The samples were then

transferred to a beaker of isopropanol IPA and sonicated for another 3 minutes. Finally, the samples were dried under nitrogen.

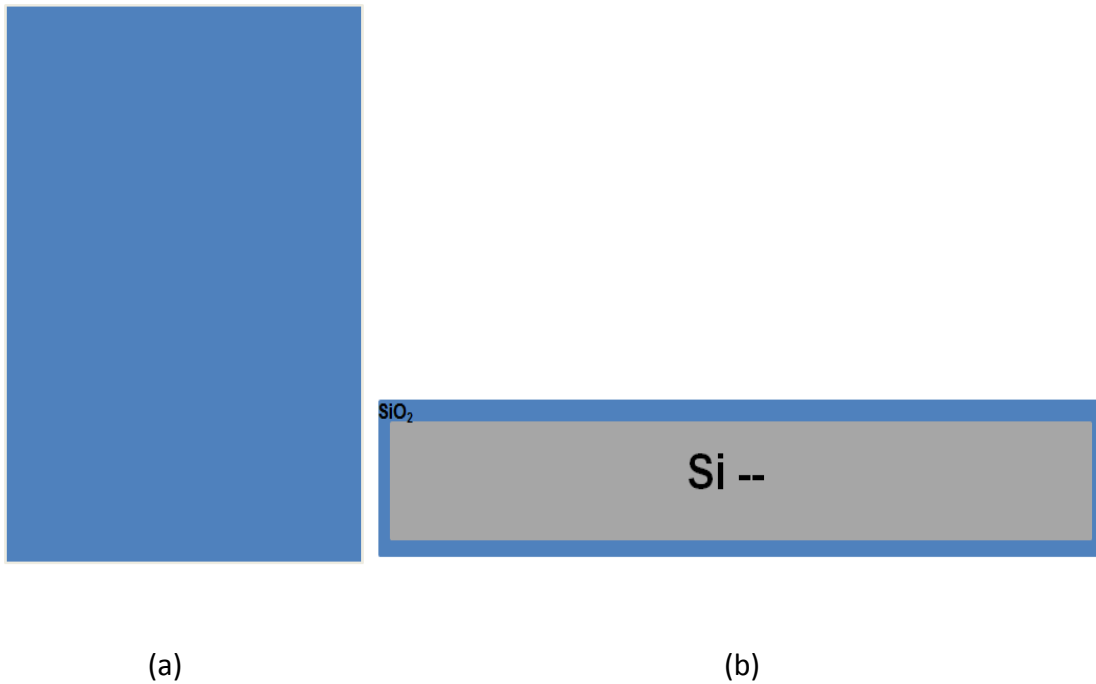


**Figure 2.9:** Clean Si/SiO<sub>2</sub> substrate (a) Top view (b) Cross section.

### 2.6.1.2 Sensing area fabrication

Based on the concept of the sensing device (discussed in chapter 1), the sensing activity is performed on a designated region on the gate surface; which means that for the Si/SiO<sub>2</sub> substrates a selected region of the Si must be exposed to be used as a sensing region. In order to do so, one end of the sample was masked with insulating tape and a photoresist layer was deposited on the rest of the sample. The tape was then removed, and the photoresist was hard-baked using a hotplate at 150 C° for 5 minutes. The exposed SiO<sub>2</sub> region was then etched using a buffered oxide etch (HF 1:6 NH<sub>4</sub>F), by dipping the sample in the solution for 4 minutes. After etching, the samples were washed thoroughly with DI water and dried with nitrogen. Finally, the hard-baked photoresist was removed by initially removing the bulk of the photoresist using cotton buds soaked in acetone before the entire sample was soaked in acetone for several hours. Finally, the sample was sonication in IPA for 3 minutes and dried under nitrogen.

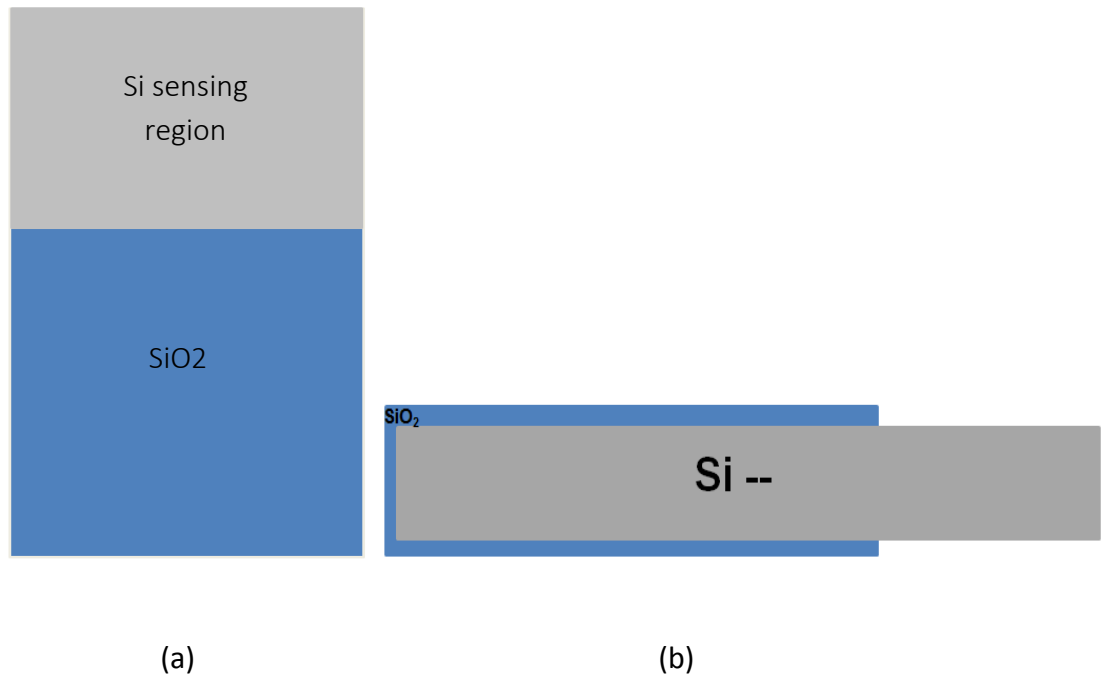


**Figure 2.10:** etched SiO<sub>2</sub> sensing region of Si/SiO<sub>2</sub> substrate (a) Top view (b) Cross section.

### 2.6.1.3 Fabrication of source, drain and control gate electrodes

Two approaches were used to pattern the S/D contacts on the substrate. At the start of the project, the electrodes were defined by conventional photolithography combined with metal evaporation. The photo-mask was designed using L-edit CAD software and subsequently manufactured by Delta Mask to produce a glass photo-mask of the design.

Prior to photolithography, the samples were cleaned using Piranha solution (H<sub>2</sub>SO<sub>4</sub> 7:3 H<sub>2</sub>O<sub>2</sub>); to ensure any residue from the hard-baked photoresist used as a mask for the SiO<sub>2</sub> etch was removed completely. Source, drain and control gate electrodes were subsequently defined using a conventional photolithography stage (full details of the photolithographic process are given in appendix A for full details). Once photolithography process is completed, the samples were loaded into a thermal evaporator for metal contact deposition. All contacts were Ti/Au 6/30 nm thick where the Ti (Titanium) acts as an adhesion layer between Au and SiO<sub>2</sub> substrate. the evaporation rate for Ti was difficult to control but largely was kept at  $1 \pm 0.2 \text{ \AA/s}$  until 6 nm is deposited, for Au the evaporation rate was gradually increased from 0.1 to  $1 \text{ \AA/s}$  and kept at  $1 \pm 0.1 \text{ \AA/s}$  until 30nm is deposited. The evaporation was carried out using an In-house designed evaporator.

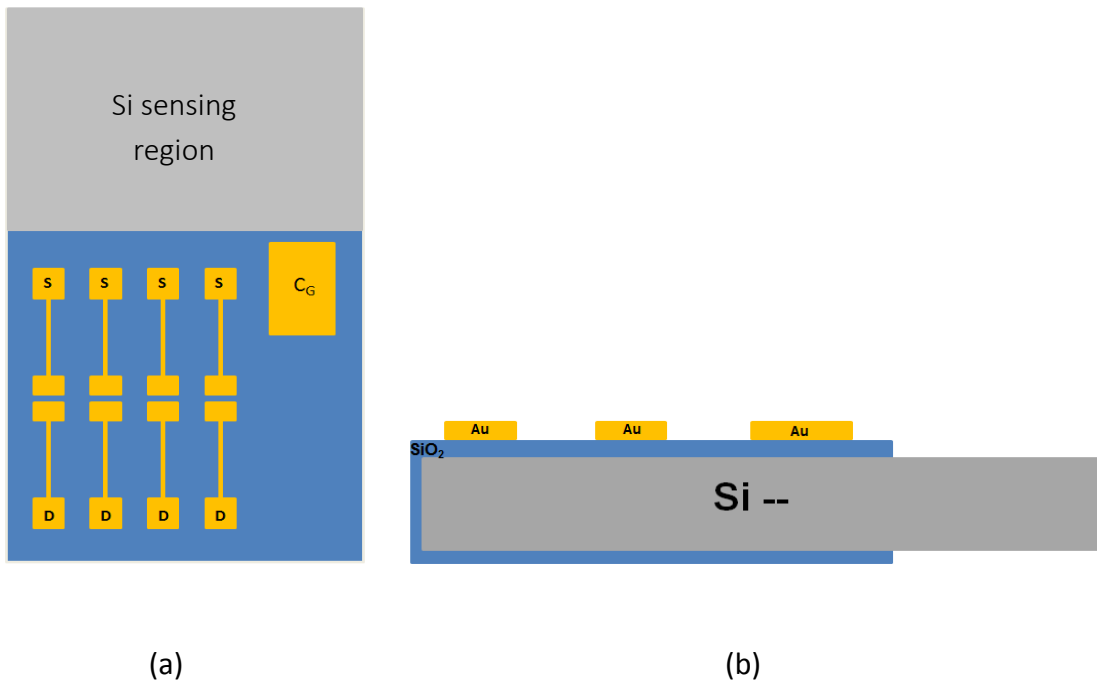


**Figure 2.11:** Deposition of device contacts on Si/SiO<sub>2</sub> substrate (a) Top view (b) Cross section.

While photolithography works well for the devices based on Si/SiO<sub>2</sub> substrates, the process is incompatible with the Al/Al<sub>2</sub>O<sub>3</sub> devices as the Al<sub>2</sub>O<sub>3</sub> layer is rapidly dissolved by the alkaline solution used for photoresist development, consequently destroying the device.

In order to deposit contacts on the Al<sub>2</sub>O<sub>3</sub> layer, contacts deposition using photolithography and evaporation was replaced with a shadow masking technique. The dimensions of the shadow mask were defined by the manufacturer of the shadow mask, and was different to the dimensions of the electrodes on the photomask (In-house designed). Thus, both the Si/SiO<sub>2</sub> and Al/Al<sub>2</sub>O<sub>3</sub> devices were later fabricated using shadow masking to ensure meaningful results when comparing the performance of the two devices.

In the shadow masking technique, the shadow mask, purchased from Ossila Ltd, is mounted below the substrate in the metal evaporator. The mask contained 12 identical sets of 5 transistors and is shown in figure B.2 appendix B.

#### 2.6.1.4 OSC deposition

Following electrode fabrication, the final stage in the construction of the OFET is the deposition of the OSC into the gap between the source and drain contacts. Selected Tipspentacene can be deposited from solution using many solution-processing techniques, for

simplicity, the Tip-pentacene was deposited by drop casting, where a small quantity of the OSC solution is deposited into the source-drain contacts area and left for the solvent to evaporate. As discussed in section 2.3, for enhanced crystal formation, a customary approach was adopted for the composition of our OSC in which the OSC is blended with an insulating polymer. 10mg of the OSC Tips-Pentacene was dissolved in 1ml of toluene and 10mg of the selected polymer (Poly( $\alpha$ -methylstyrene) (P $\alpha$ MS)) was dissolved in 1ml of a solvent (Toluene). Then a mixture of Tips-Pentacene 7:3 P $\alpha$ MS by weight ratio (wt%) was made and the mixture was thoroughly agitated.

Using a pipette, 20 $\mu$ l of the Tips-Pentacene/P $\alpha$ MS mixture was dropped onto the source-drain contact area and the device was covered and allowed to dry slowly for 20-30 minutes. Any excess solution that extended away from the source-drain region was removed by dissolving in Toluene.

Once the Tips-Pentacene has crystallized, (crystallization of the Tips-Pentacene was confirmed by visual inspection using an optical microscope) and the solvent is mostly evaporated, the sample was transferred to a hotplate for annealing. Annealing was performed in an ambient environment at 80C° for 20 minutes to drive out any solvent residue.

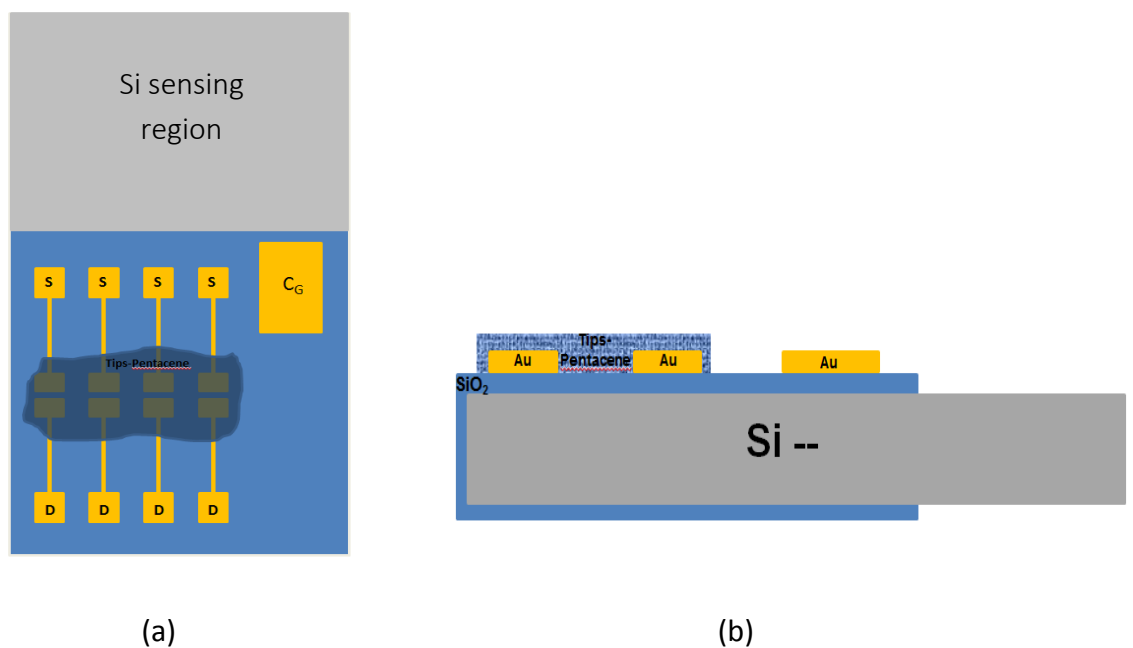


**Figure 2.12:** OSC deposition on S/D contacts of the device (a) Top view (b) Cross section.

Figure 2.13 shows how the Tips-pentacene crystals form on the source/drain electrodes.

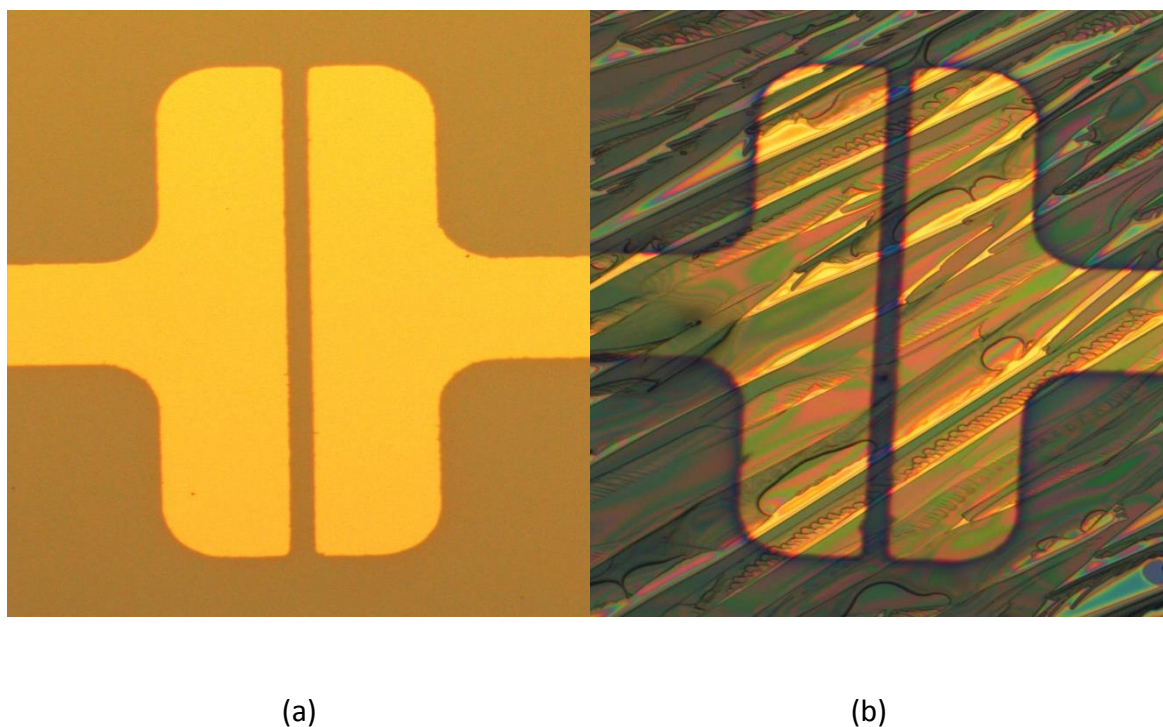


**Figure 2.13:** Optical microscope image of the source/drain electrodes (a) before and (b) after Tips-pentacene deposition. Images were captured using a 5x objective lens.

#### 2.6.1.5 Functionalizing the surface of the sensing region and microfluidic integration

In the final stages of fabrication where the transistor is actually transformed into a sensor, the sensing region exposed by the  $\text{SiO}_2$  etching stage is functionalized with a sensing recognition element in order to control the sensitivity of the exposed Si gate to the selected analyte. The completed device also needs to be integrated with a microfluidic reservoir mounted onto the sensing region to control the delivery of solutions and analytes.

As been discussed earlier in this chapter (section 2.4), the organic functionalizing molecule opted for was (3-aminopropyltriethoxysilane APTES), this molecule can be used in the various stages/applications set to be tackled for the fabricated sensor in this thesis.

The two complementary steps (sensing area functionalisation and microfluidic integration) can take place at two different stages of the fabrication process; either before or after the OSC deposition step. Regardless of the order of this step, the exposed Si region is first

cleaned using Piranha solution ( $\text{H}_2\text{SO}_4$  7:3  $\text{H}_2\text{O}_2$ ) for approximately 5 minutes, then depending on whether this step is performed before or after OSC deposition step, the order of completing the functionalizing and Microfluidic integration steps can interchange.

#### *Functionalization before the deposition of the OSC*

When the functionalization was performed before OSC deposition, the whole sample was first cleaned in Piranha solution for 5 minutes followed by Ozone cleaning for another 5 minutes. The cleaned sample was then immersed in 5% APTES solution in IPA such that only the sensing area was covered by the solution. The sample was left in the solution overnight for approximately 18 hours. The sample was then thoroughly cleaned using IPA to remove excess APTES and finally dried with nitrogen gun. This process allows for the self-assembly of the APTES monolayer on the surface of the sensing region. Immediately afterwards, a pre-prepared microfluidic chamber made from polydimethylsiloxane (PDMS) was mounted to the sensing region and sealed by pouring liquid PDMS around the perimeter of the chamber and solidifying it on a hotplate at  $90^\circ\text{C}$  for 20 minutes.

#### *Functionalization after the deposition of the OSC*

If the process of surface functionalization is performed after the deposition of the OSC, then the procedure has to be modified in order to protect the OSC from damage or change in characteristics that might be caused by the functionalizing solution or vapour.

After OSC deposition, the sample was wrapped with clean Parafilm to protect all regions other than the sensing region. The sensing region was then immersed in Piranha cleaning solution for 3-5 minutes (depending on surface wettability) before being rinsed thoroughly in water and dried under nitrogen. Immediately afterwards, the Parafilm was removed and the sample was transferred to a hotplate where a PDMS microfluidic chamber was mounted to the sensing region and sealed by pouring liquid PDMS around the perimeter of the chamber and solidifying it on the hotplate at  $90^\circ\text{C}$  for 20 minutes. Once the chamber was sealed, fluidic tubes were connected to the inlet and outlet of the chamber and a 5% APTES solution in IPA was injected over the sensing region. The functionalizing solution was

left to rest on the sensing region overnight for approximately 18 hours before being rinsed in IPA.

The difference between the two approaches will be explained in chapter 4 (section 4.4.1).

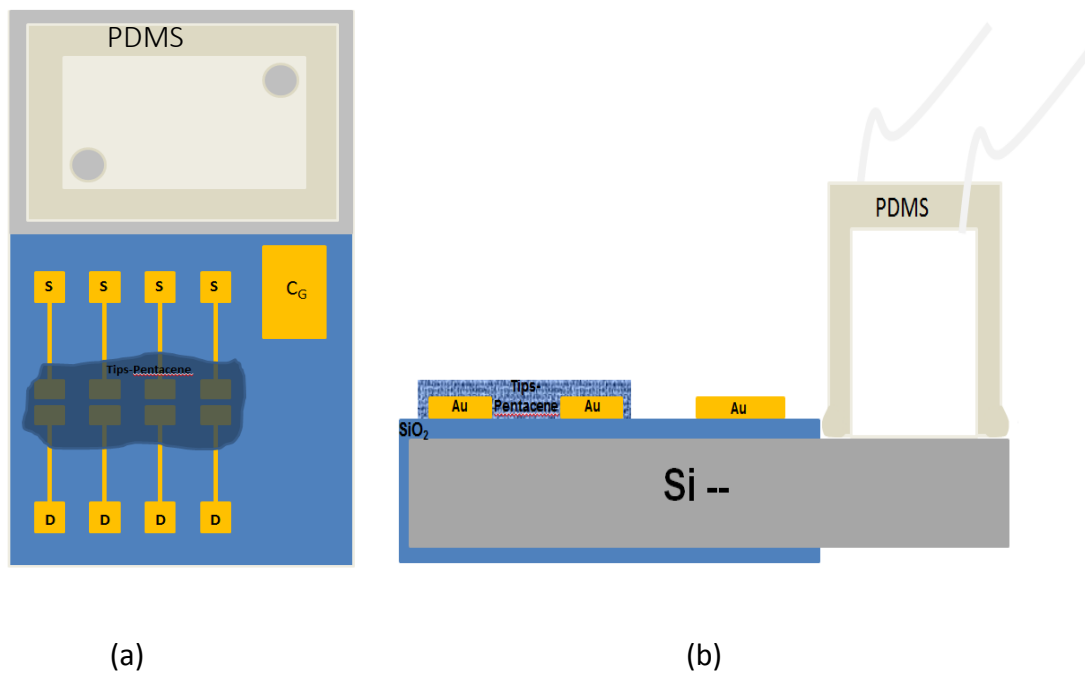


**Figure 2.14:** Complete Si/SiO<sub>2</sub> CM-OFET sensor (a) Top view (b) Cross section.

### 2.6.1.6 PDMS microfluidic chamber fabrication

PDMS was prepared by mixing a 10:1 ratio by weight of the PDMS (pre-polymer) precursor and curing agent (Sylgard 184 kit). The mixture then was placed in a vacuum desiccator to remove air bubbles formed during mixing. A 3D printed master mold of the microfluidic chamber (see figure A.5 in appendix A) was used to make multiple PDMS microfluidic chambers. A replica of the master mold is created by casting liquid PDMS over the 3D printed master which was placed in a petri dish and the PDMS allowed to cure for several hours in an oven at 60 °C. The polymerized PDMS was then gently removed from the 3D printed master and dissected into individual microfluidic chambers. Two holes were finally punched at two opposite ends of the PDMS chamber for the inlet and outlet tubing.

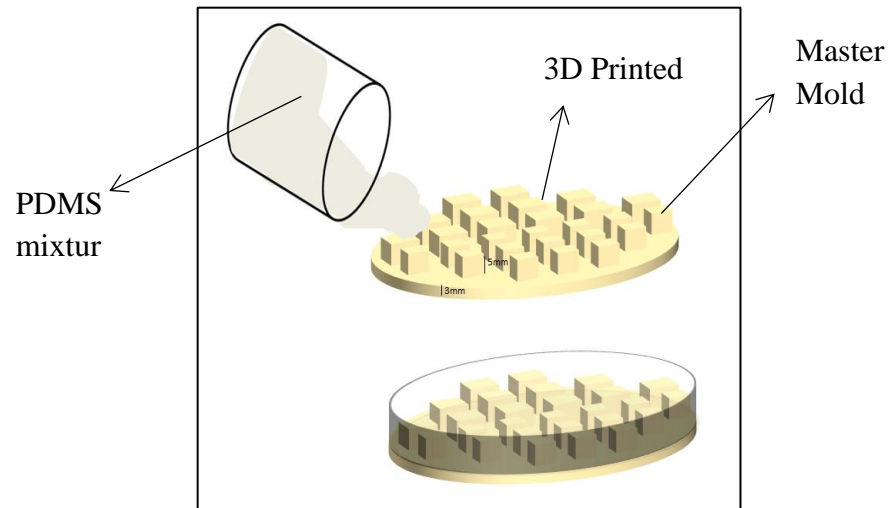


**Figure 2.15:** Making of a PDMS replica mold.

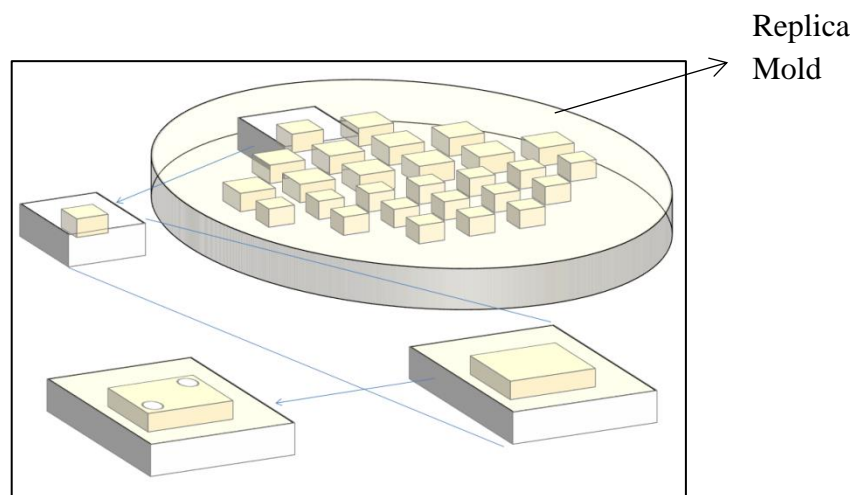


**Figure 2.16:** PDMS Microfluidic chamber with an inlet and an outlet.

## 2.6.2 Al/Al<sub>2</sub>O<sub>3</sub> Devices:

### 2.6.2.1 Substrate Preparation and Cleaning

Substrates used for device fabrication were again 3" or 4" Si wafers coated with a 300 nm thick thermal SiO<sub>2</sub> layer. Wafers were diced into appropriate sample sizes to encompass multiple transistors and the sensing area. After dicing, the samples were first blown with nitrogen to remove debris, and then sonicated in a beaker of Acetone in an ultra-sonication

bath for 3 minutes. The samples were then transferred to a beaker of isopropanol IPA and sonicated for another 3 minutes. Finally, samples were dried under nitrogen.

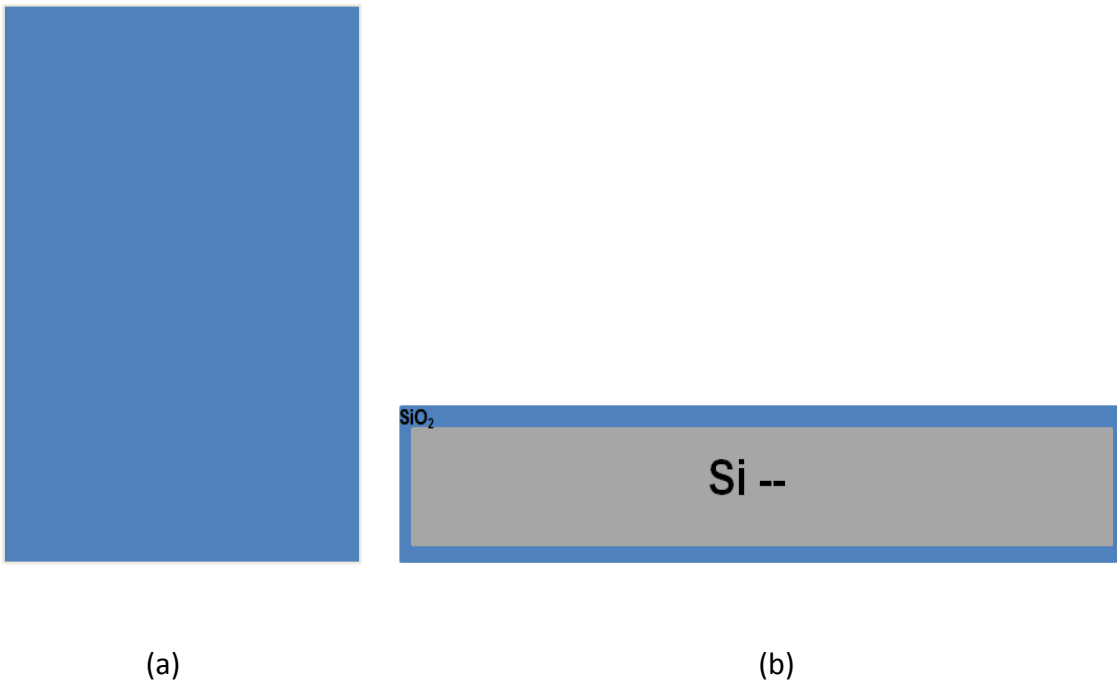


**Figure 2.17:** Clean Si/SiO<sub>2</sub> substrate (a) Top view (b) Cross section.

### 2.6.2.2 Al gate deposition

For this device, the gate electrode is formed by thermal evaporation of an Al layer on top of the Si/SiO<sub>2</sub> substrate. Initially no gate patterning was used and Al was deposited over the entire substrate surface. Devices made using Al gate layer covering the entire sample surface were susceptible to very low breakdown voltage (premature breakdown). It is believed that this was a result of electric field enhancement phenomenon which caused dielectric layer breakdown. This originated from the large overlap between S/D contacts (including the extended connection and contact pad) and the rough common Al gate layer. This large overlap increases the chances of dielectric layer overlapping with non-uniformities in the Al gate layer, for example roughness or scratches. If the dielectric layer is not thick enough to smooth these defects, then these regions will be a source of electric field enhancement.

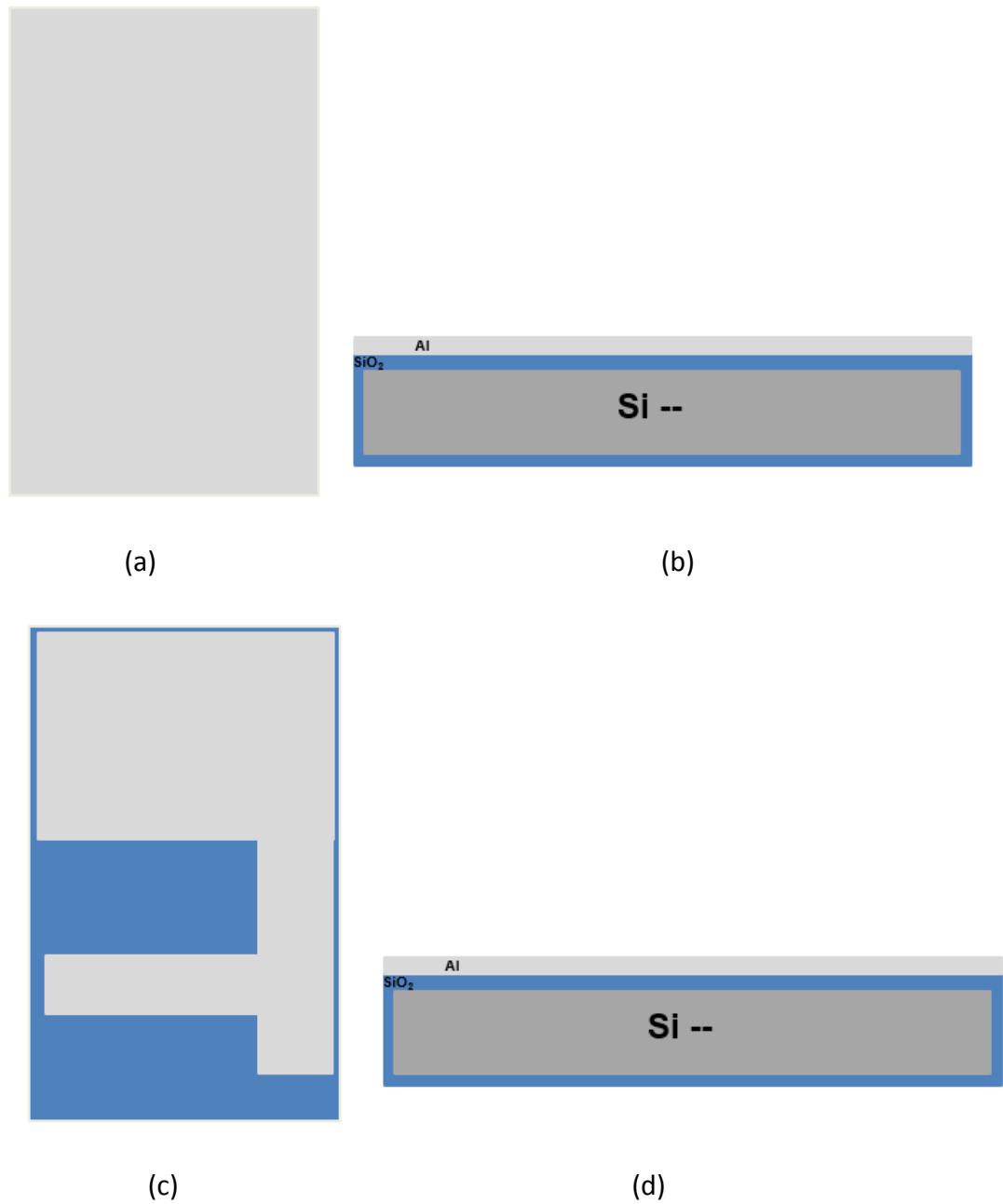


**Figure 2.18:** Deposition of Al gate layer on the entire substrate (a) Top view (b) Cross section, and pattern Al gate layer (c) Top view (d) Cross section

The gate design was revised and the choice of having all surface coverage gate was discarded and was replaced by pattern gate (see figure 2.18c). Pattern gate layer helped the new design to fully comply with the working principle of the CM-OFET device (to be discussed in chapter 5) and it appears to eliminate premature breakdown as a result of

reducing the superposition of S/D contacts with the gate layer. Pattern Al gate deposition was through a shadow mask shown in figure B.3 appendix B and the gate layer thickness was 50nm.

### **2.6.2.3 Al<sub>2</sub>O<sub>3</sub> gate dielectric deposition**

The Al<sub>2</sub>O<sub>3</sub> layer deposition was performed using the ALD system in the cleanroom of the School of Electronic and Electrical Engineering at the University of Leeds. Briefly ALD is a vapor phase thin film deposition technique based on solid-gas reactions. In the deposition process, different gaseous molecules, normally referred to as precursors, react sequentially with a solid surface one at a time without overlapping (pulsing). The reaction between a surface and reactant precursor molecules in ALD is self-limiting where the reaction stops once all reactive sites of the substrate are used/consumed [75-77]. In a simple ALD process, two precursor gases react alternately with a surface to produce the final layer. Inside the reactor chamber the substrate is exposed to the first precursor and the reaction proceeds to completion leading to the formation of the first monolayer. Subsequently, a flux of inert gas is introduced to the chamber to purge unreacted precursor and reaction by-products. These two steps are together referred to as half-cycle. To complete the cycle, the second precursor is pulsed into the chamber to react with the product terminus from the reaction of the first half-cycle. This is followed by another influx of inert gas to purge unreacted precursor and reaction by-products of the second reaction. This completes one deposition cycle. The cycle is then repeated until the targeted thickness is achieved [75-77].

ALD deposition of Al<sub>2</sub>O<sub>3</sub> is commonly performed using alternating trimethylaluminium (TMA) and H<sub>2</sub>O (or O<sub>2</sub>) half-cycles. In the first half-cycle TMA reacts with hydroxyl groups -OH in the substrate, while in the second half-cycle H<sub>2</sub>O or O<sub>2</sub> reacts with the Al(CH<sub>3</sub>)<sub>3</sub> terminus produced by first half-cycle to reverse the substrate terminal back to -OH ready for the next TMA exposure. The by-product from first half-cycle reaction is Methane (CH<sub>4</sub>) while the by-product from the reaction of the second half-cycle is either CH<sub>4</sub>, if H<sub>2</sub>O is used or H<sub>2</sub>O and CO<sub>2</sub> if O<sub>2</sub> is used [75-77].

The process carried out for depositing Al<sub>2</sub>O<sub>3</sub> in the fabrication of CM-OFETs was the TMA and O<sub>2</sub> combination which is often called plasma-enhanced ALD (PEALD) as an RF-plasma

is associated with the O<sub>2</sub> half-cycle process [75]. The chemical reactions of both half-cycles are illustrated in equation 2.3 and 2.4.



Where X represents any support material for the binding site.

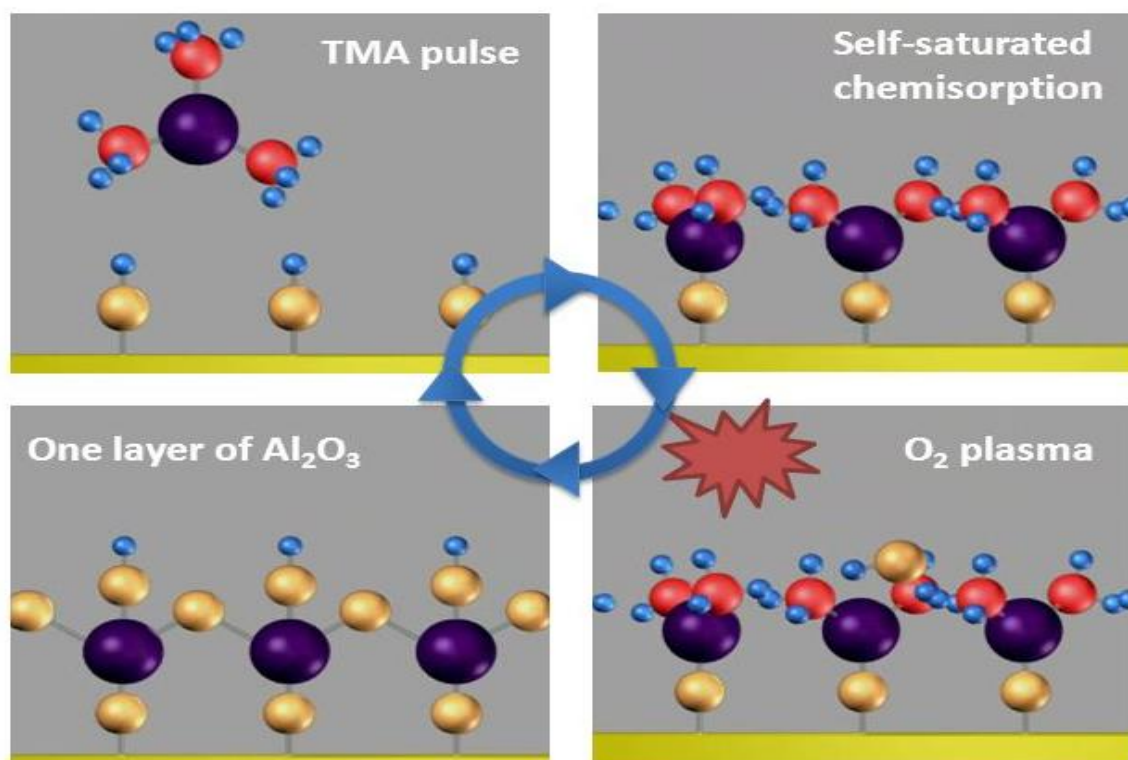


**Figure 2.19:** PE-ALD cycle for Al<sub>2</sub>O<sub>3</sub> deposition [78].

Ten to fifteen Al coated Si/SiO<sub>2</sub> samples at a time were loaded to the ALD system for Al<sub>2</sub>O<sub>3</sub> deposition. Before loading, each sample was rinsed with DI water for 20 seconds then sonicated in Acetone for 5 minutes followed by IPA for 2 minutes. Samples were then dried under nitrogen. After drying and mounting in the ALD chamber, the samples were treated with O<sub>2</sub> plasma *in situ* for 1 minute at 200C°/300W. Using alternating exposures of Al(CH<sub>3</sub>)<sub>3</sub> (trimethylaluminum [TMA]) and O<sub>2</sub>, 351 reaction cycles were performed leading to the formation of a 40nm thick Al<sub>2</sub>O<sub>3</sub> layer (each ALD cycle leads to a single layer of 0.114 nm thick).

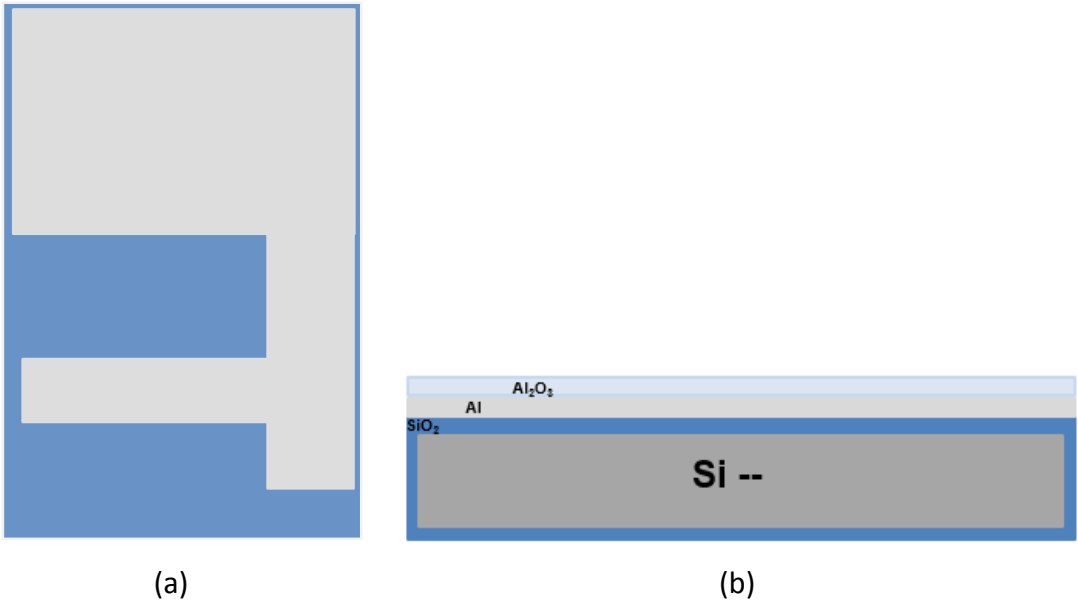


**Figure 2.20:** ALD Al<sub>2</sub>O<sub>3</sub> layer deposition on Al gate (a) Top view (b) Cross section.

#### 2.6.2.4 Contact fabrication

Following Al<sub>2</sub>O<sub>3</sub> deposition, the CM-OFET electrodes (source, drain and floating gate) were fabricated using the shadow masking technique. The samples were positioned against the mask and loaded to the evaporator for metal contact deposition under vacuum. All electrodes were 6/30 nm thick Ti/Au.

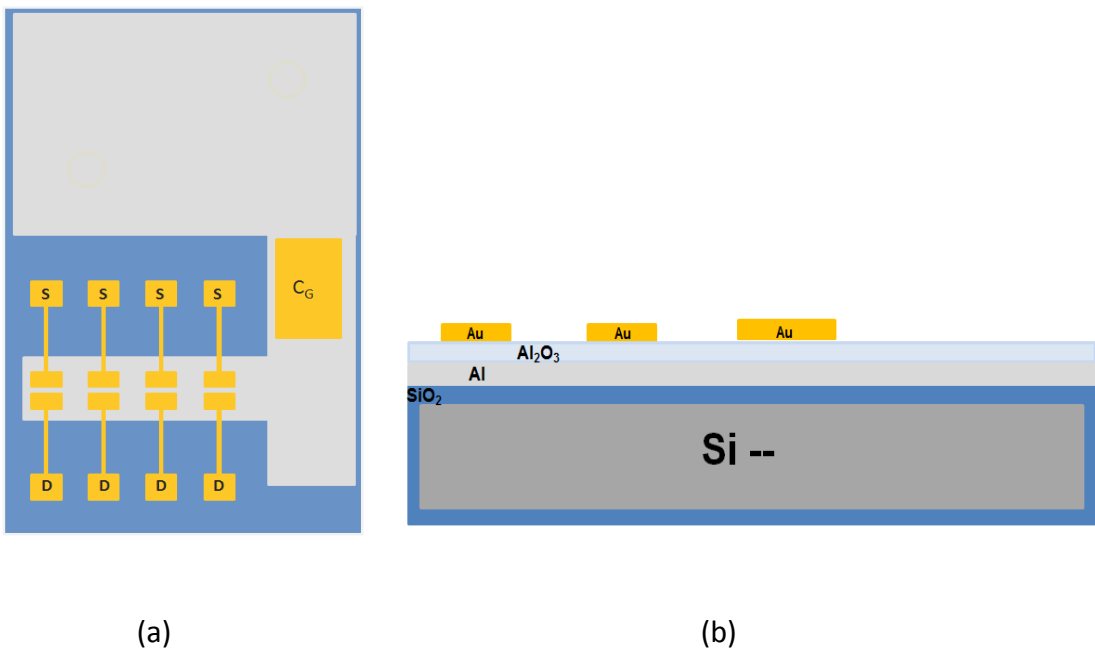


**Figure 2.21:** Deposition of device contacts on top of Al<sub>2</sub>O<sub>3</sub> layer (a) Top view (b) Cross section.

### 2.6.2.5 OSC deposition

OSC (Tips-Pentacene) deposition was performed according to the method described in (section 2.6.1.4).

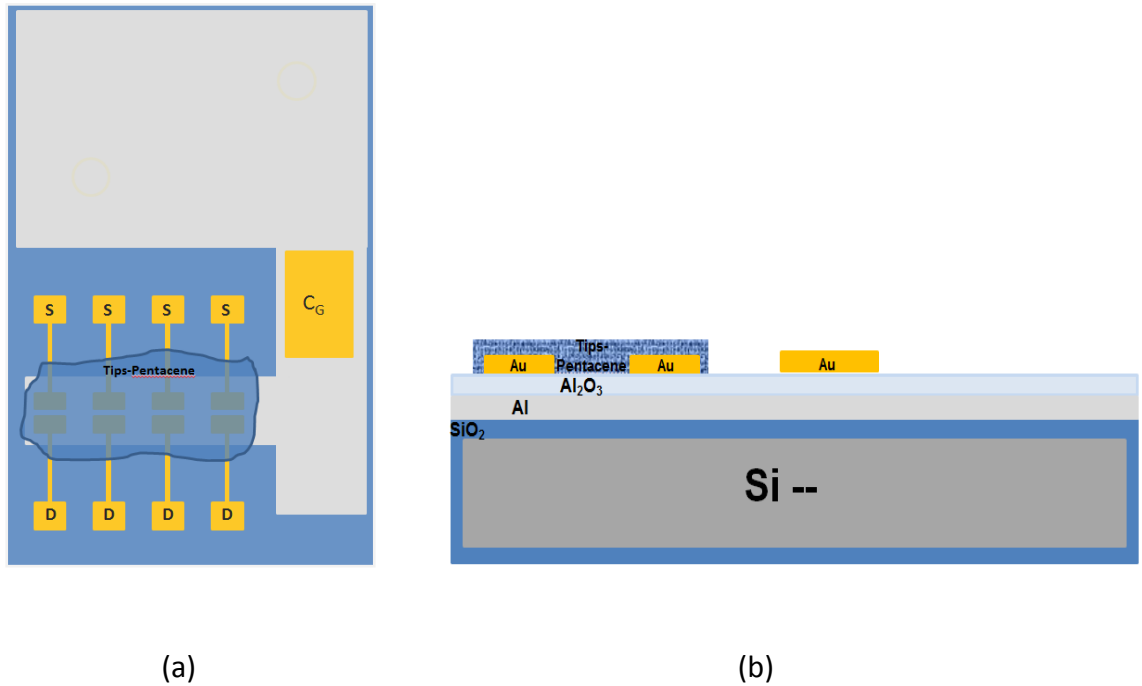


**Figure 2.22:** OSC deposition on S/D contacts of the device (a) Top view (b) Cross section.

### 2.6.2.6 Fabrication of the sensing area

The sensing activity of the device is performed on a designated region of the Al gate electrode. It was thus necessary to remove the overlying Al<sub>2</sub>O<sub>3</sub> layer from the designated sensing region. The selected region was dipped in dilute photoresist developer solution (1:3 developer: water) for 30 seconds to remove the Al<sub>2</sub>O<sub>3</sub> layer. The sample was then swiftly immersed in water to stop the etching. Finally, the sample was dried under nitrogen.

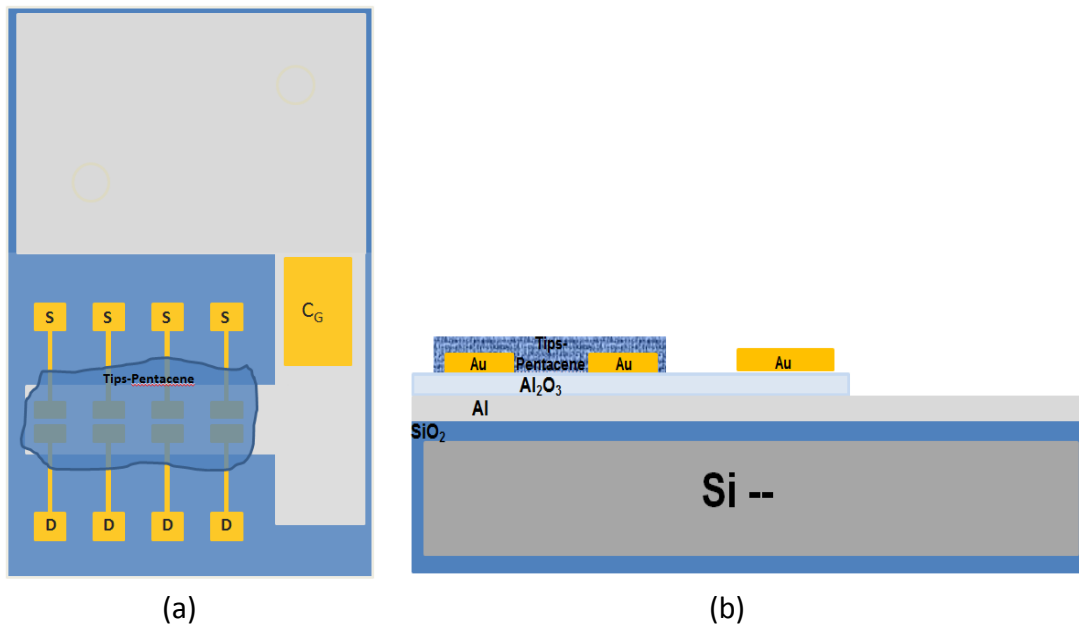


**Figure 2.23:** Etched Al<sub>2</sub>O<sub>3</sub> sensing region of Al/Al<sub>2</sub>O<sub>3</sub> bilayer (a) Top view (b) Cross section.

### 2.6.2.7 Sensing area functionalizing and Microfluidic integration

As with the CM-OFET devices based on Si/SiO<sub>2</sub>, APTES was used for sensing area functionalization. Piranha cleaning is not compatible with this structure so functionalization was performed after only 5 minutes Ozone cleaning.

#### *Functionalization before the deposition of the OSC*

After etching of the Al<sub>2</sub>O<sub>3</sub> layer to form the sensing region, the sample was dipped in APTES solution (only the exposed sensing Al area was covered by the solution) for approximately 18 hours. The sensing region was then rinsed in IPA to remove excess APTES and dried with nitrogen. Immediately after, a pre-prepared microfluidic chamber made from PDMS was mounted to the sensing region and sealed by pouring liquid PDMS around the perimeter of the chamber and solidifying it on a hotplate at 90C° for 20 minutes.

#### *Functionalization after the deposition of the OSC*

Alternatively, functionalization was performed following Tips-Pentacene deposition. Here, after etching of the Al<sub>2</sub>O<sub>3</sub> layer from the sensing region, the sample was transferred to a

hotplate where a PDMS microfluidic chamber is mounted to the sensing region and sealed by pouring liquid PDMS around the perimeter of the chamber and solidifying it on the hotplate at 90C° for 20 minutes. Once sealed, fluidic tubes were connected to the inlet and outlet of the chamber and the functionalizing solution was injected through. The functionalizing solution was left resting on the sensing region overnight (approximately 18 hours). The surface was finally washed by injecting IPA through the microfluidic chamber.

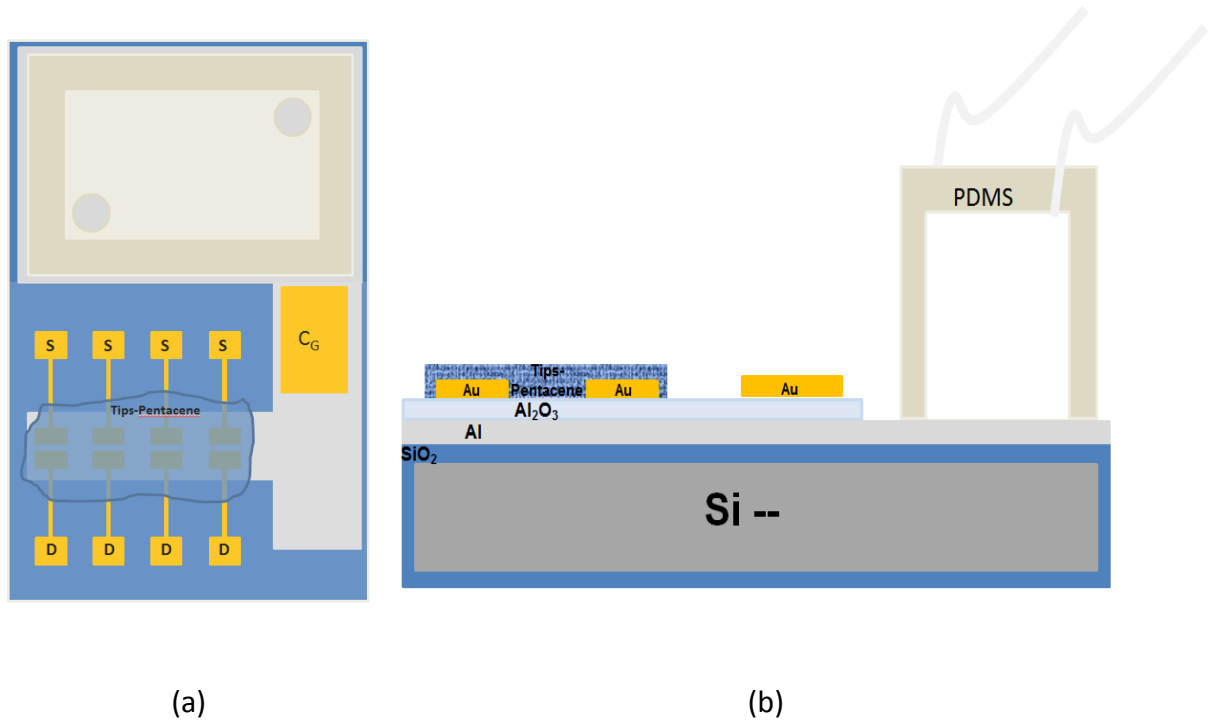


**Figure 2.24:** Complete Al/Al<sub>2</sub>O<sub>3</sub> CM-OFET sensor (a) Top view (b) Cross section.

## 2.7 References

- [1] Li, F., Nathan, A., Wu, Y., & Ong, B. S., *Organic Thin Film Transistor Integration: A Hybrid Approach*. 2013. John Wiley & Sons.
- [2] DiBenedetto, Sara A., Antonio Facchetti, Mark A. Ratner, and Tobin J. Marks. "Molecular Self-Assembled Monolayers and Multilayers for Organic and Unconventional Inorganic Thin-Film Transistor Applications." *Advanced materials* 21(14-15), 2009, 1407-1433.
- [3] Facchetti, Antonio, M-H. Yoon, and Tobin J. Marks. "Gate dielectrics for organic field-effect transistors: new opportunities for organic electronics." *Advanced Materials* 17, no. 14 (2005): 1705-1725.
- [4] Su, Yaorong, Chengliang Wang, Weiguang Xie, Fangyan Xie, Jian Chen, Ni Zhao, and Jianbin Xu. "Low-Voltage Organic Field-Effect Transistors (OFETs) with Solution-Processed Metal-Oxide as Gate Dielectric." *ACS applied materials & interfaces* 3(12) , 2011, 4662-4667.
- [5] Choi, Myeon-Cheon, Youngkyoo Kim, and Chang-Sik Ha. "Polymers for flexible displays: from material selection to device applications." *Progress in Polymer Science* 33(6), 2008, 581-630.
- [6] Jang, Jin, and Seung Hoon Han. "High-performance OTFT and its application." *Current Applied Physics* 6 (2006): e17-e21.
- [7] Miozzo, L., Yassar, A., & Horowitz, G. (2010). Surface engineering for high performance organic electronic devices: the chemical approach. *Journal of Materials Chemistry*, 20(13), 2513-2538.
- [8] Puri, M. (2014). Solution Processable Novel Organic Electronic Devices for New Generation Biomedical Applications.
- [9] Zeng, J., & Jensen, P. B. (2013). Organic light-emitting transistors with optimized gate dielectric.
- [10] L A Majewski<sup>1</sup>, R Schroeder and M Grell, Flexible high capacitance gate insulators for organic field effect transistors, *Journal of Physics D: Applied Physics*. 37 (2004) 21–24

- [11] Koo, J. B., Lim, J. W., Kim, S. H., Yun, S. J., Ku, C. H., Lim, S. C., & Lee, J. H. (2007). Pentacene thin-film transistors and inverters with plasma-enhanced atomic-layer-deposited Al<sub>2</sub>O<sub>3</sub> gate dielectric. *Thin solid films*, 515(5), 3132-3137.
- [12] Jakschik, S., Schroeder, U., Hecht, T., Gutsche, M., Seidl, H., & Bartha, J. W. (2003). Crystallization behavior of thin ALD-Al<sub>2</sub>O<sub>3</sub> films. *Thin Solid Films*, 425(1), 216-220.
- [13] Zhang, X. H., Domercq, B., Wang, X., Yoo, S., Kondo, T., Wang, Z. L., & Kippelen, B. (2007). High-performance pentacene field-effect transistors using Al<sub>2</sub>O<sub>3</sub> gate dielectrics prepared by atomic layer deposition (ALD). *Organic Electronics*, 8(6), 718-726.
- [14] Gordon Yip, *Development of Al<sub>2</sub>O<sub>3</sub> Gate Dielectrics for Organic Thin-film Transistors*, University of Toronto, 2008.
- [15] Chung-Chen Kuo, *High Performance Small-Molecule Organic Thin Film Transistors*, the Pennsylvania State University. December 2005.
- [16] Hong, J. P., Park, A. Y., Lee, S., Kang, J., Shin, N., & Yoon, D. Y. (2008). Tuning of Ag work functions by self-assembled monolayers of aromatic thiols for an efficient hole injection for solution processed triisopropylsilylethynyl pentacene organic thin film transistors. *Applied Physics Letters*, 92(14), 131.
- [17] Boudinet, D., Benwadih, M., Qi, Y., Altazin, S., Verilhac, J. M., Kroger, M., ... & Kahn, A. (2010). Modification of gold source and drain electrodes by self-assembled monolayer in staggered n-and p-channel organic thin film transistors. *Organic Electronics*, 11(2), 227-237.
- [18] Hu, W., Bai, F., Gong, X., Zhan, X., Fu, H., & Bjornholm, T., "*Organic optoelectronics*", John Wiley & Sons. 2012
- [19] Patrick Marmont, et al., *Improving charge injection in organic thin-film transistors with thiol-based self-assembled monolayers*, *Organic Electronics* 9, 2008, 419–424, Elsevier.
- [20] Majewski, L., *Modification of substrate surfaces: self-assembled monolayers (SAMs)*, *Organic Electronics, Nano Electronics*, University of Manchester. 2011
- [21] Yang, X., *Characterization of Self-assembled Monolayers by Low Energy Reactive Ion Scattering Spectrometry: Influence of Terminal Group Composition and Structures*, USA. ProQuest. 2007

- [22] Genzer, J., *Soft Matter Gradient Surfaces: Methods and Applications*, John Wiley & Sons. 2012
- [23] Yun, D., Lee, D., Jeon, H. and Rhee, S., *Contact resistance between pentacene and indium–tin oxide (ITO) electrode with surface treatment*, *Organic Electronics* 8, 2007, 690–694, Elsevier
- [24] Li, H., Zheng, R., & Shi, Q. (2012). Theoretical study of charge carrier transport in organic semiconductors of tetrathiafulvalene derivatives. *The Journal of Physical Chemistry C*, 116(22), 11886-11894.
- [25] Sherman, J. B., Moncino, K., Baruah, T., Wu, G., Parkin, S. R., Purushothaman, B., ... & Chabinyk, M. L. (2015). Crystalline Alloys of Organic Donors and Acceptors Based on TIPS-Pentacene. *The Journal of Physical Chemistry C*, 119(36), 20823-20832.
- [26] Davis, R. J., Lloyd, M. T., Ferreira, S. R., Bruzek, M. J., Watkins, S. E., Lindell, L., ... & Hsu, J. W. (2011). Determination of energy level alignment at interfaces of hybrid and organic solar cells under ambient environment. *Journal of Materials Chemistry*, 21(6), 1721-1729.
- [27] Kyoseung Sim, et al., Soluble pentacene thin-film transistor using a high solvent and heat resistive polymeric dielectric with low-temperature processability and its long-term stability, *Organic Electronics* 10, 2009, 506–510
- [28] Stewart, Z. (2013). *Organic Thin-Film Transistors and TIPS-Pentacene*.
- [29] Muller, E., *Electric Force Microscopy of Charge Trapping In Thin-Film Pentacene Transistors*, Cornell University, August 2005
- [30] Kwang Nam Choi, et al., Solvent Effect on the Electrical Properties of Triisopropylsilylethynyl (TIPS) Pentacene Organic Thin-Film Transistors, *IEEE Transactions On Device And Materials Reliability*, 9 (3) September 2009
- [31] Park, S. K., Jackson, T. N., Anthony, J. E. & Mourey, D. A., High mobility solution processed 6,13-bis(triisopropyl-silylethynyl)pentacene organic thin film transistors. *Appl. Phys. Lett.* 91, 2007, 063514.
- [32] Hamadani, B., *Electronic Charge Injection and Transport in Organic Field-Effect Transistors*, Houston, Texas. (January 2007).
- [33] Youngjun, Y., *Pentacene Based Organic Electronic Devices*, Durham University, 2010.

- [34] Bharti, D., & Tiwari, S. P. (2015, July). Improved alignment and crystallinity of TIPS-Pentacene thin films by off-center spin coating. In *Nanotechnology (IEEE-NANO), 2015 IEEE 15th International Conference on* (pp. 432-435). IEEE.
- [35] Gupta, D., Jeon, N., & Yoo, S. (2008). Modeling the electrical characteristics of TIPS-pentacene thin-film transistors: Effect of contact barrier, field-dependent mobility, and traps. *Organic electronics*, 9(6), 1026-1031.
- [36] Sele, C. W., Kjellander, B. K., Niesen, B., Thornton, M. J., Van der Putten, J. B. P. H., Myny, K., ... & van Aerle, N. (2009). Controlled deposition of highly ordered soluble acene thin films: effect of morphology and crystal orientation on transistor performance. *Advanced Materials*, 21(48), 4926-4931.
- [37] Kim, Y. H., & Park, S. K. (2011). Morphology control of inkjet-printed small-molecule organic thin-film transistors with bank structures. *Journal of Information Display*, 12(4), 199-203.
- [38] J. A. Lim, H. S. Lee, W. H. Lee, K. Cho, Control of the Morphology and Structural Development of Solution-Processed Functionalized Acenes for High-Performance Organic Transistors, *Adv. Funct. Mater.*, 19, 2009, 1515-1525.
- [39] Basiricò, L, "Inkjet printing of organic transistor devices", Doctoral dissertation, Electronic and Computer Engineering Department, University of Cagliari, 2012.
- [40] Yajun Su, Xiang Gao, Jiangang Liu, Rubo Xing and Yanchun Han, Uniaxial alignment of triisopropylsilylethynyl pentacene via zone-casting technique, *Phys.Chem. Chem. Phys.*, 15, 2013, 14396.
- [41] Kim, J., Jeong, J., Cho, H. D., Lee, C., Kim, S. O., Kwon, S. K., & Hong, Y., "All-solution-processed bottom-gate organic thin-film transistor with improved subthreshold behaviour using functionalized pentacene active layer" *Journal of Physics D: Applied Physics*, 42(11), 2009, 115107.
- [42] Sang-Il Shin, Jae-Hong Kwon, Hochul Kang and Byeong-Kwon Ju, "Solution-processed 6, 13-bis(triisopropylsilylethynyl) (TIPS) pentacene thin-film transistors with a polymer dielectric on a flexible substrate", *Semicond. Sci. Technol.*, 23, 2008, 085009.

- [43] Kim, Y. H., Lee, J. H., Han, M. K., & Han, J. I., "Electrical properties of triisopropylsilyl pentacene organic thin-film transistors by ink-jet method". *In Proc. of ASID 6*, 2006, 430-443.
- [44] Park, S. K., Anthony, J. E., & Jackson, T. N., "Solution-processed TIPS-pentacene organic thin-film-transistor circuits". *Electron Device Letters, IEEE*, 28(10), 2007, 877-879.
- [45] Jaquith, M. J., Anthony, J. E., & Marohn, J. A., "Long-lived charge traps in functionalized pentacene and anthradithiophene studied by time-resolved electric force microscopy". *Journal of Materials Chemistry*, 19(34), 2009, 6116-6123.
- [46] Chung-Chen Kuo, *High Performance Small-Molecule Organic Thin Film Transistors*, the Pennsylvania State University. December 2005.
- [47] Jae-Hong Kwon, et al., "A flexible organic thin-film transistor with 6, 13-bis (triisopropylsilylethynyl) pentacene and a methyl-siloxane-based dielectric", *Solid-State Electronics* 53, 2009, 266–270, Elsevier.
- [48] Myung-Hoon Lim, et al., "Leakage current reduction in pentacene-based thin film transistor using asymmetric source/drain electrodes", *Organic Electronics* 13, 2012, 1056–1059, Elsevier.
- [49] Takahiro Ohe, et al., (2008), *Solution-processed organic thin-film transistors with vertical nanophase separation*, *Applied Physics Letters* 93, 053303 DOI: 10.1063/1.2966350
- [50] Byoungchoo Park, et al., (2012), *High-performance organic thin-film transistors with polymer-blended small-molecular semiconductor films, fabricated using a pre-metered coating process*, *Journal of Materials Chemistry* 22, 5641–5646
- [51] Zhengran He ,etal., (2011), *Enhanced Performance Consistency in Nanoparticle/TIPS Pentacene-Based Organic Thin Film Transistors*, *Advanced Functional Material Journal* 21, 3617–3623
- [52] Materne, T., de Buyl, F., & Witucki, G. L. (2012). Organosilane technology in coating applications: review and perspectives. *Dow Corning Corporation., AGP11933, Form No.*
- [53] Glass, N. R., Tjeung, R., Chan, P., Yeo, L. Y., & Friend, J. R. (2011). Organosilane deposition for microfluidic applications. *Biomicrofluidics*, 5(3), 036501.

- [54] Acres, R. G., Ellis, A. V., Alvino, J., Lenahan, C. E., Khodakov, D. A., Metha, G. F., & Andersson, G. G. (2012). Molecular structure of 3-aminopropyltriethoxysilane layers formed on silanol-terminated silicon surfaces. *The Journal of Physical Chemistry C*, *116*(10), 6289-6297.
- [55] Howarter, J. A., & Youngblood, J. P. (2006). Optimization of silica silanization by 3-aminopropyltriethoxysilane. *Langmuir*, *22*(26), 11142-11147.
- [56] Klug, J., Pérez, L. A., Coronado, E. A., & Lacconi, G. I. (2013). Chemical and electrochemical oxidation of silicon surfaces functionalized with APTES: the role of surface roughness in the AuNPs anchoring kinetics. *The Journal of Physical Chemistry C*, *117*(21), 11317-11327.
- [57] Wu, Z., Xiang, H., Kim, T., Chun, M. S., & Lee, K. (2006). Surface properties of submicrometer silica spheres modified with aminopropyltriethoxysilane and phenyltriethoxysilane. *Journal of colloid and interface science*, *304*(1), 119-124.
- [58] Lessel, M., Bäumchen, O., Klos, M., Hähl, H., Fetzer, R., Seemann, R., & Jacobs, K. (2012). Self-assembled silane monolayers: A step-by-step high speed recipe for high-quality, low energy surfaces. *arXiv preprint arXiv:1212.0998*.
- [59] Zitka, J., Heger, Z., Zitka, O., Adam, V., & Kizek, R. Technical concept of 3D printed fluidic biosensor with polydimethylsiloxane chip based on fluorescence detection system.
- [60] Xiong, L., Chen, P., & Zhou, Q. (2014). Adhesion promotion between PDMS and glass by oxygen plasma pre-treatment. *Journal of Adhesion Science and Technology*, *28*(11), 1046-1054.
- [61] Tarbague, H., Lachaud, J. L., Destor, S., Velutini, L., Pillot, J. P., Bennetau, B., ... & Dejous, C. (2009). PDMS (polydimethylsiloxane) microfluidic chip molding for Love wave biosensor. *ECS Transactions*, *23*(1), 319-325.
- [62] Engavale and Deshmukh (2015), *Fabrication of Microfluidic Biosensor*, IOSR Journal of Pharmacy and Biological Sciences, PP 05-08
- [63] Dhruv, H. D. (2009). Controlling nonspecific adsorption of proteins at bio-interfaces for biosensor and biomedical applications.

- [64] Lisensky, G. C., Campbell, D. J., Beckman, K. J., Calderon, C. E., Doolan, P. W., Ottosen, R. M., & Ellis, A. B. (1999). Replication and compression of surface structures with polydimethylsiloxane elastomer. *J. Chem. Educ*, 76(4), 537.
- [65] Stafie, N., Stamatialis, D. F., & Wessling, M. (2005). Effect of PDMS cross-linking degree on the permeation performance of PAN/PDMS composite nanofiltration membranes. *Separation and purification technology*, 45(3), 220-231.
- [66] Ouyang, G., Wang, K., & Chen, X. Y. (2012). TiO<sub>2</sub> nanoparticles modified polydimethylsiloxane with fast response time and increased dielectric constant. *Journal of Micromechanics and Microengineering*, 22(7), 074002.
- [67] Bosq, N., Guigo, N., Persello, J., & Sbirrazzuoli, N. (2014). Melt and glass crystallization of PDMS and PDMS silica nanocomposites. *Physical Chemistry Chemical Physics*, 16(17), 7830-7840.
- [68] Melin, J. (2006). *Single-Molecule Detection and Optical Scanning in Miniaturized Formats* (Doctoral dissertation, Acta Universitatis Upsaliensis).
- [69] Pasirayi, G., Auger, V., M Scott, S., KSM Rahman, P., Islam, M., O'Hare, L., & Ali, Z. (2011). Microfluidic bioreactors for cell culturing: a review. *Micro and Nanosystems*, 3(2), 137-160.
- [70] Tang, S. K., & Whitesides, G. M. (2010). Basic microfluidic and soft lithographic techniques. *Optofluidics: Fundamentals, Devices and Applications*, 7-32.
- [71] McDonald, J. C., & Whitesides, G. M. (2002). Poly (dimethylsiloxane) as a material for fabricating microfluidic devices. *Accounts of chemical research*, 35(7), 491-499.
- [72] Sang, S., & Witte, H. (2010). A novel PDMS micro membrane biosensor based on the analysis of surface stress. *Biosensors and Bioelectronics*, 25(11), 2420-2424.
- [73] Wu, J., Wang, R., Yu, H., Li, G., Xu, K., Tien, N. C., ... & Li, D. (2015). Inkjet-printed microelectrodes on PDMS as biosensors for functionalized microfluidic systems. *Lab on a Chip*, 15(3), 690-695.
- [74] Sanchez, J. B., Schmitt, A., Berger, F., & Mavon, C. (2010). Silicon-micromachined gas chromatographic columns for the development of portable detection device. *Journal of Sensors*, 2010.

[75] Fry-Bouriaux, L. (2017). *Towards the Mass Fabrication of Single Electron Transistors for Biosensing Applications*(Doctoral dissertation, University of Leeds).

[76] Johnson, R. W., Hultqvist, A., & Bent, S. F. (2014). A brief review of atomic layer deposition: from fundamentals to applications. *Materials today*, 17(5), 236-246.

[77] Zhang, X. (2009). *Device engineering of organic field-effect transistors toward complementary circuits*. Georgia Institute of Technology.

[78] Rampelberg, G., Cremers, V., Longrie, D., Deduytsche, D., Haemers, J., Detavernier, C. (2016), *Thermal and Plasma Enhanced Atomic Layer Deposition on Powders and Particles*, Belgian Physical Society General Scientific Meeting. [Last access 12 Dec. 17] URL: <http://slideplayer.com/slide/10797197/>

# Chapter 3

## Electrical characterization of the CM-OFET device

The electrical behaviour of any type of OFET device is typically characterized by two experimental measurements; the output and transfer characteristics. Together, these measurements enable quantification of the relationship between the two transistor output variables (source drain current and source drain voltage) and the input variable (gate voltage) from which fundamental parameters of the device can be extracted. The output characteristic allows the relationship between the two output variables to be examined, while keeping the input fixed. In contrast, the transfer characteristic curve describes the relationship between the source drain current and the gate voltage while the second output variable (source drain voltage) is held constant (i.e. probes the transfer of the input function on the observed output response).

This chapter will focus on experimental characterization of the fabricated CM-OFET devices. This includes a detailed description of the experimental measurement setup, the measurement considerations taken into account as well as how the sensing response of the device was quantified.

### 3.1 Electrical characterization of the fabricated devices

Characterization of the fabricated OFET transistor is essential prior to use in any sensing application. This is required not only to provide a rigorous understanding of the device characteristics and performance but also to inform device future application as a sensor. Understanding the device's characteristics, helps distinguish between changes in the device's response related to the sensing activity (state of the transistor during or after the sensing event), from any changes in the device behaviour due to other phenomenon, for example current drifts, or possible malfunction.

Characterization of the fabricated transistors was performed using the typical output and transfer characteristics field effect measurements. The output characteristics are obtained by measuring the source drain current,  $I_{SD}$ , while sweeping the source drain voltage,  $V_{SD}$ , within a certain voltage window, at a number of fixed DC gate voltages,  $V_G$ . The resulting output characteristics are plotted to generate a set of standard  $I_{SD}$  against  $V_{SD}$  curves. The transfer characteristics are recorded by measuring the source drain current,  $I_{SD}$ , as a function of the gate voltage,  $V_G$ , at a fixed DC source-drain voltage. The resulting data is subsequently graphed by plotting  $I_{SD}$  against  $V_G$ . As is typical, the transfer characteristics were recorded with the transistor operating in the saturation regime (i.e. at very high  $V_{SD}$ ). These two characteristics were used as a benchmark during the whole project and only those transistors that exhibited typical characteristics (characteristics displaying ON/OFF and saturation behaviour) were taken forward for use as a biosensor.

### **3.1.1 Electrical measurement setup**

In order to acquire the output and transfer characteristics to analyse the electrical performance of the fabricated device, an Agilent B1500a parameter analyser was used to perform electrical measurements. All measurements were obtained using the experimental setup shown in figure 3.1.

In the setup, each electrode is connected to an independent source-measurement unit (SMU) within the parameter analyser. Each SMU is responsible for applying the allocated voltage to each electrode and for measuring the current drawn from the SMU by the device. Connections from the SMUs to the device were made through test probes and coaxial cables. The test probes were either fixed directly to the electrode or fixed on contact pads extended from the electrode. All measurements were automated and controlled by the interface of Keysight EasyEXPERT software embedded in the Agilent B1500a. Built-in functions that define the output and transfer characteristic measurements were imported from the EasyEXPERT Library and configured to the customized test conditions. Measurement data were exported in CSV format and later processed for graphing and data analysis using Origin and Microsoft Excel.

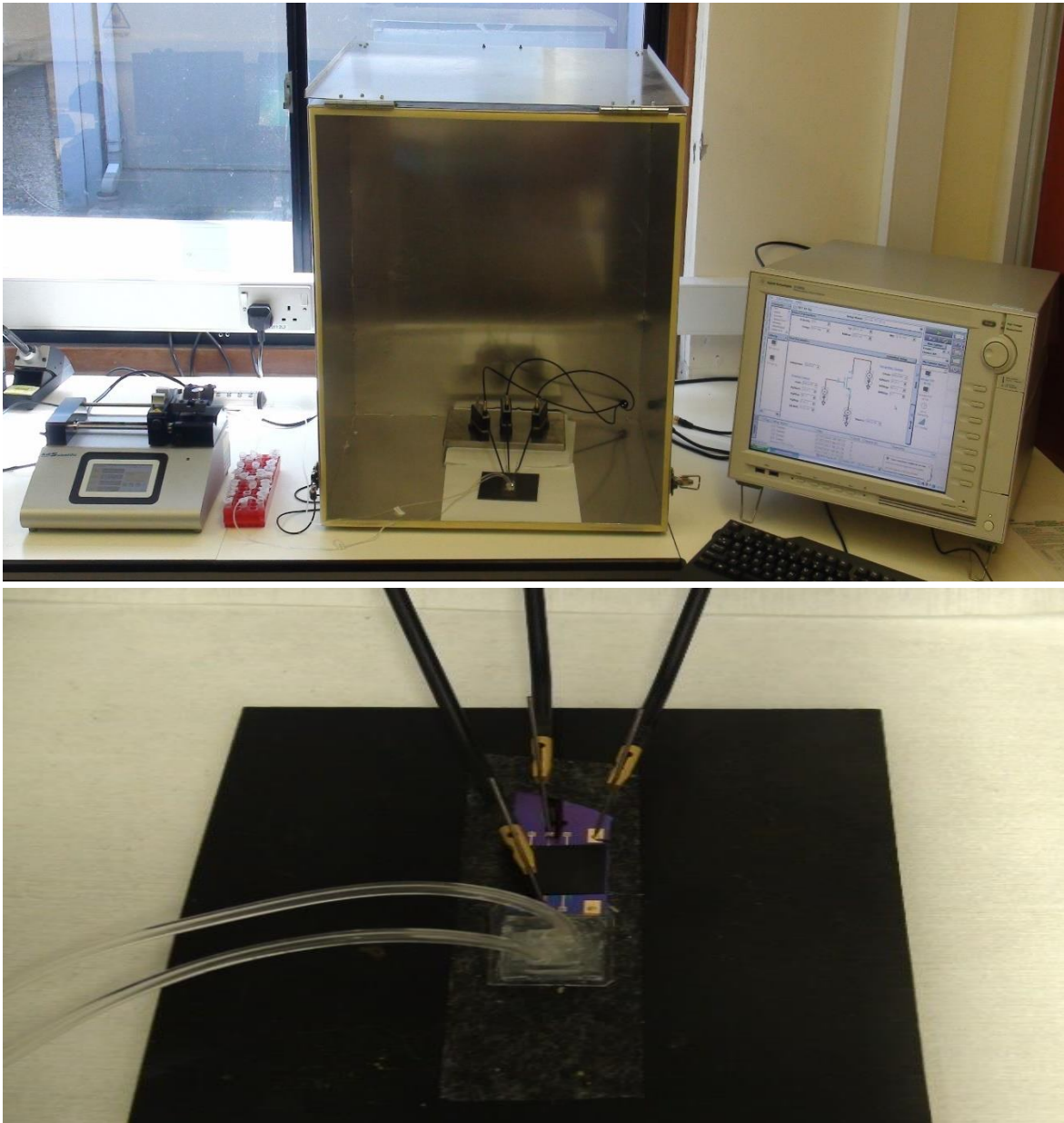


**Figure 3.1:** Electrical characterization measurement setup.

### **3.1.2 Electrical characterization of the OFET devices**

Initially, electrical characterizations were performed on standard OFET devices fabricated using photolithography process and gated directly via the common heavily doped Si gate. The purpose here was to confirm the functionality of the solution deposited Tips-pentacene and to validate the fabrication process using a conventional device geometry.

A photo of the fabricated OFETs can be seen in figure 3.2, the photo shows 4 identical transistors fabricated on the same substrate, where the common Si gate for the 4 transistors can be accessed by mechanically scratching the SiO<sub>2</sub> gate dielectric layer on top, the source and drain electrodes of each transistor are made of Au and separated by 60µm. The Tips-pentacene deposited by drop casting to cover the 4 transistors.

An example of the typical measured output and transfer characteristics for a Si/SiO<sub>2</sub> OFET is presented in figure 3.3 and 3.4, respectively.

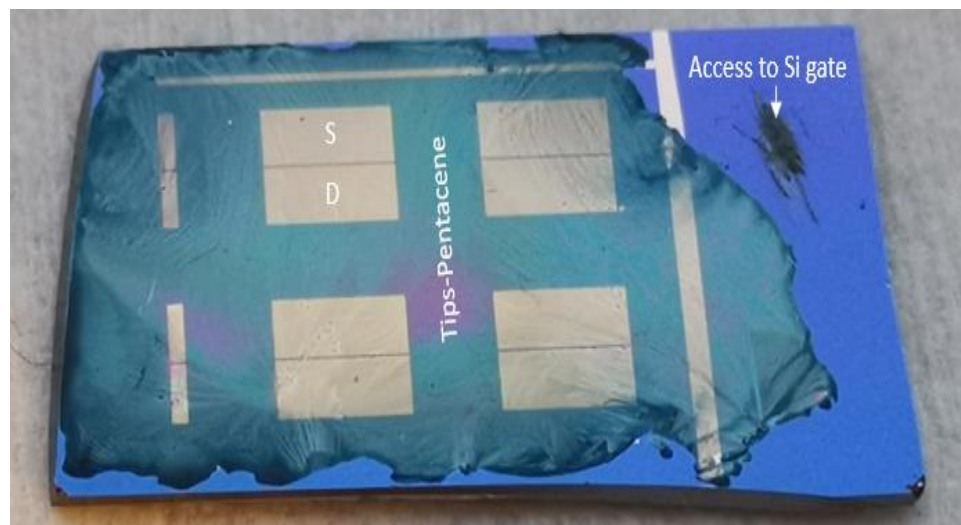


**Figure 3.2:** A photograph of four OFETs fabricated on a Si/SiO<sub>2</sub> substrate. Here, the gold source and drain electrodes were fabricated by photolithography before Tips-pentacene was drop cast over the substrate surface. Contact to the degenerately doped Si gate was achieved by mechanical removal of the 300 nm thick SiO<sub>2</sub> gate dielectric.

As a result of the relatively low dielectric constant ( $\epsilon_r = 3.9$ ) of the SiO<sub>2</sub> gate dielectric combined with the low mobility of the OSC, gate voltages in the tens of Volts range are required to operate the device, hence, the range chosen for operation was between 10 to -40V to achieve linear and saturation regimes.

The output and transfer characteristics of OFETs typically show two distinct regions. A linear region where  $I_{SD}$  increases with  $V_{SD}/V_G$  according to Ohm's Law and a saturation regime where  $I_{SD}$  reaches a maximum value and remains at this level irrespective of an increase in applied voltage.

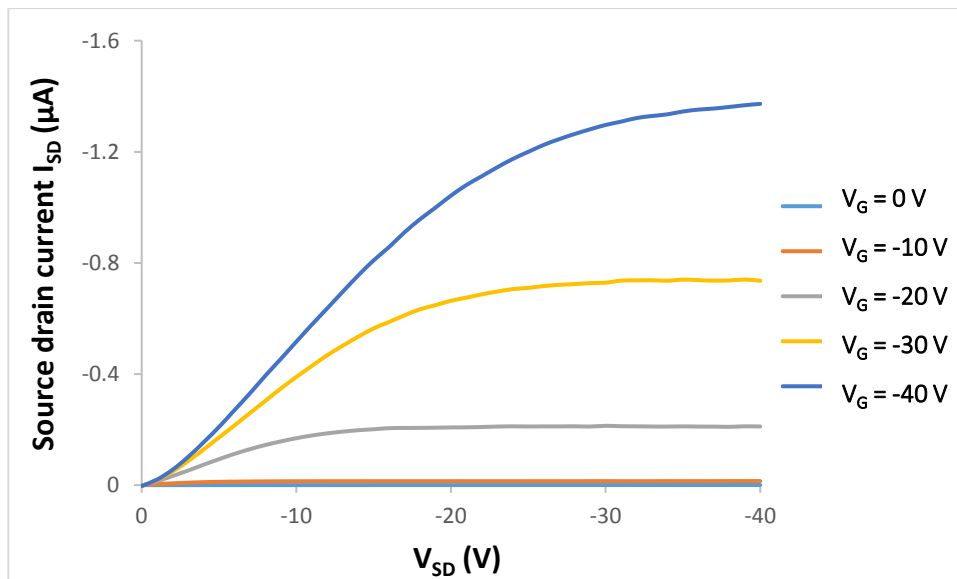


**Figure 3.3:** Measured output characteristics of one of the fabricated OFETs, the channel length of the device is 60  $\mu\text{m}$  and the thermally grown  $\text{SiO}_2$  gate dielectric has a thickness of 300 nm.

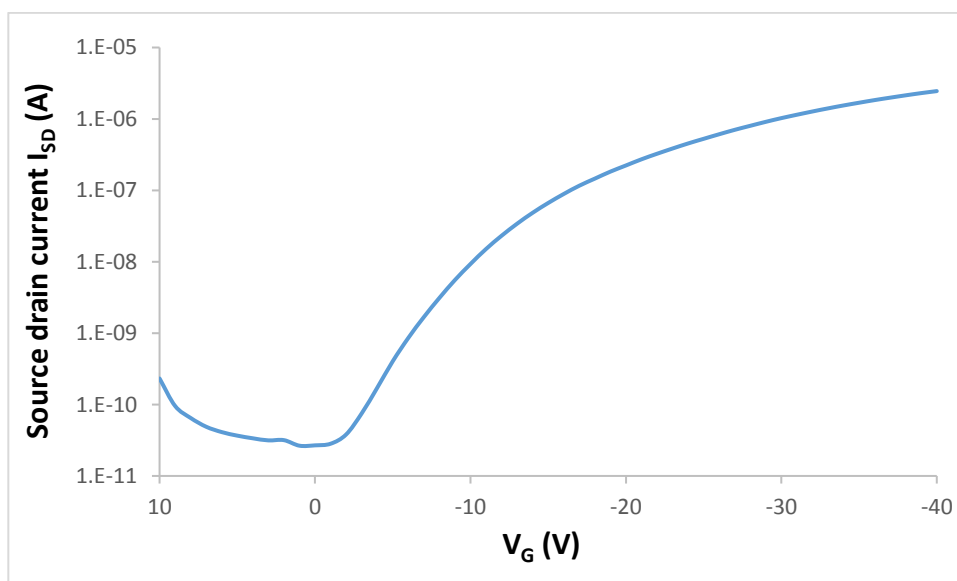


**Figure 3.4:** Measured transfer characteristics of one of the fabricated OFETs at  $V_{SD} = -40\text{V}$ , the channel length of the device is 60 $\mu\text{m}$  and the thermally grown  $\text{SiO}_2$  gate dielectric has a thickness of 300nm.

As can be seen in Figures 3.3 and 3.4, this characteristic behaviour was observed for the fabricated OFET confirming charge injection into a semiconducting Tips-pentacene OSC layer and effective gating by the underlying degenerately doped Si gate electrode. It should be noted that all devices with successful Tips-pentacene film deposition, i.e. ones in which

Tips-pentacene crystals were observed bridging the S and D contacts as can be seen in figure 3.5a, were found to operate in this characteristic manner. Those few devices where Tips-pentacene crystals were absent or insufficient in the channel between source and drain contacts, as can be seen in figure 3.5b, did not show these typical characteristics.

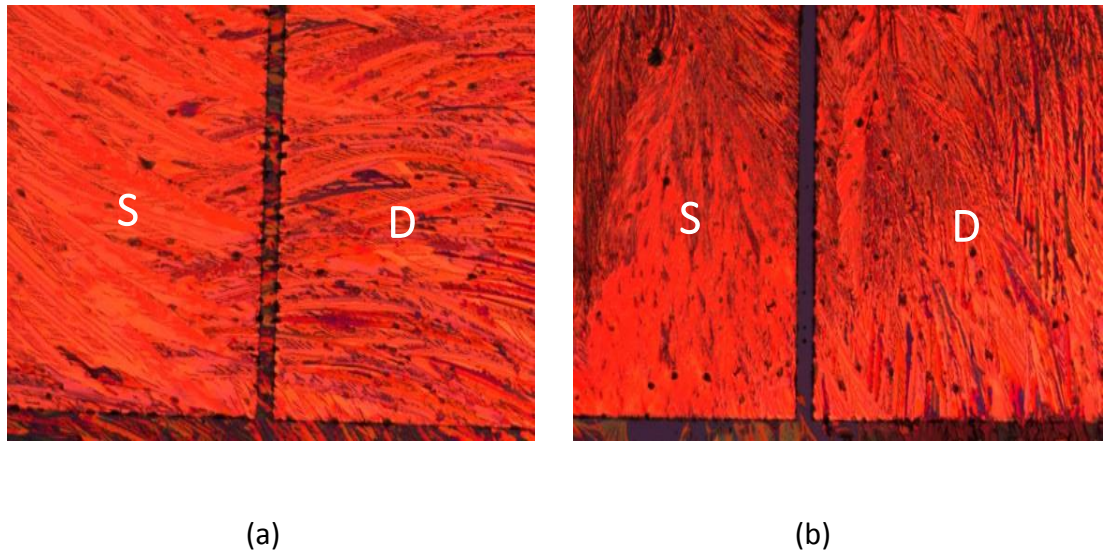


**Figure 3.5:** Optical microscope image of the formation of Tips-pentacene crystals that assemble on and between source and drain following drop casting. Images were captured using a 5x objective lens. (a) Situation where crystals bridge the S/D contacts and (b) no crystals in the channel between the S/D contacts.

The output and transfer characteristics combined with the geometrical specifications of the transistor can be used to quantify a range of fundamental parameters, also referred to as figures of merits, that together provide full characterization of the device (Appendix D details the calculation of these parameters from experimental data).

Although the vast majority (over 90%) of fabricated OFETs exhibited behaviour typical of an OFET, a large variation in terms of source drain current,  $I_{SD}$ , and other estimated figures of merit was seen among fabricated devices. For example, figure 3.6 shows the transfer characteristics of four, nominally identical OFETs fabricated on the same substrate, where the variance in terms of  $I_{SD}$  and other figures of merits is clearly visible. Such variable characteristics were commonly observed in the fabricated OFETs as a result of employment of drop casting as the deposition method for the organic semiconducting layer and can be associated with differences in the crystallinity and organization of the organic layer.

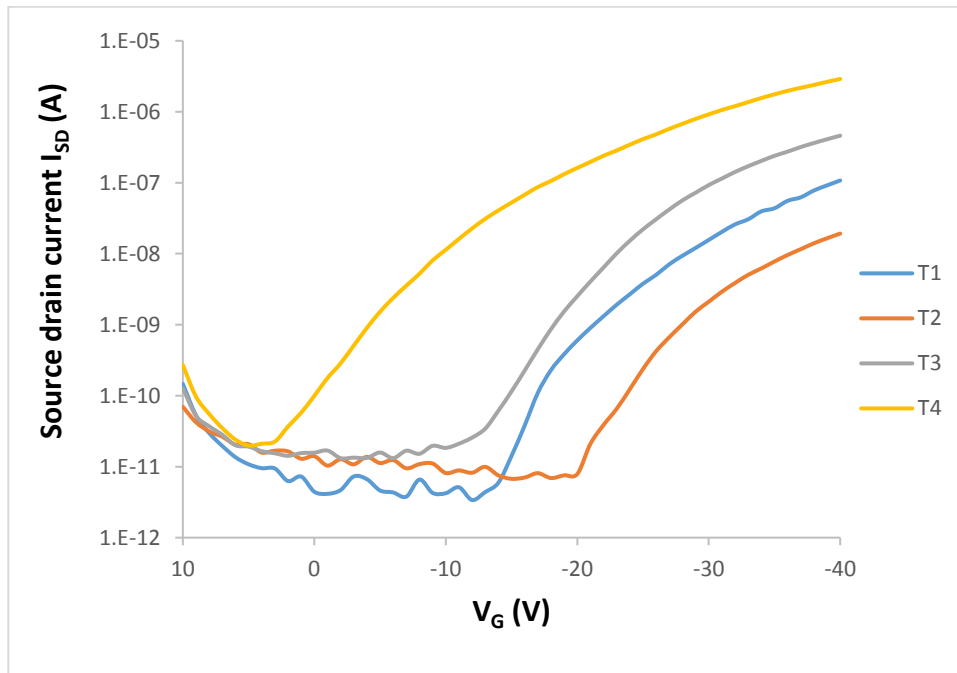


**Figure 3.6** Transfer characteristics for four nominally identical OFETs (T1 – 4) fabricated on the same Si/ SiO<sub>2</sub> substrate at  $V_{SD} = -40$  V. Here, the channel length (spacing between source and drain electrodes) is 60  $\mu\text{m}$  and the thermally grown SiO<sub>2</sub> gate dielectric has a thickness of 300 nm.

The histograms in figure 3.7 and figure 3.8 show the variation in maximum source drain current,  $I_{SDMax}$ , and ON/OFF ratio, respectively for of the 131 working OFETs. Here,  $I_{SDMax}$  is defined as the source drain current flowing between source and drain contacts at  $V_{SD} = -40$  V and  $V_G = -40$  V while ON/OFF ratio is the ratio between the highest  $I_{SD}$  in the transfer curve (i.e.  $I_{SDMax}$ ) and the lowest  $I_{SD}$  before the device turn on. Among the working OFETs, the majority (nearly 60%) displayed an ON/OFF ratio in the range of  $(1 \times 10^3 - 1 \times 10^5)$  and nearly 75% produced  $I_{SDMax}$  in the range of 0.1 – 10  $\mu\text{A}$ , in this range the estimated field effect mobility was found to be in the range of  $(0.002 - 0.02 \text{ cm}^2 \text{ V}^{-1} \text{ S}^{-1})$  and the estimated threshold voltage  $V_{TH}$  was (3 V – -16 V).

The highest estimated mobility was  $0.055 \text{ cm}^2 \text{ V}^{-1} \text{ S}^{-1}$  while the largest ON/OFF ratio was  $1.25 \times 10^7$  and the largest measured  $I_{SDMax}$  was 31.2  $\mu\text{A}$ . In general, if the devices were divided into 4 different  $I_{SD}$  ranges table 3.1 summarizes the estimated figures of merits in each range.

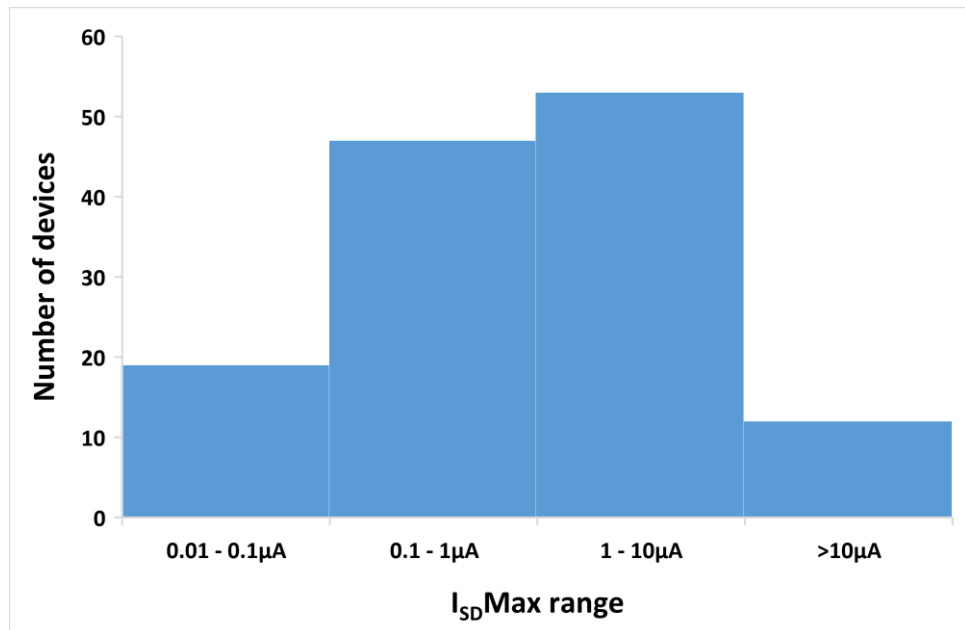


**Figure 3.7:** The range of maximum source drain current,  $I_{SD}Max$ , for all working OFET devices (total = 131). Here  $I_{SD}Max$  is defined as the source drain current flowing between source and drain contacts at  $V_{SD} = -40$  V and  $V_G = -40$  V.

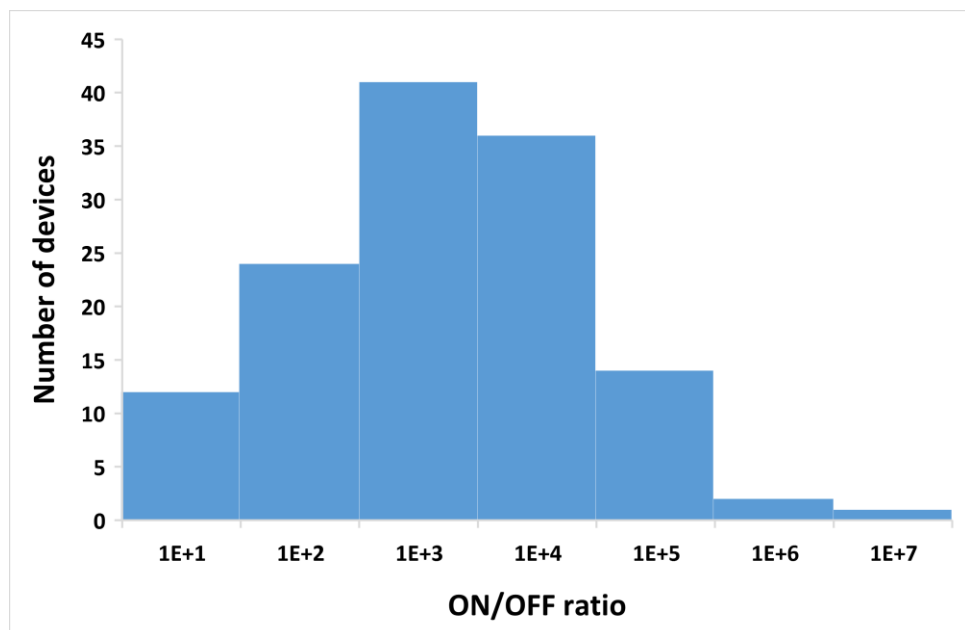


**Figure 3.8:** The range of ON/OFF ratio for all working OFET devices (total = 131).

**Table 3.1:** Average estimated values of figures of merit for characterized OFET devices.

$I_{SD}Max$ ( $\mu A$ )	Mobility $\mu_{FET}$ $cm^2 V^{-1} S^{-1}$	ON/OFF ratio $I_{ON}/I_{OFF}$	Onset Voltage $V_{SO}$ (V)	Threshold Voltage $V_{TH}$ (V)	Sub- threshold Swing S
0.01 – 0.1	0.0003	$6 \times 10^3$	-7	-11.5	11.5
0.1 - 1	0.002	$2 \times 10^4$	4	-8	7
1 - 10	0.02	$2 \times 10^5$	-1	-3	5
>10	0.05	$1 \times 10^6$	8	-2	7

### 3.1.3 Electrical characterization of the CM-OFET devices

After confirming the functionality of the fabricated OFET devices, the next stage was to transform the fabricated OFETs into a charge modulated OFET (CM-OFET) device proposed for applications in chemical and biological sensing. The CM-OFET, introduced in chapter 1 (section 1.5.1.2) and discussed further in chapters 4 and 5, differ from the typical OFET by the gating mechanism. In the CM-OFET, gating is achieved using an electrode referred to as control gate,  $C_g$ , that is coupled capacitively to a floating gate. Here the control gate is an additional gold electrode fabricated on top of the  $SiO_2$  dielectric layer which acts as a dielectric layer to capacitively couple the control gate to the degenerately doped Si floating gate.

It should be noted that during this stage of the project, a plan was made to make a second CM-OFET device based on  $Al/Al_2O_3$  as gate and gate dielectric respectively. This alternate device was designed to achieve a reduction in operating voltage and as explained in chapter 2 (section 2.6.1.3), the photolithography process was incompatible with the fabrication of such CM-OFET devices. Electrode contacts in the  $Al/Al_2O_3$  based CM-OFETs were thus deposited via shadow deposition using a commercial shadow mask. In order to enable a meaningful performance comparison between CM-OFETs fabricated on  $Si/SiO_2$  and  $Al/Al_2O_3$ , all CM-OFET devices were fabricated via shadow masking. As well as reducing the high operating voltage, The  $Al/Al_2O_3$  device was designed to comply with the geometrical considerations for optimum operation of the charge-modulated device as will explained in detail in chapter 5.

Once the slight modification was applied to the OFET configuration and it was transformed into a CM-OFET (adding the control gate on top of the SiO<sub>2</sub>), few samples were electrically characterized. The aim here, was to confirm the efficiency of the new gating mechanism, as previous characterization of the devices fabricated using photolithography enabled us to confirm the functionality of the OSC Tips-pentacene layer deposition as well as the charge carrier injection efficiency to the Tips-pentacene from the Au electrodes.

A Si/SiO<sub>2</sub> CM-OFET device fabricated using the shadow masking technique is shown in figure 3.9. As can be seen, the source and drain electrodes produced by the shadow mask have different geometrical layout compared to the source and drain electrodes previously shown produced by photolithography (Figure 3.2).

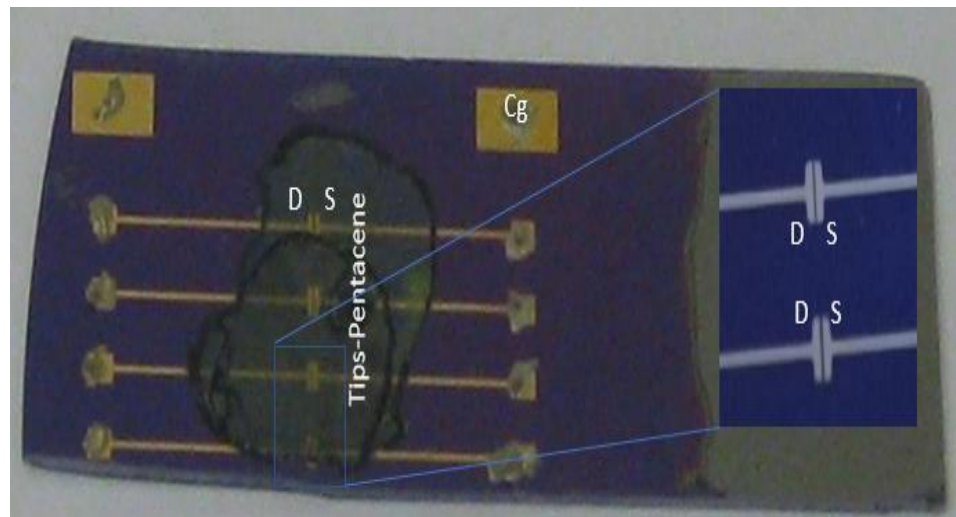


**Figure 3.9:** A photograph of four CM-OFETs fabricated on a Si/SiO<sub>2</sub> substrate. Here, the gold source, drain and control gate electrodes were fabricated by shadow masking before Tips-pentacene was drop cast over the substrate surface. The gate dielectric layer SiO<sub>2</sub> thickness is 300 nm thick.

Two critical dimensions related to the source and drain contacts can influence the output source drain current of the transistor; the transistor channel length,  $L$ , (the distance between the source and drain) and transistor channel width,  $W$ , (the cross-section length of the channel, parallel to the two electrodes). The channel lengths,  $L$ , of the two different layouts are 60  $\mu\text{m}$  while the channel width of the shadow mask transistor is 1 mm compared to 3 mm for photolithographic transistor.

According to the source drain current equation (3.1), the channel width,  $W$ , is directly proportional to the source drain current,  $I_{SD}$ .  $I_{SD}$  is thus expected to be lower for the devices made using the shadow mask layout.

$$I_{SD} = \frac{W\mu C_i}{2L} (V_G - V_{TH})^2 \quad (3.1)$$

An example of the output and transfer characteristics for a Si/SiO<sub>2</sub> CM-OFET is presented in figure 3.10 and 3.11, respectively.

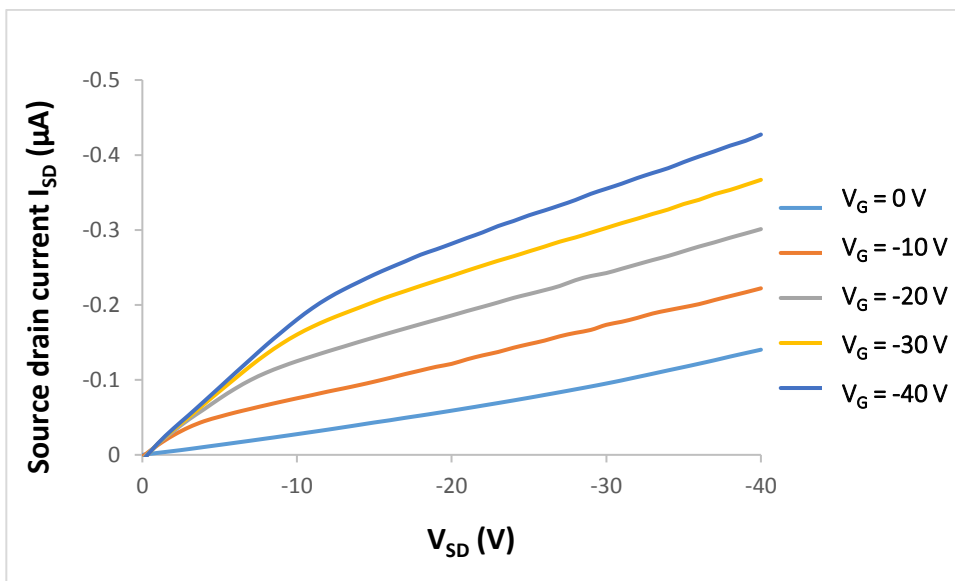


**Figure 3.10:** Measured output characteristics of one of the fabricated CM-OFETs, the channel length of the device is 60  $\mu\text{m}$  and the thermally grown SiO<sub>2</sub> gate dielectric has a thickness of 300 nm

Figure 3.10 and 3.11 shows that the CM-OFET exhibit typical output and transfer characteristics, however, with some distortion, this distortion is caused by the contribution of the voltage applied to the drain electrode in the gating of the device. This effect will be discussed in more detail in chapter 5 (section 5.5).

Due to the additional gating by the voltage applied to the drain electrode, estimating the figures of merits was problematic for the CM-OFET devices. Critically, most of the fabricated devices (78%) were in the ON state in the gate voltage range of the transfer characteristics (+10 to -40V). The threshold and subthreshold regions are thus absent in the

operating window of the transfer characteristics and hence the estimation of the figures of merits will be imprecise.

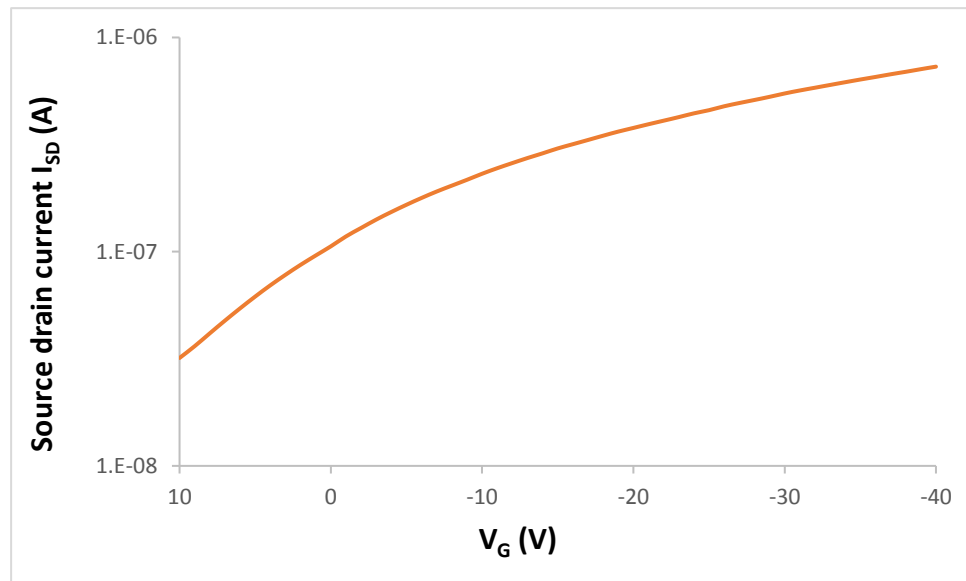


**Figure 3.11:** Measured transfer characteristics of one of the fabricated CM-OFETs at  $V_{SD} = -40V$ , the channel length of the device is  $60\mu m$  and the thermally grown  $SiO_2$  gate dielectric has a thickness of  $300nm$ .

For the Characterized CM-OFET devices, the range of maximum source drain current  $I_{SDMax}$  achieved is illustrated in figure 3.12. If the lowest  $I_{SD}$  current from the transfer characteristics for tested devices was considered as the OFF  $I_{SD}$  current (here normally the first point in the transfer characteristic curve), then the estimated range of ON/OFF ratio for the tested CM-OFET devices is between  $2 \times 10^1$  to  $2.6 \times 10^4$  and the mobility range is  $0.0002$  to  $0.014 \text{ cm}^2 \text{ V}^{-1} \text{ S}^{-1}$ . However, these figures are not accurate.

Due to the difficulty in estimating the figures of merits for the CM-OFET device, it is clear that these calculated values would not be an accurate method of quantifying the sensing activity of the CM-OFETs. Despite this difficulty, the response of the device to sensing activities that will be investigated in next chapters can be demonstrated in terms of the change in the source drain current, this in fact could be more reliable as the response is quantified by real measured values rather than estimated ones. Moreover, the change in measured source drain current can be related to the change in the threshold voltage which is the figure of interest as will be explained next section.

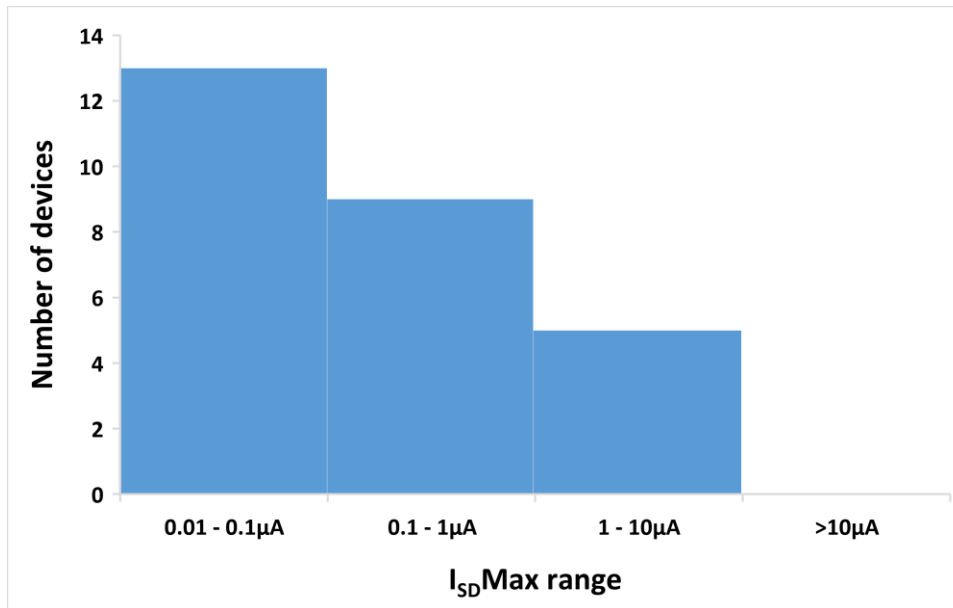


**Figure 3.12:** The range of maximum source drain current,  $I_{SD}Max$ , for characterized CM-OFET devices (total = 27). Here  $I_{SD}Max$  is defined as the source drain current flowing between source and drain contacts at  $V_{SD} = -40$  V and  $V_G = -40$  V.

The characterization presented above for devices made by photolithography and shadow masking demonstrates reliable fabrication of OFET and CM-OFET devices with high yield, these devices can be used for the proposed chemical and biological sensing for this PhD research.

## 3.2 Quantification of the CM-OFET sensing response

### 3.2.1 Maximum source drain current $I_{SD}Max$

The principle underpinning the CM-OFET sensor is that charges accumulated in the sensing area leads to a redistribution of charge in the floating gate. This redistribution of charge influences the effective gate voltage that couples capacitively to the OFET, leading to a shift in source drain current. This change in source drain current can be related to the apparent threshold voltage of the transistor using equation 3.1 which describes the source drain current,  $I_{SD}$ , of the transfer characteristics in the saturation regime.

In the CM-OFET sensor, the analyte solution does not come in contact with the OSC of the device, thus the mobility of charge carriers in the OSC is not affected by the sensing activity

and in theory remain unchanged. As a result, the only parameter that changes in equation 3.1 is the apparent threshold voltage,  $V_{TH}$ , or more accurately the  $(V_G - V_{TH})$  term. The capacitance per unit area of the gate insulator,  $C_i$ , can be estimated using equation 3.2.

$$C_i = \epsilon_r \epsilon_0 / t \quad (3.2)$$

Where  $\epsilon_0$  is the free space permittivity and  $\epsilon_r$  is the relative permittivity of the gate insulator material (here silicon dioxide) and  $t$  is the oxide thickness.

For a CM-OFET device with a 300 nm thick SiO<sub>2</sub> gate dielectric layer, the capacitance per unit area is thus:

$$C_i = (3.9 \times 8.854 \times 10^{-14} \text{ F/cm}) / (300 \times 10^{-7} \text{ cm})$$

$$C_i = 11.51 \text{ nF/cm}^2$$

The width,  $W$ , and length,  $L$ , of the transistor channel in the CM-OFET are 0.1 cm and  $L = 60 \times 10^{-4}$  cm respectively. Applying these values to equation (3.1) using a value of mobility within measured range for the fabricated CM-OFETs ( $1 \times 10^{-3} \text{ cm}^2 \text{ V}^{-1} \text{ S}^{-1}$ ).

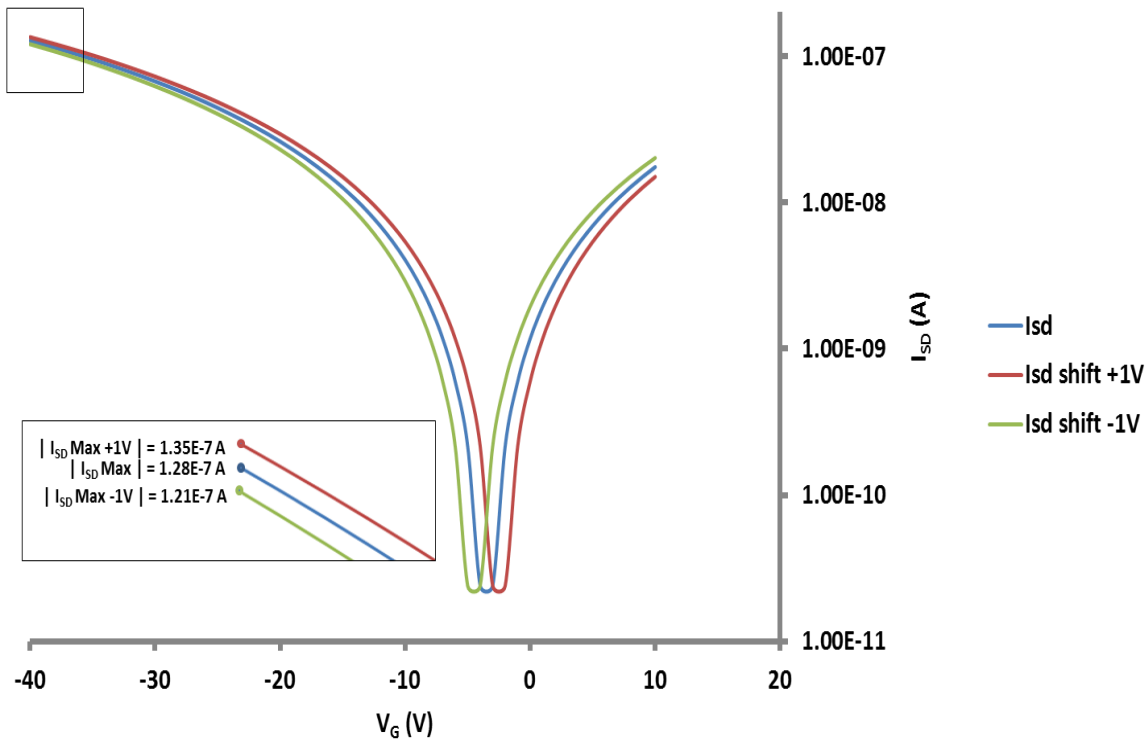
$$I_{SD} = 0.96 \times 10^{-10} (V_G - V_T)^2 \quad (3.1a)$$

Figure 3.13 displays the calculated effect that a shift of  $\pm 1$  V ( $V_G - V_{TH}$ ) has on the source drain current,  $I_{SD}$ , which mimics the effect induced by the sensing activity.

A positive 1V threshold shift results in a 7nA increase of  $I_{SD}$  at  $V_G = -40$ V, while a negative threshold -1V shift caused  $I_{SD}$  to decrease by 7nA at  $V_G = -40$ V.

Quantifying the sensing activity by estimating  $\Delta V_{TH}$  could be prone to error because  $\Delta V_{TH}$  is estimated by fitting (as shown in appendix D) to a plot of  $I_{SD}^{1/2}$  vs  $V_G$  and may not be accurate if the threshold voltage difference is small.  $V_{TH}$  estimation which is especially with unideal curves produced by CM-OFETs could be within an error margin that is close or higher than the shift induced by the sensing activity. Therefore, comparing the measured  $I_{SD}$  can be simple and reliable method for quantifying the sensing activity. In order to have a reliable quantification using the change in  $I_{SD}$  as criterion, efforts must be made to eliminate or minimize any effects that may influence behaviour of the investigated CM-OFET device that is not related or caused by the sensing activity. This may include

environmental conditions in which the measurement is carried out in as will be explained in the following section.



**Figure 3.13:** Effect of  $\pm 1V$  gate voltage range shift on the  $I_{SD}$  of a transfer characteristic, (inset) shows the difference between  $I_{SD} \text{ Max}$ . (simulated curves for Si/SiO<sub>2</sub> CM-OFET device with  $W = 0.1 \text{ cm}$ ,  $L = 60 \times 10^{-4} \text{ cm}$ ,  $C_i = 11.51 \text{ nF/cm}^2$  and  $\mu = 1 \times 10^{-3} \text{ cm}^2 \text{ V}^{-1} \text{ S}^{-1}$ ).

### 3.3 Environmental considerations

All electrical measurements to characterize fabricated CM-OFETs were performed in ambient conditions, however, some measures were taken in order to minimise external interference and to ensure that the devices are not influenced by undesirable effects during measurements.

#### 3.3.1 Electrical noise:

In order to reduce electrical interference due to electrostatic and electromagnetic fields generated from surrounding equipment in the laboratory, all measurements were conducted inside a grounded Faraday cage, as can be seen in the setup of figure 3.1.

### **3.3.2 Temperature:**

The mobility of charge carriers in OSCs, including those in Tips-pentacene, is known to be temperature dependant [1-4] since carrier transport occurs through hopping between localized states in the OSC which can be thermally activated. However, depending on the type of OSC film the temperature dependency of mobility may differ. For example, some OSCs exhibit an Arrhenius dependency ( $\mu \propto \exp(-1/T)$ ), while others show a non-Arrhenius behaviour (for example  $\mu \propto \exp(-1/T^2)$ ). For polycrystalline films like Tips-pentacene films, the mobility is widely considered to exhibit an Arrhenius temperature dependency [3,5]. Nonetheless, in order to minimize the effect of temperature on the CM-OFETs, all measurements were performed in a laboratory environment in which the room temperature was regulated at  $20 \pm 1$  °C.

#### **3.3.2.1 Self device heating**

Device heating during measurement is generally considered tolerable during short term, discrete I-V measurements of organic transistors. The so-called self-heating or joule-heating effect is normally only investigated for long-term device operation when performing continuous scanning or prolong transistor biasing. However, recent enhancements in organic semiconductor mobilities means that self-heating levels similar to those observed in inorganic electronics might be reached even for short term operation, particularly if a large operating voltage is used.

A recent study by Nikiforov et.al. [6] investigated real-time temperature evolution in the channel region of Tips-pentacene transistor during I-V scans. Using a platinum (Pt) resistance temperature sensor they monitored the channel temperature during I-V measurements under various conditions. Although the experiment was conducted in low to near room temperatures, these measurements confirmed that the extent of self-heating depends on the substrate material of the transistor. For example, a significant amount of self-heating could develop during I-V measurements at large fields on high mobility Tips-pentacene OFTs if substrates with low thermal conductivity such as glass or polymer are used. However, the use of a more heat conducting substrate such as doped silicon can largely minimize the heating effect and hence self-heating becomes negligible. According to their study, even at 278 K base temperature the transistor channel temperature increased by less than 3 K at  $V_{SD} = -40$  V and  $V_G = -40$  V and at room temperature no significant

Joule heating induced current is observed for Tips-pentacene devices on Si/SiO<sub>2</sub> substrates. It must be noted that the mobility in the devices they have fabricated was 0.9 cm<sup>2</sup> V<sup>-1</sup> S<sup>-1</sup> which is much higher than the mobility achieved in our fabricated devices, therefore joules heating effect on our fabricated devices is expected to be insignificant.

In fact, the amount of temperature increase in the OSC Tips-pentacene channel for fabricated CM-OFET devices can be estimated using Nikiforov et.al. Current-Induced Joule Heating model. In the model they derived an equation (3.3) describing the dissipated power-heating relationship in the transistor. The equation clearly show the significant influence of the thermal conductivities and thicknesses of both the OSC layer (Tips-pentacene) and the substrate on the transistor channel heating.

$$H = \Delta T \left( \frac{3}{8} \frac{d_{Tips}^2}{\kappa_{Tips}} + \frac{d_{Tips}d_{sub}}{\kappa_{sub}} \right)^{-1} \quad (3.3)$$

Where  $\Delta T = (T_{[d_{Tips}/2]} - T_{sub})$ ,  $T_{[d_{Tips}/2]}$  is temperature in the middle of the Tips-pentacene layer and  $T_{sub}$  = substrate temperature (approximately the room temperature).  $d_{Tips}$  and  $d_{sub}$  are the Tips-pentacene and substrate thicknesses, respectively,  $\kappa_{Tips}$  and  $\kappa_{sub}$  are thermal conductivities of Tips-pentacene and the substrate, respectively, and H is the dissipated power per unit volume and is calculated by:

$$H = \frac{I_{SD}V_{SD}}{W L d_{Tips}} \quad (3.4)$$

Considering  $\kappa_{Tips} = 0.1 \pm 0.009 \text{ W.m}^{-1}.\text{K}^{-1}$  [7] and  $\kappa_{sub} (\text{Si}) = 149 \times 10^{-2} \text{ W.cm}^{-1}.\text{K}^{-1}$  [6], feeding the known parameters' values for the fabricated CM-OFETs  $d_{sub} = 525 \mu\text{m}$ ,  $L = 60 \mu\text{m}$ ,  $W = 1 \text{ mm}$  and the Tips-pentacene thickness  $d_{Tips}$  is expected to be 0.1 - 1  $\mu\text{m}$  combined with the measured power enable the estimation of heating for any of the fabricated devices.

Figure 3.14 shows the power dissipated during an I-V measurement of one of the fabricated CM-OFET devices (defined as  $I_{SD} \times V_{SD}$ ), the power consumed ranges from 0.07 to 85  $\mu\text{W}$  across the transfer curve and the total accumulated dissipated power during the whole measurement was 1.64 mW. Therefore utilizing equation 3.3 and 3.4 for  $d_{Tips}$  0.1 - 1  $\mu\text{m}$ , the rise in temperature  $\Delta T$  is only  $\approx 0.11 - 0.2 \text{ K}$  which is insignificant particularly considering that the margin of environment temperature change is  $\pm 1$  degree.

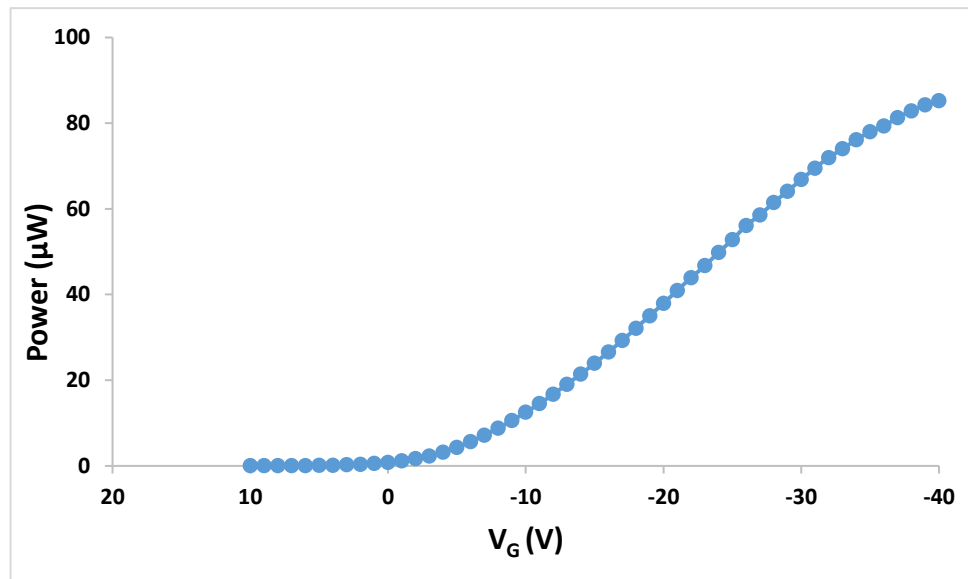


**Figure 3.14:** Power consumed during a transfer characteristics measurement of one CM-OFET device.

For long term measurement, the picture is more complicated when continuous biasing is applied to the device. A combination of bias stress and self-heating will occur simultaneously during measurement and the stronger of the two effects may dominate. The two phenomena have the opposite effects in organic transistors; bias stress causes charge trapping that leads to a negative shift in threshold voltage (for p-type OSC) and current reduction, while self-heating can assist hopping of charges between localized states enhancing the mobility. It has also been suggested that long term operation induces microstructural modifications of the OSC thin film [8], which depending on the packing of the OSC molecules and the direction of the applied electric field, may result in increased intermolecular interactions and enhance the charge transport between molecules.

### 3.3.3 Light:

The electrical behaviour of OFET devices using a Tips-pentacene OSC has been shown to be strongly influenced by exposure to light [9-12]. Exposure to light at different illumination intensities can produce a sizeable variation in the measured source drain current. Here, the effect of laboratory room light illumination on the behaviour of fabricated CM-OFETs was briefly investigated by measuring the source drain current (output/transfer characteristics) under light and dark conditions. Specifically, the combination of light exposure to measurement interval was investigated in order to highlight the interplay between light induced changes in current and changes due to measurement biasing.

Here, the laboratory room light consists of fluorescent illumination. Unlike incandescent light which gives a continuous spectrum, fluorescent light gives discrete lines typical of the combined spectrum of mercury and phosphor. The spectrum of light differs depending on the type phosphor material used however, peaks in light intensity are typically observed in the blue region of the spectrum, with less at green and red wavelengths. The decorative plastic covers covering the lamp may also affect the spectrum. The spectrum of the laboratory fluorescent lights is shown in figure 3.15, with large spikes at 436 nm (violet) and 546 nm (green) which correspond to 2.84 eV and 2.27 eV respectively and two smaller peaks one at 404 nm (violet) and 577 nm (yellow), corresponding to 3.07 eV and 2.15 eV respectively, all these energies are higher than the energy band gap between the HOMO and LUMO levels reported for Tips-pentacene (<2 eV) [13-14].

It must be mentioned that while the intensity of the light was low, the effect on the CM-OFET behaviour was evident as will be discussed in the next experiment.

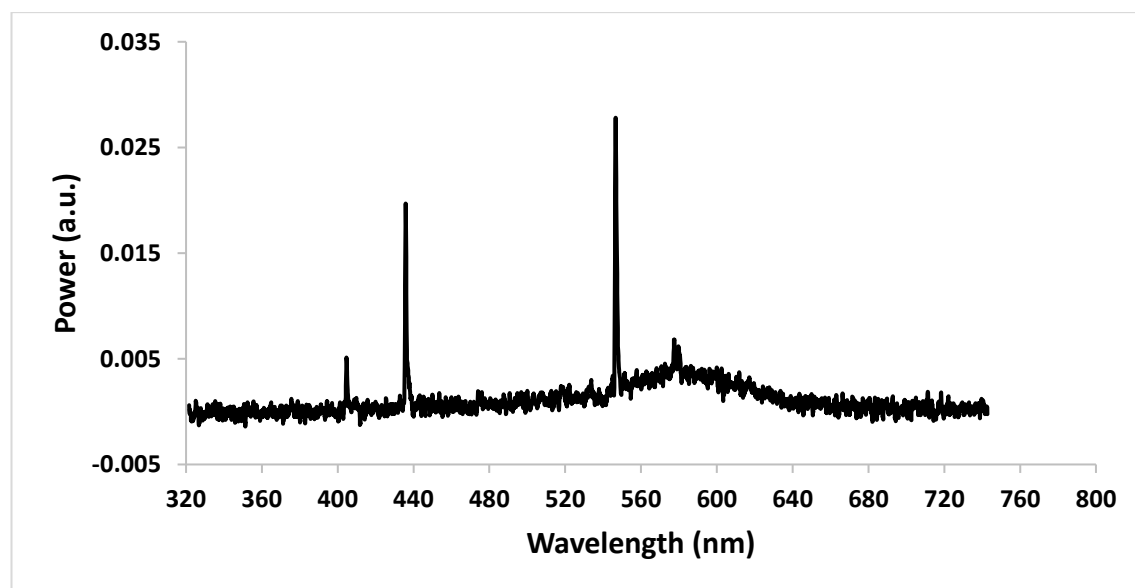


**Figure 3.15:** spectrum of laboratory fluorescent light measured at the position of the tested CM-OFET devices.

For each of the tested CM-OFET devices, the source drain current was measured periodically under transition from light to dark and back to light. The effect of the transition between light and dark on the source drain current was examined by recording the transfer characteristics first every 25 minutes between successive measurement and then with a 5 minute interval.

The sequence of the experiment is as follows:

- 1- Under light illumination the transfer characteristics of the CM-OFET device is measured. The source drain current is here called  $I_{SD}(0)$ .
- 2- Under the same light conditions, the transfer characteristics of the device is measured five times with 25 minutes between successive measurements.
- 3- An opaque black tape is placed on the Tips-pentacene region of the device to block the light. The transfer characteristics were immediately measured and then repeated five times with 25 minutes between successive measurements.
- 4- The opaque tape is removed so the device is once again exposed to the light. The transfer characteristics were immediately measured and then repeated five times with 25 minutes between successive measurements.
- 5- The same sequence is then repeated but with a 5 minute interval between successive measurements.

The behaviour of each experiment is summarized in the form of  $I_{SDMax}(t)/I_{SDMax}(0)$  as a function of time, where  $I_{SDMax}(0)$  is the maximum source drain current in the transfer characteristics of the first measurement in light at the beginning of the experiment,  $I_{SDMax}(t)$  represent the  $I_{SDMax}$  for each measurement relevant to the starting of the measurement. The results for five different devices is presented in figure 3.16.

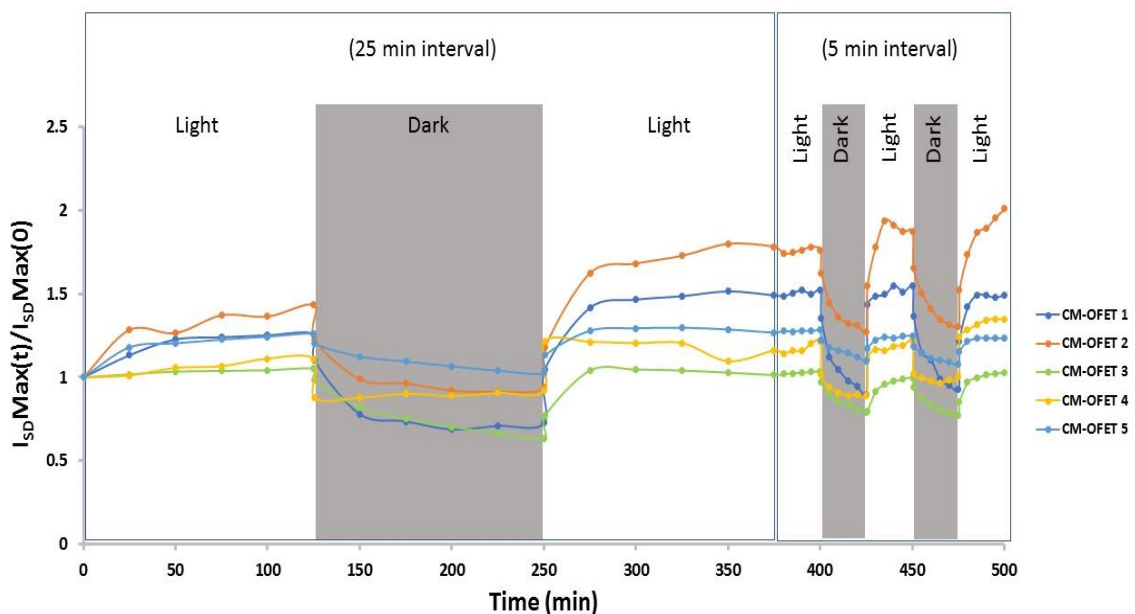


**Figure 3.16:** The change in  $I_{SDMax}$  periodically measured for 5 CM-OFET under light and dark conditions.

The change in  $I_{SD}$  for each CM-OFET when moving between light and dark conditions was consistent over the whole transfer curve. This can be seen more clearly in figure 3.17 for one of the tested devices. Figure 3.17 shows the measured  $I_{SD}(t)$  change at four different gate voltages,  $V_G$ , -10, -20, -30 and -40 V from the transfer characteristics curve.

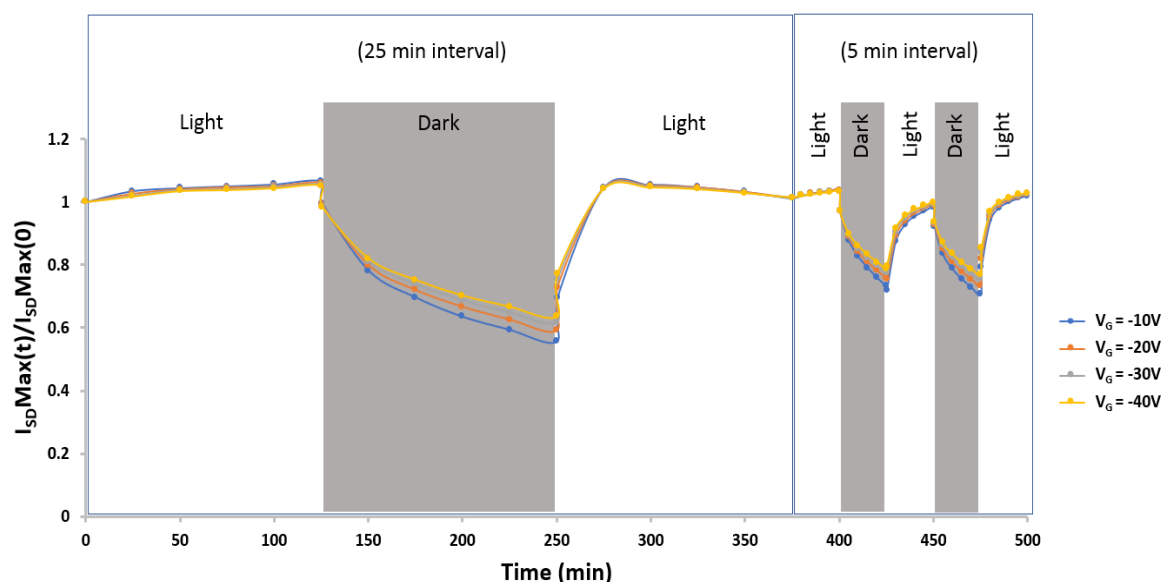


**Figure 3.17:** The change in  $I_{SD}$  periodically measured for a CM-OFET under light and dark conditions at  $V_G = -10, -20, -30$  and  $-40V$ .

Although the five devices differ quantitatively, the general, qualitative behaviour of the CM-OFET devices was similar. The behaviour can be explained in terms of trapping/detrapping of trap states, since the device operates in a trap-dominated regime. The general picture is that carriers generated by optical excitation contribute to the source drain current. The increase in carrier concentration under light illumination is observed as an increase in source drain current. Upon removal of the external light source, these additional photogenerated carriers become trapped, reducing the overall carrier density, leading to a corresponding decrease in source drain current. The photogeneration and subsequent trapping of charge carriers are observed in the experiments shown here. However, the application of external voltages required to bias the OFET also influence the trapping/de-trapping of charge carriers. Specifically, in this experiment, devices show Initial large  $I_{SD}$  increase in light followed by slower increase and large initial  $I_{SD}$  decrease in dark followed by slower decrease. For the slow phase, when the device is biased more

frequently (short intervals between measurements), the rate of change in  $I_{SD}$  (increase/decrease) is smaller than when there is a long interval between measurements. The influence of optical excitation and bias on carrier concentration is discussed in detail below.

**Under illumination (light):**

Electrons and holes are photogenerated rapidly within the OSC layer upon exposure to an external optical source. With an electric field applied (i.e. with the transistor biased), the electrons and holes will separate and, because of the direction of the source-drain electric field (here, negative drain voltage), the holes drift through the OSC and contribute to the charge transport while the electrons are thought to accumulate at the OSC/gate dielectric interface where they become trapped. With a  $\text{SiO}_2$  dielectric layer, the electrons are trapped by hydroxyl groups on the  $\text{SiO}_2$  surface. These traps are believed to be deep (i.e. the energy required to release them is much greater than the thermal energy) such electrons remain trapped for a sufficiently long time to influence subsequent measurements [15-20].

Initially, the space charge electric field associated with the trapped electrons can reduce the injection barrier at the source electrode. This reduction in barrier height accounts for the large increase in  $I_{SD}$ . However, if the device remains under photoexcitation, these trapped electrons can play additional roles that modulate the source drain current. For example, the trapped electrons can restrain the release of additional holes, it can also increase the extraction barrier at the drain electrode. This latter effect is caused by the accumulation of excess holes at the drain electrode, where holes can experience Coulomb repulsion or increased recombination before extraction. As a result, the increase in source drain current reduces between successive measurements [18,21-23].

The reduced source drain current increment under continuous optical excitation (after the initial large increment) is more pronounced when the time interval between measurements reduces, as can be seen in figure 3.16 where the increase in  $I_{SD}$  between measurements performed every 5 minutes is smaller than the case where measurements are performed every 25 minutes. The possible explanation is that with less time between measurement, lesser number of holes experience trapping when they are injected by the source electrode in the following measurement and therefore, rapid higher holes

concentration near the drain electrode can be expected and higher probability of Coulomb repulsion or recombination.

### **Without illumination (dark):**

The current decay following removal of direct illumination is generally explained by a combination of fast and slow trapping of free holes. Fast trapping of free holes occurs at deep trap states located at grain boundaries. These trapped holes reduce the trapping rate of remaining free holes, evidenced by a slow decay in  $I_{SD}$  after an initial large decay.

Another phenomenon that can contribute to the slow decay in  $I_{SD}$ , is the slow release of trapped electrons that have accumulated at the OSC/dielectric interface during light exposure. This can lead to a reduction in the trapping of injected holes due to the electric field associated with remaining trapped electrons [18-19,21,23-27]. Furthermore, it is also possible that when transistor is biased, holes injected into the OSC may form excitons by coulombic attraction to the trapped electrons. These generated excitons may exhibit a long lifetime and can thus influence charge transport in subsequent measurements. The combination of these effects contributes to the observed slow decay of the source drain current.

With a long duration between successive measurements (i.e. with infrequent biasing of the transistor), it is thus expected there will be an increase in trapping of free holes generated during the previous measurement alongside an increase in the number of electrons released from the interfacial trap states. Both of these effects will lead to a reduction in free holes, and thus a large decrease in source drain current between successive measurements.

In contrast, as the time interval between successive measurements reduces, fewer electrons are released from trap states, leading to a reduction in trapping of the current carrying free hole (i.e. there will be a higher density of holes that can contribute to  $I_{SD}$ ).

As for holes, It can be said that the rate of trapping decreases with time, this is because, when traps with shorter time constants are filled, the time constants associated with the remaining empty traps becomes longer, therefore, frequently filling trap states by injected carriers (generated by the electric field applied during measurements) can further increase

the time constant related to trapping free charges. Therefore, the current decay is slower when the time interval between measurements is shorter and vice versa.

The results shown in figure 3.16 indicate that influence of photoexcited charge carriers (either free or trapped) must be considered when operating the CM-OFET device for sensing applications. Furthermore, the influence of these free and trapped carriers can last for a significant time after a change in light conditions, for example after placing in the dark. This residual effect needs to be minimized, or ideally eliminated before using the device for any sensing application. As has been shown, the rate at which the CM-OFET current reaches steady state upon moving to different illumination conditions depends on the frequency with which the transistor is biased. Furthermore, the relative difference in the decay in  $I_{SD}$  upon removal of external illumination between nominally identical devices can be attributed to the randomness of Tips-pentacene formation in drop casting deposition. It may thus be necessary that the minimization of the effect of light on the CM-OFETs needs to be considered for each device individually. This will be discussed further in chapter 4 section (4.4.2).

### **3.4 Conclusions**

This chapter has presented experimental characterization of the fabricated CM-OFET devices, focussing on electrical characterization using the conventional output and transfer characteristics. Preliminary characterization was performed on OFET-like structure devices produced by photolithography in which gating of the OFET was achieved through the silicon bottom-gate. To assess and optimize the fabrication protocol and to validate the efficiency of the charge injection to the Tips-pentacene, a large number of OFET devices were fabricated and characterized and the results demonstrate successful fabrication of working OFETs with over 90% yield, however, with large variations between devices. For example, a wide range of charge carrier mobility was achieved across devices ( $0.0002 - 0.055 \text{ cm}^2 \text{ V}^{-1} \text{ S}^{-1}$ ). Variations between devices is related to the drop-casting method employed for deposition of the Tips-pentacene layer. Following successful fabrication of OFET devices, the fabrication CM-OFET devices was demonstrated in which gating is achieved through a capacitively coupled control gate. Here, fabrication was performed using a shadow masking

technique. Electrical characterization of a number of CM-OFETs showed that while they exhibited transistor-like behaviour, a distortion in the output and transfer characteristics was observed that was attributed to the contribution of the drain voltage on the gating of the CM-OFET devices. Again, it was demonstrated that the approach adopted for fabrication of the CM-OFET devices was effective. Variation between nominally identical CM-OFETs was also observed, with the saturation current varying between 18nA and 3.9 $\mu$ A for functioning devices, variations are ascribed to differences in the OSC layer as a result of the drop-casting deposition method as well. Despite the distortion in the output and transfer characteristics of CM-OFET devices, it was demonstrated that such devices can be employed for sensing application and the sensing activity can be quantified by the change in the source drain current at the maximum point in the transfer characteristics curve. Finally, the chapter highlighted several factors relating to the measurement environment that must be considered for reliable and consistent operation of the CM-OFET. Critically, the influence of light on the behaviour of the CM-OFET was discussed in detail, highlighting the importance of controlling ambient light in order to minimize its effect on the CM-OFET.

### 3.5 References

- [1] Meneau, A. Y., Olivier, Y., Backlund, T., James, M., Breiby, D. W., Andreasen, J. W., & Sirringhaus, H. (2016). Temperature Dependence of Charge Localization in High-Mobility, Solution-Crystallized Small Molecule Semiconductors Studied by Charge Modulation Spectroscopy. *Advanced Functional Materials*, 26(14), 2326-2333.
- [2] Worne, J. H., Anthony, J. E., & Natelson, D. (2010). Transport in organic semiconductors in large electric fields: From thermal activation to field emission. *Applied physics letters*, 96(5), 24.
- [3] Coropceanu, V., Cornil, J., da Silva Filho, D. A., Olivier, Y., Silbey, R., & Brédas, J. L. (2007). Charge transport in organic semiconductors. *Chemical reviews*, 107(4), 926-952
- [4] Zhu, M., Liang, G., Cui, T., & Varshney, K. (2005). Temperature and field dependent mobility in pentacene-based thin film transistors. *Solid-state electronics*, 49(6), 884-888.
- [5] Craciun, N. I., Wildeman, J., & Blom, P. W. M. (2008). Universal Arrhenius temperature activated charge transport in diodes from disordered organic semiconductors. *Physical review letters*, 100(5), 056601.
- [6] Nikiforov, G. O., Venkateshvaran, D., Mooser, S., Meneau, A., Strobel, T., Kronemeijer, A., ... & Sirringhaus, H. (2016). Current-Induced Joule Heating and Electrical Field Effects in Low Temperature Measurements on TIPS Pentacene Thin Film Transistors. *Advanced Electronic Materials*, 2(12), 1600163.
- [7] Yao, Y., Shahi, M., Payne, M. M., Anthony, J. E., & Brill, J. W. (2016). Thermal resistances of thin films of small molecule organic semiconductors. *Journal of Materials Chemistry C*, 4(37), 8817-8821.
- [8] Cheng, H. L., Chou, W. Y., Kuo, C. W., Wang, Y. W., Mai, Y. S., Tang, F. C., & Chu, S. W. (2008). Influence of Electric Field on Microstructures of Pentacene Thin-Films in Field-Effect Transistors. *Advanced Functional Materials*, 18(2), 285-293.
- [9] Bharti, D., Raghuwanshi, V., Varun, I., Mahato, A. K., & Tiwari, S. P. (2017). Photo-Response of Low Voltage Flexible TIPS-pentacene Organic Field-Effect Transistors. *IEEE Sensors Journal*, 17(12), 3689-3697.
- [10] Park, J., Kim, D. W., Lee, B. K., Jeong, Y. S., Petty, M., Choi, J. S., & Do, L. M. (2013). Light-Exposure Effects on Electrical Characteristics of 6, 13-Bis (triisopropylsilyl)ethynyl Pentacene/CdTe Composite Thin-Film Transistors. *Japanese Journal of Applied Physics*, 52(5S1), 05DC12.

- [11] Jouili, A., Mansouri, S., Al-Ghamdi, A., El Mir, L., & Yakuphanoglu, F. (2016). Controlling of DOS of TFTs based 6, 13-bis (triisopropylsilylethynyl) pentacene by solar light illumination. *Synthetic Metals*, 220, 591-598.
- [12] Park, J. G., Vasic, R., Brooks, J. S., & Anthony, J. E. (2005). Functionalized pentacene field-effect transistors with logic circuit applications. *arXiv preprint cond-mat/0510317*.
- [13] Griffith, O. L., Anthony, J. E., Jones, A. G., & Lichtenberger, D. L. (2009). Electronic properties of pentacene versus triisopropylsilylethynyl-substituted pentacene: Environment-dependent effects of the silyl substituent. *Journal of the American Chemical Society*, 132(2), 580-586.
- [14] Gunduz, B., & Yakuphanoglu, F. (2012). Effects of UV and white light illuminations on photosensing properties of the 6, 13-bis (triisopropylsilylethynyl) pentacene thin film transistor. *Sensors and Actuators A: Physical*, 178, 141-153.
- [15] Han, T., Liu, L., Wei, M., Wang, C., Wu, X., Xie, Z., & Ma, Y. (2017). Light-activated electric bistability for evaporated silver nanoparticles in organic field-effect transistors. *Physical Chemistry Chemical Physics*, 19(27), 17653-17660.
- [16] Ostroverkhova, O., Platt, A. D., & Shepherd, W. E. (2010). Optical, Photoluminescent, and Photoconductive Properties of Novel High-Performance Organic Semiconductors. In *Advances in Lasers and Electro Optics*. IntechOpen.
- [17] Plugaru, R., Anghel, C., & Ionescu, A. M. (2007). Charge carriers photogeneration in pentacene field effect transistors. *SCIENCE AND TECHNOLOGY*, 10(3), 233-241.
- [18] Zhou, T. C., Chen, G., Liao, R. J., & Xu, Z. (2011). Charge trapping and detrapping in polymeric materials: Trapping parameters. *Journal of Applied Physics*, 110(4), 043724.
- [19] Noh, Y. Y., Ghim, J., Kang, S. J., Baeg, K. J., Kim, D. Y., & Yase, K. (2006). Effect of light irradiation on the characteristics of organic field-effect transistors. *Journal of applied physics*, 100(9), 094501.
- [20] Liguori, R. (2014). A Study on Defects in Organic Semiconductors for Field Effect Transistors.
- [21] Häusermann, R. (2013). *Fast and slow charge trapping and transport in organic semiconductors* (Doctoral dissertation, ETH Zurich).

- [22] Liu, B., Xu, F., Zhang, X., Yan, D., & Lu, D. (2015). Influence of extraction barrier on the loss process of photogenerated charge carrier in polymer bulk heterojunction solar cells. *Chemical Research in Chinese Universities*, 31(5), 809-813.
- [23] Mansouri, S., Jouili, A., El Mir, L., Al-Ghamdi, A. A., & Yakuphanoglu, F. (2015). Studies of photosensitivity and photo-induced negative differential resistance (NDR) of TIPS-pentacene-poly (3-hexyl) thiophene blend organic thin film transistor. *Synthetic Metals*, 207, 1-12.
- [24] Ostroverkhova, O. (Ed.). (2013). *Handbook of organic materials for optical and (opto) electronic devices: properties and applications*. Elsevier.
- [25] Ostroverkhova, O., Platt, A. D., Shepherd, W. E., Day, J., & Anthony, J. E. (2009, August). Optical and electronic properties of functionalized pentacene and anthradithiophene derivatives. In *Linear and Nonlinear Optics of Organic Materials IX* (Vol. 7413, p. 74130A). International Society for Optics and Photonics.
- [26] Ryu, K. K., Nausieda, I., Da He, D., Akinwande, A. I., Bulovic, V., & Sodini, C. G. (2010). Bias-stress effect in pentacene organic thin-film transistors. *IEEE Transactions on Electron Devices*, 57(5), 1003-1008.
- [27] Miyadera, T., Minari, T., Wang, S. D., & Tsukagoshi, K. (2008). Dynamic bias stress current instability caused by charge trapping and detrapping in pentacene thin film transistors. *Applied Physics Letters*, 93(21), 428.

# Chapter 4

## CM-OFET Device as pH sensor

This chapter will discuss the possibility of using the charge modulated OFET device described previously and shown in figure 4.1, as a sensor for local pH. Here, the sensitivity of the CM-OFET to charge was exploited in order to detect changes in the local concentration to protons (strictly, the hydronium ion  $\text{H}_3\text{O}^+$  ions), and thus able to operate as a pH sensor. In order to provide sensitivity to proton concentration, the designated sensing region of the CM-OFET was functionalized with molecular species able to change charge as a function of local concentration of  $\text{H}_3\text{O}^+$  ions. The chapter first provides a comprehensive explanation of the operating principle of the CM-OFET pH sensor, before experimental measurements of the CM-OFET pH sensor are discussed.

### 4.1 Architecture of the pH CM-OFET charge sensor

The charge modulated OFET developed in this project is shown in figure 4.1. The device comprises an OFET coupled to a sensing region that extends away from the organic semiconductor layer, thus isolating the sensing function from the transistor. Coupling between the sensing region and the OFET is achieved via the floating gate, which capacitively couples the charge stored in the sensing region to the transistor. Any change in the charge local to the surface of the sensing region leads to a corresponding change in the transistor behaviour (i.e. modulation of the transistor output source drain current), that is proportional to the charge accumulated in the sensing area. For example, a change in charge density on the surface of the floating gate in the sensing region due to a chemical reaction between an aqueous solution and active sites on the floating gate surface or due to binding of a charged biomolecule to the surface, will change the charge distribution in the floating gate. This, in turn, effectively changes the gate potential at the conducting channel of the OSC. Given that the sensing ability arises from a change in charge density at the surface of the floating gate, it is necessary to understand and engineer this surface in

order to render the device sensitive to the required analyte, here the local concentration of protons.

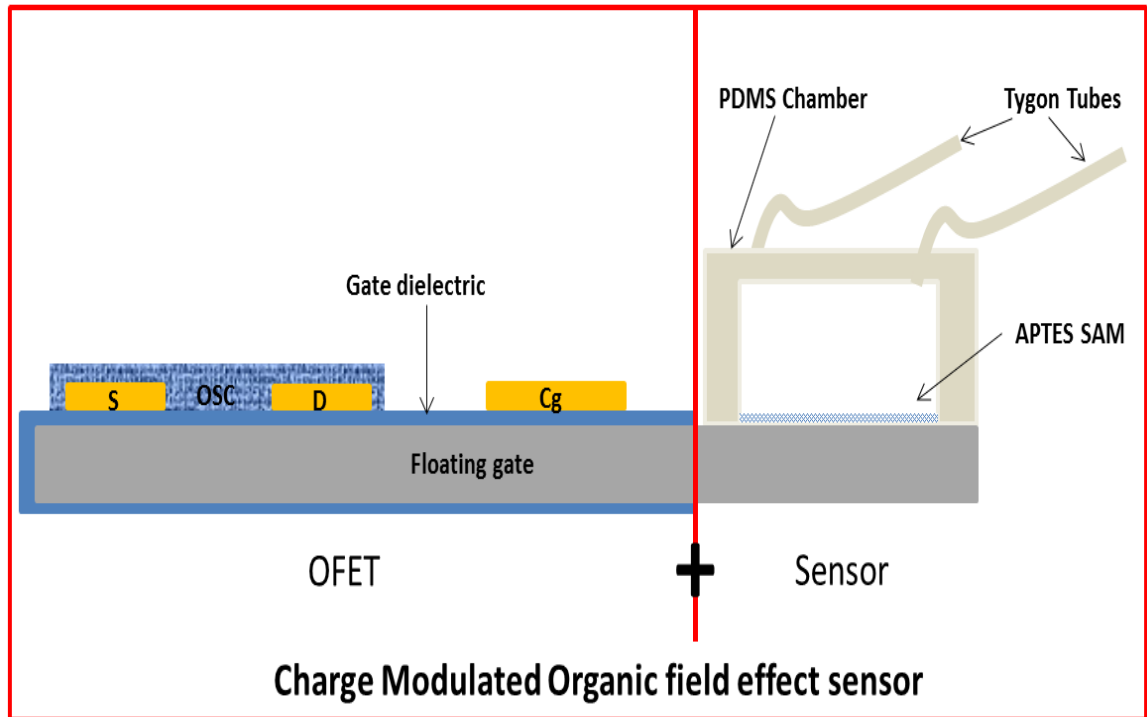
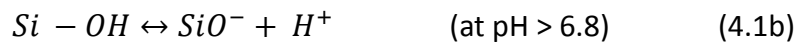


**Figure 4.1:** Schematic diagram of the CM-OFET sensor showing the two key components of the device; the OFET and the sensing region which can be exposed to an analyte through a PDMS microfluidic manifold. Coupling between the two components is achieved via the floating gate. The control gate,  $C_g$ , is used to bias the OFET without the need for applying a potential directly to the floating gate. Here, the schematic shows a CM-OFET responsive to pH where the pH sensitivity arises from amine groups introduced on the surface of the sensing region by the APTES self-assembled monolayer.

## 4.2 Surface chemistry and surface engineering for pH sensitivity

In the Si/SiO<sub>2</sub> CM-OFET, the floating gate is a degenerately doped Si substrate. The silicon surface typically contains a large density of active sites ( $5 \times 10^{14} \text{ cm}^{-2}$ ) [1] that spontaneously react with ambient oxygen to develop a native oxide layer which is normally hydroxylated to form silanol groups, Si – O – H. When in contact with aqueous solution, these silanol groups can become ionized by the dissociation of H<sup>+</sup> ions. Here, the surface hydroxyl sites of the silanol groups are in equilibrium with ions in the solution. This equilibrium is

described by the site binding model first introduced by Yates *et.al.* [2]. The model describes the acid-base reaction occurring at the silicon-solution interface. Here, the silanol groups are considered to be amphoteric, donating and accepting protons depending on pH of the solution. This is described by equations 4.1a and b:



As shown by equations 4.1 a and b, the silanol surface sites can go through three different ionization states depending on the pH of the solution in contact with the silicon surface. At low pH (acidic medium) the Si – OH will be protonated, Si – OH<sub>2</sub><sup>+</sup>, resulting in a positively charged surface. As the solution becomes increasingly basic, the Si – OH<sub>2</sub><sup>+</sup> groups start to deprotonate to become Si – OH such they carry no charge. Finally, at high pH, the Si – OH groups deprotonate to Si – O<sup>-</sup> and thus the surface carries a net negative charge [1,3]. Figure 4.2 shows the pH levels at which each ionization states of the silanol group dominates and the corresponding change in net surface charge.

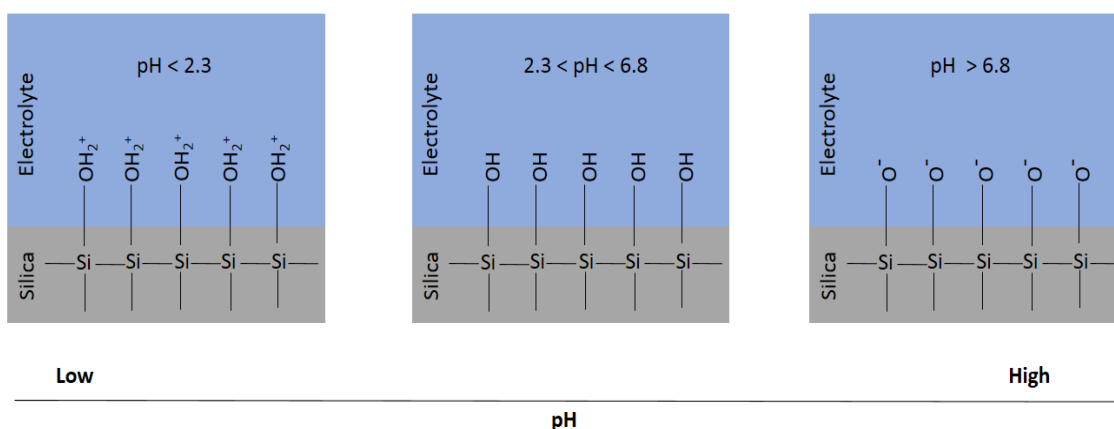


**Figure 4.2:** ionization states of silanol groups at the interface between the native silica formed on silicon substrate and an aqueous electrolyte as a function of solution pH [4].

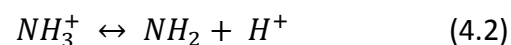
Although the oxidized silicon surface exhibits a surface charge that is sensitive to local pH, the surface exhibits two features that are undesirable for use as the proton sensitive

surface in a pH sensor. First, buried oxide sites respond slower to a change in solution pH than those sites located directly on the silica surface due to slow ion diffusion. This rate dependence leads to a drift in the response of silicon oxide based pH sensors [1,5]. Secondly, the response is not linear over a wide range of pH. Instead, the silicon surface shows two characteristic linear regimes of pH dependency. In the range pH 2 – 6, where the silanol groups carry no charge, there is little response of the Si – OH due to solution pH i.e. the surface charge remains effectively constant. In contrast, at higher pH (in the range pH 6 – 9), the rate of change of the surface is high [6-8]. Finally, it is worth noting that it is difficult to control the surface density of silanol groups which could lead to significant variation in pH sensitivity between nominally identical devices.

Rather than simply exploit the pH dependency of the bare silicon surface, it was therefore decided to chemically modify the silica with a self-assembled monolayer (SAM) in order to provide a more repeatable, controlled and reliable pH sensitive surface. For silica surfaces, modification with an amine terminated SAM, such as 3-aminopropyltrimethoxysilane (APTES) has been reported to enhance the performance of ISFET pH sensors, particularly in acidic solutions [6,9-11]. APTES functionalized silica yields a surface with two pH responsive receptor groups; amine groups, NH<sub>2</sub>, and naturally occurring silanol groups (Si – OH). Both these chemical groups act as hydrogen ion receptors. Critically, however the receptor groups undergo protonation and deprotonation at different pH ranges leading to a combined response that increases the linearity of the sensor response over what can be achieved with a silica surface only [12-15].

#### **4.2.1 Combined pH sensitivity of a NH<sub>2</sub> and Si – OH terminated silicon surface**

As discussed in section 4.2, silanol groups have three different ionization states depending on the pH level of the solution in contact with the surface. In contrast, amine groups only have two ionization states described by equation 4.2:



At equilibrium, where the surface density of protonated (NH<sub>3</sub><sup>+</sup>) and unprotonated groups (NH<sub>2</sub>) are equal, the equilibrium constant, known as the acid dissociation constant,  $K_a$ , is expressed as:

$$K_a = \frac{[NH_2][H^+]}{[NH_3^+]} \quad (4.3)$$

Where the  $[NH_2]$ ,  $[H^+]$  and  $[NH_3^+]$  represent the concentration of the amine, proton and protonated amine groups respectively.

Taking the negative  $\log_{10}$  of equation 4.3 and rearranging, the relationship between the pH of the solution, the dissociation constant and the concentration of the protonated,  $[NH_3^+]$  and deprotonated  $[NH_2]$  form of the amine group can be obtained. This relationship, known as the Henderson-Hasselbalch equation, is shown in equation 4.4 [16-17].

$$[H^+] = K_a \frac{[NH_3^+]}{[NH_2]}$$

$$pH = pK_a - \log \frac{[NH_3^+]}{[NH_2]} = pK_a + \log \frac{[NH_2]}{[NH_3^+]} \quad (4.4)$$

From the Henderson-Hasselbalch relationship it can be deduced that, when the solution pH is lower than the  $pK_a$ , the amine groups tend to be in the protonated form, and *vice versa*. At a solution pH equal to the  $pK_a$ , the concentration of the protonated and deprotonated form of the amine groups are equal such that the net charge is zero. This is shown schematically in the plot of the Henderson-Hasselbalch relationship in Figure 4.3. According to the Henderson-Hasselbalch relationship, 99% of protonation and deprotonation happens  $\pm 2$  pH units below and above the  $pK_a$  value [18].

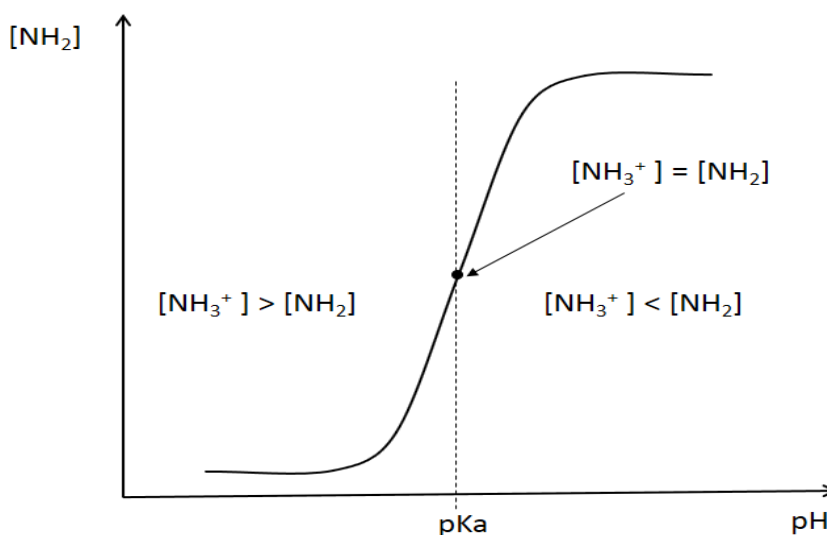


**Figure 4.3:** Schematic plot of the Henderson-Hasselbalch relationship of the amine group.

The precise  $pK_a$  of an amine group depends on the specific molecule and position of the amine within that molecule. However, for most molecules containing an amine terminal group, the  $pK_a$  is typically greater than pH 9 in bulk solution [9,19]. However, when grafted onto a surface, the amine  $pK_a$  is typically reported to be much lower than in solution [17,20-21]. For example, a  $pK_a$  as low as 3.9 was reported for an APTES monolayer [22] where the significant reduction in  $pK_a$  was assumed to be related to the very hydrophobic environment around the terminal groups. The reduced  $pK_a$  associated with surface immobilised amines explains the improvement in pH response of the APTES modified silica surface compared to the pure silica surface. Specifically, within the range pH 2 – 6, where the silanol groups of the silica surface are only weakly responsive to pH, the amine groups of APTES will be in the high sensitivity range around the  $pK_a$  (i.e.  $pK_a \pm 2$  pH units) where 99% protonation and deprotonation happens. Outside of this range (particularly the upper side of the range  $>$  pH 6.8), where the amine groups are either fully protonated or deprotonated, the silanol groups will be more responsive to pH change. The combined acidic and basic response provided by the amine and silanol groups enhances the linearity of the modified surface response to pH over a wider pH range.

#### **4.2.2 The CM-OFET pH sensor containing both $NH_2$ and Si-OH surface groups.**

Here the improved pH response of APTES functionalized silica surfaces is exploited to create a CM-OFET pH sensor. The silica surface within the sensing region is functionalized with an APTES SAM in order to introduce amine groups. At low pH (i.e. a pH below the  $pK_a$  of APTES:  $pK_a \approx 4 - 5$ ), the surface silanol groups will be neutral while the amine groups will be predominantly protonated ( $NH_3^+$ ). As a result, the surface of the sensing region will be positively charged. This will, in turn, result in accumulation of negative charge in the floating gate underneath the sensing region. The corresponding redistribution of charge within the floating gate will effectively cause a negative shift in the apparent gate voltage, leading to a decrease in the source drain current,  $I_{SD}$ . Conversely, as the pH increases towards the  $pK_a$  of APTES, the amine groups become increasingly deprotonated, leading to a reduction in the net positive charge in the sensing region, in turn causing a slight positive gate voltage shift. Increasing the pH further, leads to deprotonation of the silanol groups

(from Si – OH to Si – O<sup>-</sup>), further increasing the positive gate voltage shift and hence, the increase in  $I_{SD}$ .

### 4.3 APTES surface analysis

Before proceeding to characterise the electrical performance of the fabricated CM-OFET pH sensor, the surface of APTES functionalized sensing region was first characterised. Here, x-ray photoelectron spectroscopy (XPS), a standard surface analytical technique, was used to characterize APTES films assembled on a silicon surface.

#### 4.3.1 APTES SAM XPS Spectra

XPS is a standard tool for surface characterization that can provide a quantitative analysis of the elemental composition and chemical state of the surface. In XPS, a surface is irradiated with x-rays (commonly Al K $\alpha$  or Mg K $\alpha$  x-ray photons equivalent to 1486.6 eV and 1254.6 eV respectively) in an ultrahigh vacuum environment. The energetic incident x-ray photons cause ejection of core-level electrons from the surface atoms [23-24]. These characteristic electrons are subsequently collected, and their kinetic energy and number are measured using an electron energy analyser. The kinetic energy,  $E_k$ , of an emitted electron is related to its binding energy,  $E_B$ , by equation 4.5:

$$E_k = h\nu - E_B - \phi_{spec} \quad (4.5)$$

Where  $h\nu$  is the energy of the incident x-ray photons ( $h$  is Planck's constant and  $\nu$  is the x-ray frequency), and  $\Phi_{spec}$  is the work function of the spectrometer [23].

By mapping the number of electrons against the binding energy, it is possible to generate an XPS spectra consisting of multiple peaks that occur at specific energies. Each peak within this spectra is related to a specific element in the sample under study and the intensity of the peaks is related to the concentration of that element.

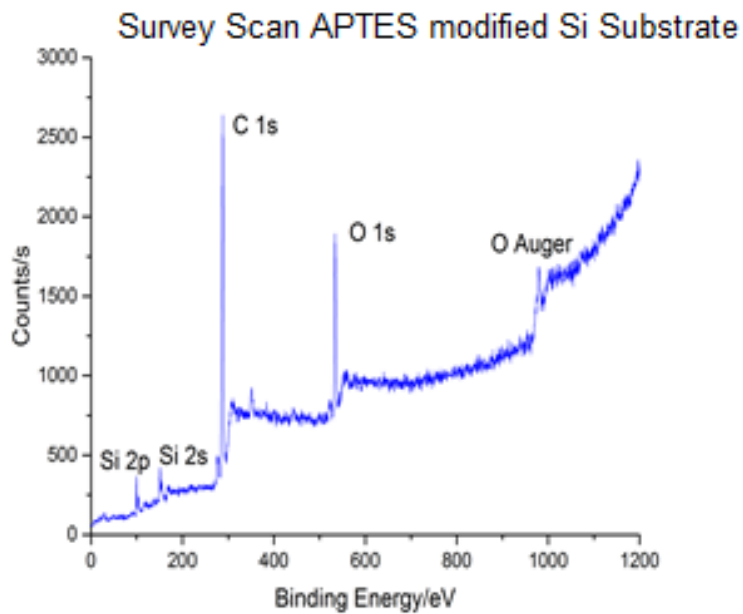
#### 4.3.1.1 XPS: Experimental Procedure

Two Si substrates were prepared for XPS characterization. The reference sample was a bare silicon surface with a native oxide but without APTES functionalization. The second sample was a bare silicon surface with a native oxide and functionalized with APTES by self-assembly. In self-assemble monolayer, initial monolayer coverage can be achieved very fast (within seconds to minutes), however, the surface coverage from the monolayer formed within this time scale is quite low and contains conformational disordering, allowing longer assembly time (typically >12 hours up to days) increases adsorbates packing and reordering and reduces inter-separation leading to a more organised and compact monolayer [25-28]. To deposit/assemble APTES layer on Si and other surfaces, APTES concentration lower than 10% in various solvents (typically 5% or less) is used [29-32]. Here, 5% APTES in IPA and 18 hours were chosen.

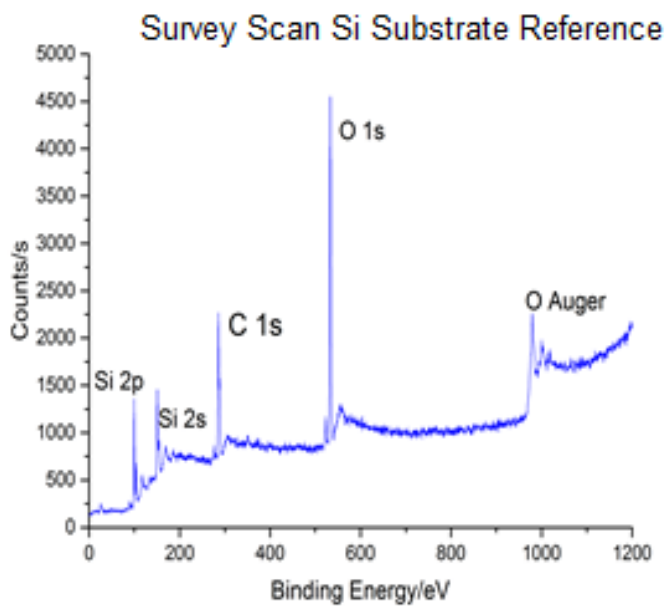
Both Si samples (reference bare Si substrate and APTES functionalized Si substrate) were initially cleaned in Piranha solution for 5 minutes followed by 5 minutes of UV ozone cleaning. The reference substrate was then immersed in IPA solution while the second substrate was immersed in 5% APTES in IPA. Both samples were left immersed in their respective solutions for approximately 18 hours. Both samples were rinsed with IPA and dried with nitrogen before immediately being transferred to the XPS specimen chamber and placed under vacuum for scanning.

The X-ray source was an Al anode on a dual anode X-ray source (Al  $K_{\alpha}$  = 1486 eV). The chamber base pressure was  $2.5 \times 10^{-9}$  mbar. A wide survey scan for binding energies 0-1200 eV was first taken to get an overview of the elements present on the sample surface. The survey scans, shown in figure 4.4, for both the APTES modified and un-modified Si substrates showed distinct emission peaks for Si 2s, Si 2p, C 1s and O 1s peaks [33]. No other elements show a strong signal in these scans.

The survey scans also showed a more intense C peak for the APTES modified Si compared to the reference unmodified Si. This is as expected, owing the greater C content introduced by the APTES-modified surface. In order to investigate the origin of this carbon content in more detail, scans for C 1s, Si 2s, and Si 2p regions were performed, along with the N 1s region to look for the presence of nitrogen.



(a)



(b)

**Figure 4.4:** A representative XPS survey scan showing the elemental composition of the surfaces of (a) APTES modified Si substrate, (b) reference Si substrate. The APTES modified Si sample spectrum has a reduced intensity compared to the reference sample. This is because a smaller aperture was used to reduce artefacts associated with photoelectrons generate from the sample plate.

#### 4.3.1.2 Detailed spectra of Si XPS peaks

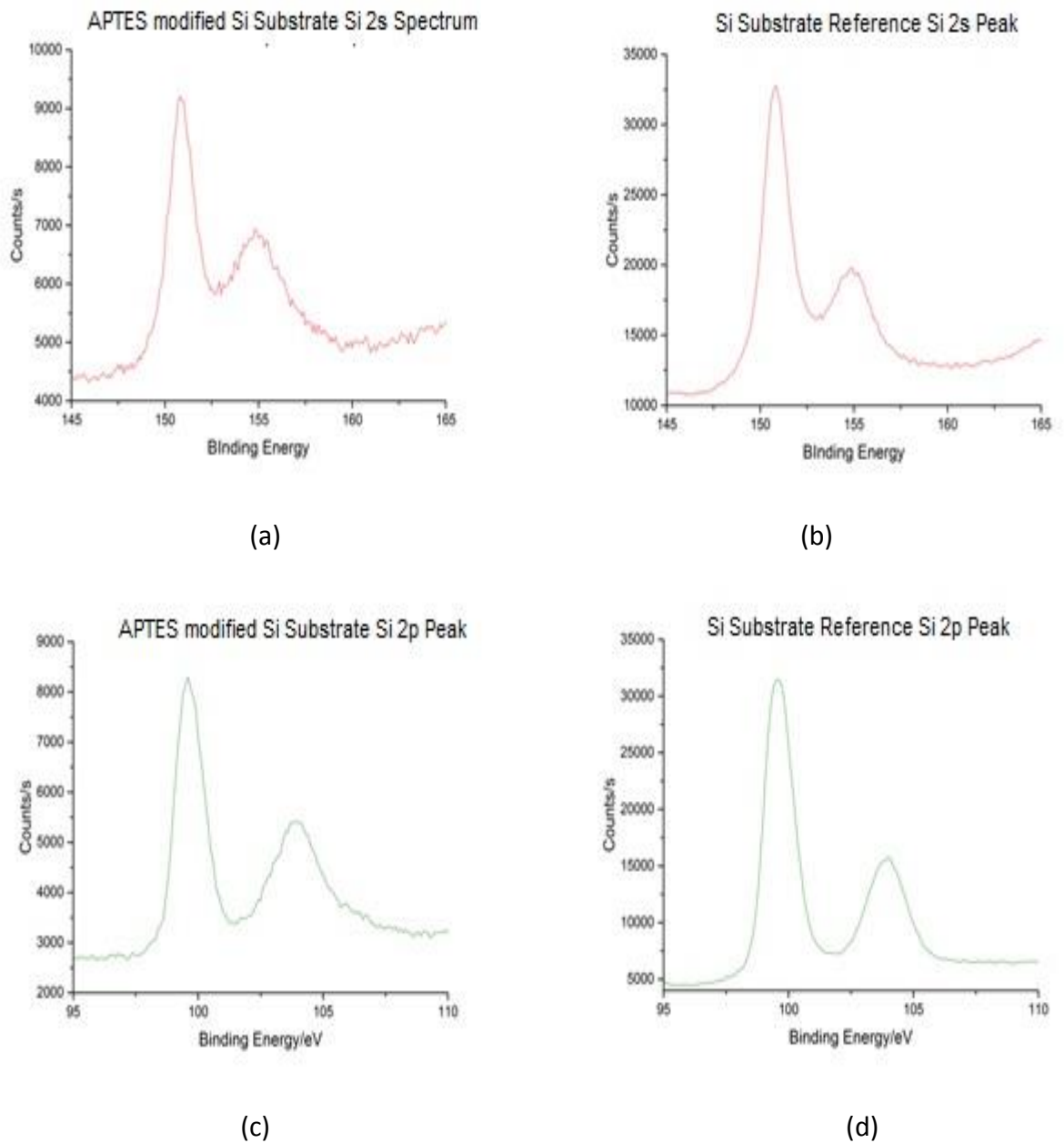


**Figure 4.5:** Experimental XPS spectra for Si (2s & 2p) peaks for the (a and c) APTES modified Si substrate and (b and d) for the unmodified reference Si substrate.

XPS spectra of the Si 2s and 2p peaks for both the APTES modified Si and unmodified Si surfaces are shown in Figure 4.5. Critically, both the APTES modified and reference samples revealed two peaks for both the Si 2s and 2p photoelectrons, separated by 3 – 4 eV. The dominant peaks at 99 eV and 151 eV both correspond to the Si – Si bond while the smaller peaks are associated with Si – O [34-37]. Comparing the peaks between the APTES modified

sample and the reference, the overall shapes were very similar. However, the spectra indicate the binding between APTES and substrate is through Si-O bonds, as the ratio between the Si – O peak to the Si – Si peak has increased compare to the reference sample. A small negative shift of 2p from the expected peak position ( $\sim 101$  eV), suggest the presence of Si – C bonds on the sample surface as well [36-38].

#### 4.3.1.3 Detailed spectra N 1s XPS peaks

XPS spectra of the N 1s peaks for both the APTES modified Si and unmodified Si surfaces are shown in Figure 4.6 (a) and (b), respectively. XPS scans around the energy associated with N 1s revealed a small but distinct peak on the APTES modified Si substrate. In contrast, no N 1s peak was observed for the reference silicon surface. The position of the peak observed on the APTES surface was found to be around 401 eV (the low intensity makes identification of the precise energy challenging). This is the correct binding energy range expected for N 1s transitions for amine groups [34-36].

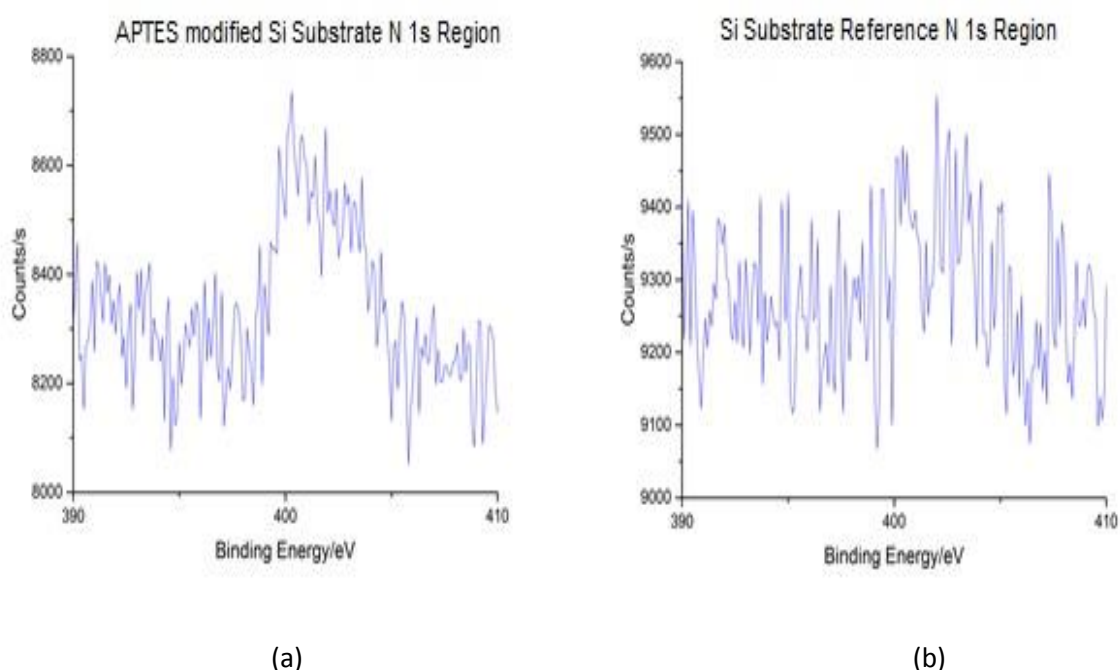


**Figure 4.6:** XPS spectra for N (1s) on (a) APTES modified Si substrate, and (b) reference Si substrate.

Although the spectra is noisy, the N 1s peak observed for the APTES functionalized surface was seen to be slightly asymmetric suggesting the presence of two individual peaks. Using peak fitting, it was possible to identify two individual XPS peaks at binding energies of 400.2

eV and 401.8 eV, which correspond to the neutral ( $\text{NH}_2$ ) and protonated ( $\text{NH}_3^+$ ) forms of the terminal amino group of APTES [34-36,39]. As shown in Figure 4.7, the intensities of the two fitted peaks suggest that there is similar amounts of neutral ( $\text{NH}_2$ ) and protonated ( $\text{NH}_3^+$ ) groups present on the sample.

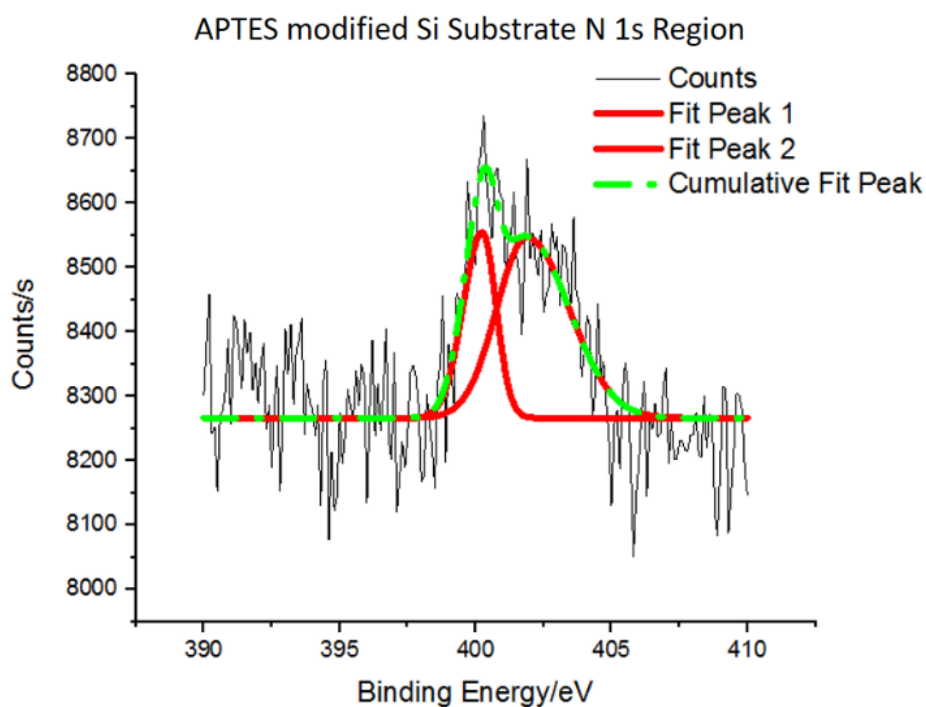


**Figure 4.7:** Detailed XPS spectra for N (1s) peaks for APTES modified Si substrate. Peak fitting reveals two peaks associated with the neutral ( $\text{NH}_2$ ) and protonated ( $\text{NH}_3^+$ ) binding energies. All deconvoluted fitted peaks are Gaussian functions.

#### 4.3.1.4 Detailed spectra C 1s Peaks

As shown in Figure 4.8, the C 1s spectrum for the APTES modified Si is markedly different in shape to that observed on the Si reference. Furthermore, the C 1s peak for the APTES functionalized Si surface is higher in intensity. The dominant peak for the APTES functionalized occurs at 288 eV. In contrast, the dominant peak on the Si reference occurs at a low energy of 286 eV. This indicates that the surface carbon on the surface of the two samples are in a different state.

The C 1s peak is commonly attributed to contamination, however, the higher intensity of the C 1s peak in the APTES modified Si can be a reasonable indication to the presence of APTES. Furthermore, the broadness of the C 1s peak is indicative of a contribution by multiple bonds, such as C – C  $\sim$ 284.4 eV, C – N  $\sim$ 286.2 eV and C = O  $\sim$ 288 eV. The presence of the dominant signal of the peak on the C = O side in the APTES modified Si compared to the reference is also an indication for the presence of APTES [33-35,39].

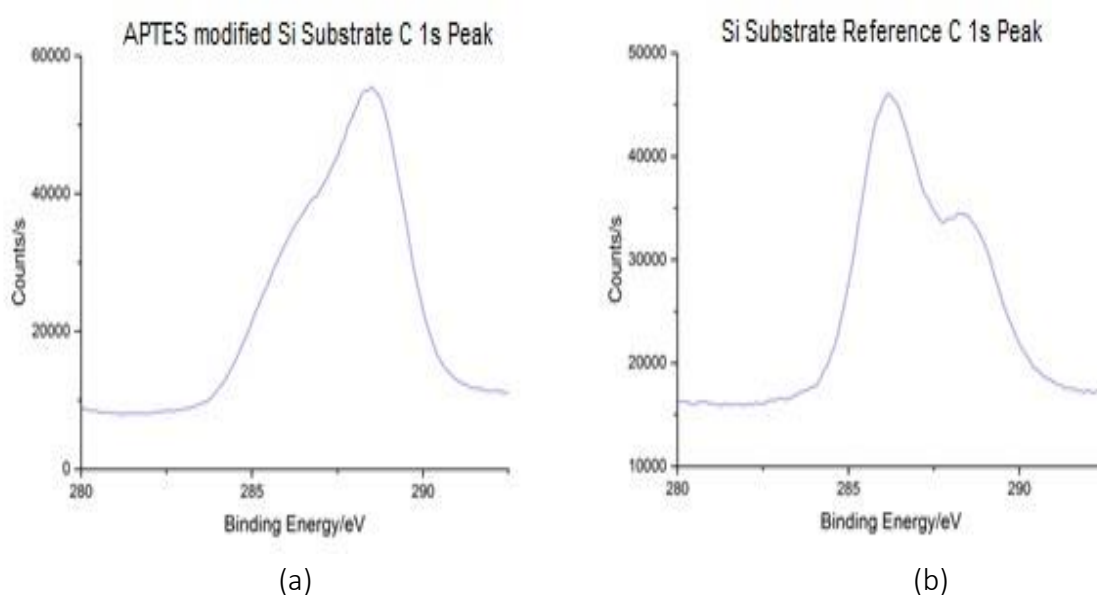


**Figure 4.8:** Detailed XPS spectra for C (1s) peaks on (a) APTES modified Si substrate and (b) reference Si substrate.

Using peak fitting (figure 4.9) to probe the proportions of each of the main bonds (C – C  $\sim$ 284.4 eV, C – N  $\sim$ 286.2 eV and C = O  $\sim$ 288 eV) for both the APTES modified Si substrate and the reference Si substrate shows that, for the reference Si substrate the dominant peaks are the C – C and C = O which can be expected due to contamination from exposing the silica surface to IPA for long time, the C – N is very small for the reference substrate. In contrast, for the APTES modified Si substrate, a large increase in both C – N and C = O and a large decrease in C – C indicate the binding of the APTES to the silica surface.

Overall, the XPS data suggests that forming APTES on the Si surface was successful and that the protocol used for functionalizing the surface can be employed for functionalizing the sensing region of the CM-OFET devices.

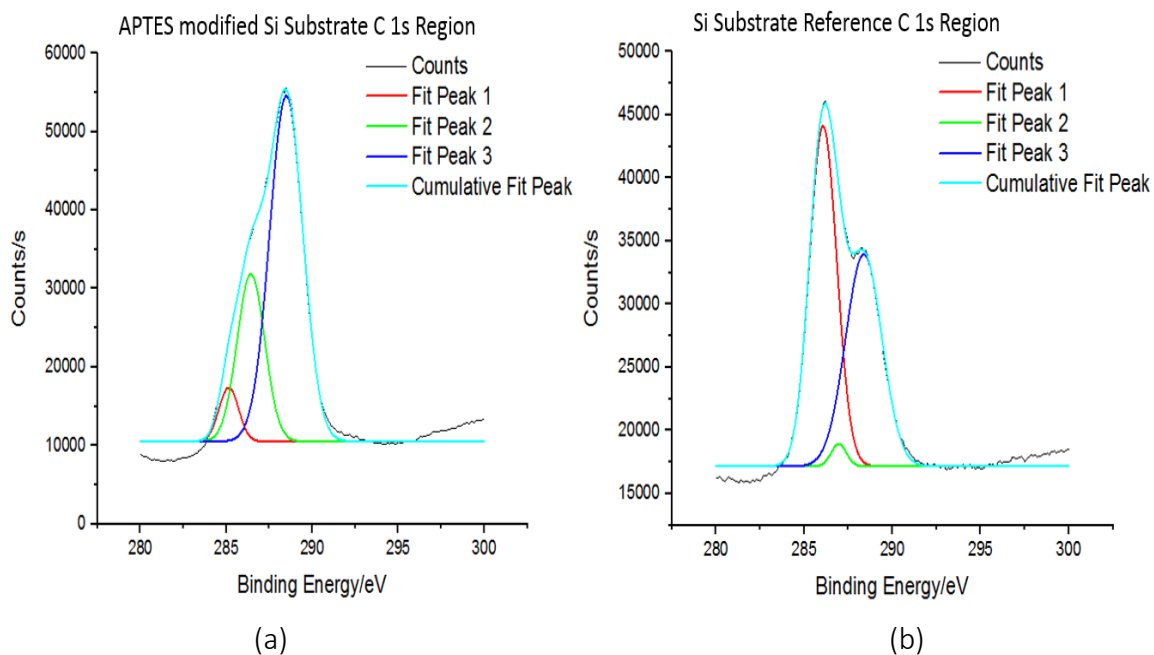


**Figure 4.9:** Detailed XPS spectra for C (1s) peaks for (a) APTES modified Si substrate and (b) reference Si substrate. Peak fitting reveals three peaks associated with binding energies of C – C ~284.4 eV (peak 1), C – N ~286.2 eV (peak 2) and C = O ~288 eV (peak 3). All deconvoluted fitted peaks are Gaussian functions.

## 4.4 pH CM-OFET: Results and discussion

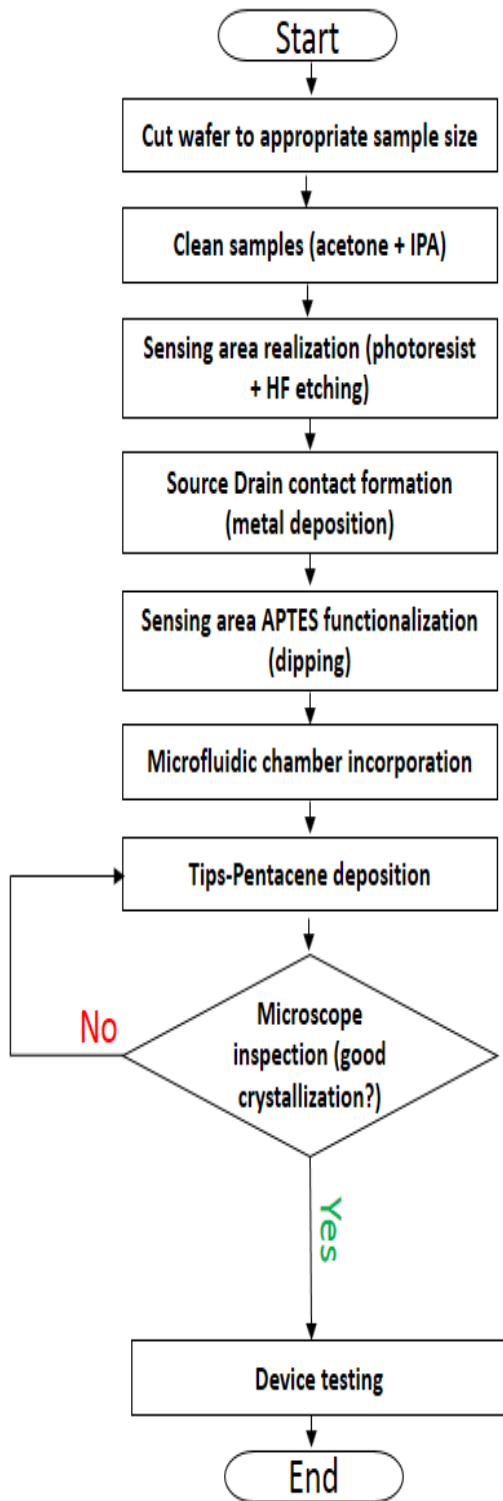
### 4.4.1 Surface modification of Si floating gate using APTES and its effect on the OSC layer

Having confirmed the assembly of an APTES SAM on Si substrates, now this section proceeds to discuss APTES functionalization of the Si sensing surface of the CM-OFET. As discussed in chapter 2, the sensing area can be functionalized with APTES either before or after deposition of the Tips-pentacene OSC. Here, the relative advantages and disadvantages of the two approaches will be explained. First, a reminder of the two strategies is illustrated in the flowcharts shown in Figure 4.10 showing the sequence of the fabrication steps for each approach.

Initially, CM-OFET devices were fabricated according to approach 1, where the sensing region was functionalized with APTES prior to Tips-pentacene deposition. However, devices fabricated through this approach consistently suffered from very low source-drain currents. To confirm if APTES contamination was the cause, new devices were fabricated

and the transfer characteristics of the CM-OFET were measured before and after APTES functionalization.

**Approach 1 (APTES before OSC)**



**Approach 2 (APTES after OSC)**

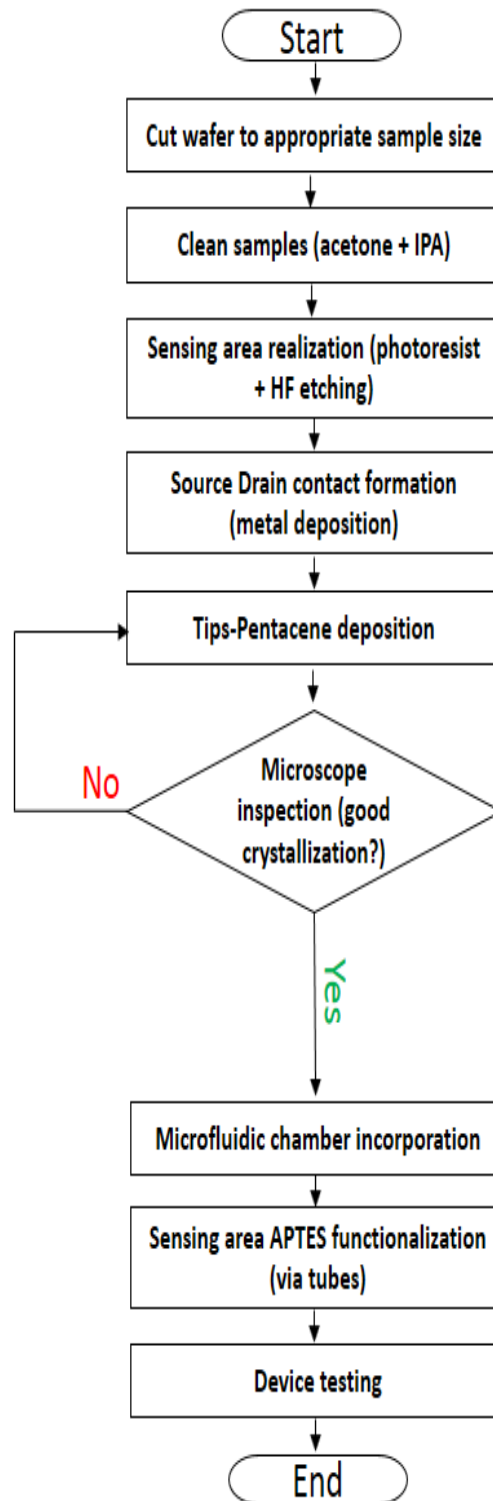


**Figure 4.10:** The two fabrication sequences implemented for fabricating the CM-OFET devices.

As can be seen in figure 4.11, following exposure to APTES, the source drain current decreased significantly, falling by around an order of magnitude at the maximum gate voltage,  $V_G = -40$  V. While only the sensing region of the device was immersed in the APTES solution, other regions of the sample surface have the potential to become contaminated with APTES due to vapour deposition. The presence of the  $\text{NH}_2$  groups in the APTES adsorbed layer which act as traps for the majority charges carriers (holes for Tips-pentacene) could explain the observed reduction in source drain current [40-42].

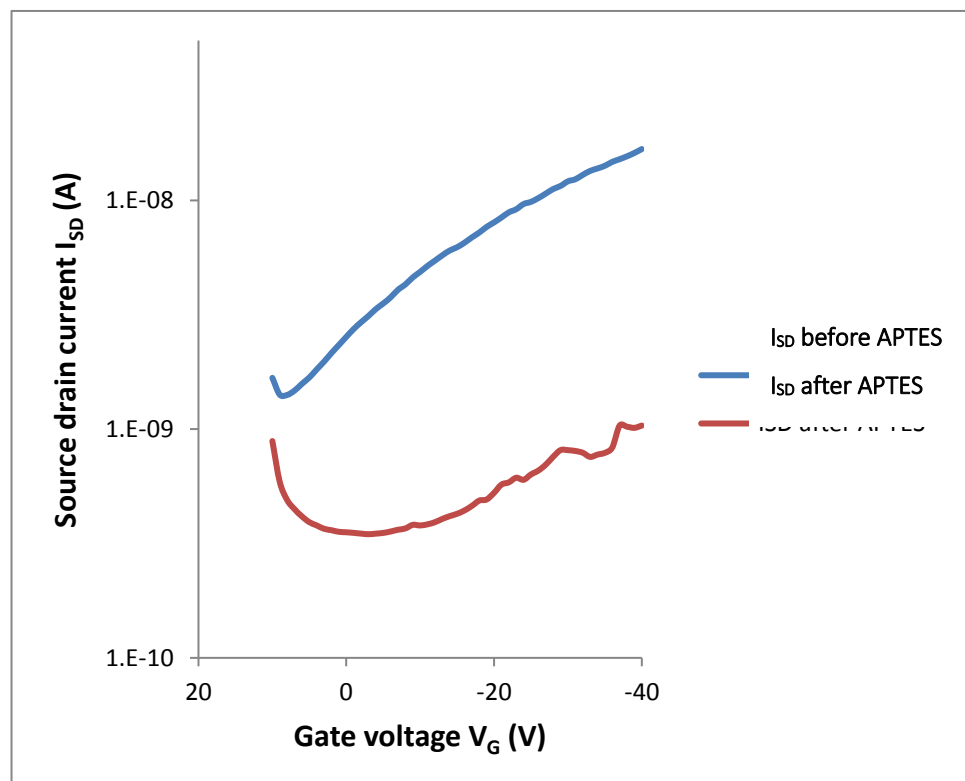


**Figure 4.11:** Transfer characteristics of a CM-OFET before and after functionalization of the Si sensing region with 5% APTES in IPA. Here,  $V_{SD} = -40$  V.

The fabrication process was thus modified to minimise exposure of the OFET to APTES. In this alternative approach (approach 2 of figure 4.10), APTES monolayer assembly was performed following Tips-pentacene deposition through an enclosed PDMS chamber, minimising the exposure of the Tips-pentacene region to APTES contamination.

Figure 4.12 shows the transfer characteristics of a CM-OFET that was functionalized using the PDMS microfluidic chamber of approach 2. Critically, the source drain current now

remains constant before and after APTES functionalization. However, when the OFET region of the same device was subsequently exposed to APTES vapour, the transfer characteristics again showed a decrease in source drain current (a reduction by nearly 60% at a gate voltage -40 V) and an increase in the threshold voltage.

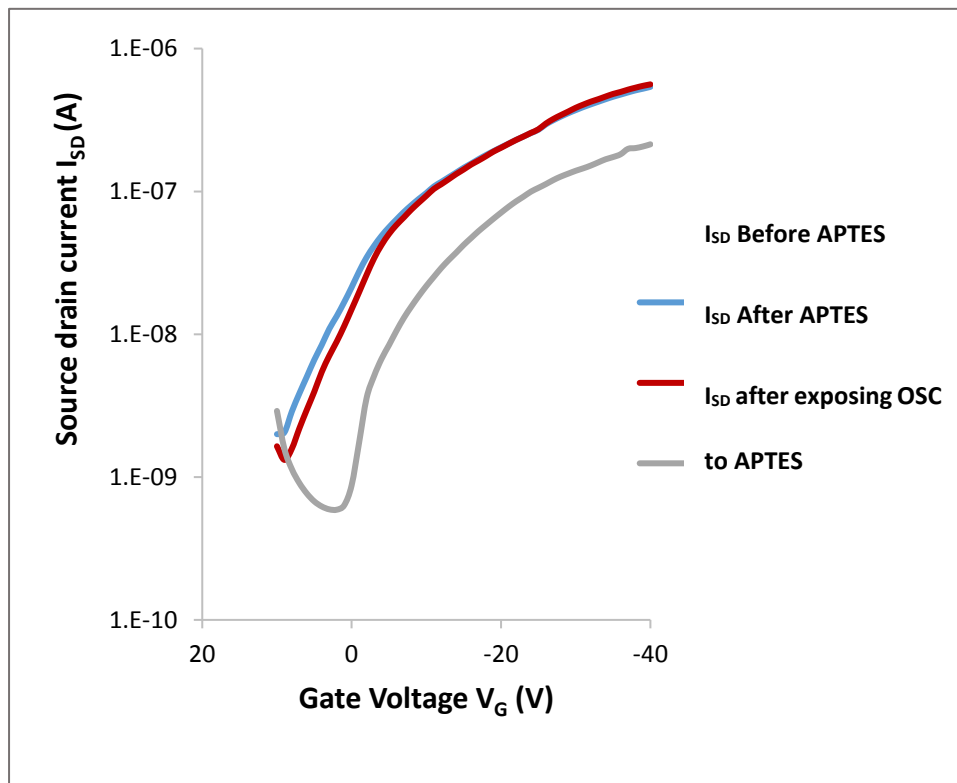


**Figure 4.12:** Transfer characteristics of a device before and after APTES functionalization using approach 2 and after exposing the device to APTES vapour ( $V_{SD} = -40V$ ).

Comparing the two approaches to CM-OFET fabrication, it can be concluded that exposure to APTES vapour significantly degrades carrier transport in the OSC Tips-pentacene. In contrast, the OSC Tips-pentacene is protected from APTES vapour deposition using approach 2. However, due to the delay between hydroxylation of the Si surface and APTES functionalization (including an additional fabrication step), the quality of the assembled APTES layer may be compromised. Also, as APTES functionalization occurs inside the PDMS chamber, the choice of APTES solvents is limited. For example, nonpolar solvents such as toluene which are ideal for APTES functionalization, are not compatible with PDMS, as they infuse through PDMS walls causing them to swell [43-45]. Polar solvents, such as IPA, have

been shown to significantly reduce PDMS swelling and was thus chosen here. For example, Honda *et. al.* [43] have shown that the degree of swelling in a PDMS plate immersed in toluene solution is 90% compared to less than 10% in IPA solution over the same time period (24 hours). This is also shown in figure 4.13 which compares the PDMS microfluidic chamber following exposure to a 5% APTES solution in Toluene and IPA. Within only 2 hours of immersing the chamber in APTES-Toluene, the PDMS chamber has clearly swollen. During the same time, no visible swelling was observed following immersion of a PDMS chamber in APTES-IPA solution. In fact, no visible swelling of the PDMS was observed when using APTES-IPA solution even after 18 hours. While swelling was not visible to the naked eye, it is possible that swelling to a small degree could influence the geometry of the sensing area. However, the change in surface area is expected to be negligible compared to the large sensing region area ( $0.49 \text{ cm}^2$ ). Moreover, since APTES functionalization is performed prior to any pH sensing experiment, the new (slightly changed) sensing surface area as a result of APTES functionalization will be the same for all subsequent measurements.

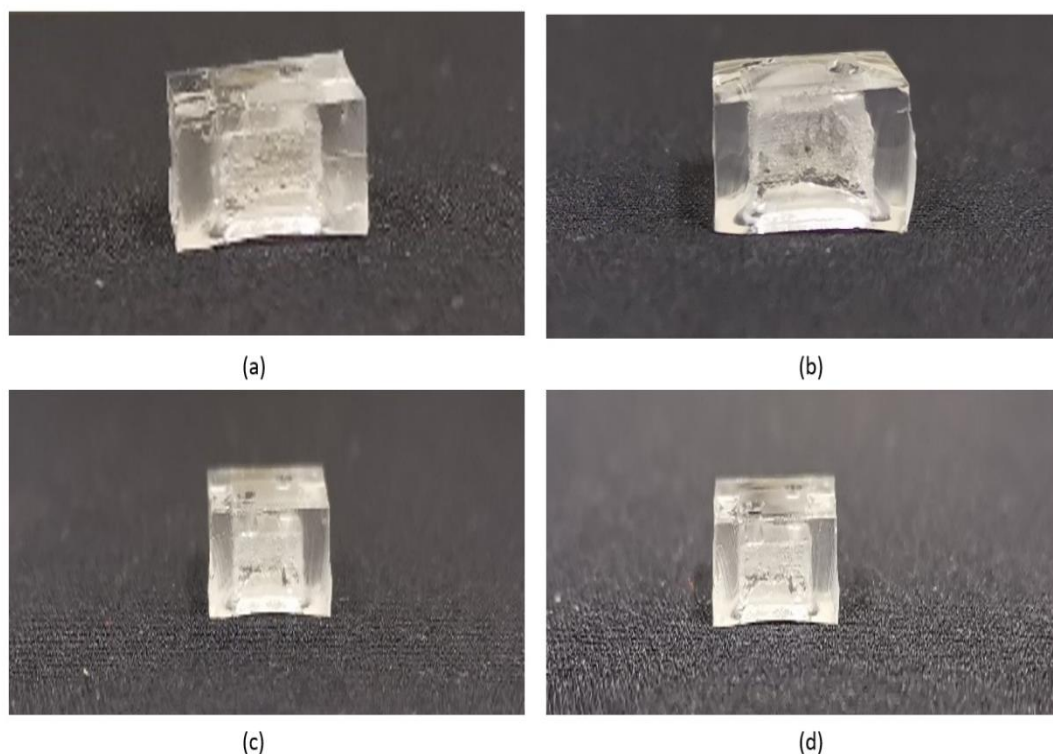


**Figure 4.13:** Effect of immersion in (APTES-Toluene) and (APTES-IPA) solutions on PDMS chamber, (a) before (b) after immersion in (APTES-Toluene) solution, (c) before (d) after immersion in (APTES-IPA) solution.

#### 4.4.2 Experimental consideration for CM-OFET testing; the influence of light

A critical consideration in the development of any chemical and biological sensor is the minimisation of measurement artefacts which otherwise could lead to false positive or false negative results. As discussed in section 3.3.3, the transfer characteristics of the CM-OFET is highly influenced by the photogeneration of charge carriers within the Tips-pentacene layer that occurs upon exposure to ambient light. Although all pH testing measurements are conducted in dark (i.e. the OSC is blocked from exposure to ambient light) to minimise the photogeneration of carriers, it was demonstrated that the effect of the photoexcitation may last for some time even after the CM-OFET was shielded from light and it is critical to ensure that this residual effect do not have an impact on the observed response of the CM-OFET when used as a biosensor.

The dynamic of photogenerated carriers as a result of transferring the CM-OFET from light to dark conditions can be monitored by recording the reduction in measured source drain current,  $I_{SD}$ , of the transfer characteristics as a function of time. Figure 4.14 shows the decay in  $I_{SD}$  after shielding a CM-OFET from ambient light. As can be seen,  $I_{SD}$  decays gradually over time, with large initial decay in the recorded source drain current, followed by a slow component decay in the recorded source drain current.

The source drain current decay in dark was found to be fitted reasonably well with a stretched exponential function (equation 4.6) [46], which is commonly used to describe the source drain current decay in OFETs due to bias stress effect in dark.

$$I_{SD}(t) = I_{SD}(0) \exp \left[ - \left( \frac{t}{\tau} \right)^\beta \right] \quad (4.6)$$

Here  $I_{SD}(0)$  is the first measurement in the dark,  $\tau$  is the decay time constant (also referred to as relaxation time), and  $\beta$  is the stretching or dispersion parameter ( $0 < \beta \leq 1$ ) (a dispersion exponent related to the characteristic width of the band tail of the insulator) [47].

It must be stressed that, the relaxation time  $\tau$  in this case refers to the general term describing the time required for the exponentially decreasing current of the entire decay curve to drop from the initial current value at  $t(0)$  to  $1/e$  or 0.368 of that initial value and is

not a physical characteristic time related to return to equilibrium after individual excitation (biasing).

The fitting is explained in appendix E, and the values of  $\tau$  and  $\beta$  extracted from the fitting for six nominally identical CM-OFETs are presented in table 4.1.

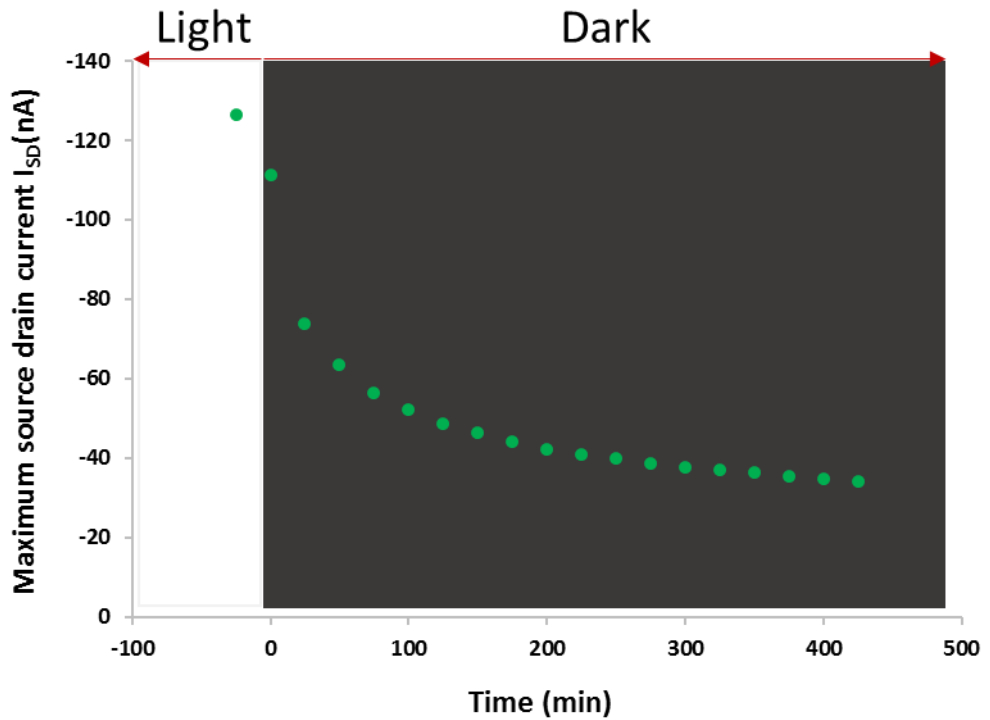


**Figure 4.14:** Time dependence of the maximum source drain current for a CM-OFET device due to shielding from ambient light. Here, the Tips-pentacene layer is covered by black tape and the transfer characteristics were measured every 25 minutes for 7 hours and  $I_{SD}$  is the maximum source drain current recorded at  $V_G = -40$  V.

**Table 4.1:** the extracted values of  $\tau$  and  $\beta$  from the fitting of equation 4.6 to  $I_{SD}$  decay for six CM-OFET devices.

CM-OFET	1	2	3	4	5	6
$\tau$ (s)	946	1304	895	1818	938	952
$\beta$	0.34	0.23	0.34	0.38	0.26	0.29
$R^2$ value	0.984	0.936	0.988	0.97	0.94	0.98

The values of  $\tau$  here indicate a much faster decay than reported values for Tips-pentacene OFETs ( $10^4 - 10^5$  s) [38-39] which suggests a higher concentration of traps in the fabricated CM-OFETs, however, as explained in chapter 3 section 3.3.3, the longer the time between measurements the faster the  $I_{SD}$  decay, which could also explain the small values of  $\tau$  estimated here, where the device is relaxed for 25 minutes between successive points in the decay curve, unlike the bias stress measurement where the current is continuously measured.

For the particular CM-OFET device measured for Figure 4.14 and given the associated measurement conditions (transfer characteristics measured every 25 minutes), the maximum source drain current immediately after the OSC Tips-pentacene was covered was seen to decrease by 12%. The current decreased by 61% in the first 2 hours of the experiment relative to the current measured just before covering the Tips-pentacene, compared to nearly 10% for the rest of the experiment and only less than 3% in the last 2 hours of the experiment. Similar behaviour was also observed in other nominally identical CM-OFET devices. The percentage change in the measured maximum source drain current  $I_{SDMax}$  over time for six CM-OFETs is summarized in Table 4.2 and figure 4.15.

**Table 4.2:** The percentage change in the measured maximum source drain current,  $I_{SDMax}$ , during a 7 hours period in the dark compare to  $I_{SDMax}$  in light.

Max $I_{SD}$ change%	CM-OFET 1	CM-OFET 2	CM-OFET 3	CM-OFET 4	CM-OFET 5	CM-OFET 6
0 – 2 hrs	59.1	31.2	39.7	52.1	57.6	61.3
2 – 7 hrs	9.7	5.6	12.4	3	3.7	9.8
5 – 7 hrs	2.3	2.8	3	3	3.6	2.8

The large decrease in source drain current observed in the early dark period is also associated with large measurement to measurement source drain current change (i.e. difference in  $I_{SD}$  between successive measurements), the measurement to measurement source drain current change can be expressed in terms of the relative standard deviation RSD over a particular period of time in the experiment.

Figure 4.16 compare the RSD between measurements at different periods during the light to dark experiment.

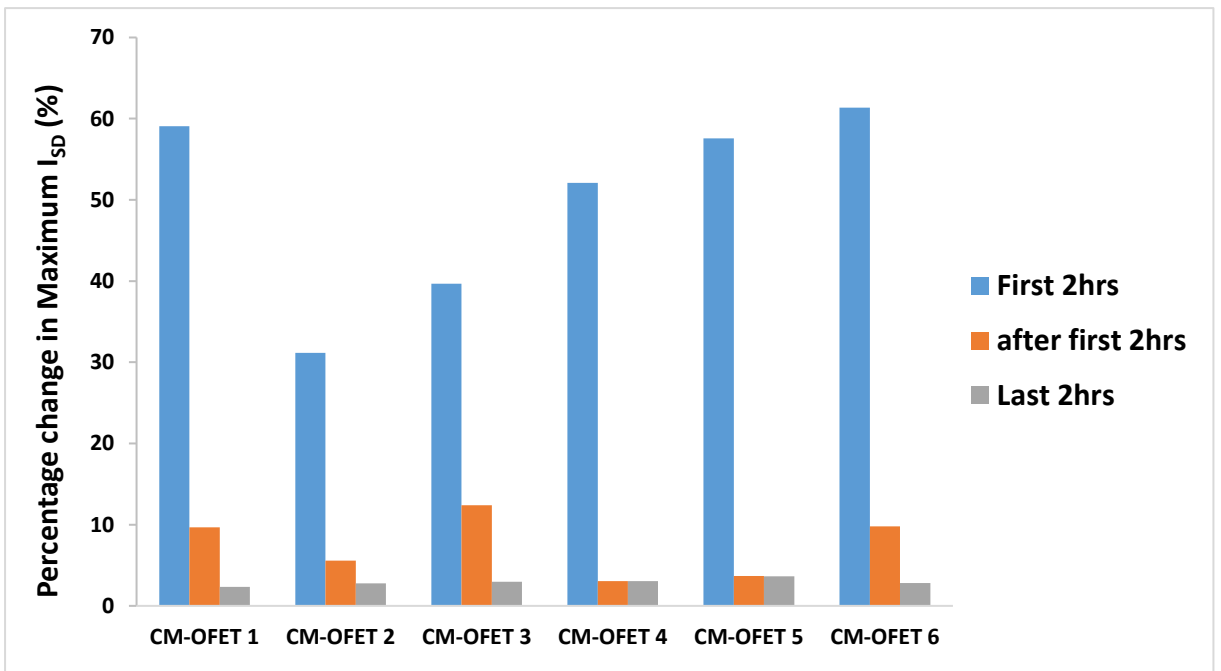


**Figure 4.15:** The percentage of change in the measured maximum source drain current  $I_{SD\text{Max}}$  for six CM-OFETs.

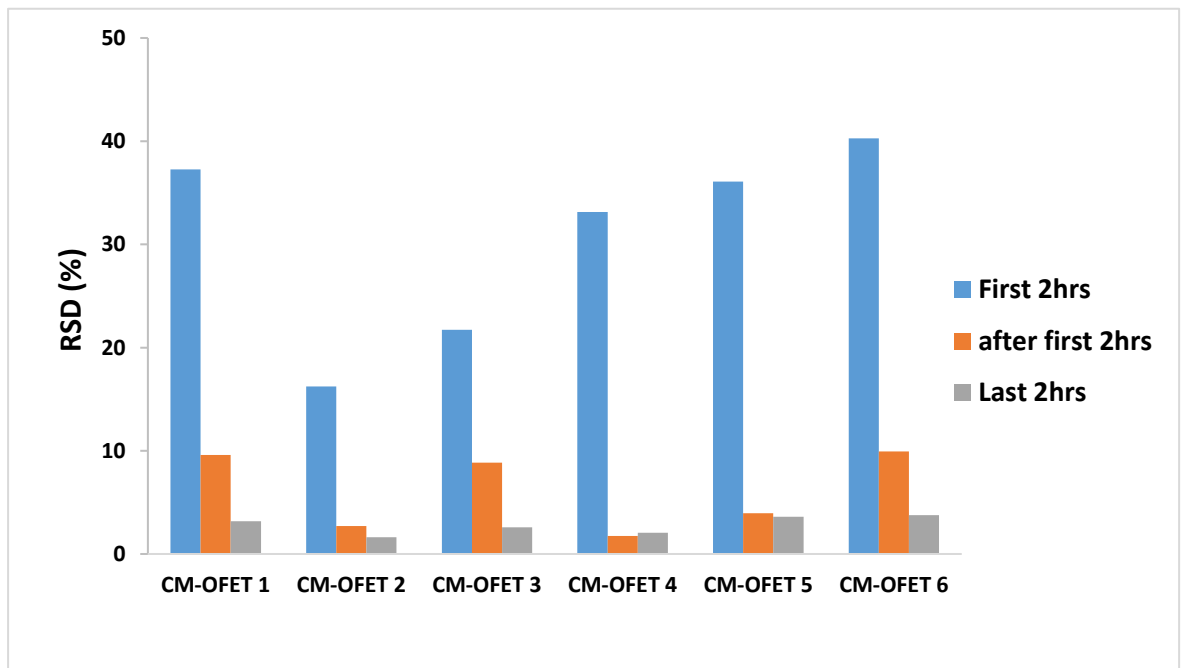


**Figure 4.16:** comparison of the RSD between recorded  $I_{SD\text{Max}}$  at different periods of the experiment for six CM-OFETs.

Figure 4.16 clearly shows that in the first period under dark condition the measurement to measurement change every 25 minutes is far greater compare than that in later stages in the dark. This observation is of great importance when sensing activity is to be investigate, where the measured  $I_{SD}$  is compared before and after the sensing activity. If the sensing activity is studied shortly after the CM-OFET device was put in dark condition, the likelihood is that the effect of sensing activity will be dominated by the stronger photogenerated charge carrier releasing process and hence, any sensing interpretation and subsequent drawn conclusion within this period will be inaccurate and may be misleading. Therefore, it was important to ensure that the influence of photogenerated carriers was greatly reduced for all tested devices before any pH sensing measurement was conducted.

#### **4.4.3 pH sensing using the CM-OFET**

To demonstrate the functionality of the fabricated CM-OFET operating as a chemical sensor, the performance of the fabricated CM-OFET devices was assessed for monitoring pH. In order to test the pH response of a CM-OFET device, the sensing region was first functionalized with APTES and exposed to a set of buffer solutions of different pH. The pH solutions that were used for testing the fabricated devices were based on Mcilvaine's buffer solutions [48]. Mcilvaine buffer solutions are prepared by mixing stock solutions of 0.2 M disodium phosphate and 0.1 M citric acid at different concentrations. The pH range covered by Mcilvaine buffer is from 2.2 to 8 and the relative ratios and associated pH level used are illustrated in table 4.3. Experimentally, the different pH buffer solutions were made using the ratios provided in table 4.3 and pH of each made solution was subsequently measured using a pH meter (METTLER TOLEDO – FiveEasy F20). The table shows the measured pH of each solution compared to the target pH level.

According to the mechanism described in section 4.2, the charge density of the APTES functionalized Si surface in the sensing area will change depending on the pH of the solution. This change in surface charge density will in turn lead to a redistribution of charge in the floating gate and hence, modulate the charge carrier density inside the channel of the transistor. Effectively, a charge equal in magnitude but opposite in sign to that accumulated in sensing area of the floating gate, will be distributed over the three, transistor electrodes (source, drain and control gate), causing a shift in the gate voltage applied to the transistor. Assuming everything else remains constant apart from the pH of

the solution, the charge accumulation on the surface of the sensing region, will result in an apparent change in the threshold voltage according to the following expression [49].

$$\Delta V_{TH} = \Delta V_{Fg} = \frac{-Q_{SENS}}{C_{TOT}} \quad (4.7)$$

Here,  $Q_{SENS}$  is the charge on the surface of the sensing region induced by the protonation/deprotonation of surface amine and hydroxyl groups,  $C_{TOT}$  is the sum of all the capacitances in the device structure i.e.  $C_{TOT} = C_{cg} + C_s + C_D$ , where  $C_{cg}$ ,  $C_s$  and  $C_D$  are the control gate, source and drain capacitance, respectively,  $V_{TH}$  is the CM-OFET threshold voltage and  $V_{FG}$  is the floating gate potential.

**Table 4.3:** Mixing table for making 50ml of citric and Mcilvaine buffer solutions and the measured pH of prepared buffer solutions compare to the targeted pH.

Targeted pH	0.2M Disodium phosphate ( $\text{Na}_2\text{HPO}_4$ ) ml	0.1M Citric acid ( $\text{C}_6\text{H}_8\text{O}_7$ ) ml	Measured pH
Citric (reference)	0	50	2.54
2.2	1	49	2.65
3	10.275	39.725	3.24
4	19.275	30.725	4.05
5	25.75	24.25	5.62
6	31.575	18.425	6.5
7	41.175	8.825	7.19
8	48.625	1.375	8.12

#### 4.4.3.1 pH sensing using the CM-OFET: Transfer characteristics

The variation in the source-drain current as a consequence of the redistribution of charge in the floating gate induced by the change in the pH level of the solution was used to

confirm the sensing capabilities of the CM-OFET. Specifically, the maximum drain-source current,  $I_{SDMax}$ , from the transfer characteristics of the device measurements was used to compare the response of the device to each pH solution.  $I_{SDMax}$  on the transfer characteristics curve is at a gate voltage (applied through the control gate)  $V_G = -40$  V while the drain voltage was held constant at  $-40$  V.

The measurement was performed using the following protocol:

(1) A reference pH solution, here citric acid (pH 2.54) was first introduced to the sensing region of the CM-OFET sensor via the PDMS chamber and the transfer characteristics of the device measured. This provided a baseline measurement against which the test solution was measured.

(2) The reference pH solution was replaced by a test pH buffer solution and the transfer characteristics of the CM-OFET measured. This process was repeated for each pH buffer solution in the range pH 2.2 – 8. The percentage change in  $I_{SDMax}$  between the test pH solution and the previous citric acid reference pH solution was calculated using equation 4.8 and used to compare the response of the device to different pH test solutions:

$$\Delta I_{SDMax}\% = \frac{(I_{SDMax}(pH) - I_{SDMax}(citric))}{I_{SDMax}(citric)} \% \quad (4.8)$$

Here,  $I_{SDMax}(pH)$  is the maximum source-drain current of the test pH solution and  $I_{SDMax}(citric)$  is the maximum source drain current measured for the citric acid reference pH solution.

At different pH levels, the amine and silanol groups on the surface of the sensing region are expected to change ionization states, thus the surface charge density will vary in the sensing region accordingly. In the pH sensing experiment described above, each time the citric acid solution is replaced by a given buffer solution, the surface charge of the sensing region is expected to change where the amount of change is dependent on the difference in pH between the citric acid reference and the test solution. For example, replacing the citric acid solution with a buffer solution of pH 8 will result in the silanol groups changing from  $Si - OH_2^+$  or  $Si - OH$  in acidic conditions (citric acid) to  $Si - O^-$  at pH 8. At the same time the surface amines initially protonated in citric acid will become deprotonated at pH 8. As a result, the surface changes from being predominantly positively charged to a surface with a large negative charged density. Ultimately, this is expected to be translated to a large

positive shift in apparent gate voltage and thus an increase in  $I_{SDMax}$ . In contrast, replacing the citric acid with a low pH 2.6 buffer solution, means that the surface groups will remain largely unchanged (with similar ionization states). Correspondingly, small to negligible change in the magnitude and sign of the surface charge is expected.

Two types of responses may be observed in the investigated CM-OFET devices based on the quality of the APTES layer in the sensing region.

- 1) Devices with a dense APTES monolayer assembled in the sensing region, should exhibit a linear pH sensitivity response over the investigated pH range (pH 2.2 – 8), as a result of the combined pH response of both amine and silanol groups as explained in section 4.2. Here, the linearity should be observed as a linear increase in the percentage change in the maximum source drain current as the pH increase.
- 2) In devices with poor quality APTES layer, the density of amine groups is significantly reduced such that the pH sensitivity of the CM-OFET is dominated by silanol groups on the silica surface. As discussed in section 4.2, these Si-OH groups are known to exhibit a weak response to pH change between pH 2.3 and 6.8, hence, the change in  $I_{SDMax}$  is expected to be minimal in this range.

A total of eight, nominally identical CM-OFET devices were tested for pH sensing. Each device was challenged with the seven pH solutions presented in table 4.3 before the transfer characteristics of each device was measured. Each device was tested three times over the full pH range (pH 2.2 - 8). In two of the three tests, the transfer characteristics were recorded immediately after the solution was introduced to the sensing area and 25 minutes after being introduced (referred to as the 25min measurement). In the third test, the pH solutions were measured only after 25 minutes of it being introduced to the sensing area. The latter test was done to investigate if reducing the biasing stress that is generated from immediate measurement affects the pH response.

Experimental results of the eight devices are shown in figures 4.17 to 4.24. Each figure displays for a particular CM-OFET device (a) the percentage change in the maximum source drain current between each pH buffer solution and the reference citric solution (calculated using equation 4.8) for three independent measurements when the transfer characteristics were measured 25 minutes after the introduction of the pH buffer solution. (b) the average

percentage change over the three (25min measurement) tests. (c) the percentage change in the maximum source drain for the two measurements performed immediately after the pH buffer solution has replaced the citric solution in the sensing region. (d) the average percentage change for the two immediate measurement tests.

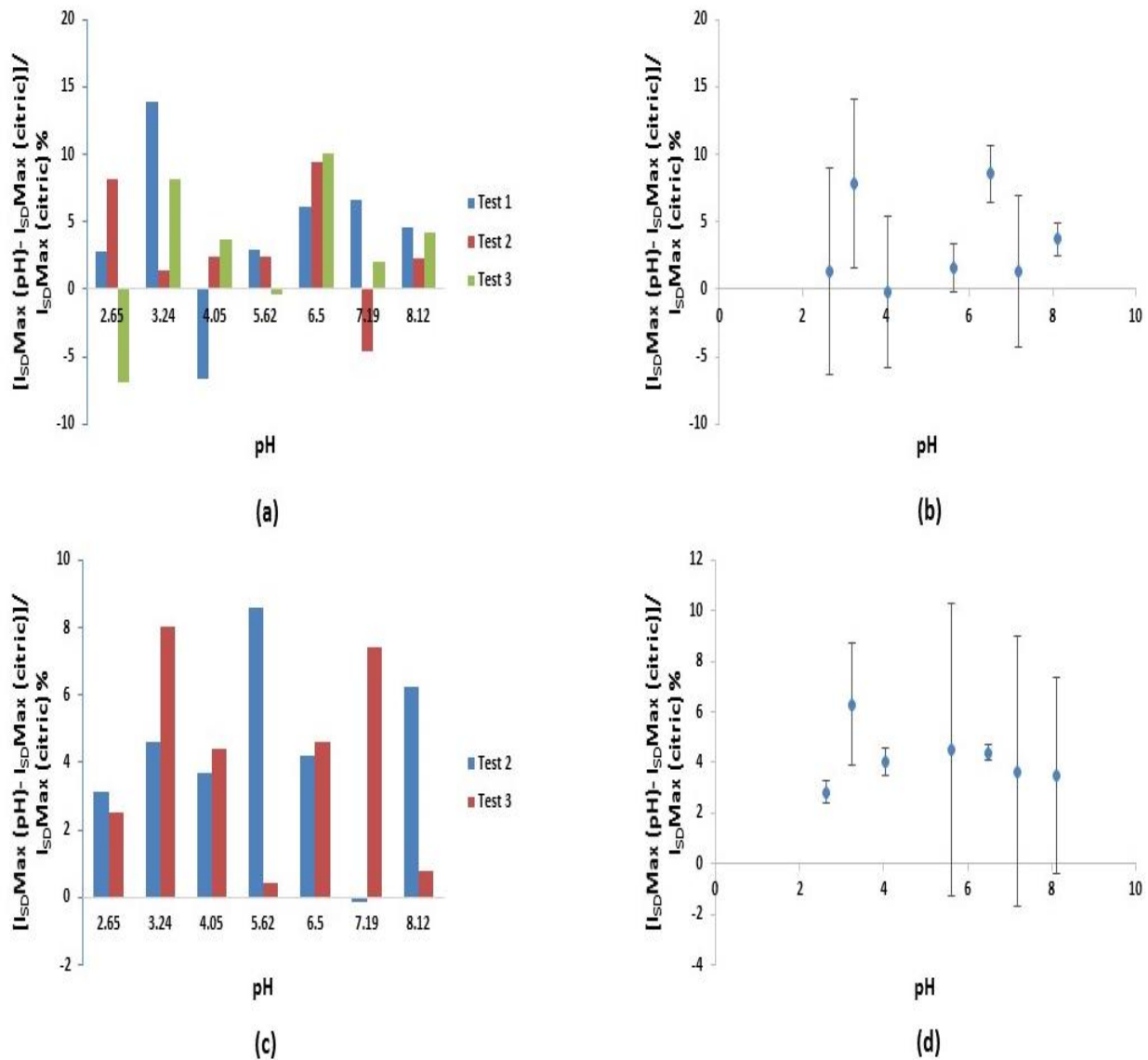
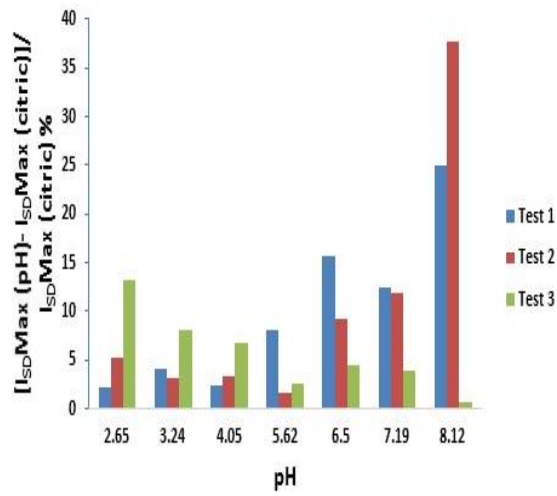
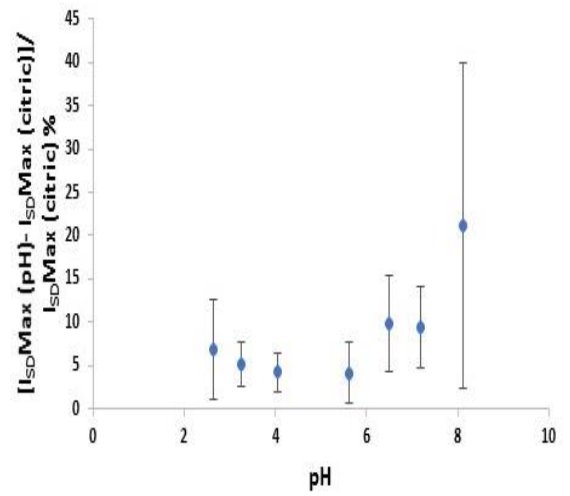


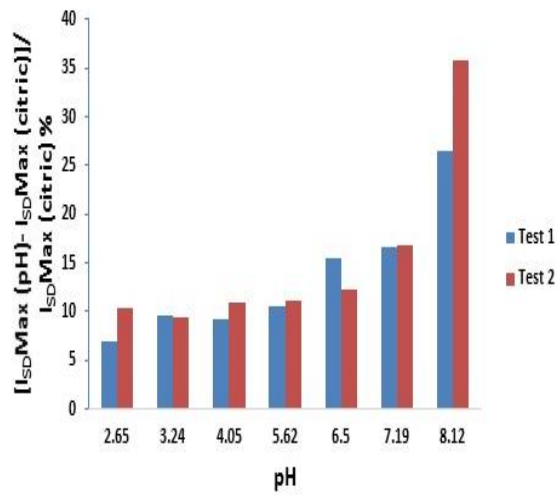
**Figure 4.17:** Experimental results of pH sensing using CM-OFET device 1. (a) Percentage change in  $I_{SD}Max$  for three independent measurements over the full pH range. Here, the transfer characteristics were measured 25 mins after introduction of the test pH solution. (b) The average change in  $I_{SD}Max$  for the three independent measurements (25min measurement). (c) Percentage change in  $I_{SD}Max$  for two independent measurements over the full pH range. Here, the transfer characteristics were measured immediately after introduction of the test pH solution. (d) The average change in  $I_{SD}Max$  for the two independent measurements (immediate measurement). Error bars are  $\pm SD$ .



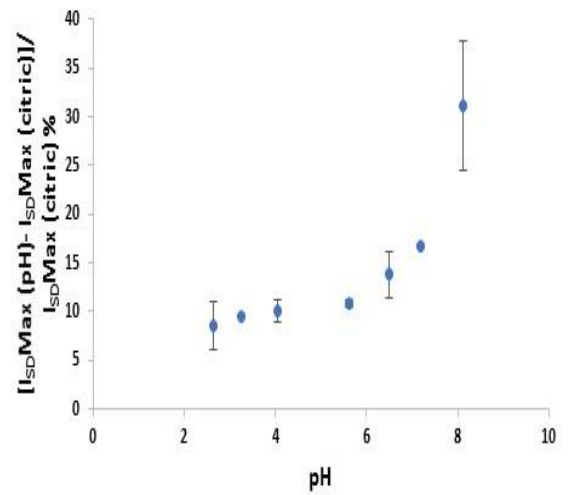
(a)



(b)

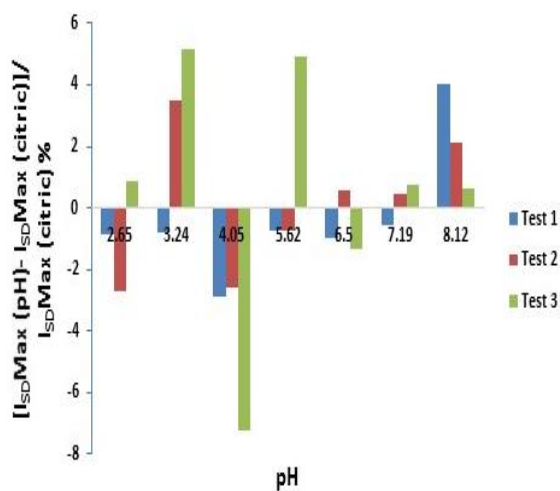


(c)

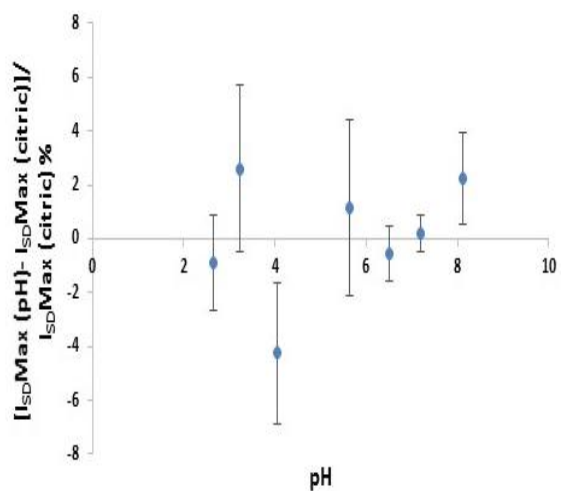


(d)

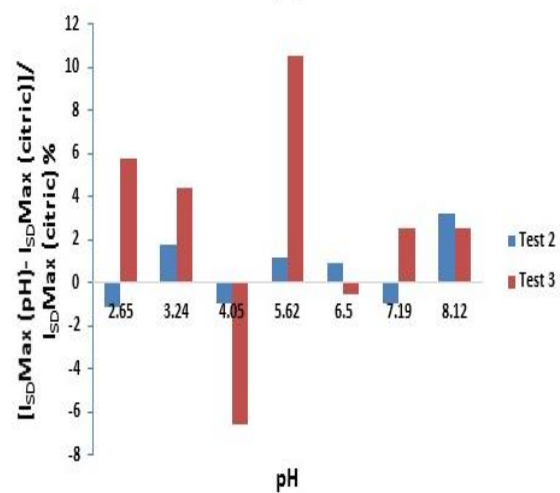
**Figure 4.18:** Experimental results of pH sensing using CM-OFET device 2. (a) Percentage change in  $I_{SDMax}$  for three independent measurements over the full pH range. Here, the transfer characteristics were measured 25 mins after introduction of the test pH solution. (b) The average change in  $I_{SDMax}$  for the three independent measurements (25min measurement). (c) Percentage change in  $I_{SDMax}$  for two independent measurements over the full pH range. Here, the transfer characteristics were measured immediately after introduction of the test pH solution. (d) The average change in  $I_{SDMax}$  for the two independent measurements (immediate measurement). Error bars are  $\pm SD$ .



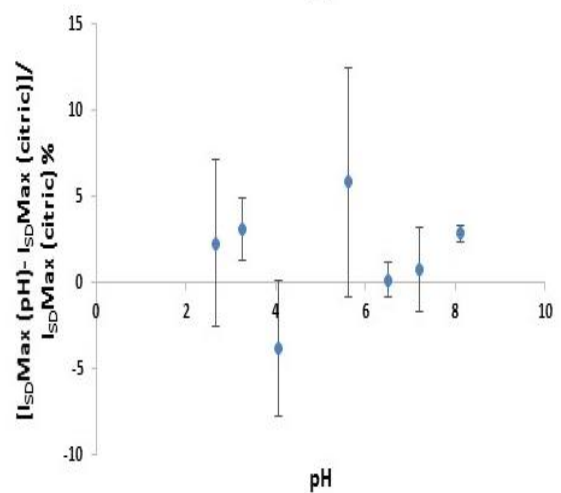
(a)



(b)



(c)



(d)

**Figure 4.19:** Experimental results of pH sensing using CM-OFET device 3. (a) Percentage change in  $I_{SDMax}$  for three independent measurements over the full pH range. Here, the transfer characteristics were measured 25 mins after introduction of the test pH solution. (b) The average change in  $I_{SDMax}$  for the three independent measurements (25min measurement). (c) Percentage change in  $I_{SDMax}$  for two independent measurements over the full pH range. Here, the transfer characteristics were measured immediately after introduction of the test pH solution. (d) The average change in  $I_{SDMax}$  for the two independent measurements (immediate measurement). Error bars are  $\pm SD$ .

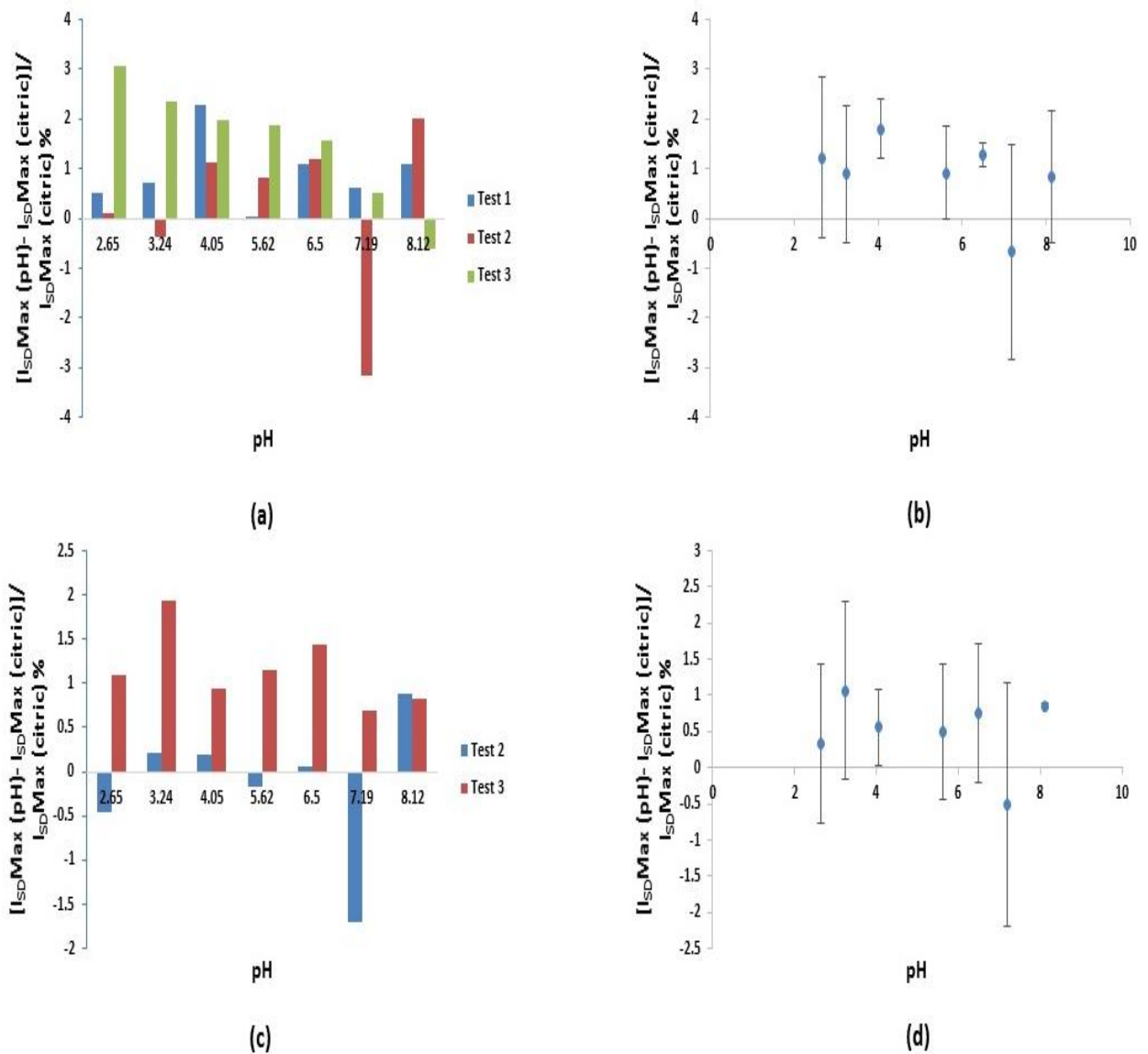
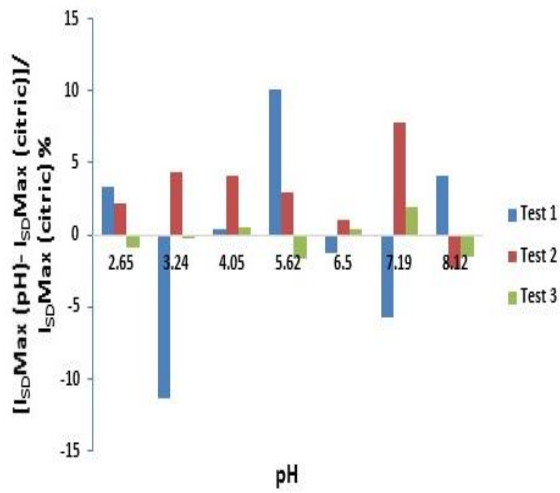
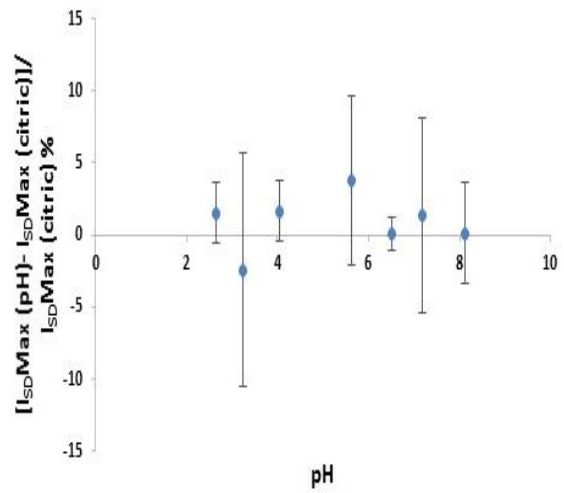


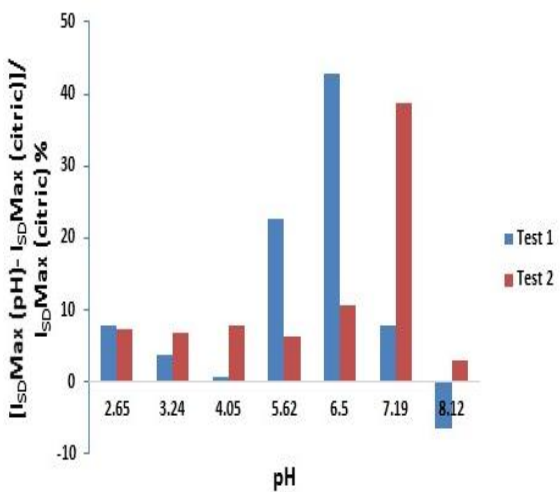
**Figure 4.20:** Experimental results of pH sensing using CM-OFET device 4. (a) Percentage change in  $I_{SDMax}$  for three independent measurements over the full pH range. Here, the transfer characteristics were measured 25 mins after introduction of the test pH solution. (b) The average change in  $I_{SDMax}$  for the three independent measurements (25min measurement). (c) Percentage change in  $I_{SDMax}$  for two independent measurements over the full pH range. Here, the transfer characteristics were measured immediately after introduction of the test pH solution. (d) The average change in  $I_{SDMax}$  for the two independent measurements (immediate measurement). Error bars are  $\pm SD$ .



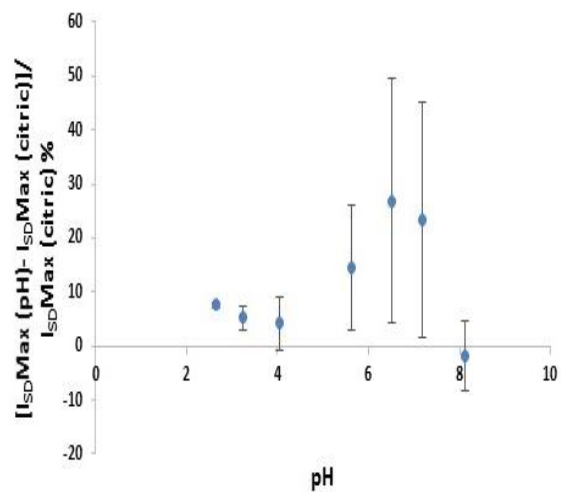
(a)



(b)



(c)



(d)

**Figure 4.21:** Experimental results of pH sensing using CM-OFET device 5. (a) Percentage change in  $I_{SDMax}$  for three independent measurements over the full pH range. Here, the transfer characteristics were measured 25 mins after introduction of the test pH solution. (b) The average change in  $I_{SDMax}$  for the three independent measurements (25min measurement). (c) Percentage change in  $I_{SDMax}$  for two independent measurements over the full pH range. Here, the transfer characteristics were measured immediately after introduction of the test pH solution. (d) The average change in  $I_{SDMax}$  for the two independent measurements (immediate measurement). Error bars are  $\pm SD$ .

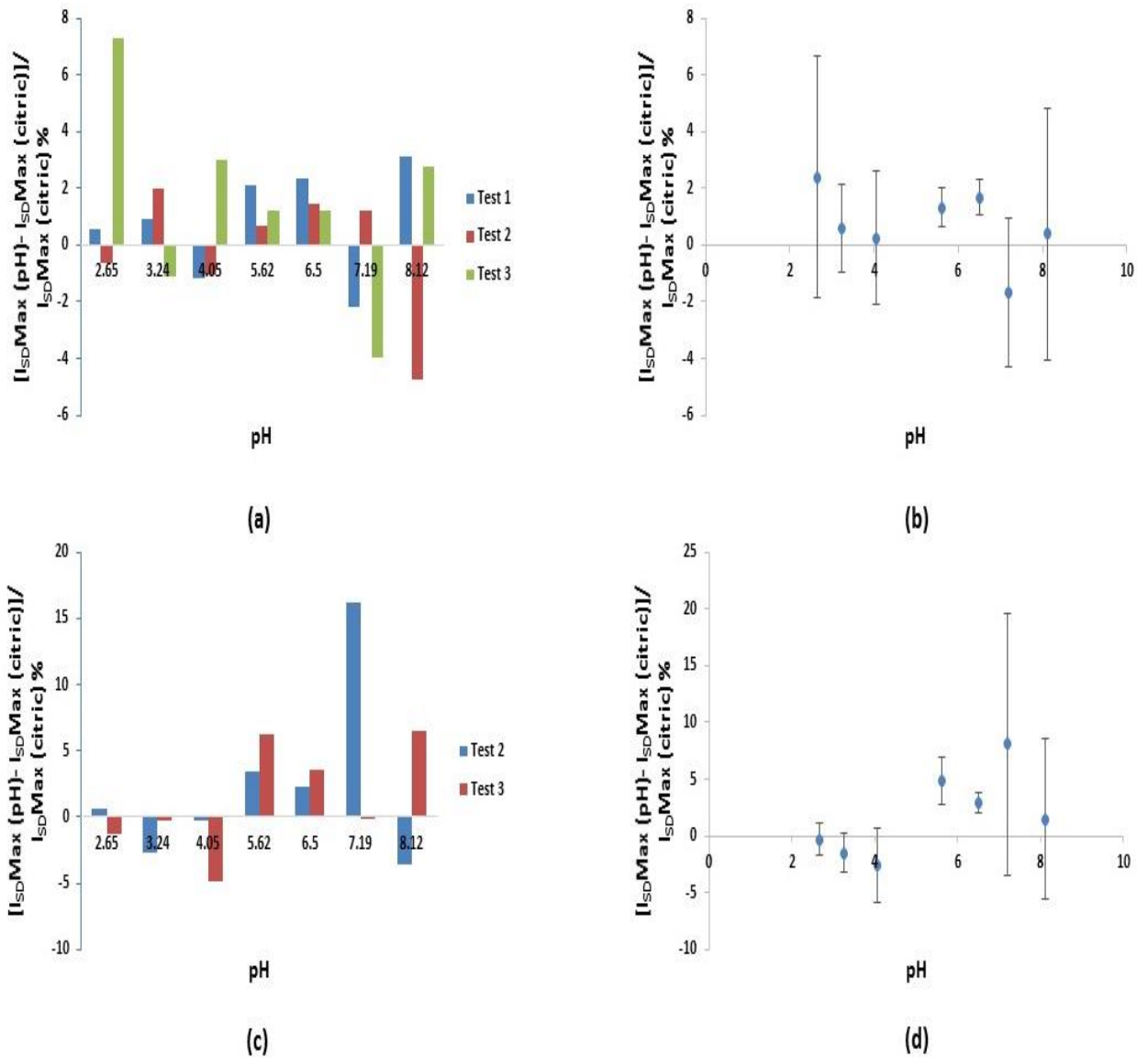
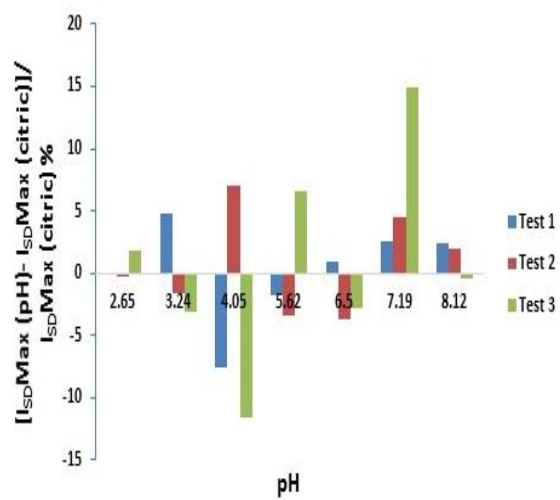
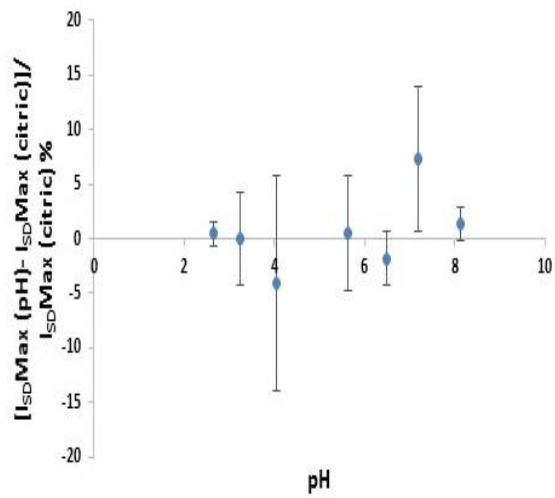


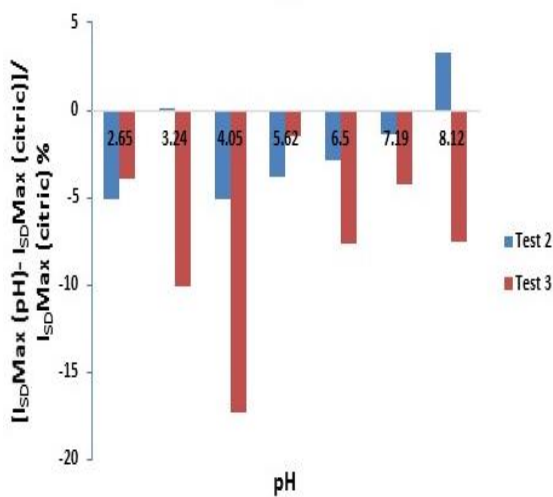
**Figure 4.22:** Experimental results of pH sensing using CM-OFET device 6. (a) Percentage change in  $I_{SD}Max$  for three independent measurements over the full pH range. Here, the transfer characteristics were measured 25 mins after introduction of the test pH solution. (b) The average change in  $I_{SD}Max$  for the three independent measurements (25min measurement). (c) Percentage change in  $I_{SD}Max$  for two independent measurements over the full pH range. Here, the transfer characteristics were measured immediately after introduction of the test pH solution. (d) The average change in  $I_{SD}Max$  for the two independent measurements (immediate measurement). Error bars are  $\pm SD$ .



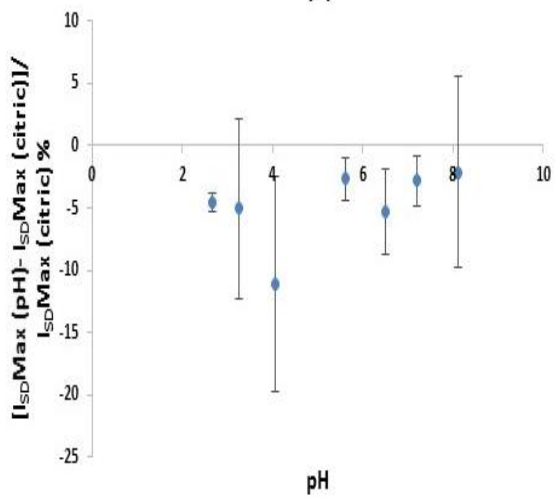
(a)



(b)



(c)



(d)

**Figure 4.23:** Experimental results of pH sensing using CM-OFET device 7. (a) Percentage change in  $I_{SDMax}$  for three independent measurements over the full pH range. Here, the transfer characteristics were measured 25 mins after introduction of the test pH solution. (b) The average change in  $I_{SDMax}$  for the three independent measurements (25min measurement). (c) Percentage change in  $I_{SDMax}$  for two independent measurements over the full pH range. Here, the transfer characteristics were measured immediately after introduction of the test pH solution. (d) The average change in  $I_{SDMax}$  for the two independent measurements (immediate measurement). Error bars are  $\pm SD$ .

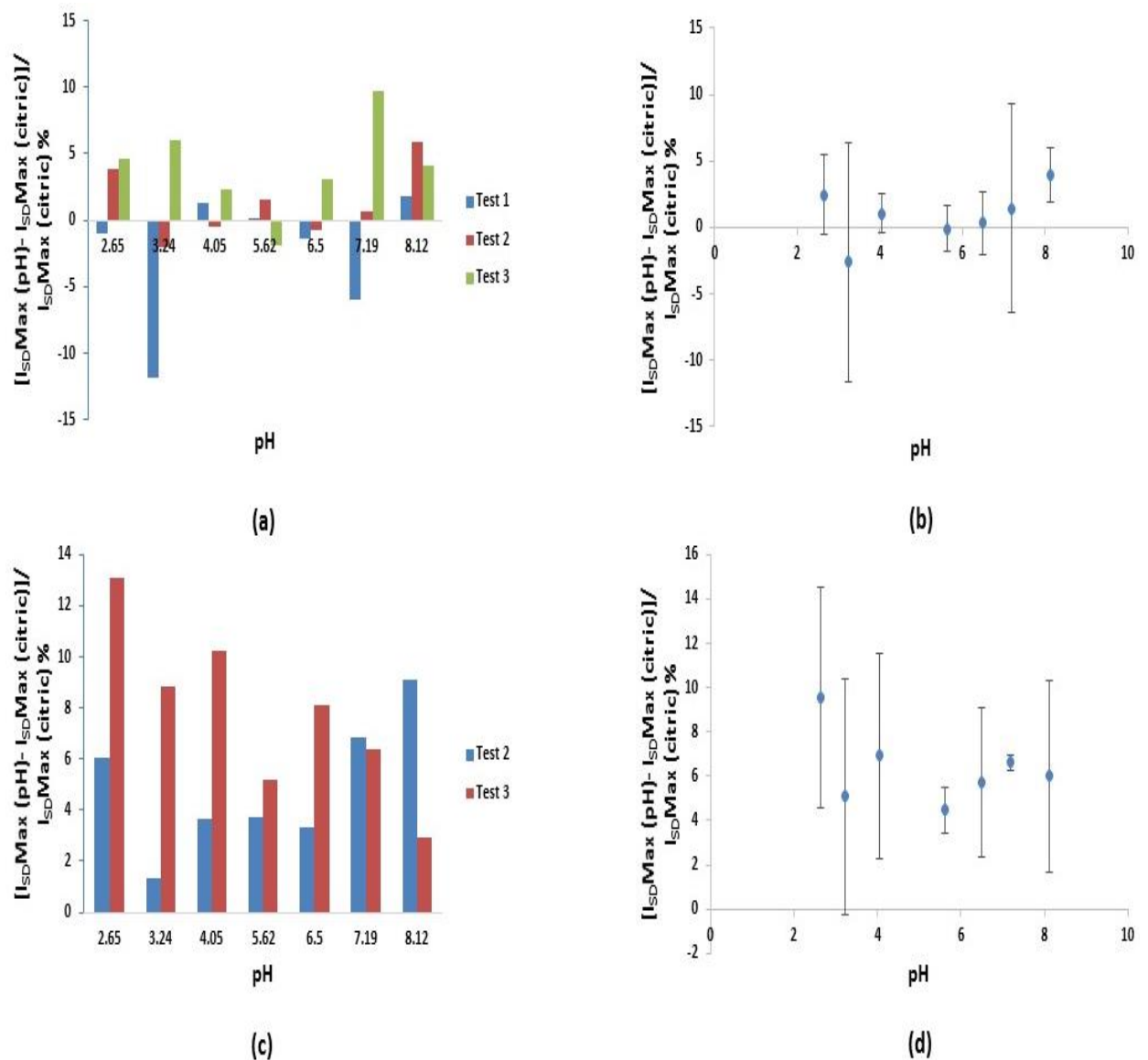


**Figure 4.24:** Experimental results of pH sensing using CM-OFET device 8. (a) Percentage change in  $I_{SDMax}$  for three independent measurements over the full pH range. Here, the transfer characteristics were measured 25 mins after introduction of the test pH solution. (b) The average change in  $I_{SDMax}$  for the three independent measurements (25min measurement). (c) Percentage change in  $I_{SDMax}$  for two independent measurements over the full pH range. Here, the transfer characteristics were measured immediately after introduction of the test pH solution. (d) The average change in  $I_{SDMax}$  for the two independent measurements (immediate measurement). Error bars are  $\pm SD$ .

The results obtained for the eight CM-OFET devices tested for pH sensing showed:

- 1) The responses of the eight nominally identical devices to pH test solutions was inconsistent. Similarly, repeat measurements of identical devices also show inconsistent responses.
- 2) None of the devices displayed the expected response to the pH solutions. Specifically, none of the devices showed the linear response (linear increase in source drain current with pH) expected for CM-OFETs functionalized with a good quality APTES layer in the sensing area, nor a response with nonlinear current increase in the middle of the pH range for devices with a poor APTES layer where the silanol groups would dominate pH response.
- 3) No repeatable or distinguishable trend can be extracted from experimental data of the pH response for the eight devices.
- 4) There was no clear effect of excluding the immediate measurement on the pH response behaviour of the examined CM-OFET devices.
- 5) Overall, in almost 70% of measurements, the source drain current was found to increase after replacement of the citric acid solutions with a test pH buffer.
- 6) The change in  $I_{SDMax}$  between the citric acid solution and the test pH solution was routinely very small. Specifically, in almost 90% of measurements  $I_{SDMax}(pH)$  changed less than 10% relative to  $I_{SD}(citric)$ .

The average change in  $\Delta I_{SDMax}$  across all devices for each pH buffer is shown in figure 4.25 and it concur with the above-mentioned conclusions, particularly, the error margins for the detection was high and the change in  $\Delta I_{SDMax}$  was largely within the noise range of the devices.

From these experimental results, it is clear that there is no consistent, predictable or distinguishable response for CM-OFET when challenged with buffers of changing pH. Also, except in limited cases (7.7% of the times), the change in maximum source drain current of the investigated pH buffer solution  $I_{SDMax}(pH)$  relative to the source drain current of the corresponding citric solution  $I_{SDMax}(citric)$  was below 10%. This is comparable to the shifts in maximum source drain current,  $I_{SDMax}$ , due to the inherent behaviour of the OSC. In the following section, an alternative test was performed in which the source drain current was recorded as a function of time while the bias voltages remain constant.

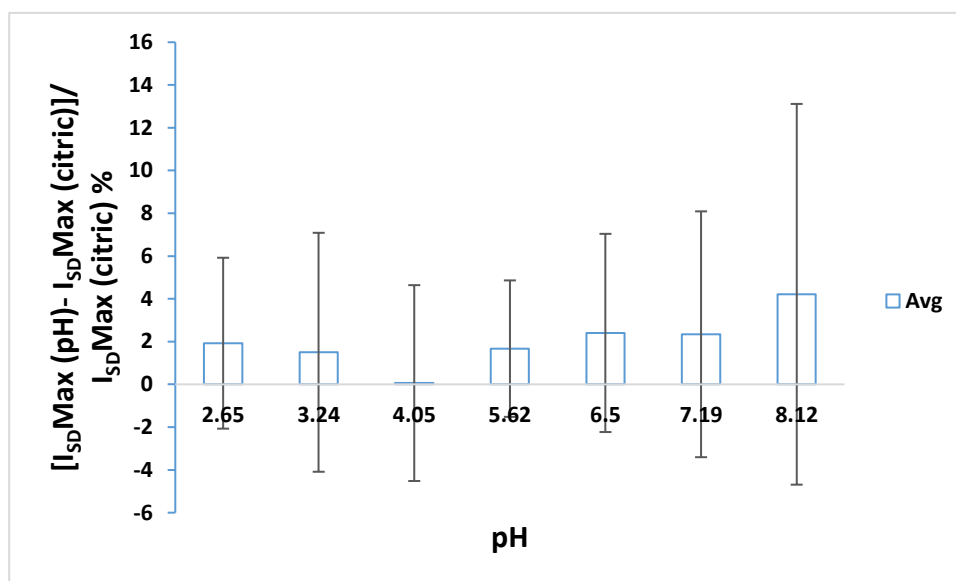


**Figure 4.25:** The average of  $[(I_{SD}Max (pH) - I_{SD}Max (citric)) / I_{SD}Max (citric)] \%$  change for each investigated pH level across all tested CM-OFET devices (25min measurement). Error bars are  $\pm SD$ .

#### 4.4.3.2 CM-OFET pH sensor: Time domain measurements

Another measurement used to investigate the pH sensitivity of the CM-OFET devices was time domain measurement. Time domain measurements were performed on APTES functionalized CM-OFET pH sensors to monitor the instantaneous change in the source drain current  $I_{SD}$  of the devices as a function of solution pH. Exposure of the sensing region to a buffer is expected to induce a change in the source drain current corresponding to the change in charge accumulated in the sensing area.

It is expected that the source drain current of the CM-OFETs will increase when an alkaline solution replaces an acidic solution in the sensing region, due to deprotonation of both the  $NH_2$  and  $Si - O^-$  groups. The reverse is expected when the solution becomes increasingly acidic due to the protonation of surface amines to  $NH_3^+$  as well as  $Si-O^-$  converting to  $Si - OH$  and  $Si - OH^+$  depending on the pH level of the investigated solution.

For the source drain current,  $I_{SD}$ , versus time measurement,  $I_{SD}$  was monitored in real time (one acquisition per 1s) while  $V_D$  and  $V_G$  remained fixed at -40 V. Measurements were started prior to flowing any solution into the microfluidic chamber after which solutions were introduced to the sensing region via microfluidic tubes inserted into the PDMS

chamber. For each solution, the current was recorded for a period of time after the solution was introduced to allow time for the response to stabilize.

Two types of sequencing were used in terms of solution flowing into the sensing region of the examined devices. In the first, each pH solution was injected sequentially over the sensing region. In the second, air was injected into the PDMS prior to the injection of each pH buffer. The second approach was performed to establish a possible  $I_{SD}$  baseline for each investigated pH solution.

The general behaviour of the  $I_{SD}$  vs time measurements obtained for fabricated CM-OFET devices can be seen in figure 4.26 for the case where the PDMS chamber was filled with air. The large initial current decay in the  $I_{SD}$  vs time measurement is typical of bias stress in OFETs. The large initial current decay in the  $I_{SD}$  vs time measurement can be problematic when examining the sensing effect, as the large decay could be far greater than shifts in  $I_{SD}$  due to charge accumulated in the sensing region. In order to minimise the influence of bias stress, the electrode voltages were applied and maintained for 5 minutes before data acquisition was started.

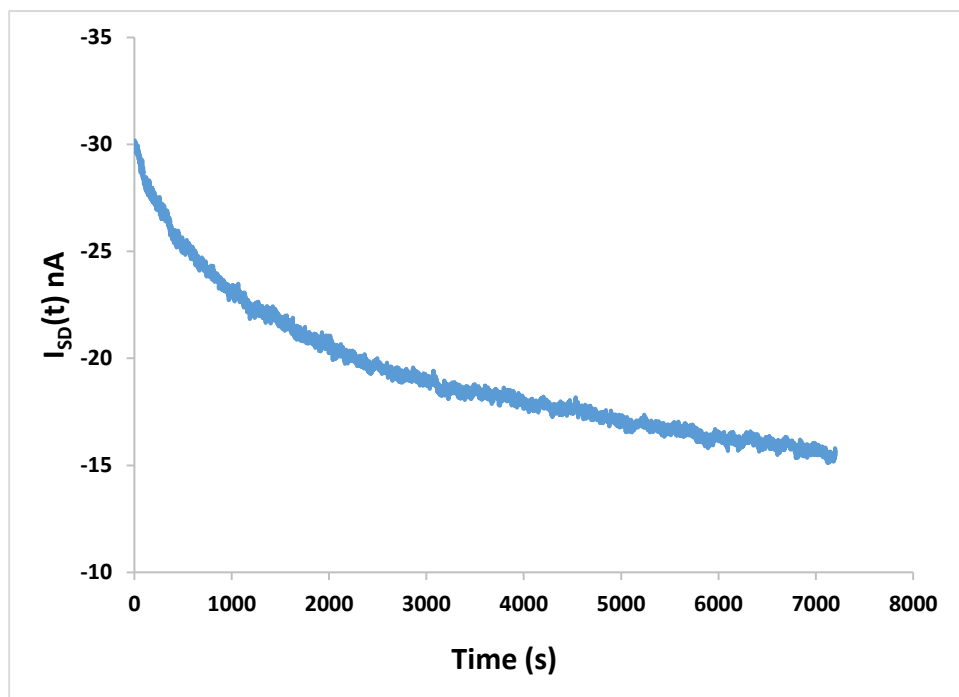


**Figure 4.26:** Source drain current decay over time due to bias stress effect for a CM-OFET device.

Figures 4.27 to 4.33 show experimental  $I_{SD}$  vs time traces for seven nominally identical CM-OFETs with APTES assembled on the surface of the Si sensing region. Here, three different buffers were used corresponding to pH 2.2, pH 5 and pH 8. The change in source drain current over time is presented as  $I_{SD}(t)/I_{SD}(0)$  in order to enable comparison between different CM-OFETs where  $I_{SD}(0)$  is the source drain current at  $t=0$ .

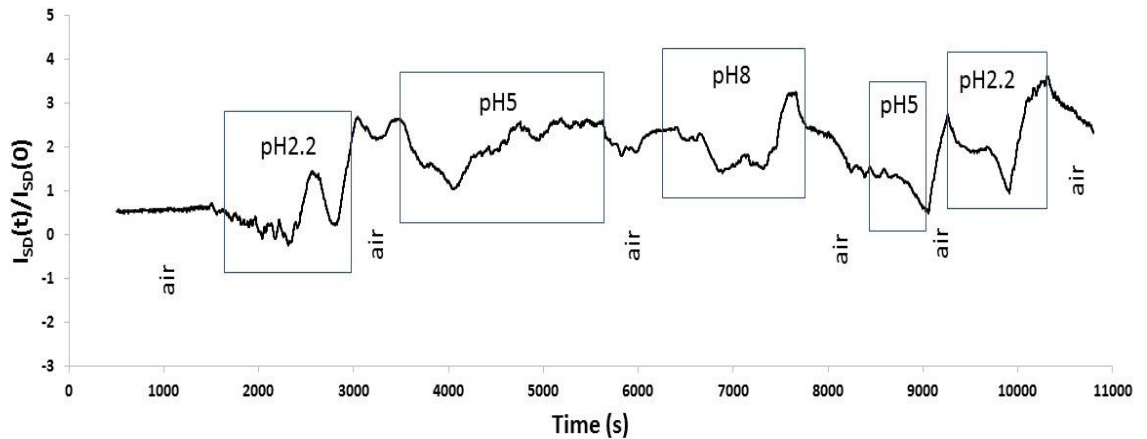


**Figure 4.27:** Normalized real time source drain current as a function of solution pH for CM-OFET device 1. The data has been smoothed using a 200s averaging period. Here, air was injected into the PDMS chamber prior to the injection of each buffer.

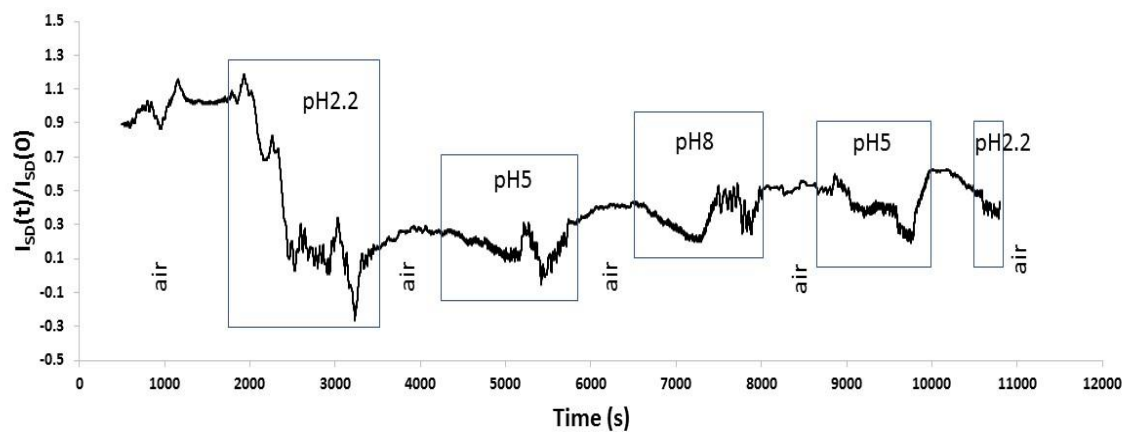


**Figure 4.28:** Normalized real time source drain current as a function of solution pH for CM-OFET device 2. The data has been smoothed using a 200s averaging period. Here, air was injected into the PDMS chamber prior to the injection of each buffer.

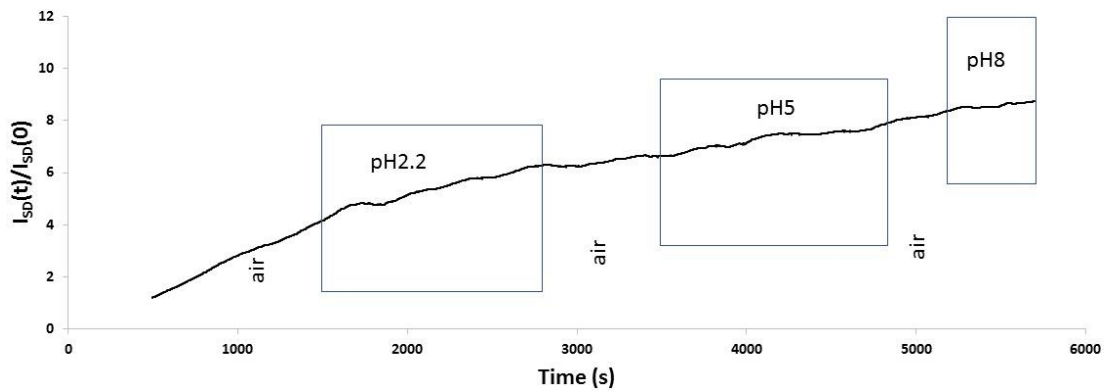


**Figure 4.29:** Normalized real time source drain current as a function of solution pH for CM-OFET device 3. The data has been smoothed using a 200s averaging period. Here, air was injected into the PDMS chamber prior to the injection of each buffer.

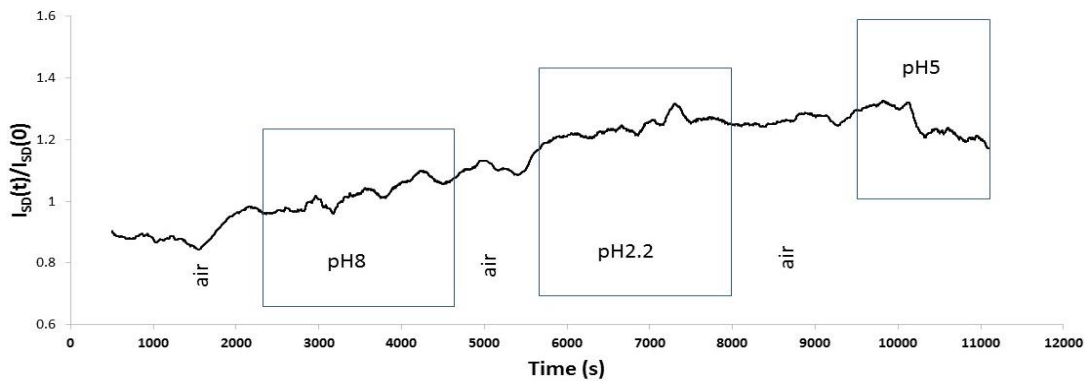


**Figure 4.30:** Normalized real time source drain current as a function of solution pH for CM-OFET device 4. The data has been smoothed using a 200s averaging period. Here, air was injected into the PDMS chamber prior to the injection of each buffer.

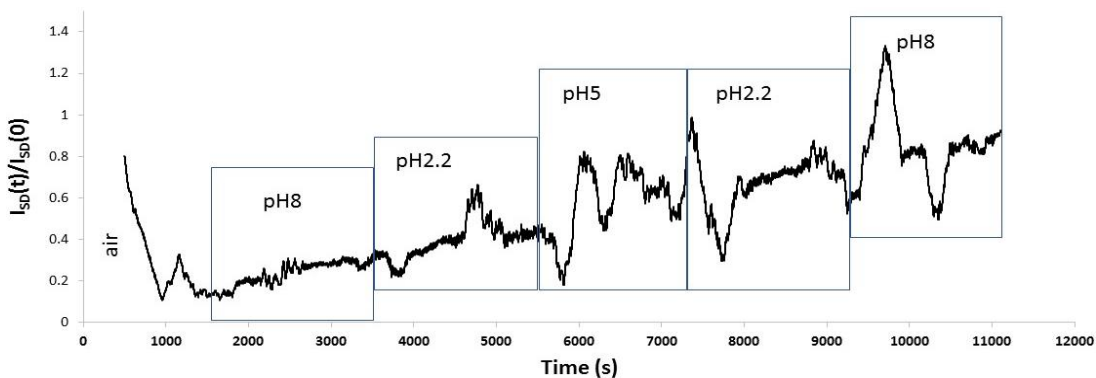


**Figure 4.31:** Normalized real time source drain current as a function of solution pH for CM-OFET device 5. The data has been smoothed using a 200s averaging period.

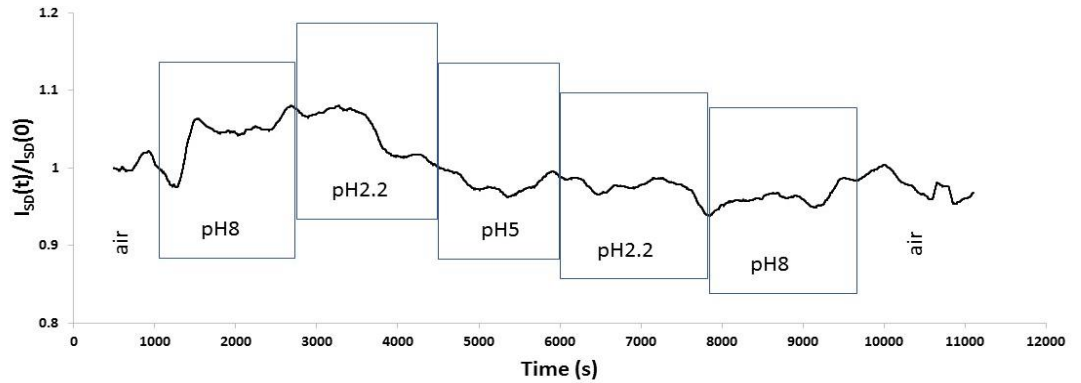


**Figure 4.32:** Normalized real time source drain current as a function of solution pH for CM-OFET device 6. The data has been smoothed using a 200s averaging period.

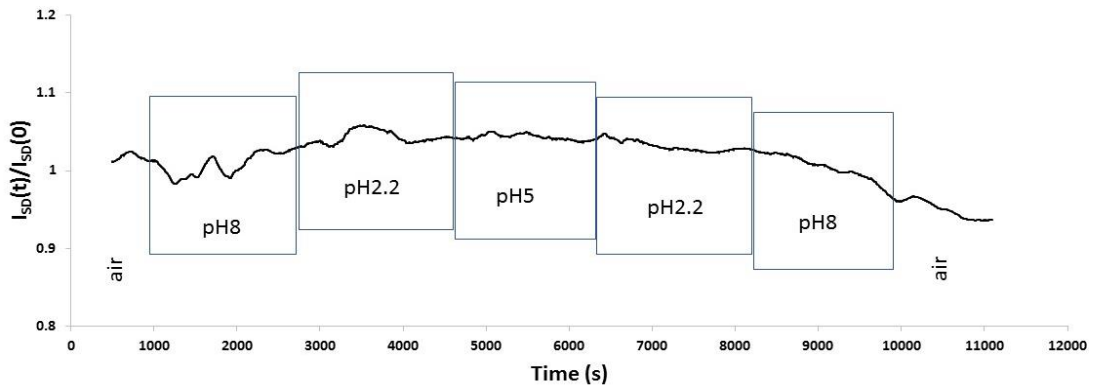


**Figure 4.33:** Normalized real time source drain current as a function of solution pH for CM-OFET device 7. The data has been smoothed using a 200s averaging period.

It must be noted, that in some of the examined devices (figures 4.27, 4.28 and 4.31), the source drain current was very low when the data acquisition has started ( $< 3\text{ nA}$ ), indicating the possibility of massive holes migrating into the gate dielectric layer which can screen the electric field from the gate [50]. In these devices, associating the current change to the sensing effect may be inaccurate.

The source drain current of CM-OFET device 3 shown in figure 4.29, seems to be unaffected by the introduction of buffer solutions. An unknown effect dominated the device response, manifested as a constant current increase over time, possibly due to an effect at the contacts/Tips-pentacene interface that causes decrease in contact resistance.

The remaining devices (associated with figures 4.30, 4.32 and 4.33), did not show a repeatable behaviour with solution pH. Instead, the CM-OFET response is dominated by current fluctuations which make it difficult to make accurate judgement on what can be considered increase or decrease within the timeframe each pH solution was present in the sensing region. It should be noted that if migration of holes into the gate dielectric is indeed happening during bias stress, then it is expected that the longer the measurement runs the higher the accumulation of holes in the gate dielectric and the weaker the charge sensing effect will be on the modulation of  $I_{SD}$ . Therefore, the relative change in current due to a change in charge density in the sensing region is expected to reduce with time.

## 4.5 Conclusion

Using a simple fabrication process, an OFET structure was transformed into a CM-OFET device and explored as pH a sensor. Here, the CM-OFET sensor exploits modulation in charge on the surface of the sensing region due to a change in pH. Specifically, the silicon surface of the sensing region naturally contains silanol groups, which can become protonated and deprotonated as a function of local pH. The associated change in surface charge couples capacitively to the OFET leading to a change in the source drain current, seen either in the transfer characteristics or time domain measurements. Due to the limited range of pH over which the silanol groups are expected to change charge, the surface was further modified using silane chemistry to introduce amine groups at the surface. These amine groups were introduced to the Si floating gate surface by assembly with a 3-aminopropyltrimethoxysilane self-assembled monolayer which was characterized by x-ray photoelectron spectroscopy (XPS) to confirm the assembly of the layer and successful functionalization with amine groups. Characterization of pH-sensitive CM-OFET devices using both transfer characteristics and time domain measurements, did not demonstrate a consistent response to pH changes in the sensing region of the devices. Specifically, the changes in source drain current observed following changing of solution pH were unrepeatable between and within devices and typically comparable in magnitude to the changes in current inherent to the OFET. The final section of Chapter 5 will address the sensitivity limitation of the proposed CM-OFET device that may have led to the deficient performance.

## 4.6 References

- [1] Misra, D., Worhoff, K., & Mascher, P. (2003). Dielectrics in Emerging Fields. In D. Misra, K. Worhoff, & P. Mascher (Eds.), *Dielectrics in Emerging Fields* (pp. -). Pennington, New Jersey: The Electrochemical Society Inc..
- [2] Yates, D. E., Levine, S., & Healy, T. W. (1974). Site-binding model of the electrical double layer at the oxide/water interface. *Journal of the Chemical Society, Faraday Transactions 1: Physical Chemistry in Condensed Phases*, 70, 1807-1818.
- [3] Yang, X., Frensley, W. R., Zhou, D., & Hu, W. (2012). Performance analysis of Si nanowire biosensor by numerical modeling for charge sensing. *IEEE Transactions on Nanotechnology*, 11(3), 501-512.
- [4] Moretto, L. M., & Kalcher, K. (2014). *Environmental analysis by electrochemical sensors and biosensors*. New York: Springer.
- [5] Bousse, L., & Bergveld, P. (1984). The role of buried OH sites in the response mechanism of inorganic-gate pH-sensitive ISFETs. *Sensors and Actuators*, 6(1), 65-78.
- [6] Cui, Y., Wei, Q., Park, H., & Lieber, C. M. (2001). Nanowire nanosensors for highly sensitive and selective detection of biological and chemical species. *Science*, 293(5533), 1289-1292.
- [7] Patolsky, F., & Lieber, C. M. (2005). Nanowire nanosensors. *Materials today*, 8(4), 20-28.
- [8] Tian, R., Regonda, S., Gao, J., Liu, Y., & Hu, W. (2011). Ultrasensitive protein detection using lithographically defined Si multi-nanowire field effect transistors. *Lab on a Chip*, 11(11), 1952-1961.
- [9] Chen, S., Bomer, J. G., Carlen, E. T., & van den Berg, A. (2011). Al<sub>2</sub>O<sub>3</sub>/silicon nanoISFET with near ideal Nernstian response. *Nano letters*, 11(6), 2334-2341.
- [10] Cheng, Y., Xiong, P., Yun, C. S., Strouse, G. F., Zheng, J. P., Yang, R. S., & Wang, Z. L. (2008). Mechanism and optimization of pH sensing using SnO<sub>2</sub> nanobelt field effect transistors. *Nano letters*, 8(12), 4179.

- [11] Kumar, N., Kumar, J., & Panda, S. (2015). Sensitivity enhancement mechanisms in textured dielectric based electrolyte-insulator-semiconductor (EIS) sensors. *ECS Journal of Solid State Science and Technology*, 4(3), N18-N23.
- [12] Chen, Y., Wang, X., Erramilli, S., Mohanty, P., & Kalinowski, A. (2006). Silicon-based nanoelectronic field-effect p H sensor with local gate control. *Applied physics letters*, 89(22), 223512.
- [13] Zang, P., Liang, Y., Spurgin, L., & Hu, W. (2013, August). pH sensing comparison of vapor and solution APTES coated Si nanograting FETs. In *Nanotechnology (IEEE-NANO), 2013 13th IEEE Conference on* (pp. 301-304). IEEE.
- [14] Bhushan, B. (Ed.). (2010). Springer handbook of nanotechnology. Springer Science & Business Media.
- [15] Coffey, J. L. (Ed.). (2014). Semiconducting Silicon Nanowires for Biomedical Applications. Elsevier.
- [16] Wipf, M. (2010). *Dual-gated field effect transistor for sensing applications* (Doctoral dissertation, Master's thesis, University of Basel).
- [17] Caboni, A., Orgiu, E., Barbaro, M., & Bonfiglio, A. (2009). Flexible organic thin-film transistors for pH monitoring. *IEEE Sensors Journal*, 9(12), 1963-1970.
- [18] van der Maaden, K., Tomar, J., Jiskoot, W., & Bouwstra, J. (2014). Chemical Modifications of Silicon Surfaces for the Generation of a Tunable Surface Isoelectric Point. *Langmuir*, 30(7), 1812-1819.
- [19] Harris, D. C. (2007). Quantitative chemical analysis. W. H. Freeman and Company.
- [20] Abiman, P., Wildgoose, G. G., Crossley, A., Jones, J. H., & Compton, R. G. (2007). Contrasting pKa of Protonated Bis (3-aminopropyl)-Terminated Polyethylene Glycol "Jeffamine" and the Associated Thermodynamic Parameters in Solution and Covalently Attached to Graphite Surfaces. *Chemistry—A European Journal*, 13(34), 9663-9667.
- [21] Mengistu, T. Z., Goel, V., Horton, J. H., & Morin, S. (2006). Chemical force titrations of functionalized Si (111) surfaces. *Langmuir*, 22(12), 5301-5307.

- [22] Vezenov, D. V., Noy, A., Rozsnyai, L. F., & Lieber, C. M. (1997). Force titrations and ionization state sensitive imaging of functional groups in aqueous solutions by chemical force microscopy. *Journal of the American Chemical Society*, *119*(8), 2006-2015.
- [23] Wang, H., & Linford, M. R. (2015). X-ray Photoelectron Spectroscopy and Auger Electron Spectroscopy: Comparison and Basic Principles. *Vacuum Technology & Coating*.
- [24] Watts, J. F. (1994). X-ray photoelectron spectroscopy. *Vacuum*, *45*(6-7), 653-671.
- [25] Boeckl, M., & Graham, D. (2006). Self-assembled monolayers: Advantages of pure alkanethiols. *Material matters*, *1*(2), 3-5.
- [26] Prashar, D. (2012). Self assembled monolayers-a review. *Int J ChemTech Res*, *4*(1), 258-265.
- [27] Celestin, M., Krishnan, S., Bhansali, S., Stefanakos, E., & Goswami, D. Y. (2014). A review of self-assembled monolayers as potential terahertz frequency tunnel diodes. *Nano Research*, *7*(5), 589-625.
- [28] Bensebaa, F., Voicu, R., Huron, L., Ellis, T. H., & Kruus, E. (1997). Kinetics of formation of long-chain n-alkanethiolate monolayers on polycrystalline gold. *Langmuir*, *13*(20), 5335-5340.
- [29] Khuat, T. T. H., Liang, L., Phan, T. T., Mizutani, G., & Rutt, H. N. (2019). Sum frequency generation study of immobilized 3-aminopropyltriethoxysilane self-assembled layer on Si (111) substrates. *Surface and Interface Analysis*, *51*(1), 120-125.
- [30] Gammoudi, H., Belkhiria, F., Helali, S., Assaker, I. B., Gammoudi, I., Morote, F., ... & Chtourou, R. (2017). Chemically grafted of single-walled carbon nanotubes onto a functionalized silicon surface. *Journal of Alloys and Compounds*, *694*, 1036-1044.
- [31] Ghorbanpour, M. (2016). Amine accessibility and chemical stability of silver SPR chips silanised with APTES via vapour phase deposition method. *Journal of Physical Science*, *27*(1), 39.
- [32] Li, S. Y., Ma, W., Zhou, Y., Chen, X., Ma, M., Xu, Y., ... & Wu, X. (2013). 3-aminopropyltriethoxysilanes modified porous silicon as a voltammetric sensor for determination of silver ion. *Int. J. Electrochem. Sci*, *8*, 1802-1812.

- [33] Zhang, F., Sautter, K., Larsen, A. M., Findley, D. A., Davis, R. C., Samha, H., & Linford, M. R. (2010). Chemical vapor deposition of three aminosilanes on silicon dioxide: surface characterization, stability, effects of silane concentration, and cyanine dye adsorption. *Langmuir*, *26*(18), 14648-14654.
- [34] Lecoq, E., Duday, D., Bulou, S., Frache, G., Hilt, F., Maurau, R., & Choquet, P. (2013). Plasma polymerization of APTES to elaborate nitrogen containing organosilicon thin films: influence of process parameters and discussion about the growing mechanisms. *Plasma Processes and Polymers*, *10*(3), 250-261.
- [35] Landoulsi, J., Genet, M. J., El Kirat, K., Richard, C., Pulvin, S., & Rouxhet, P. G. (2011). Silanization with APTES for controlling the interactions between stainless steel and biocomponents: reality vs expectation. In *Biomaterials-Physics and Chemistry*. InTech.
- [36] Haddada, M. B., Blanchard, J., Casale, S., Krafft, J. M., Vallée, A., Méthivier, C., & Boujday, S. (2013). Optimizing the immobilization of gold nanoparticles on functionalized silicon surfaces: amine-vs thiol-terminated silane. *Gold Bulletin*, *46*(4), 335-341.
- [37] Paredes, V., Salvagni, E., Rodríguez-Castellon, E., Gil, F. J., & Manero, J. M. (2015). Study on the use of 3-aminopropyltriethoxysilane and 3-chloropropyltriethoxysilane to surface biochemical modification of a novel low elastic modulus Ti–Nb–Hf alloy. *Journal of Biomedical Materials Research Part B: Applied Biomaterials*, *103*(3), 495-502.
- [38] Williams, E. H., Davydov, A. V., Motayed, A., Sundaresan, S. G., Bocchini, P., Richter, L. J., ... & Rao, M. V. (2012). Immobilization of streptavidin on 4H–SiC for biosensor development. *Applied surface science*, *258*(16), 6056-6063.
- [39] Kyaw, H. H., Al-Harhi, S. H., Sellai, A., & Dutta, J. (2015). Self-organization of gold nanoparticles on silanated surfaces. *Beilstein journal of nanotechnology*, *6*, 2345.
- [40] Gholamrezaie, F., Andringa, A. M., Roelofs, W. S., Neuhold, A., Kemerink, M., Blom, P. W., & de Leeuw, D. M. (2012). Charge Trapping by Self-Assembled Monolayers as the Origin of the Threshold Voltage Shift in Organic Field-Effect Transistors. *Small*, *8*(2), 241-245.
- [41] Yu, J., Yu, X., Zhang, L., & Zeng, H. (2012). Ammonia gas sensor based on pentacene organic field-effect transistor. *Sensors and Actuators B: Chemical*, *173*, 133-138.

- [42] Chuan-ling Wu & Hsiao-Wen Zan (2008). *Functional Group Modification on Dielectric Interface of Pentacene-Based OTFTs for Ammonia Sensor* (Doctoral thesis), Institute of Electro-Optical Engineering, National Chiao Tung University.
- [43] Honda, T., Miyazaki, M., Nakamura, H., & Maeda, H. (2005). Controllable polymerization of N-carboxy anhydrides in a microreaction system. *Lab on a Chip*, 5(8), 812-818.
- [44] Lee, J. N., Park, C., & Whitesides, G. M. (2003). Solvent compatibility of poly (dimethylsiloxane)-based microfluidic devices. *Analytical chemistry*, 75(23), 6544-6554.
- [45] Rumens, C. V., Ziai, M. A., Belsey, K. E., Batchelor, J. C., & Holder, S. J. (2015). Swelling of PDMS networks in solvent vapours; applications for passive RFID wireless sensors. *Journal of Materials Chemistry C*, 3(39), 10091-10098.
- [46] Obaidulla, S. M., Singh, S., Mohapatra, Y. N., & Giri, P. K. (2017). Ambient condition bias stress stability of vanadium (IV) oxide phthalocyanine based p-channel organic field-effect transistors. *Journal of Physics D: Applied Physics*, 51(1), 015110.
- [47] Lee, B., Wan, A., Mastrogiovanni, D., Anthony, J. E., Garfunkel, E., & Podzorov, V. (2010). Origin of the bias stress instability in single-crystal organic field-effect transistors. *Physical Review B*, 82(8), 085302.
- [48] McIlvaine, T. C. (1921). A buffer solution for colorimetric comparison. *Journal of Biological Chemistry*, 49(1), 183-186.
- [49] Spanu, A., Lai, S., Cosseddu, P., Tedesco, M., Martinoia, S., & Bonfiglio, A. (2015). An organic transistor-based system for reference-less electrophysiological monitoring of excitable cells. *Scientific reports*, 5.
- [50] Lee, B., Wan, A., Mastrogiovanni, D., Anthony, J. E., Garfunkel, E., & Podzorov, V. (2010). Origin of the bias stress instability in single-crystal organic field-effect transistors. *Physical Review B*, 82(8), 085302.

# Chapter 5

## Protein Detection Using the CM-OFET Device

In the previous chapter the CM-OFET was configured for pH monitoring, where changes in pH were detected by the corresponding change in charge of a molecular monolayer immobilised on the surface of the CM-OFET sensing region. In this chapter, the charge sensing capability of the device is explored to detect biomolecular interactions occurring at the sensing surface of the device. The ability to detect and quantify specific biomarkers is central to next generation clinical diagnostics. The label-free CM-OFET biosensor presented in this chapter has the potential to address this challenge. The biosensor is investigated here for monitoring one of the strongest non-covalent interactions, the binding of biotin to avidin. The combination of this biologically active protein (avidin) and the small biomolecule biotin is widely used as a model for biorecognition studies.

In the chapter, firstly a brief overview on both biotin and avidin and their interactions is given. Then a study of quartz crystal microbalance with dissipation (QCM-D) that were used to assess a protocol for biotinylation of the sensing surface and confirm the immobilisation of avidin is presented. Finally, the use of CM-OFET device for label-free detection avidin is discussed.

### 5.1 Biotin, Avidin and their interaction

#### 5.1.1 Biotin

Biotin (chemical structure shown in figure 5.1), sometimes called vitamin B7, vitamin H, and also known as coenzyme R as it a co-factor for five biotin-dependent carboxylase enzymes [1-2] is a water-soluble vitamin necessary for metabolising carbohydrates. Despite its importance to human health, this vitamin is not naturally produced by the human body but rather is extracted from food or synthesized by bacteria found in the human intestine [2-3].

The ability to detect and quantify biotin in clinical samples is itself of interest because of its importance as an indicator for some health problems. For example, it has been reported that cancerous tumours contain higher biotin concentration than non-cancerous tissues [4]. Biotin deficiency has also been linked to metabolic disruptions that could lead to more serious health problems. For example, biotin deficiency during pregnancy could lead to neonatal complications for new born babies [5-6]. However, because the human body requires only small quantities of biotin, and many consumed foods are relatively rich in biotin, biotin deficiency for individuals who consume a regular diet is rare [7].

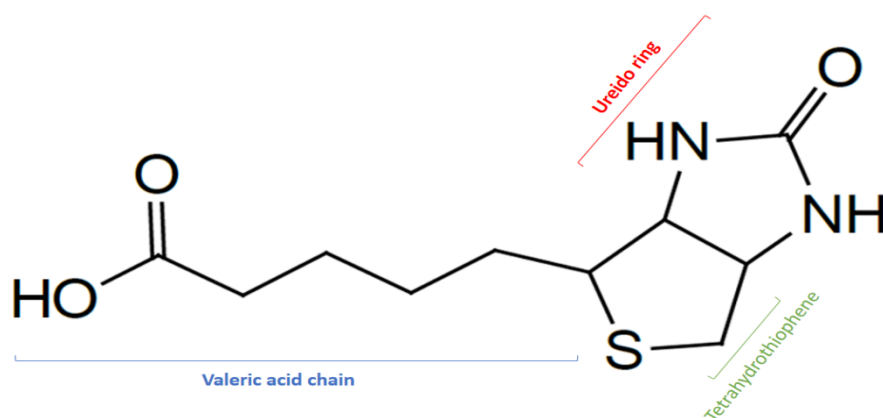


**Figure 5.1:** Chemical structure of biotin molecule.

Biotin has another interesting characteristic that is used widely in biosensors, both commercially and in research. Specifically, the wide use of biotin in biosensing applications stems from the fact that biotin is relatively a small molecule with a carboxyl group that can be derivatized to conjugate with many biomolecules including antibodies and enzymes, or with a range of surfaces. This conjugation reaction does not significantly affect the biomolecule functionality (conformation, size or biological activity) [8-9]. This merit is very useful in the field of biosensor/biology research. Here the ability to conjugate biotin to surfaces was exploited to biotinylate the surface of the sensing region and thus render it specific for avidin.

### 5.1.2 Avidin

Avidin (tertiary structure shown in figure 5.2) is a highly stable tetrameric glycoprotein, isolated from egg white. Not only is avidin soluble in aqueous solutions, it is also stable over a wide range of pH and temperature. Structurally, avidin is a homotetramer formed from

four, identical subunits (each 128 amino acids long) with twofold symmetry, and molecular dimension of 6 x 5.5 x 4 nm [1,9-11].

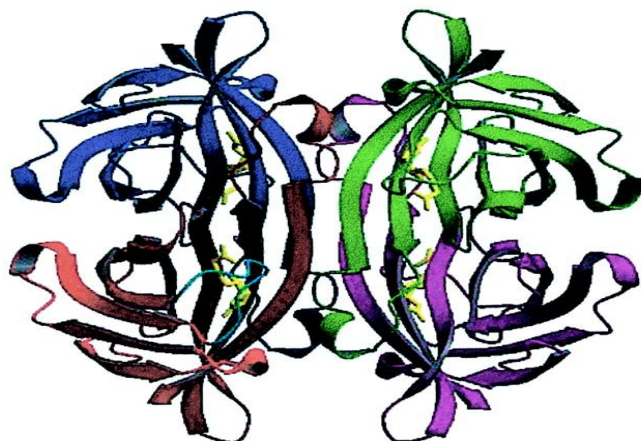


**Figure 5.2:** A ribbon representation of the avidin tetrameric arrangement [12].

The scientific and commercial value of avidin comes from its ability to bind biotin and biotinylated molecules with extremely high affinity (the binding affinity constant of avidin to biotin around  $10^{15} \text{ M}^{-1}$  [1,10,13]). This has been exploited in a great number of biotechnological applications including protein and nucleic acid detection and purification [14]. Each of the four identical subunits have a biotin binding site (two on each side of the two 6 x 5.5 faces) [1,10] enabling avidin to bind up to four biotin or biotinylated molecules. Because of the carbohydrate chains present in its structure, avidin exhibits basic nature with a high isoelectric point ( $pI = 10-10.5$ ) [10,15]. This feature of avidin can be exploited to enable non-specific, electrostatic binding to negatively charged surfaces and nanoparticles. The charge of avidin at pH below its  $pI$  point was exploited here as the detection mechanism using the CM-OFET device as will be explained in section 5.3.2.

### **5.1.3 Biotin-Avidin interactions for surface functionalization**

Immobilization of the biotin-avidin complex to the surface of a biosensor device can be achieved either by physical adsorption of avidin to the transducer surface followed by binding of biotin or biotinylated biomolecule to the available binding sites on the opposite face of the immobilized avidin. Alternatively, the carboxylic moiety on biotin allows it to be chemisorbed to the surface and utilized as a primary tether to which avidin can

subsequently bind. As avidin contains four biotin binding sites, the surface immobilised avidin can be used as a bridge for further binding other biotinylated biomolecules using the remaining binding site on the opposite facet. A schematic diagram of the two strategies can be seen in figure 5.3.

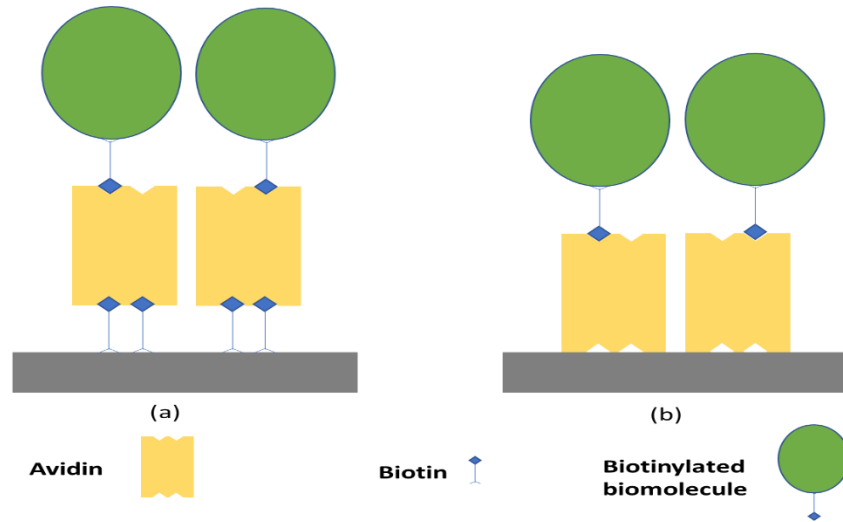


**Figure 5.3:** Schematic representation of the two methods utilizing biotin-avidin conjugation to bind targeted biomolecules to sensor surface. In a) the surface is first chemically modified for conjugation to biotin. In contrast, the approach shown schematically in b) employs physisorption of avidin to the solid support.

A common approach to obtain a biotinylated surface is to deposit biotin to a pre-silanized surface. This method was adopted here. Silanization of the Si surface of the sensing region of the CM-OFET floating gate was demonstrated in chapter 2 (section 2.6.1.5) and was utilized as a charge sensing surface as explained in chapter 4. Here, the very same surface is exploited to biotinylate the sensing region.

### 5.1.3.1 Biotin-Avidin stacking on Si

The layer by layer stacking shown in figure 5.4 starts with a Si floating surface silanized using APTES SAM as described in chapter 2 (section 2.6.1.5). To biotinylate the amine derivatised surface, a synthetic derivative of biotin functionalized with N-hydroxysulfosuccinimide (NHS) was used. Specifically, biotin modified with the sulfonated version of NHS (Sulfo-NHS, NHS esters with a sulfonate ( $-\text{SO}_3$ ) group on the N-hydroxysuccinimide ring) was used, in which the charged sulfonate group increases water-

solubility. The N-hydroxysuccinimide (NHS) ester of this modified biotin can be attacked by nucleophiles [16-18], in our case it is the amine group ( $\text{NH}_2$ ) of APTES, leading to the formation of a covalent chemical bond.

The amine group has to be deprotonated ( $\text{NH}_2$ ) to attack the NHS ester. The reaction between the APTES functionalized surface and the Sulfo-NHS-Biotin was thus performed in sodium phosphate buffer solution at pH 8 at which the amine groups will be deprotonated. Avidin was also deposited onto the biotinylated surface using the same buffer. In this step, the ureido ring of biotin molecule which should be pointing away from the surface will be buried in one of the avidin pockets forming multiple hydrophobic interactions and hydrogen bonds inside the pocket, these bonds are responsible for the extremely high affinity between the two molecules [1,10,15,17].

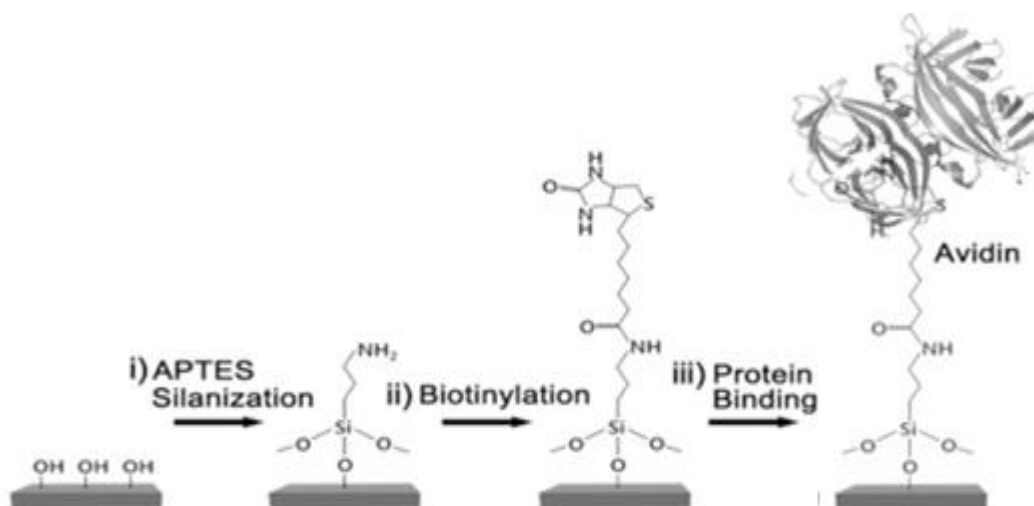
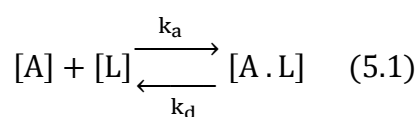


**Figure 5.4:** Si surface functionalization, biotinylation and Avidin binding process, from left to right, a hydroxylated Si surface was first silanized with APTES, then biotinylated and finally avidin binds to the biotinylated surface [19].

Binding affinity is a characterization term used to describe the stability of binding between two biomolecules with mutual affinity (biomolecule partners) generally referred to as receptor and ligand (but can also be referred to as ligand and analyte as in SPR presented in section 1.1.1.2.1). It is a measure of the strength of noncovalent intermolecular forces interactions at specific binding sites in the ligand and its analyte. For example, in antibody-antigen interactions, binding affinity is the strength with which an epitope (specific segment on the antigen) binds to a paratope (specific segment on the antibody) or antigen-

binding site on the antibody. This means, the greater intermolecular force between an analyte and its ligand the higher the binding affinity and vice versa [20-22].

In reality, the binding process between a ligand and an analyte involves a combination of noncovalent interactions such as hydrogen bonds, hydrophobic interactions, electrostatic and van der Waals forces between the binding sites on both the ligand and the analyte. This interaction is dynamic, which means that the relationship between the concentration of free analyte, ligand and the analyte-ligand complex exists in a dynamic equilibrium govern by basic reversible biomolecular interaction expressed as:



Where  $k_a$  (also referred to as  $k_{on}$  or  $k_1$ ) and  $k_d$  (also referred to as  $k_{off}$  or  $k_2$ ) are the rate constants for the association and dissociation reaction, respectively and  $[A]$ ,  $[L]$ , and  $[A \cdot L]$  are the concentrations of free analytes, free ligands, and analyte–ligand complexes at equilibrium, respectively.

The concentration of analyte-ligand complex at equilibrium can be calculated by the so-called association constant,  $K_A$ , or its reciprocal, the dissociation constant,  $K_D$ , by:

$$K_A = \frac{k_{on}}{k_{off}} = \frac{[A \cdot L]}{[A][L]} = \frac{1}{K_D} \quad (5.2)$$

The association constant,  $K_A$ , (with units of  $M^{-1}$ ) and its reciprocal, the dissociation constant,  $K_D$ , (units  $M$ ) are used widely to quantify the strength of a ligand receptor affinity interaction. The higher the magnitude of  $K_A$  (or conversely, the lower the value of  $K_D$ ), the higher the affinity of ligand-analyte.

In practical terms, as was introduced in section (1.1.1.2.1),  $K_D$  is defined as the concentration of analyte that leads to 50% occupancy of the ligand's binding site or in other words, the concentration of analyte at which the concentration of analyte-ligand complex equals the concentration of ligand with no analyte bound. This means that a system with low  $K_D$  requires a lower analyte concentration to achieve 50% occupancy.

On the noncovalent binding affinity scale, the biotin–avidin complex investigated in this chapter comes at the higher end with very strong affinity (around  $10^{15} M^{-1}$ ) comparable to

the strength of weak covalent bonds. Typical antibody-antigen interactions have a binding affinity in the range of  $10^7$  to  $10^{11} \text{ M}^{-1}$  [23-24].

### 5.1.3.2 Biotin-Avidin immobilizing protocol on Si

Once the sensing region of the Si floating gate of the CM-OFET device is silanized, biotinylation was performed inside the PDMS chamber of the CM-OFET device. 1 mg of Sulfo-NHS biotin was dissolved in 0.1 M sodium phosphate buffer solution (SPB) at pH8 and was injected over the pre-silanized Si surface through the PDMS fluidic channel. After 25 minutes, the biotinylated Si surface was washed with a stream of the SPB (pH8) for several minutes to remove excess unreacted biotin. The biotinylated Si surface was then exposed to 0.1 mg of avidin in 0.1 M sodium phosphate buffer solution SPB (pH8) through the PDMS chamber and left to incubate on the biotinylated Si surface for 25 minutes. Finally, excess avidin was washed from the surface with SPB (pH8).

The SPB concentration (0.1 M) was selected to ensure that the molecular stack of APTES + Biotin + Avidin is shorter than the Debye length,  $\lambda_D$ , and the molecular charges on the avidin surface are thus not fully screened by free ions in the buffer solution. The Debye length was calculated using equation 5.3 [25].

$$\lambda_D = \sqrt{\frac{\epsilon_r \epsilon_0 kT}{2N_A q^2 I}} \quad (5.3)$$

Where  $\epsilon_0$  is the electrical permittivity of the vacuum,  $\epsilon_r$  is the relative dielectric constant of the solution,  $k$  the Boltzmann constant,  $T$  the absolute temperature,  $N_A$  is Avogadro's number,  $q$  the elementary charge and  $I$  the ionic strength of the solution.

At room temperature, this can be reduced to

$$\lambda_D = 1.085 \times 10^{-9} \sqrt{\frac{\epsilon_r}{I}}$$

$$\lambda_D = 1.085 \sqrt{\frac{\epsilon_r}{I}} \text{ nm}$$

The relative dielectric constant for SPB was  $\epsilon_r \approx 80$  [26] while  $I$  was calculated using equation 5.4:

$$I = \frac{1}{2} \sum_{i=1}^n c_i z_i^2 \quad (5.4)$$

Where  $c_i$  is the molar concentration of ion  $i$  (M, mol/L) and  $z_i$  is the charge number of that ion.

The Debye length for the 0.1 M SPB pH buffer was calculated to be  $\lambda_D \approx 10.8\text{nm}$  which is larger than the APTES + Biotin + Avidin stacking (approximately 6-8nm).

## 5.2 Quartz Crystal Microbalance with Dissipation Monitoring (QCM-D)

In order to confirm and quantify the effectiveness of the surface biotinylation and avidin binding protocol, it was initially tested using a quartz crystal microbalance with dissipation monitoring (QCM-D). Commercial QCM-D systems were developed in the 1990's by Q-Sense AB (Göteborg, Sweden) and it is a special variant of the conventional mechanical QCM sensing technique [27] which has been used for decades to measure film thicknesses in thin film deposition systems.

The quartz crystal microbalance is an extremely sensitive mass sensor that exploits the piezoelectric properties of a quartz crystal. A conventional QCM sensor, shown schematically in figure 5.5, comprises an AT-cut quartz crystal sandwiched between two electrodes, normally gold.

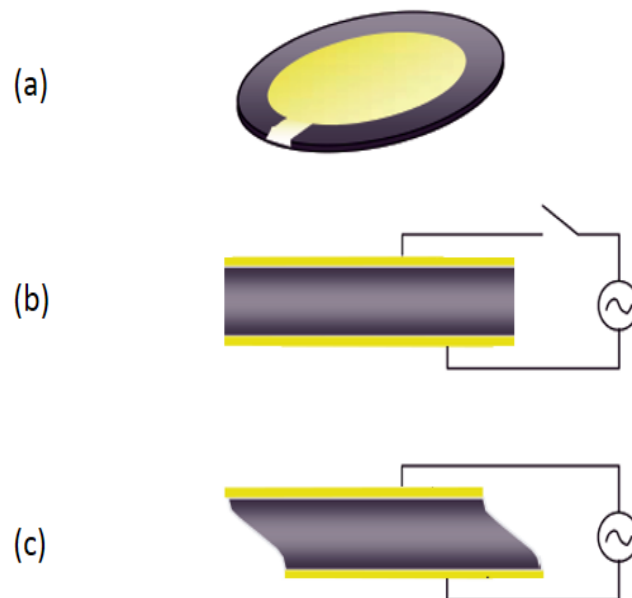


**Figure 5.5:** Schematic diagram of (a) QCM quartz crystal sensor with drive electrodes, (b) initial geometry of the crystal before applying the AC drive voltage and (c) oscillation of the crystal upon applying AC voltage.

Because of its piezoelectric nature, when an AC voltage is applied between the two electrodes on the opposite sides of the quartz crystal, the crystal lattice experiences alternating expansion and contraction. When the applied AC voltage alternates with a frequency near the resonant frequency of the crystal, the crystal can be seen to resonate at its fundamental frequency [28-29]. This occurs when the wavelength of the standing wave produced by the alternating expansion and contraction is twice the thickness of the crystal. At resonance, the nodes and anti-nodes of the standing wave occur at the opposite sides of the crystal, which means the odd harmonics (overtones) of the fundamental frequency can also be excited, as shown in figure 5.6.

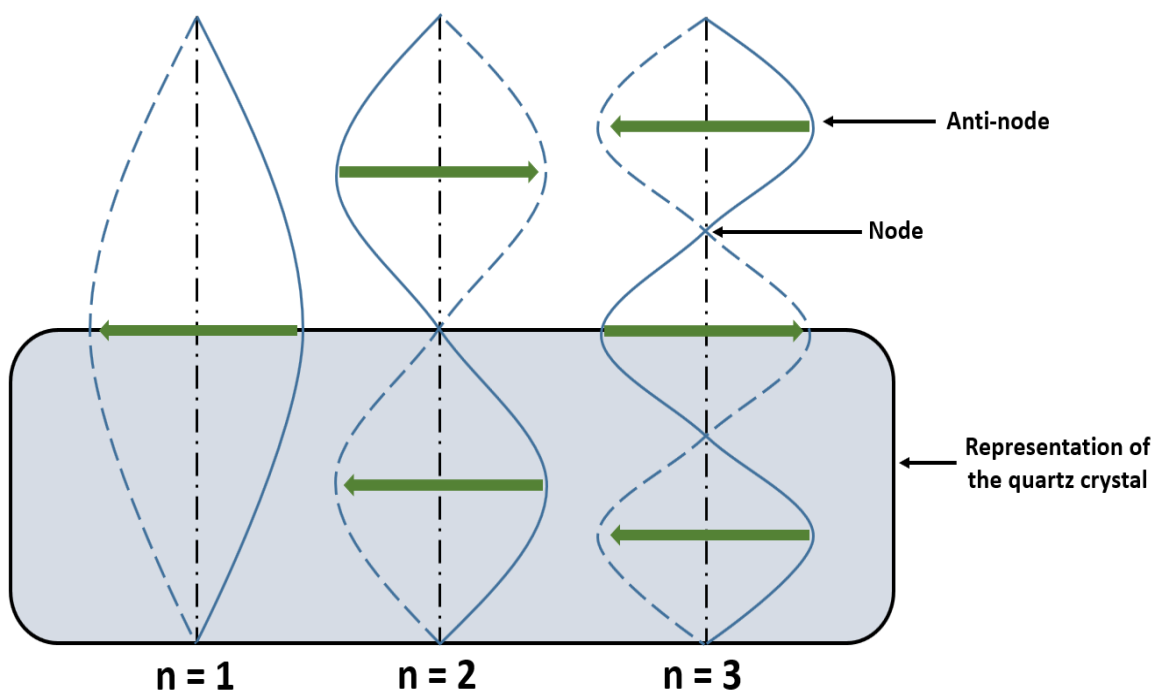


**Figure 5.6:** Representation of the fundamental resonant frequency ( $n=1$ ) and the first two harmonics ( $n=2$  and  $3$ ) produced by crystal oscillation [30].

When mass is adsorbed to the surface of the quartz crystal, the resonant frequency of the crystal shifts proportional to the newly added mass. In 1959, Sauerbrey [31] studied and analysed the physics of the QCM and determined the mass sensitivity of the sensor to be:

$$\Delta m = -\frac{C\Delta f}{n} \quad (5.5)$$

Where  $\Delta f$  is the change in resonant frequency,  $\Delta m$  is the mass of the newly adsorbed layer,  $n$  is the harmonic number and  $C$  is the mass sensitivity constant. This relationship became known after his name and commonly referred to as the Sauerbrey equation.

QCM became popular after Sauerbrey's findings and began to be used in many applications. Early applications of QCM were limited to applications in dry environments, notably for the measurement of film thickness in thin film deposition systems [27]. However, in 1982 Nomura and Okahura [32] demonstrated the use of QCM in liquid environments and later, in 1985, Kanazawa and Gordon studied the influence of the solution phase on the oscillation frequency and modified the Sauerbrey equation to account for the liquid environment, opening up the possibility of QCM as a tool for investigating biological systems [33]. The use of QCM for biological studies posed a challenge to the Sauerbrey model. This is because, the linear relationship between added mass and shift in resonant frequency predicted by Sauerbrey equation assumes the adsorbed film to be relatively thin, rigid and evenly distributed over the crystal active area to be valid. These three conditions mean that the adlayer is considered to be fully coupled with the oscillatory motion of the crystal (i.e. treated as an extension of the underlying quartz). This is however not necessarily true when soft or viscoelastic layers are adsorbed onto the quartz crystal. Such viscoelastic layers deform in the shear direction of the crystal oscillation due to their viscoelastic character introducing frictional dissipative losses that rapidly damp the oscillation of the crystal [27-29,34]. In these films, the Sauerbrey relationship underestimates the adsorbed mass and hence, a new and more complex model is needed to fully quantify the new adlayer beyond the simple Sauerbrey regime [28,35].

Structural flexibility or viscoelasticity can be hidden when simple single parameter QCM measurement (frequency shift  $\Delta f$ ) of QCM is used. Investigating the energy loss (dissipation) in the system alongside frequency shift can reveal more information about these mechanical characteristics. Dissipation, usually described by the dissipation factor ( $D$ ), is described by equation 5.6.

$$D = \frac{1}{Q} = \frac{1}{2\pi} \frac{E_{dissipated}}{E_{stored}} \quad (5.6)$$

Here,  $Q$  is the quality factor of the resonator while  $E_{dissipated}$  and  $E_{stored}$  are the energy dissipated and stored during one period of oscillation, respectively.

In QCM-D, dissipation is measured by exciting the crystal with a voltage pulse i.e. periodically switching on and off the driving voltage. The time taken for the oscillation to decay is recorded during the off state and is related to the energy dissipated in the system as described in equation 5.7:

$$D = \frac{2}{\omega\tau} \quad (5.7)$$

Here  $\tau$  is the decay time and  $\omega$  is the angular frequency of the oscillation [28,34].

Dissipation in rigid and viscoelastic layers unfolds differently; the energy in viscoelastic systems dissipates faster than for rigid layers, as shown schematically in figure 5.7.

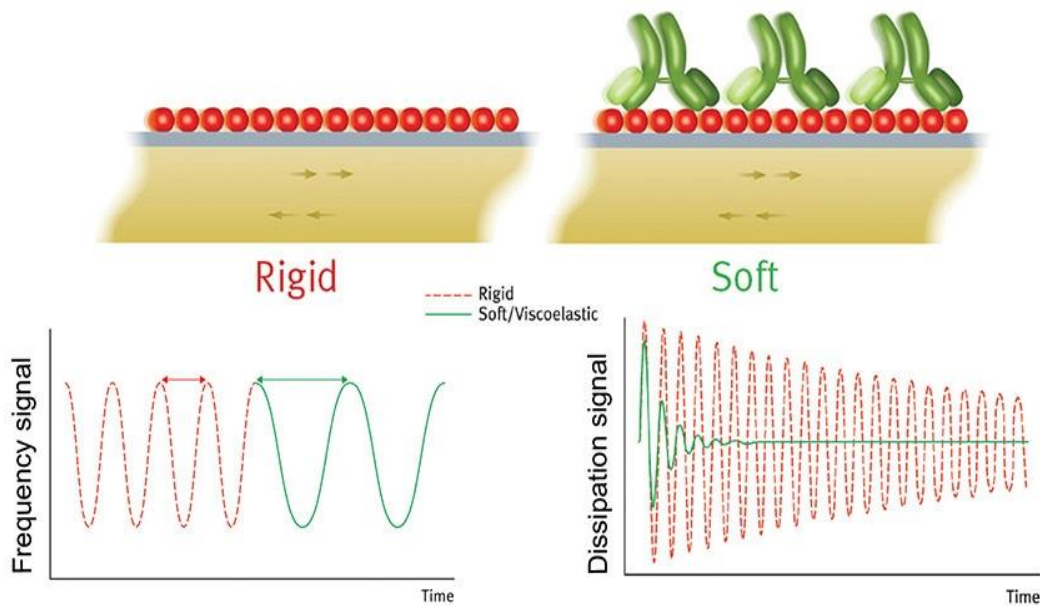


**Figure 5.7:** Illustration of the difference in frequency and dissipation response in a QCM-D system for rigid and soft films [36].

Combining information from the shift in resonant frequency,  $\Delta f$ , with energy dissipated,  $D$ , can provide a finger print of the characteristics of the adsorbed layer, and measurements of both parameters can be utilized in a comprehensive model that take into account the viscoelastic properties of the adsorbed layer. The Voigt model (sometimes called Kelvin-Voigt model) is one of the most widely used QCM-D models used to analyse viscoelastic and soft films [37-38]. In the Voight model, the viscoelastic properties of the adsorbed film including the density, viscosity, elasticity, and thickness are correlated with the measured

$\Delta f$  and  $D$ , so when they are recorded for multiple overtones these parameters can be estimated (some valid assumptions are needed as the Voigt model deal with multi-unknown parameters) [37,39].

## 5.3 Results and discussion

### 5.3.1 QCM-D results

QCM-D was used to monitor surface biotinylation and subsequent binding of avidin to the biotinylated silicon oxide surface. Measurements were performed using a Q-sense E4 instrument (Q-Sense, Biolin Scientific, Sweden) with SiO<sub>2</sub> coated quartz crystal sensors (QSX 303). The frequency and dissipation responses were recorded at the fundamental resonant frequency (5 MHz) and several overtones (harmonics),  $n = 3, 5, 7, 9, 11$  and  $13$ . For clarity, only the frequency shift,  $\Delta f$ , and the dissipation shift,  $D$ , for the 3<sup>rd</sup> overtone is presented. The measurements were conducted at 21°C maintained by a Peltier within the fluidic chamber.

Four measurements were performed simultaneously, two replicates designed to quantify the specific binding of avidin to biotinylated crystal (sensors 1 and 2) and two replicates to investigate the degree of non-specific binding of avidin to a silanized, non-biotinylation crystal (sensors 3 and 4).

#### 5.3.1.1 Experimental protocol

- Four, SiO<sub>2</sub>-coated QCM-D sensors were immersed in a 5% APTES IPA solution overnight (approximately 18 hours) to form an APTES SAM layer. The sensors were then washed in IPA and dried under nitrogen before being loaded into the four, independent QCM-D flow chambers.
- After loading the sensors into the QCM-D system, sodium phosphate buffer (SPB at pH8) was first pumped over both crystal resonators at 20  $\mu\text{l}/\text{min}$  and left running until the frequency and dissipation response curves were stable ( $\Delta f < \pm 0.5$  Hz).
- After a stable baseline was obtained, sensors 1 and 2 were biotinylated by exposure to Sulfo-NHS Biotin (1 mg/mL in SPB, pH8 at 20  $\mu\text{l}/\text{min}$ ) for 48 mins. Simultaneously, sensors 3 and 4 (control measurement) were left with SPB (pH8) running through the system.

- Sensors 1 and 2 were then rinsed with SPB (pH8) to remove unreacted Sulfo-NHS Biotin and left for approximately 20 minutes until a stable baseline was achieved. During this time the flow of SPB (pH8), was maintained over sensors 3 and 4.
- Following system equilibration, 0.1 mg/mL of avidin protein in SPB (pH8) was injected over all sensors and left to flow for 48 mins to couple to the biotinylated surface of sensors 1 and 2 and to the silanized silica surface of sensors 3 and 4.
- SPB (pH8) was finally injected over all sensor surfaces for 60 mins to remove excess avidin.

**Table 5.1:** Summary of QCM-D experiment stages

Sensor	Preparation	Stage 1	Stage 2	Stage 3	Stage 4	Stage 5
1,2	Silanization overnight	SPB to establish stable baseline	Sulfo-NHS biotin introduced	SPB to wash away unreacted biotin	Avidin solution introduced	SPB to wash away unreacted avidin
3,4	Silanization overnight	SPB to establish stable baseline	SPB	SPB	Avidin solution introduced	SPB to wash away unreacted avidin
Approx. time	18 hrs	10 min	48 min	20 min	48 min	1 hrs

Note: The 48 minutes chosen for stage 2 and 4, was the time to draw 96% of a 1 ml solution of Sulfo-NHS biotin and avidin at 20  $\mu$ l/min; this is to ensure no air bubbles are introduced to the system if the 1 ml is completely drawn and the vial is emptied.

### 5.3.1.2 QCM-D measurement

The stages of the QCM-D measurement will first be explained for one measurement of the biotinylated surface and one non-biotinylated surface. The results of the four sensors will be presented at the end of the section.

Raw QCM-D data following surface APTES functionalized of the crystals surface of sensor 1 is shown in Figure 5.8.

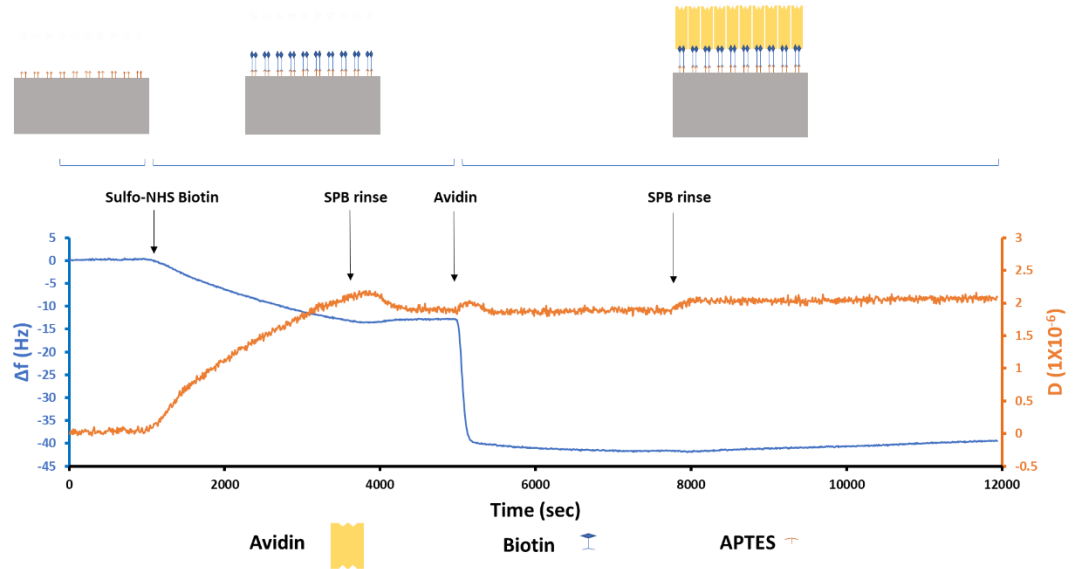


**Figure 5.8:** QCM-D  $\Delta f$  and  $D$  vs time response for the 3<sup>rd</sup> overtone to the layer by layer adsorption on the  $\text{SiO}_2$  coated crystal for sensor 1.

The introduction of Sulfo-NHS-Biotin (stage 2 at around 1,000 s) resulted in a decrease in resonant frequency and an increase in dissipation indicating the start of the biotinylation of the crystal surface. After 48 minutes and subsequent exposure to SPB solution to remove excess Sulfo-NHS-Biotin, new baselines were achieved and the change in dissipation was  $D \approx 2.1 \times 10^{-6}$  while the frequency shift was around -12 Hz. Introduction of the avidin solution at the beginning of stage 4 (around 5,000 s) resulted in a sharp frequency change ( $\Delta f \approx -30$  Hz) combined with a small dissipation change, associated with the binding of avidin to surface immobilized biotin. The final SPB rinse showed negligible change in frequency or dissipation.

In contrast, as shown in figure 5.9, during the first 3 stages of the experiment performed on the non-biotinylated surface (sensor 3), both the frequency and dissipation curves were largely stable as only SPB solution was flowing over the silanized crystal surface. However, when avidin solution was introduced to the system (at around 5,000s), a shift in frequency was observed accompanied by a very small change in dissipation indicating avidin absorption onto the crystal surface. By the end of the avidin injection, the frequency shift was around -7 Hz while the dissipation was  $0.2 \times 10^{-6}$ . In the final stage, flowing SPB solution

to the system resulted in a positive frequency shift by nearly 5.25 Hz indicating mass removal from the crystal surface, characteristic of the dissociation and release of weakly bound material back into solution.

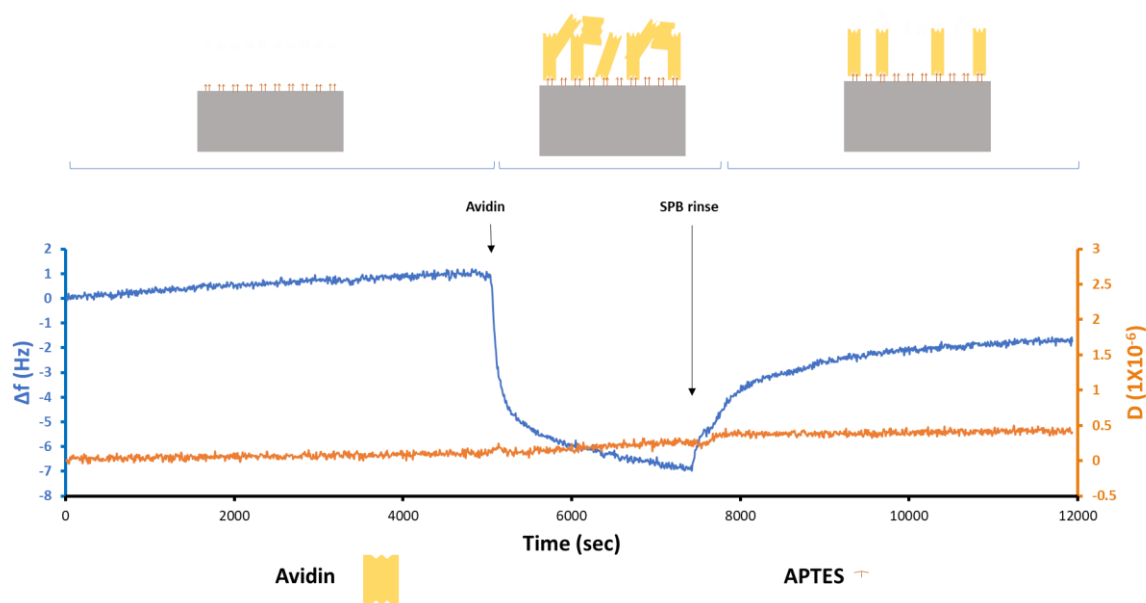


**Figure 5.9:** QCM-D  $\Delta f$  and  $D$  vs time response for the 3<sup>rd</sup> overtone to the layer by layer adsorption on the SiO<sub>2</sub> coated crystal for a non-biotinylated surface (sensor 3).

Comparing the binding of avidin to the biotinylated and non-biotinylated surfaces, for the specific binding of avidin to biotin, the frequency shift due to the avidin binding was much larger ( $\Delta f \approx -30$  Hz) than the corresponding frequency shift observed due to nonspecific binding to the silanized surface ( $\Delta f \approx -7$  Hz). This is as expected due to the less dense coverage of the crystal surface from nonspecific binding of avidin. Both sensors showed very small dissipation shift ( $\approx 0.07 \times 10^{-6}$ ) indicating rigid coupling to the crystal surface. The final washing stage after avidin deposition also confirmed that avidin was bound to the surface of sensor 1 with high affinity, as flowing SPB solution did not alter the frequency of the system indicating that avidin remains tightly bound to the biotinylated surface. In contrast, flowing SPB on sensor 3 resulted in a positive frequency shift ( $\Delta f \approx 5.25$  Hz) suggesting dissociation of avidin molecules bound non-specifically from the surface. These measurements confirm the effectiveness of the avidin binding protocol.

The frequency and dissipation responses (frequency shift,  $\Delta f$ , and dissipation shift,  $D$ ) for the 4 sensors (using the 3<sup>rd</sup> overtone) are shown in figure 5.10 and 5.11, respectively.

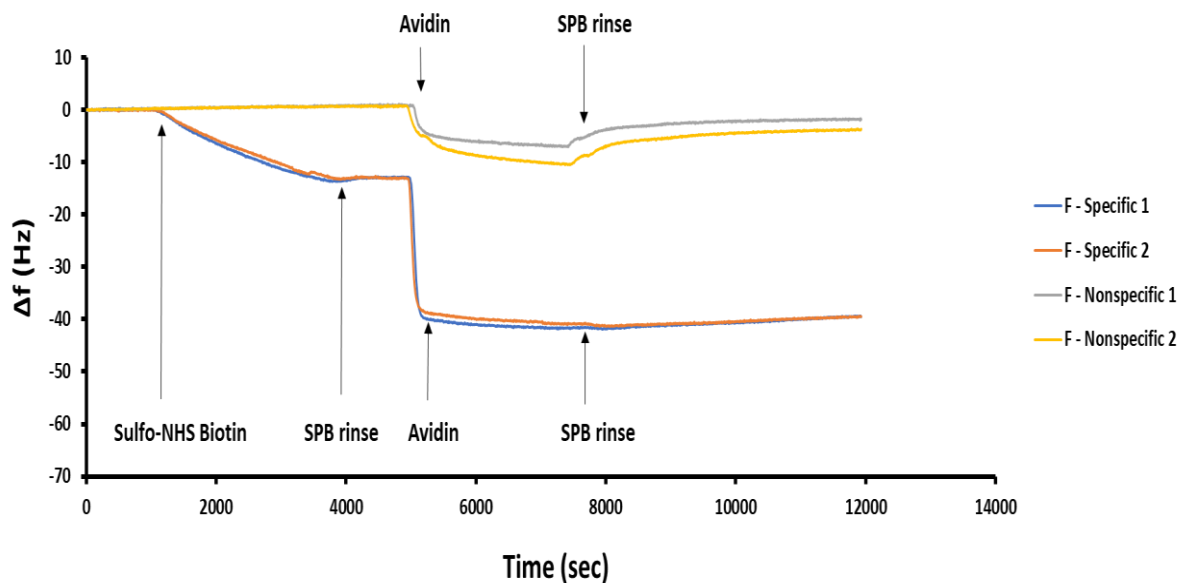


**Figure 5.10:** QCM-D  $\Delta f$  vs time response for the 3<sup>rd</sup> overtone to the layer by layer adsorption on the 4 crystal sensors.

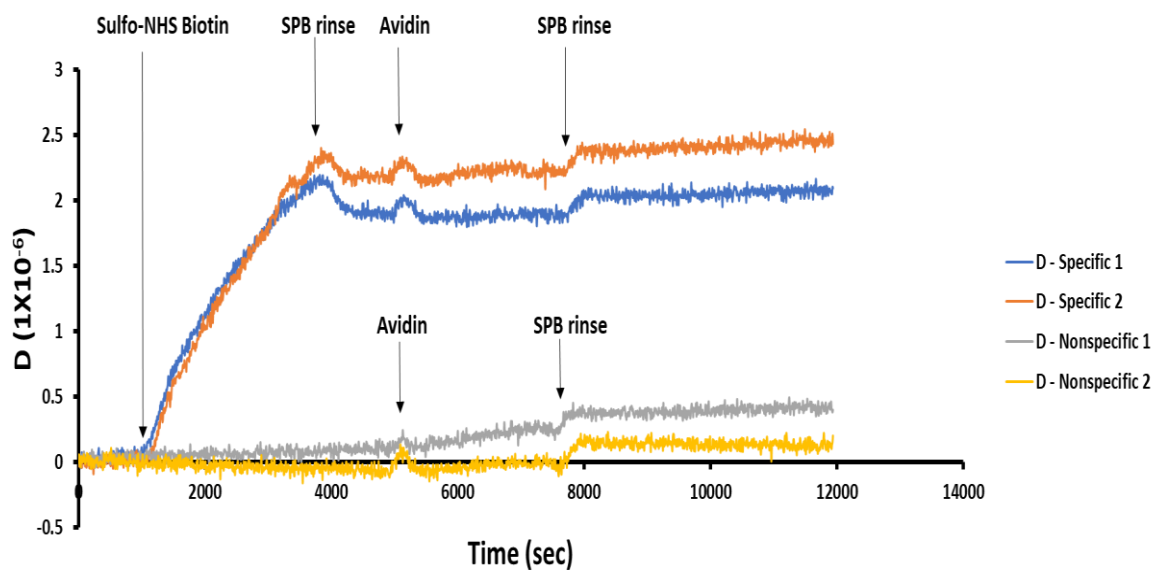


**Figure 5.11:** QCM-D  $D$  vs time response for the 3<sup>rd</sup> overtone to the layer by layer adsorption on the 4 crystal sensors

It is clear that the responses shown by the two sensors used to investigate specific and non-specific avidin binding are consistent. Table 5.2 and figure 5.12 summarize the estimated avidin mass adsorbed to each of the 4 sensors, based on the frequency shift and Sauerbrey equation (5.5) with the mass sensitivity constant  $C = 17.7 \text{ ng.cm}^{-2}.\text{Hz}^{-1}$ . It must be noted

that, as a result of the change in dissipation associated with biotinylation of the surface, the mass calculated using the Sauerbrey equation is likely to be overestimated.

**Table 5.2:** Estimated avidin mass adsorbed to each of the 4 investigated sensors.

	Specific 1 (ng.cm <sup>-2</sup> )	Specific 2 (ng.cm <sup>-2</sup> )	Nonspecific 1 (ng.cm <sup>-2</sup> )	Nonspecific 2 (ng.cm <sup>-2</sup> )
Avidin	177	173.5	41.3	52.5
Avidin after 1hr rinse	171.1	165.2	10.3	21.8

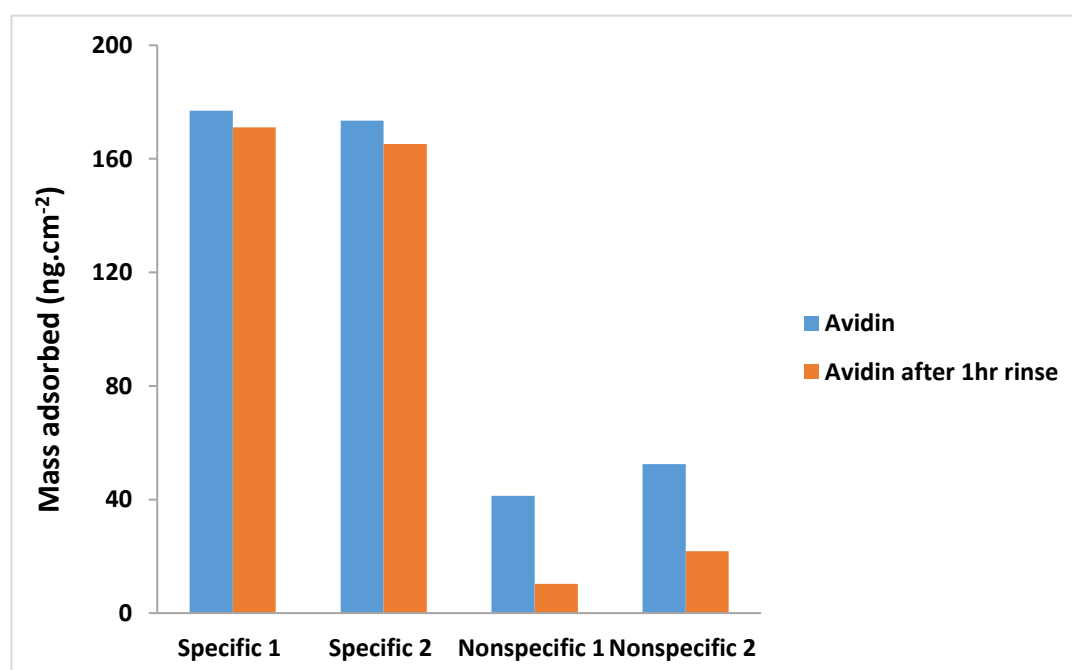


**Figure 5.12:** Estimated avidin mass adsorbed to each of the 4 investigated sensors and the effect of 1 hour rinse in SPB solution.

The average final avidin mass adsorbed to the sensor surface for specific and nonspecific binding is presented in figure 5.13.

The estimated surface coverage from the calculated mass of the specific binding measurement is  $1.6 \times 10^{12}$  avidin molecules/cm<sup>2</sup>. This value is within the same range of previously reported surface coverage of similar QCM-D study [40].

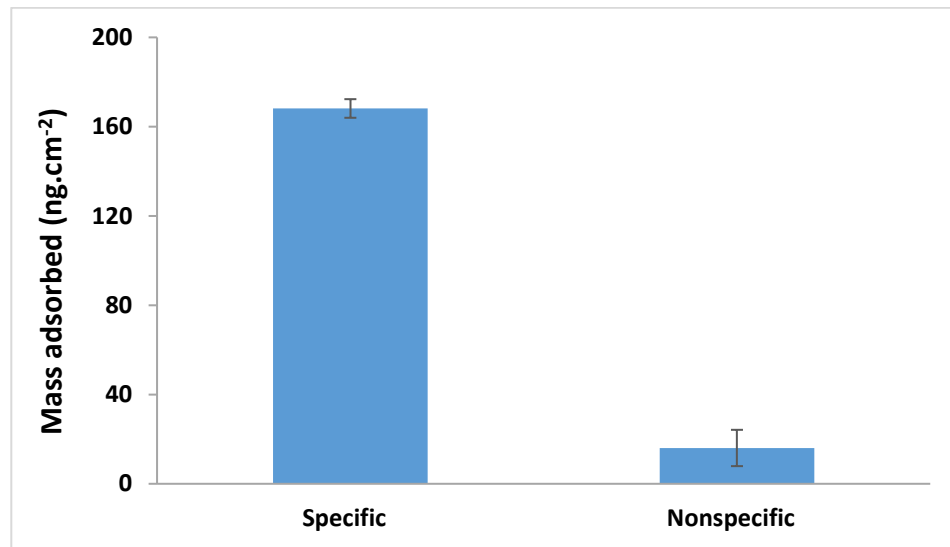


**Figure 5.13:** The average calculated final avidin mass adsorbed in the carried-out measurement for specific and nonspecific binding to the QCM-D sensors. Error bars are  $\pm$ SD.

### 5.3.2 CM-OFET results

As discussed in chapter 4 (section 4.1), a charge on the surface of the CM-OFET sensing region will attract an equivalent and opposite charge in the floating gate, leading to redistribution of charge in the remainder of the floating gate. As this gate is capacitively coupled to the OFET, this charge redistribution will be reflected in a shift in the source drain current.

Here, the charge sensitivity of the CM-OFET is explored for detecting the change in local charge which occurs upon biotinylation and subsequent binding of avidin to the sensing region. The biosensing capabilities of the CM-OFET device was tested at  $\text{pH} \approx 8$ , at which, the biotin is neutral, but following avidin binding, the surface will become positively charged, as the avidin has an isoelectric point,  $\text{pI} = 10 - 10.5$  [14,41-42]. The change from neutral to positively charge surface after avidin binding should lead to negative gate voltage shift and a reduction in the source drain current.

Similar to the investigation performed for pH sensing (chapter 4), the protein sensing capabilities of the CM-OFET was investigated by quantifying the change in source-drain current as a consequence of the redistribution of charge in the floating gate induced by the

change in sensing region surface charge. The maximum source-drain current,  $I_{SDMax}$ , was used to compare the response of the device at each phase of surface functionalization. Here,  $I_{SDMax}$  was extracted from the transfer characteristics and defined as the current measured at a gate voltage (applied through the control gate),  $V_G = -40$  V and a constant drain voltage,  $V_D = -40$  V. In addition to specific binding of avidin to biotinylated CM-OFET, non-specific adsorption of avidin to a silanized surface of the CM-OFET sensing device i.e. without prior biotinylation, was also investigated.

### 5.3.2.1 Specific binding of avidin to biotinylated CM-OFET devices

#### Measurement protocol for (SPB → NHS-Biotin → Avidin) test:

First, a CM-OFET device with a silanized sensing surface was challenged with SPB (pH8) introduced to the sensing region via the PDMS microfluidic manifold. The transfer characteristics of the device was recorded every 25 minutes until the variation in  $I_{SDMax}$  between successive measurements became less than  $\pm 8\%$ . After that, the NHS-Biotin solution (1 mg/mL in SPB pH8) was introduced to the sensing region and left to incubate for 25 minutes. Excess NHS-Biotin was rinsed from the surface using the same SPB (pH8) solution and the output/transfer characteristics were measured three times, each measurement spaced by 25 minutes. Finally, the Avidin solution (0.1 mg/mL in SPB pH8) was introduced to the sensing region and left to incubate for 25 minutes. After 25 minutes the excess Avidin (unbound avidin) was washed away from the sensing region using the same SPB (pH8) solution and the output/transfer characteristics were again measured three times spaced by 25 minutes.

#### Results

This series of measurements was repeated for nine devices and the response of each CM-OFET was then compared at the two different stages of surface functionalization (following biotinylation and after exposure to avidin, respectively). Figure 5.14 shows an example the raw data of one CM-OFET biosensor. Figures 5.15 to 5.23 show the **average** of the recorded maximum source drain current,  $I_{SDMax}$ , at the two stages of surface functionalization for the 9 different CM-OFETs. Note, in the last three samples (Devices 7,8 and 9) only one measurement was taken for biotinylation stage.

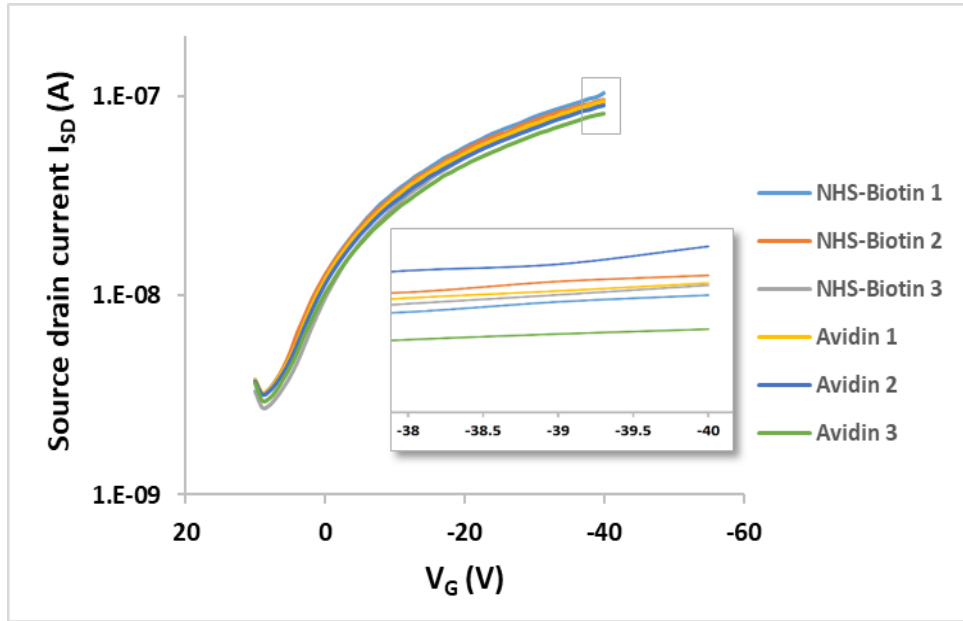


**Figure 5.14:** The raw data of the three measurements after biotinylation of the sensing region of one CM-OFET device and three measurements after avidin binding.

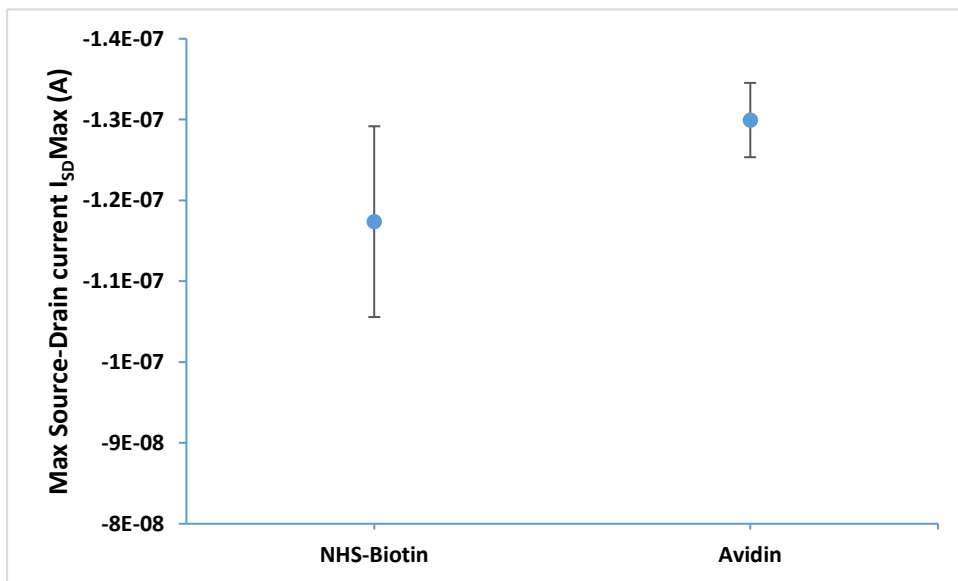


**Figure 5.15:** The average measured  $I_{SD}Max$  for CM-OFET device 1 for (a) The three measured transfer characteristics with SPB pH8 solution on the biotinylated sensing surface and (b) The three measured transfer characteristics with SPB pH8 solution on the avidin covered sensing surface. Error bars are  $\pm SD$ .

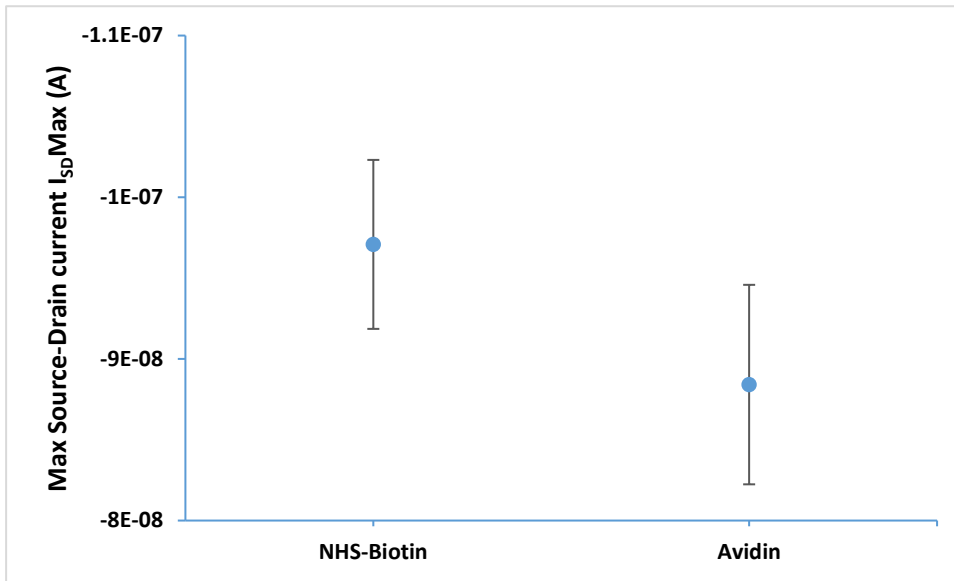


**Figure 5.16:** The average measured  $I_{SDMax}$  for CM-OFET device 2 for (a) The three measured transfer characteristics with SPB pH8 solution on the biotinylated sensing surface and (b) The three measured transfer characteristics with SPB pH8 solution on the avidin covered sensing surface. Error bars are  $\pm SD$ .

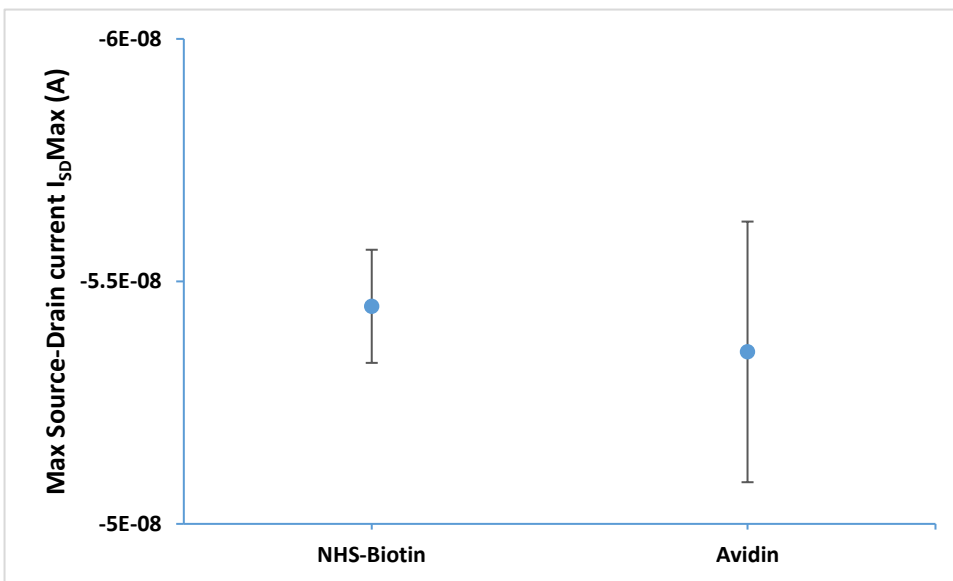


**Figure 5.17:** The average measured  $I_{SDMax}$  for CM-OFET device 3 for (a) The three measured transfer characteristics with SPB pH8 solution on the biotinylated sensing surface and (b) The three measured transfer characteristics with SPB pH8 solution on the avidin covered sensing surface. Error bars are  $\pm SD$ .

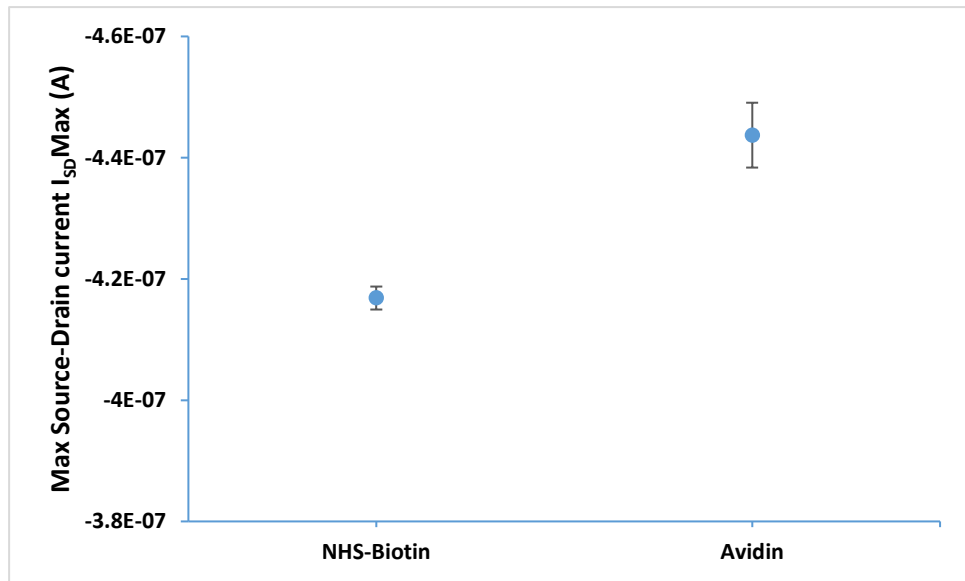


**Figure 5.18:** The average measured  $I_{SD}Max$  for CM-OFET device 4 for (a) The three measured transfer characteristics with SPB pH8 solution on the biotinylated sensing surface and (b) The three measured transfer characteristics with SPB pH8 solution on the avidin covered sensing surface. Error bars are  $\pm SD$ .

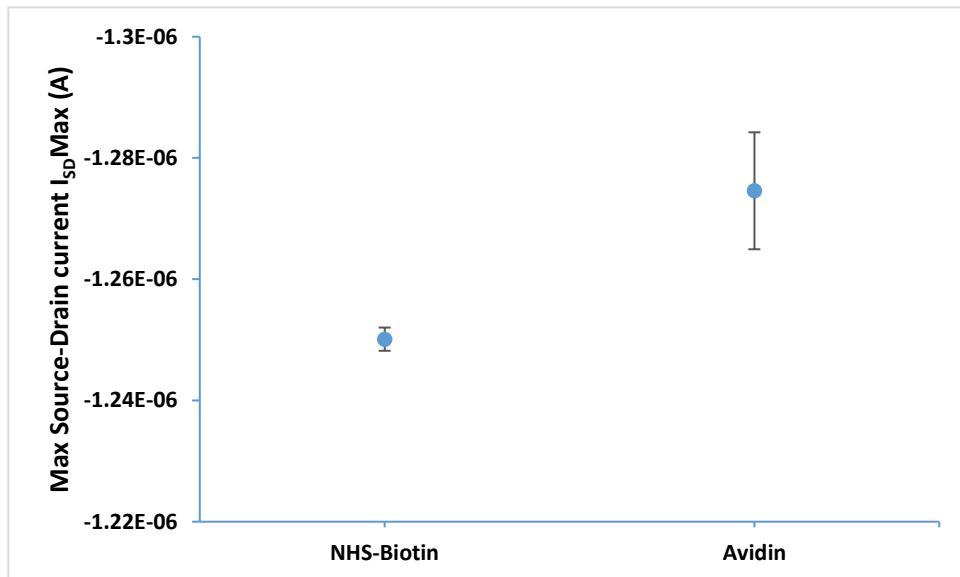


**Figure 5.19:** The average measured  $I_{SD}Max$  for CM-OFET device 5 for (a) The three measured transfer characteristics with SPB pH8 solution on the biotinylated sensing surface and (b) The three measured transfer characteristics with SPB pH8 solution on the avidin covered sensing surface. Error bars are  $\pm SD$ .

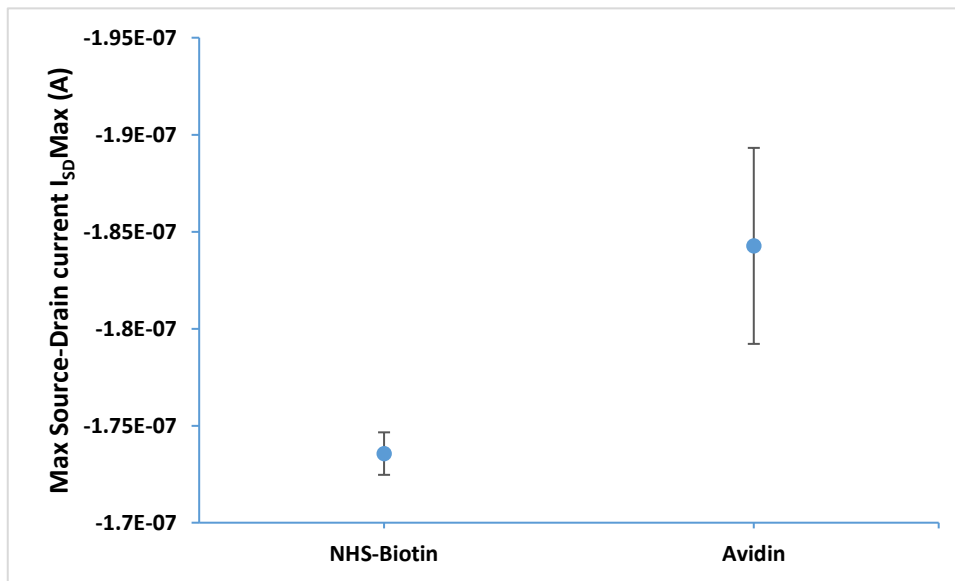


**Figure 5.20:** The average measured  $I_{SD}Max$  for CM-OFET device 6 for (a) Three measured transfer characteristics with SPB pH8 solution on the biotinylated sensing surface and (b) The three measured transfer characteristics with SPB pH8 solution on the avidin covered sensing surface. Error bars are  $\pm SD$ .

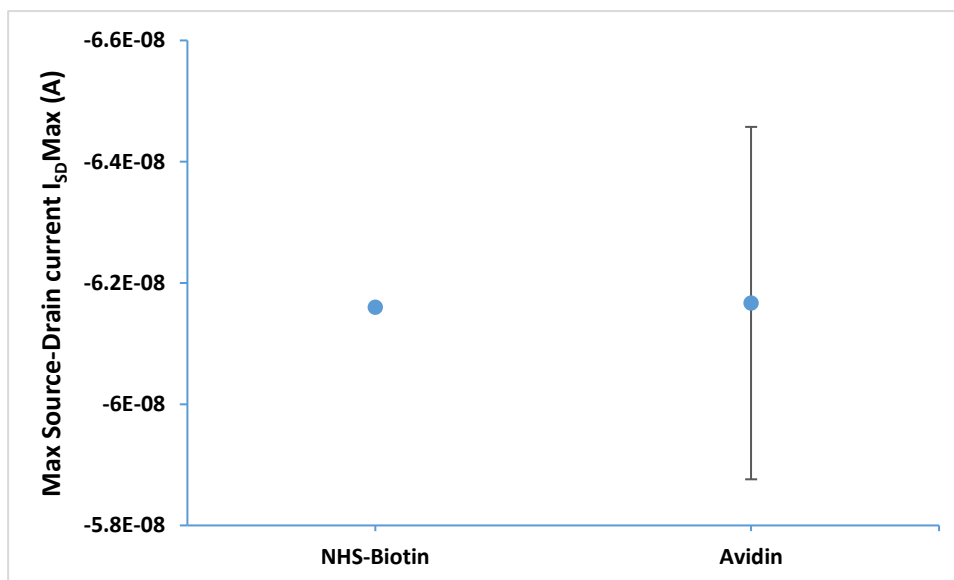


**Figure 5.21:** The average measured  $I_{SD}Max$  for CM-OFET device 7 for (a) The single measured transfer characteristics with SPB pH8 solution on the biotinylated sensing surface and (b) The three measured transfer characteristics with SPB pH8 solution on the avidin covered sensing surface. Error bars are  $\pm SD$ .

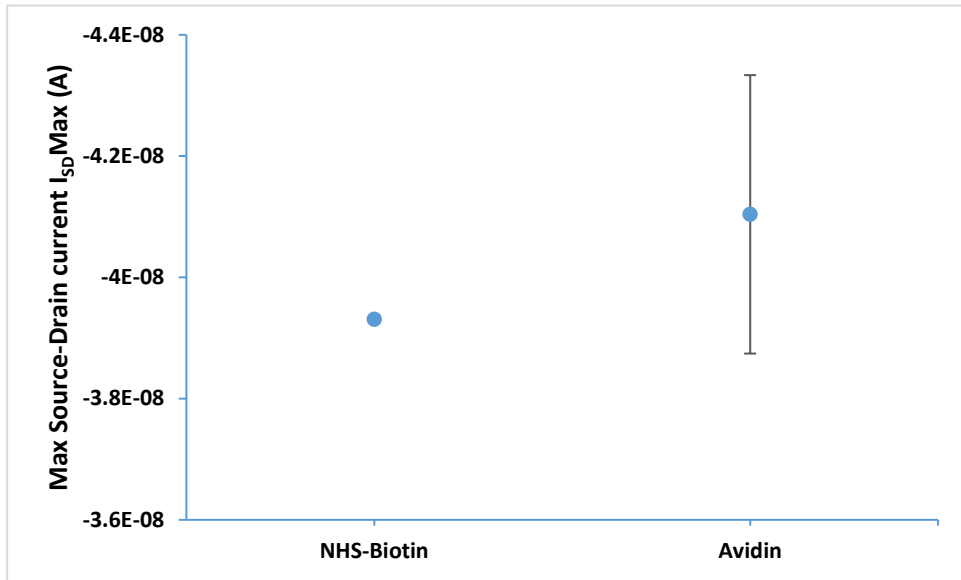


**Figure 5.22:** The average measured  $I_{SD} \text{Max}$  for CM-OFET device 8 for (a) The single measured transfer characteristics with SPB pH8 solution on the biotinylated sensing surface and (b) The three measured transfer characteristics with SPB pH8 solution on the avidin covered sensing surface. Error bars are  $\pm \text{SD}$ .

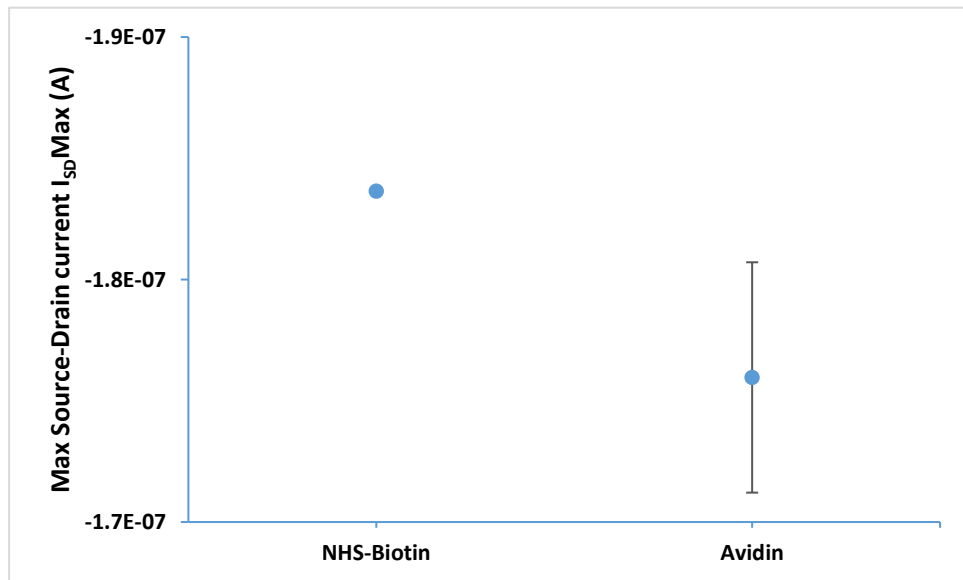


**Figure 5.23:** The average measured  $I_{SD} \text{Max}$  for CM-OFET device 9 for (a) The single measured transfer characteristics with SPB pH8 solution on the biotinylated sensing surface and (b) The three measured transfer characteristics with SPB pH8 solution on the avidin covered sensing surface. Error bars are  $\pm \text{SD}$ .

The magnitude of the current differs between devices due to differences in the quality of the organic semiconducting layer. In order to quantifiably compare CM-OFETs, the measured sensing response was translated into a percentage change in  $I_{SD}Max$  relative to the  $I_{SD}Max$  base line. Specifically, the percentage change in  $I_{SD}Max$  for a biotinylated CM-OFET following exposure to avidin was calculated as follows:

$$\frac{\text{Avg } I_{SD}Max (Av) - \text{Avg } I_{SD}Max (Biotin)}{\text{Avg } I_{SD}Max (Biotin)} \%$$

Here, Avg  $I_{SD}Max (Av)$  is the average  $I_{SD}Max$  of the three measurements following exposure to avidin while Avg  $I_{SD}Max (Biotin)$  is the average  $I_{SD}Max$  of the biotin baseline. The response of all CM-OFET biosensor devices following exposure to avidin is presented in table 5.3 and graphically in figure 5.24.

**Table 5.3:** Average percentage change in maximum source drain current after avidin deposition relative to the maximum source drain current before avidin deposition for nine, biotinylated CM-OFET devices.

	Device 1	Device 2	Device 3	Device 4	Device 5	Device 6	Device 7	Device 8	Device 9
Change %	10.7	-8.9	-1.7	6.4	2	6.2	0.12	4.4	-4.2
Error %	± 3.5	± 7	± 5	± 1.2	± 0.8	± 2.7	± 4.7	± 5.6	± 2.7

Figure 5.24 demonstrates a lack of consistent change in source drain current when the biotinylated devices are exposed to avidin. Considering the magnitude of the error bars, the measured source drain current after avidin deposition for devices 3,5,7 and 8 cannot be consider to conclusively increase or decrease relative to the measured source drain current prior to avidin deposition. For devices 1,4 and 6, the measured source drain current after avidin deposition increases moderately relative to the measured source drain current before avidin deposition, corresponding to an increase in current of  $10.7\% \pm 3.5$ ,  $6.4\% \pm 1.2$  and  $6.2\% \pm 2.7$  for devices 1, 4 and 6 respectively. This increase in current is the opposite to the reduction in current expected for a positively charged avidin layer at pH8. Only two devices (devices 2 and 9) showed the expected response after avidin deposition with a decrease in source drain current of  $-8.9\% \pm 7$  and  $-4.2\% \pm 2.7$ , respectively. However, here the change in source drain current  $I_{SD}(Av)$  relative to the source drain current of  $I_{SD}(Biotin)$

was below 10%, which is comparable to the measurement to measurement change in source drain current inherent to the CM-OFET device.

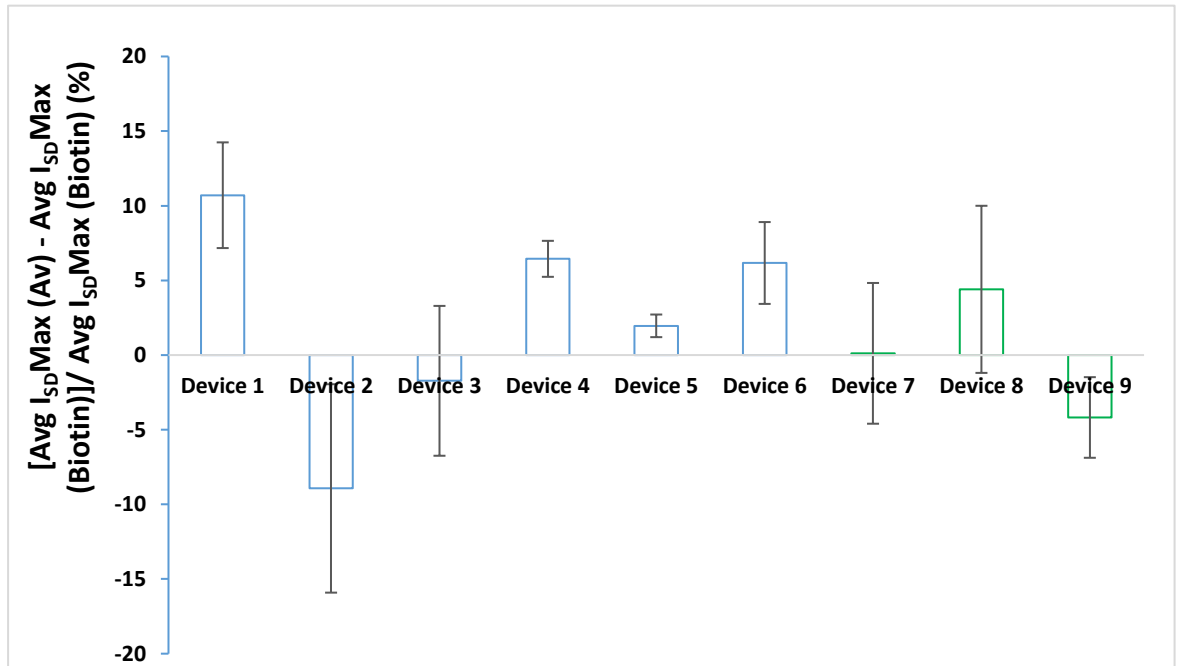


**Figure 5.24:** Comparison of average percentage change in  $I_{SD}Max$  after avidin deposition  $I_{SD}Max$  (Av) relative to the  $I_{SD}Max$  (Biotin) before avidin deposition for the nine biotinylated CM-OFET devices.

### 5.3.2.2 Nonspecific avidin binding test using CM-OFET devices

#### Measurement protocol for (SPB → Avidin) test:

First, a CM-OFET device with a silanized sensing surface was challenged with SPB (pH8) introduced to the sensing region via the PDMS microfluidic manifold. The transfer characteristics of the device was recorded every 25 minutes until the variation in  $I_{SD}Max$  was less than  $\pm 4\%$  between successive measurements. After that, avidin solution (0.1 mg/mL of SPB pH8) was introduced to the sensing region and allowed to incubate for 25 minutes. After 25 minutes the excess Avidin was washed away using SPB (pH8). Finally, three output/transfer characteristics measurement spaced by 25 minutes were taken for the device with SPB (pH8) solution covering sensing surface.

#### Results

This series of measurements was repeated for four devices and the response of each CM-OFET was then compared at the two different stages of surface functionalization (silanized surface and after exposure to avidin). Figures 5.25 to 5.28 show the **average** of the

recorded maximum source drain current,  $I_{SDMax}$ , at the two stages of surface functionalization for the 4 different CM-OFETs.

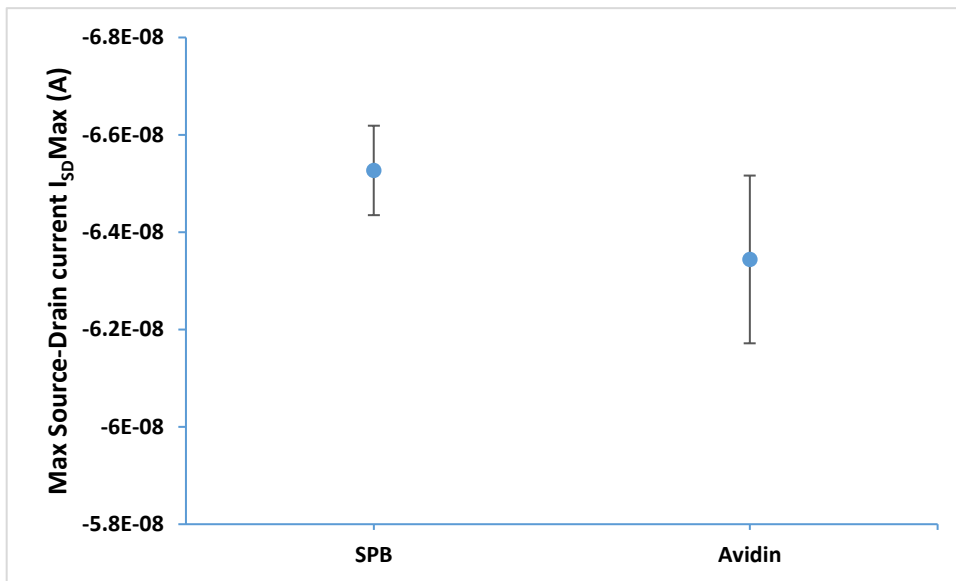


**Figure 5.25:** The average measured  $I_{SDMax}$  for CM-OFET device 1 for (a) The last three transfer characteristics recorded with SPB solution on silanized sensing surface, (b) The three measured transfer characteristics with SPB pH8 solution on nonspecific avidin covered sensing surface. Error bars are  $\pm$ SD.

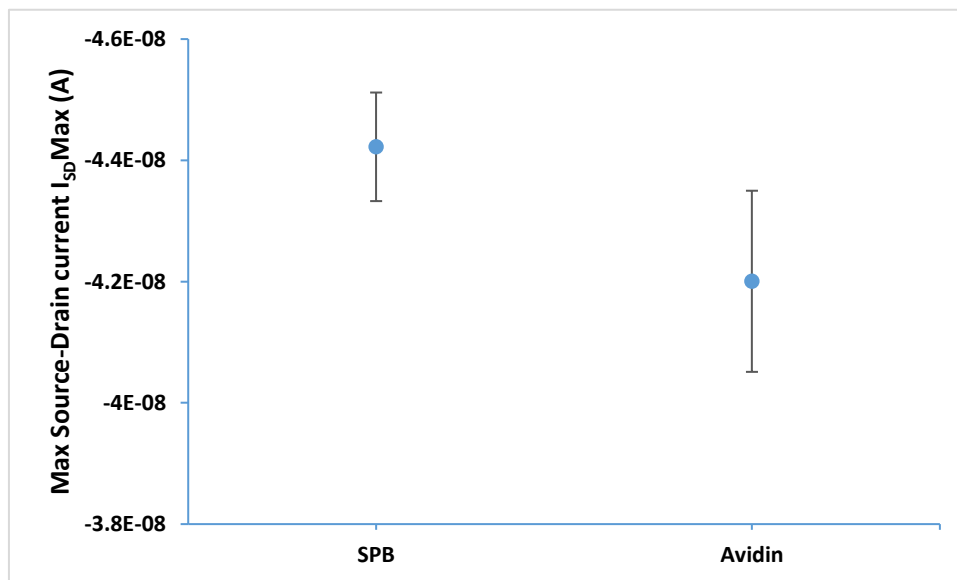


**Figure 5.26:** The average measured  $I_{SDMax}$  for CM-OFET device 2 for (a) The last three transfer characteristics recorded with SPB solution on silanized sensing surface, (b) The three measured transfer characteristics with SPB pH8 solution on nonspecific avidin covered sensing surface. Error bars are  $\pm$ SD.

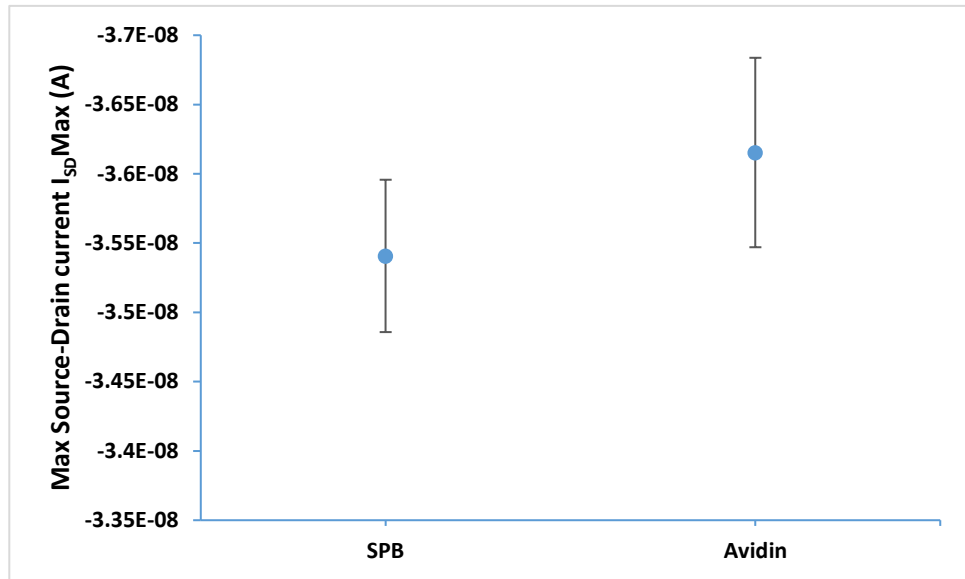


**Figure 5.27:** The average measured  $I_{SD\text{Max}}$  for CM-OFET device 3 for (a) The last three transfer characteristics recorded with SPB solution on silanized sensing surface, (b) The three measured transfer characteristics with SPB pH8 solution on nonspecific avidin covered sensing surface. Error bars are  $\pm$ SD.

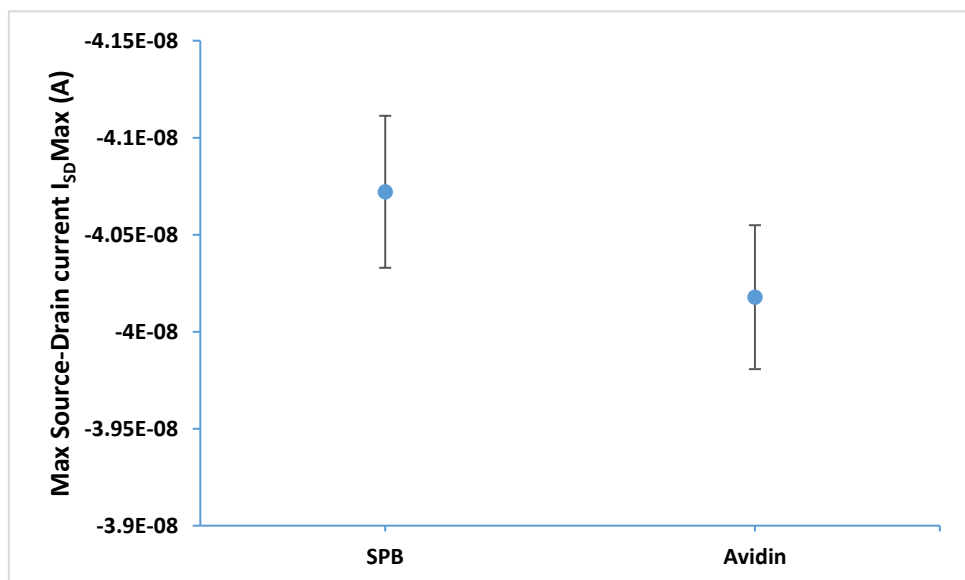


**Figure 5.28:** The average measured  $I_{SD\text{Max}}$  for CM-OFET device 4 for (a) The last three transfer characteristics recorded with SPB solution on silanized sensing surface, (b) The three measured transfer characteristics with SPB pH8 solution on nonspecific avidin covered sensing surface. Error bars are  $\pm$ SD.

Again, in order to compare the responses of the four devices, the measured sensing response following exposure to avidin was translated into a percentage change in  $I_{SDMax}$  relative to the  $I_{SDMax}$  base line, here the silanized sensor surface. This is shown in table 5.4 and figure 5.29.

**Table 5.4:** Average percentage change in maximum source drain current after avidin deposition relative to the maximum source drain current before avidin deposition for the non-biotinylated, silanized CM-OFET biosensors.

	Device 1	Device 2	Device 3	Device 4
Change %	-2.8	-5	2.1	-1.3
Error %	±2.7	±3.6	±1.9	±0.9

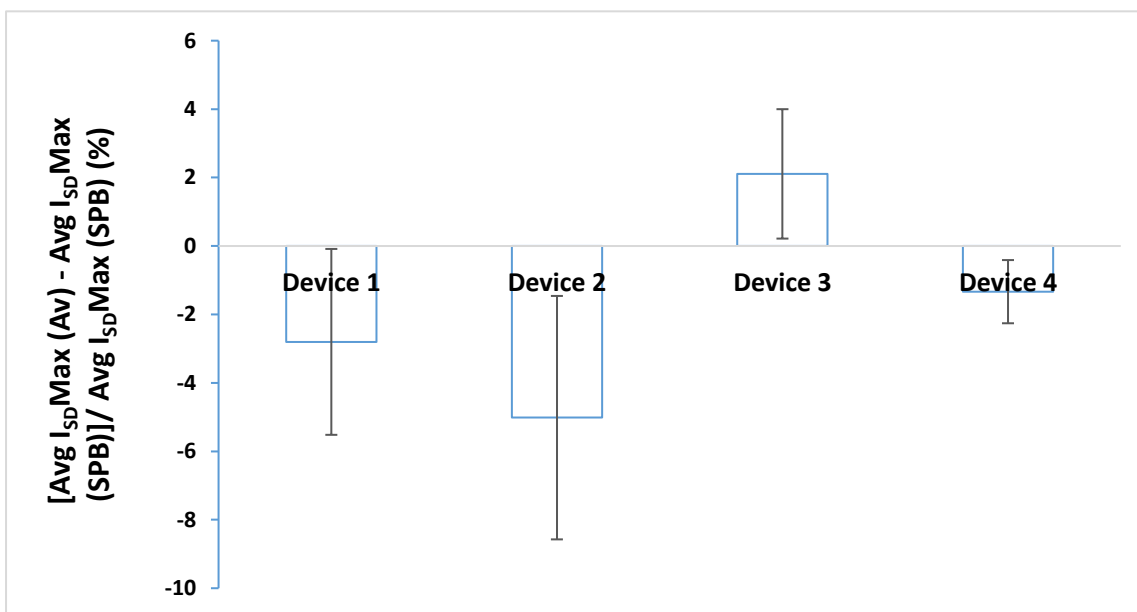


**Figure 5.29:** Average percentage change in  $I_{SDMax}$  after avidin deposition  $I_{SDMax}$  (Av) relative to  $I_{SDMax}$  before avidin deposition for the non-biotinylated, silanized CM-OFET biosensors. Error bars are  $\pm SD$ .

It is clear from figure 5.29 and table 5.4, that the magnitude and sign of the percentage change in source drain current after avidin deposition varied significantly between devices. Furthermore, the measurement error between successive measurements was significant. It is thus likely that the observed changes are associated with variations inherent to the OSC characteristics, rather than due to changes in charge in the sensing region due to avidin binding.

## 5.4 Discussion of the Si/SiO<sub>2</sub> CM-OFET biosensor

It is clear from the results of this chapter and the previous chapter of a CM-OFET based pH sensor, that the proposed Si/SiO<sub>2</sub> CM-OFET device does not display the sensitivity required to detect the change in surface charge within the sensing region of the device that occurs due to a chemical or biochemical interaction. Therefore, it is appropriate to reflect on what could be at fault in this proposed device.

It is instructive to compare the Si/SiO<sub>2</sub> CM-OFET fabricated here to the similar CM-OFET transistor developed by Lai *et al.*, and that was successfully employed as a charge sensitive device for detecting biochemical interactions [43].

A schematic diagram of the CM-OFET device employed by Lai *et al.* [43] for monitoring DNA hybridization is depicted in figure 5.30. Four key differences can be highlighted between this device and the Si/SO<sub>2</sub> CM-OFET device developed in this thesis.

1. *Sensing region materials:* The sensing region within the Si/SO<sub>2</sub> CM-OFET was the degenerately doped Si surface which was silanized in order to integrate functional chemical groups. The Device of Lai *et al.* was an aluminium floating gate capped with a gold layer. The gold layer was included for biocompatibility and ease of modification with various biological assemblies, and therefore this material difference between their choice and the Si surface chosen in our case, is not believed to affect the sensing mechanism.
2. *Gate dielectric:* The Lai *et al.* devices employed a hybrid gate dielectric layer consisting of a very thin ( $\approx 6$  nm) Al<sub>2</sub>O<sub>3</sub> layer grown on the Al floating gate capped with a Parylene C layer. The Parylene C layer can play two roles, first it can serve as a barrier layer to cover the thin Al<sub>2</sub>O<sub>3</sub> grown by UV-Ozone treatment which is likely to contain pinholes. Parylene C can also reduce the concentration of traps at the interface with the OSC compared to bare Al<sub>2</sub>O<sub>3</sub> which is known to have a high concentration of surface traps [44]. While this does not influence the fundamental detection mechanism, the potential reduction in trap states provided by the Parylene C could be beneficial in terms of the operational stability.
3. *Floating gate area:* Due to patterning, the floating gate in the Lai *et al.* device has a smaller area than the degenerately doped Si floating gate used in the Si/SO<sub>2</sub> CM-

OFET, However, the area of the floating gate was shown to have no effect on the threshold change,  $\Delta V_{TH}$ , in the CM-OFET due to a change in charge in the sensing area [45].

4. *Device geometry*: While the area of the floating gate itself does not impact on the CM-OFET sensitivity, the arrangement of the floating gate with respect to the other CM-OFET electrodes is however critical. This will be discussed in more detail in the following section.

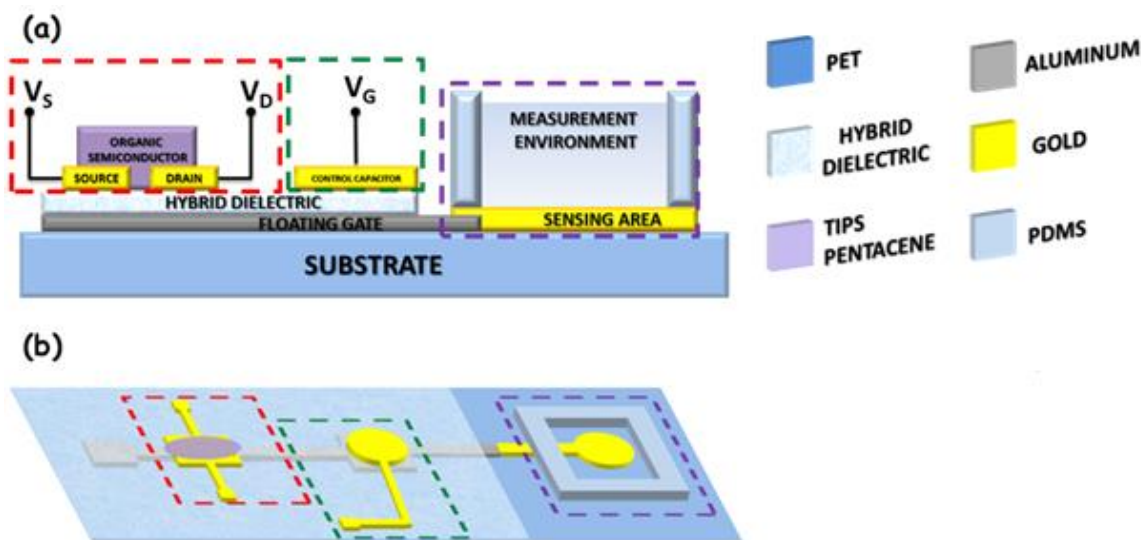


**Figure 5.30:** (a) Cross section of CM-OFET device proposed by Lai et.al [43]; the employed materials are reported in the palette; (b) the layout of the device.

## 5.5 Gating by the control gate; the effect of device geometry

In the CM-OFET biosensor, the transistor is typically biased into the operating regime via a control gate electrode that is capacitively coupled to the floating gate. The efficiency of this gating mechanism is dependent on the geometry and layout of the device electrodes. To understand and quantify this dependency, a simple model of the device structure was developed (figure 5.31) that can be used to understand the relationship between the various geometrical components of the device and the device characteristics.

As can be seen in figure 5.31, in addition to the control gate, both the source and drain electrodes are also capacitively coupled to the floating gate. The potential applied to these

electrodes will also contribute to the charge stored in the floating gate, and thus affect the transistor bias.

Using the principle of charge conservation for this simplified equivalent circuit of the CM-OFET device, it is possible to analyse the contribution of each capacitively coupled electrode. From Figure 5.32, charge conservation yields equation 5.8:

$$Q_S = Q_0 - Q_{Cg} - Q_D \quad (5.8)$$

Where  $Q_S$  is the total charge accumulated in the floating gate opposite the source electrode,  $Q_0$  is the inherent charge trapped in the floating gate,  $Q_{Cg}$  is the charge induced on the floating gate by the control gate and  $Q_D$  is the charge induced on the floating gate by the drain electrode. Equation 5.8 can also be expressed as:

$$(V_{Fg} - V_S)C_S = Q_0 - (V_{Fg} - V_{Cg})C_{Cg} - (V_{Fg} - V_D)C_D \quad (5.9)$$

$$V_{Fg}C_S + V_{Fg}C_{Cg} + V_{Fg}C_D = V_S C_S + V_{Cg}C_{Cg} + V_D C_D + Q_0 \quad (5.9a)$$

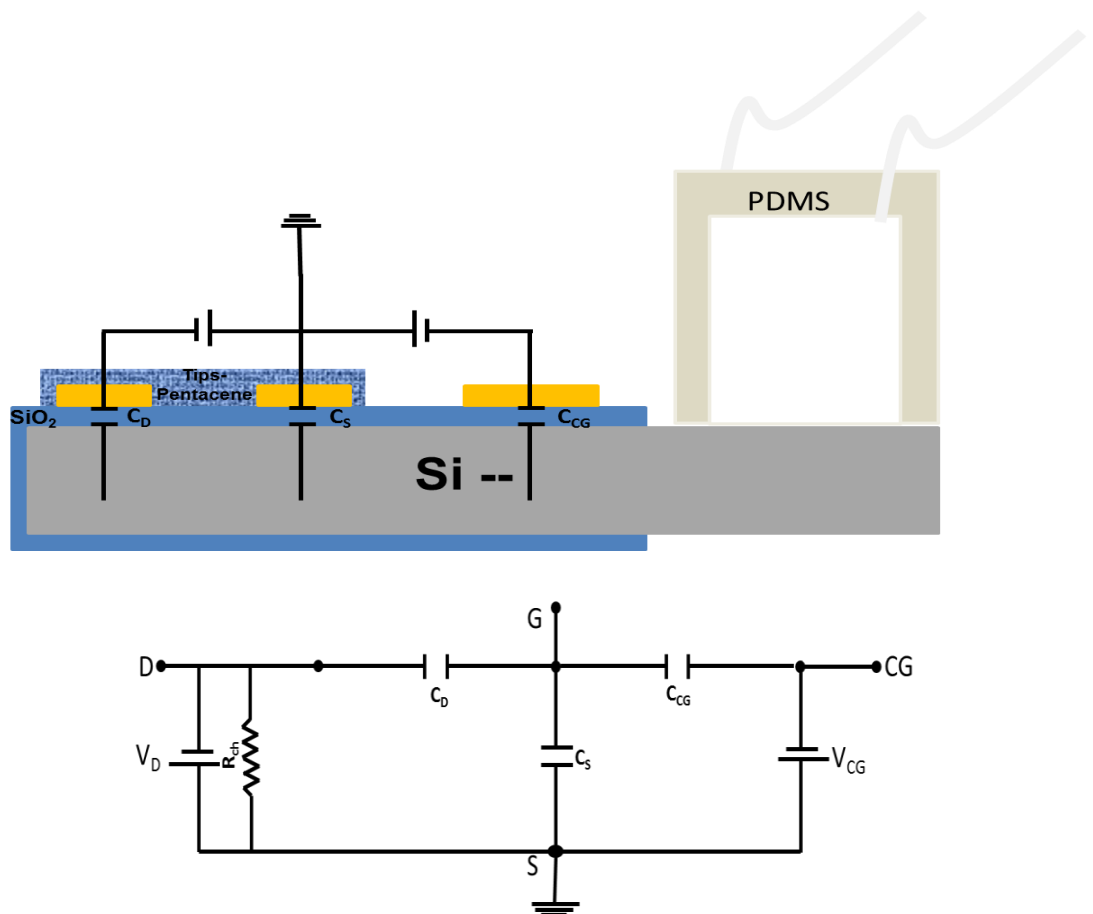


**Figure 5.31:** Capacitive coupling in the CM-OFET device and simplified equivalent circuit considering only capacitive contributions.

Where  $V_{FG}$  is the floating gate voltage,  $V_S$  is the source voltage,  $C_S$  is the capacitance between the source and floating gate,  $V_{CG}$  is the control gate voltage,  $C_{CG}$  is the capacitance between the control gate and floating gate,  $V_D$  is the drain voltage and  $C_D$  is the capacitance between the drain and floating gate. Rearranging 5.9a and setting  $V_S = 0$  (grounded), equation 5.9a becomes:

$$V_{FG} = \frac{C_{CG}}{C_{CG} + C_S + C_D} V_{CG} + \frac{C_D}{C_{CG} + C_S + C_D} V_D + \frac{1}{C_{CG} + C_S + C_D} Q_0 \quad (5.10)$$

From equation 5.10, it is clear that the contribution of the control gate to the total floating gate voltage will be  $\frac{C_{CG}}{C_{CG} + C_S + C_D} V_{CG}$  and the contribution due to the drain electrode  $\frac{C_D}{C_{CG} + C_S + C_D} V_D$ .

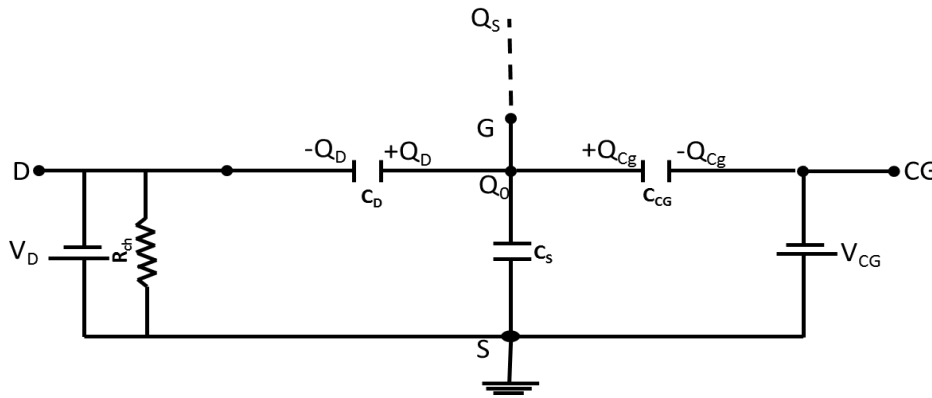


**Figure 5.32:** Charge distribution and charge conservation in floating gate.

Since all electrodes (source, drain and control gate) are separated from the floating gate by the same dielectric layer with a constant thickness, the expressions of the capacitance ratio can be simplified to be an area ratio. The contributions of the control gate and drain electrodes in terms of the electrode areas will be:

Control gate contribution  $\frac{A_{CG}}{A_{CG} + A_S + A_D} V_{CG}$

Drain contribution is  $\frac{A_D}{A_{CG} + A_S + A_D} V_D$

According to these terms, if the device has large source and drain electrodes, their contribution to the floating gate potential is increased relative to the contribution due to the control gate. This can have an undesirable impact on the performance of the device as will be explained shortly.

As a result of the electrode arrangement in the Si/SiO<sub>2</sub> CM-OFET device, shown in figure 5.33, the surface area of source and drain electrodes overlaps fully with the common Si floating gate beneath the SiO<sub>2</sub> dielectric.

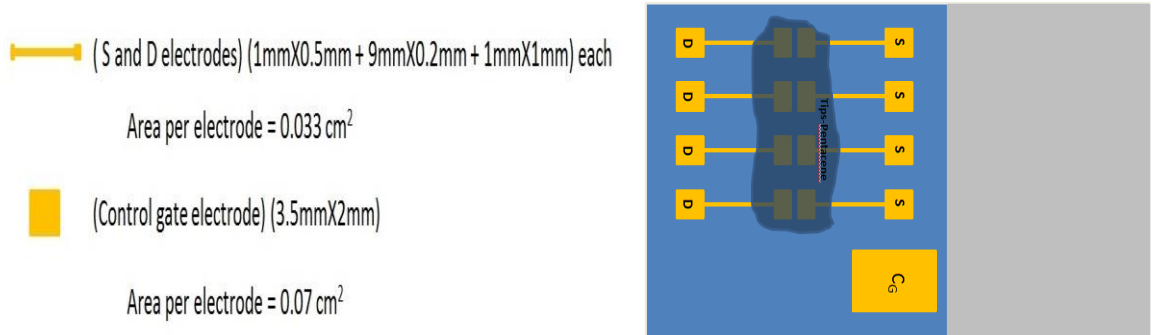


**Figure 5.33:** Electrodes geometrical dimensions and the Si/SiO<sub>2</sub> CM-OFET device general layout.

In this structure, the area of the control gate is 0.07 cm<sup>2</sup> and each S/D electrode has a surface area of 0.0305 cm<sup>2</sup>. At the maximum applied voltage ( $V_{Cg} = V_D = -40V$ ), the contribution of each electrode to the gating of the device is:

$$\frac{A_{Cg}}{A_{Cg} + A_S + A_D} V_{Cg} = (0.07/0.131) \times -40 = -21.374V$$

$$\frac{A_D}{A_{Cg} + A_S + A_D} V_D = (0.0305/0.131) \times -40 = -9.313V$$

Which means the overall biasing is -30.7V, i.e. 77% of the intended gating and the control gate only contributes by 53% of the intended gate and 70% of the effective gating.

Here, the intended gating is the desired biasing applied by the SMU to the control gate (i.e. -40V) and effective gating is the sum of biasing contribution by the control gate and drain electrodes (here=-30.7V).

The drain contribution 23% of the overall intended gating and 30% of the effective gating which is a sizable undesirable contribution.

One can use the contribution fraction terms of the control gate and drain to maximize the control gate contribution and minimize the drain contribution based on the surface area ratio between the control gate and drain electrodes as illustrated in figure 5.34.

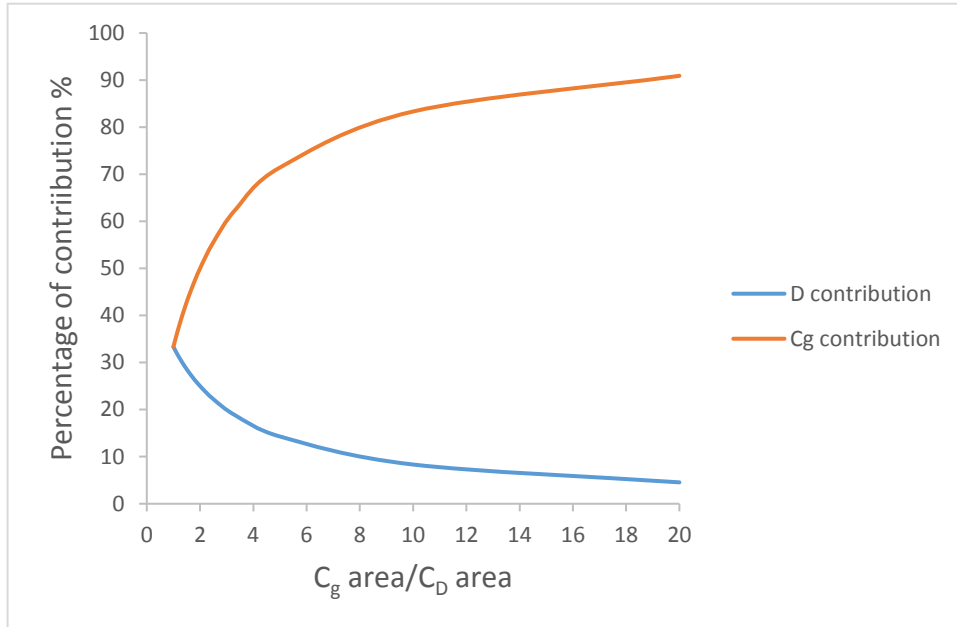


**Figure 5.34:** The relationship between the control gate and drain area ratio and the contribution of each one in biasing the floating gate.

To reduce the contribution of the drain voltage on the gate bias, a new design was proposed with a patterned floating gate, in this design the floating gate is Al and the dielectric layer is  $\text{Al}_2\text{O}_3$ . In the modified Al/ $\text{Al}_2\text{O}_3$  structure (figure 5.35), the overlap of the S/D electrodes with the patterned Al gate is reduced significantly (from  $0.0305 \text{ cm}^2$  to  $0.0055 \text{ cm}^2$ ), which in turn reduces capacitive coupling of the source drain voltage to the floating gate.

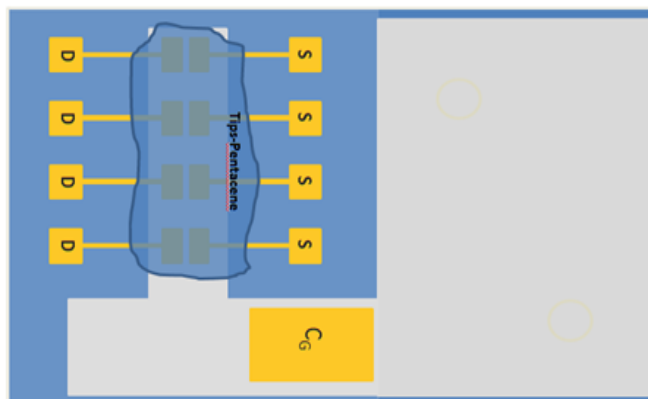


**Figure 5.35:** Al/ $\text{Al}_2\text{O}_3$  CM-OFET device with modified electrodes' layout.

Furthermore, due to the large dielectric constant of the  $\text{Al}_2\text{O}_3$ , the maximum required applied voltage in the transfer characteristics is significantly reduced from -40 V to -5 V. Due to the reduced overlap between S/D electrodes and the floating gate, the contribution of the control gate will be  $(0.07/0.081) \times -5 = -4.32$  V and the drain contribution is  $(0.0055/0.081) \times -5 = -0.34$  V.

Which means that the overall biasing is -4.66V, 93% of the intended gating out of which the control gate contributes by 86% of the intended gate and 93% of the effective gating. The drain contribution is only 6% of the overall intended gating and 7% of the effective gating.

It is clear from the previous calculations that the implication of having a large overlap between the S/D electrodes and the floating gate electrode is that the device will have smaller overall biasing and reduced control on the biasing by the control gate, moreover, due to the contribution of the drain electrode to the gate voltage, the conducting channel in the OSC will be turned ON even with 0 V applied to the control gate, making the estimation of  $V_{\text{TH}}$  difficult.

The effect of having relatively large source and drain electrodes can be observed in both the output and transfer characteristics of the Si/SiO<sub>2</sub> CM-OFET. The difference in the behaviour of the output characteristics for the Si/SiO<sub>2</sub> device and the modified Al/Al<sub>2</sub>O<sub>3</sub> device are displayed in figure 5.36 and 5.37, respectively where the effect of reducing the effective source and drain areas can be seen.

In the output characteristics of the Si/SiO<sub>2</sub> device, the large contribution of the drain electrode in the biasing of the device causes bending in the output curves. For example, at 0 V gate voltage, only a very low current is expected to be drawn from the device, due to the low intrinsic conductivity of the OSC and the high trapping probability that the charge carriers may experience while participating in the OSC conducting channel. However, the gating effect of the drain voltage in the Si/SiO<sub>2</sub> CM-OFET is considerable, leading to a linear increase in source drain current with drain voltage (highlighted by the red rectangle in figure 5.36). By reducing the source and drain areas this effect is minimized as can be seen from the output curves of the modified Al/Al<sub>2</sub>O<sub>3</sub> device in figure 5.37.

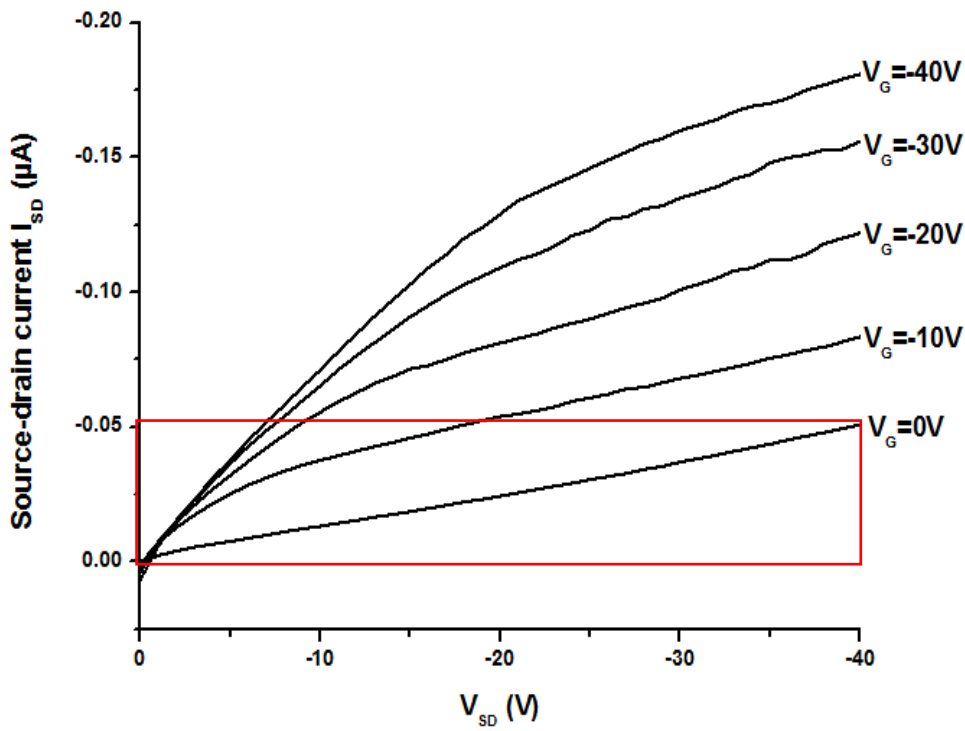


**Figure 5.36:** An example of an output characteristics of a Si/SiO<sub>2</sub> CM-OFET device. Red rectangle indicate increase of  $I_{SD}$  with  $V_{SD}$  increase.

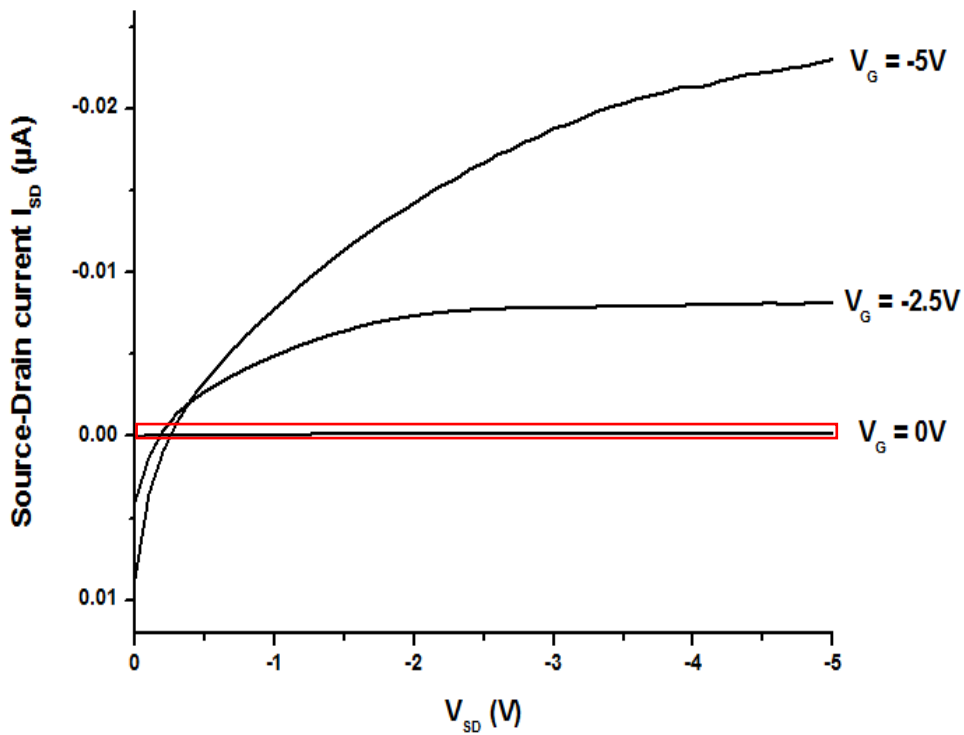


**Figure 5.37:** An example of an output characteristics of an Al/Al<sub>2</sub>O<sub>3</sub> CM-OFET device. Red rectangle shows the massive reduction in of  $V_D$  gating.

The effect of the large source/drain electrode overlap is also evident in the transfer characteristics. Here, the current is recorded as a function of gate voltage with the transistor biased in the saturation regime i.e. where  $V_{SD}$  is large. For the Si/SiO<sub>2</sub> devices in which the area of overlap between the source and drain electrodes and floating gate is large, the large  $V_{SD}$  means that a large charge is induced in the floating gate, which gates the transistor channel such that it is either be on or turned on in the positive gate voltage range of the transfer characteristics (within the selected operating gate voltage range), as shown in figure 5.38 and figure 5.39. By reducing geometrical overlap of the source and drain electrodes with the floating gate, the transistor can be turned fully OFF in the Al/Al<sub>2</sub>O<sub>3</sub> device, as can be seen in figure 5.40.

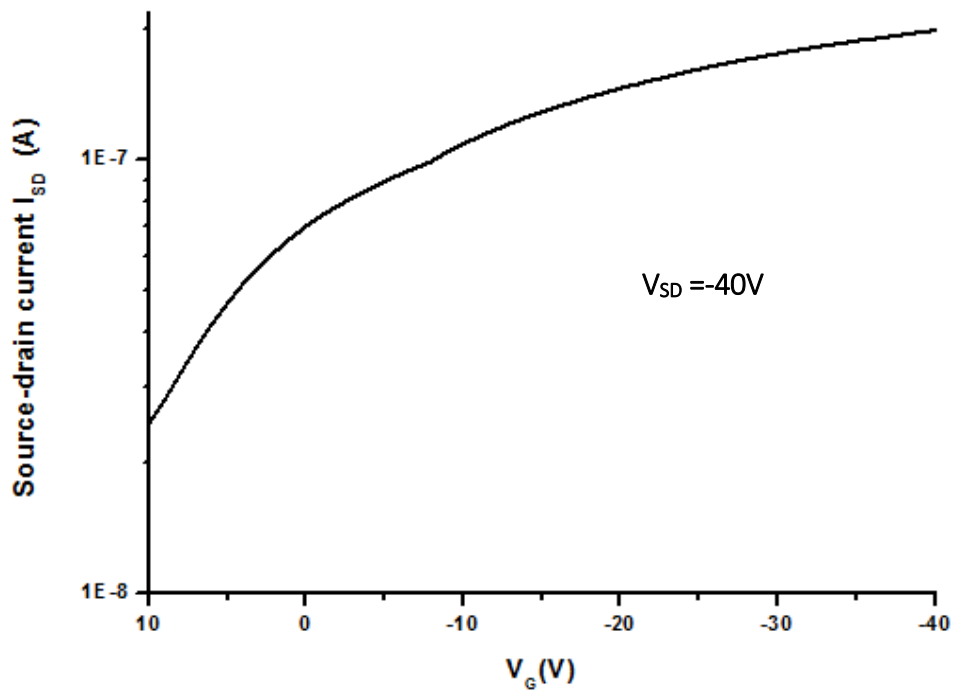


**Figure 5.38:** An example of a transfer characteristics of a Si/SiO<sub>2</sub> CM-OFET device (transistor on from start).

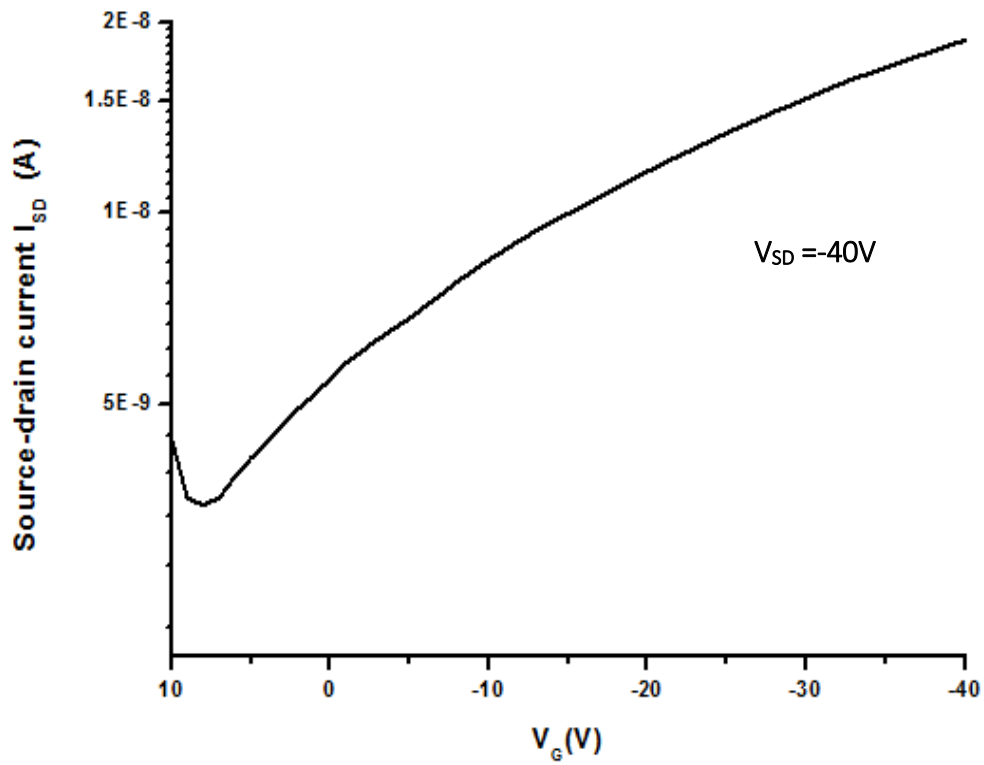


Figure 5.39: An example of a transfer characteristics of a Si/SiO<sub>2</sub> CM-OFET device (transistor turn on in the positive gate voltage region).

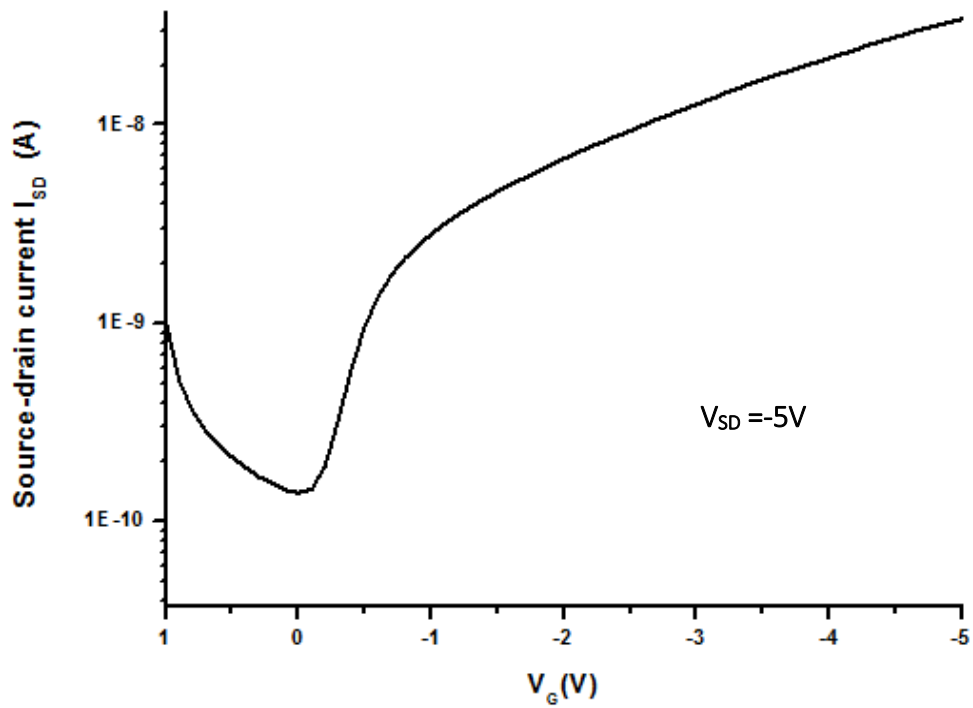


Figure 5.40: An example of a transfer characteristics of an Al/Al<sub>2</sub>O<sub>3</sub> CM-OFET device.

## 5.6 Device geometry and sensitivity

The geometry of the device also has an impact on the sensitivity of the CM-OFET when operated as a sensor. This can be modelled by the addition of an additional term,  $Q_{Sens}$ , into equation 5.10, which accounts for charge accumulated in the sensing area from the sensing activity:

$$V_{Fg} = \frac{C_{Cg}}{C_{Cg} + C_S + C_D} V_{Cg} + \frac{C_D}{C_{Cg} + C_S + C_D} V_D + \frac{1}{C_{Cg} + C_S + C_D} (Q_0 \pm Q_{Sens}) \quad 5.11$$

The overall contribution of charge in the sensing area to the floating gate voltage is thus:

$$\frac{Q_{Sens}}{C_{Cg} + C_S + C_D}$$

Again, a large overlap between the S/D electrodes and floating gate will reduce the effect of  $Q_{Sens}$ , and thus the sensitivity of the sensor. Recently Lai et.al. [46], derived an equation that describes the sensitivity in terms of the geometrical dimensions of the various active portions of a charge modulated device. Starting from the equation that describes the change in threshold voltage as a result of the charge accumulated in the sensing area (equation 5.12) they deduced a relationship between the sensitivity of the device and the areas of the other device elements.

$$\Delta V_{TH} = \frac{-Q_{Sens}}{C_{TOT}} \quad (5.12)$$

Here,  $C_{TOT}$ , is the total capacitance of the device. The sensitivity of the device, defined as  $|dV_{TH}/dQ_{Sens}|$ , is thus:

$$\left| \frac{dV_{TH}}{dQ_{Sens}} \right| = \frac{1}{C_i A_{Sens}} \frac{1}{A_{TOT}/A_{Sens} - 1} \quad (5.13)$$

Where  $C_i$  is the capacitance per unit area of the gate dielectric layer,  $A_{Sens}$  is the surface area of the sensing region,  $A_{TOT}$  is the sum of all areas composing all elements of the device (including  $A_{Sens}$ , area of the control gate  $A_{Cg}$ ,  $A_S/A_D$ , the area of the area of S/D electrodes and the transistor channel area width (W)×(L) length).

For a given gate dielectric layer, the sensitivity can be optimized by tailoring the different areas in the device to tune the  $A_{TOT}/A_{Sens}$  ratio. The smaller the  $A_{TOT}/A_{Sens}$  ratio the higher

the sensitivity. In the Si/SiO<sub>2</sub> device the  $A_{TOT}/A_{Sens}$  ratio = 9.184 while in the modified Al/Al<sub>2</sub>O<sub>3</sub> CM-OFET, the  $A_{TOT}/A_{Sens}$  ratio = 5.51.

## 5.7 The trade-offs of the design

- 1- The sensitivity of the charge modulated device can be tuned by the  $A_{TOT}/A_{Sens}$  ratio; increasing sensitivity can be achieved by decreasing this ratio. This can be achieved by having a large sensing area that comprises the largest surface area of the sensor. However, according to the sensitivity equation (5.13), the sensing area is also inversely proportional to the sensitivity so reducing the areas of other elements in the sensor device is a more rational approach.
- 2- Other areas that can be reduced to reduce the total area of the sensor device include the control gate area  $A_{Cg}$ , the areas of the S/D electrodes,  $A_S$  and  $A_D$ , and the transistor channel area. While these can be reduced, care must be taken to ensure the area of the control gate electrode,  $A_{Cg}$ , is considerably larger than  $A_S$  and  $A_D$  to ensure proper control over biasing of the device.
- 3- Reducing the surface area of the source and drain electrodes relative to the control gate area,  $A_{Cg}$ , and the sensing area,  $A_{Sens}$ , must be performed with care as these also influence the output source-drain current. According to the  $I_{SD}$  equation (see chapter 1, equation 1.9),  $I_{SD}$  is directly proportional to the transistor channel width,  $W$ , which corresponds to one of the S/D electrodes dimensions, so reducing this dimension will reduce the measured source-drain current,  $I_{SD}$ .

In the modified Al/Al<sub>2</sub>O<sub>3</sub> CM-OFET, the transistor channel width  $W$  was maintained while the length of the overlap between the source and drain electrodes and the floating gate,  $L_S$  and  $L_D$ , respectively were reduced, as in figure 5.41.

## 5.8 The modified Al/Al<sub>2</sub>O<sub>3</sub> CM-OFET device behaviour as a transistor

In the modified device, the dielectric constant for Al<sub>2</sub>O<sub>3</sub> is 9-10; nearly 2.5 times higher than that of the SiO<sub>2</sub>. Moreover, due to the uniformity and defect free nature of ALD deposited layers, it was possible to reduce the thickness of the Al<sub>2</sub>O<sub>3</sub> gate dielectric layer to only 40

nm compare to 300 nm for the Si/SiO<sub>2</sub> CM-OFET. Together, these factors enabled a device in which the operating voltage range is reduced by almost an order of magnitude, from (0 to -40V) for the Si/SiO<sub>2</sub>-based CM-OFET sensor to only (0 to -5V) for the Al/Al<sub>2</sub>O<sub>3</sub> CM-OFET.

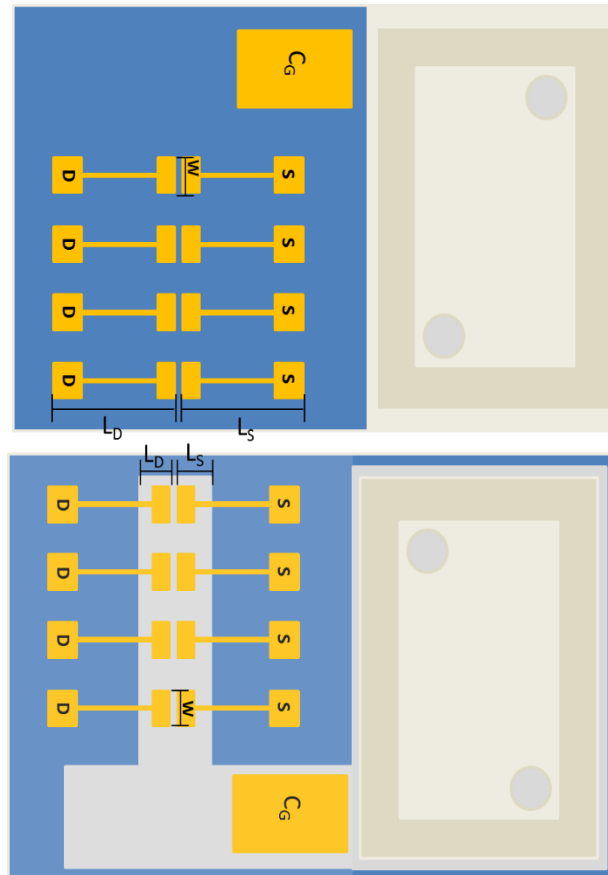


**Figure 5.41:** Comparison between the effective S/D areas  $A_S/A_D$  in the CM-OFET Si/SiO<sub>2</sub> and Al/Al<sub>2</sub>O<sub>3</sub> devices ( $W=1\text{mm}$  and  $L_S=L_D=10.5\text{mm}$  for Si/SiO<sub>2</sub> devices and  $W=1\text{mm}$  and  $L_S=L_D=1.5\text{mm}$  for Al/Al<sub>2</sub>O<sub>3</sub> devices).

An example of the output and transfer characteristic of the Al/Al<sub>2</sub>O<sub>3</sub> CM-OFET device has been already presented in figure 5.37 and 5.40 respectively. It must be said that although the device showed typical transistor behaviour, the source drain current was relatively low compared to the Si/SiO<sub>2</sub> CM-OFET devices. The highest maximum source drain current produced among all device was around 70 nA and the yield for devices that produced

maximum source drain current above 10 nA was low 40%. The mobility of devices was in the range from 0.0004 to 0.001  $\text{cm}^2\text{V}^{-1}\text{S}^{-1}$  and the ON/OFF current ratio was  $109\pm 68$ .

The interface of the  $\text{Al}_2\text{O}_3$  with the OSC is believed to be the cause for the reduced source drain current and low mobility. High k dielectrics such as  $\text{Al}_2\text{O}_3$  are more polar compared to  $\text{SiO}_2$  and that can increase the energetic disorder at the interface with the OSC, which results in a higher localization of the charge carriers and reduced field-effect mobility. A simple solution to reduce this effect is the formation of a self-assembled monolayer (SAM) on the  $\text{Al}_2\text{O}_3$  surface prior to OSC deposition [47-49].

Fumagalli et.al. [50] studied the effect of different SAMs (differing in the polar head group and alkyl chain length) on the electrical properties of transistors with an ALD  $\text{Al}_2\text{O}_3$  gate dielectric. They concluded that the length of the SAM is the most important parameter in improving transistor performance. A long chain SAM, such as n-octadecyltrichlorosilane (OTS), moves the active channel of the OSC away from the disordered surface dipoles present on the surface of  $\text{Al}_2\text{O}_3$ . The improvement is attributed to the combination of reduction of the broadness of the density of states and the improvement of the effective wavefunction overlap compare to the bare  $\text{Al}_2\text{O}_3$ . Critically, SAM modification is simple and does not required chemical vapor deposition (CVD) instrument to produce as in Parylene C layer.

## 5.9 Conclusions

This chapter discussed the use of the Si/ $\text{SiO}_2$  CM-OFET device for protein detection. Avidin protein binding to a biotinylated sensing region surface was chosen to examine the device sensitivity. In the chapter, the protocol used for biotinylating the sensing region of the CM-OFET device and subsequent avidin binding was presented. The effectiveness of the protocol was confirmed using QCM-D measurement which validated both the specific avidin binding to the biotinylated surface and minimal nonspecific avidin binding to a silanized surface.

Using the CM-OFET device, the binding of avidin to the biotinylated Si gate surface was investigated. Experimental results on a nine, nominally identical biotinylated CM-OFETs

showed significant variation between devices and no clear indication of sensitivity to the change in charge accumulated in the sensing region following avidin binding.

This chapter then discussed and analysed the shortcomings of the Si/SiO<sub>2</sub> CM-OFET sensor and proposed a modified CM-OFET sensor based on Al/Al<sub>2</sub>O<sub>3</sub> as gate and gate dielectric layers. The shortcomings of the geometrical arrangement of the Si/SiO<sub>2</sub> CM-OFET sensor were discussed and solutions to overcoming some of the Si/SiO<sub>2</sub> CM-OFET limitations were proposed for implementation in the design of new modified Al/Al<sub>2</sub>O<sub>3</sub> CM-OFET sensor. Practical trade-offs in the design of the modified CM-OFET device were also investigated. Finally, measurements of the Al/Al<sub>2</sub>O<sub>3</sub> CM-OFET as a transistor have shown typical transistor behaviour, validating the design and fabrication approach. While the measured source drain current was low, suggestions to improve charge mobility of the OSC were given.

It must be mentioned that, although geometrical considerations have been employed in the modified Al/Al<sub>2</sub>O<sub>3</sub> CM-OFET layout, the inherent measurement/current noise level seen in tested fabricated Si/SiO<sub>2</sub> CM-OFET devices attributed to the Tips-pentacene deposition method is considerably high (largely within  $\pm 10\%$ ), and could still presents a sensitivity issue for the modified Al/Al<sub>2</sub>O<sub>3</sub> CM-OFET. The improved sensitivity response that can be achieved by the new geometrical layout optimization may still be hampered by the existing noise associated with the current fabrication (particularly the OSC deposition method). Therefore, this needs to be addressed in order to produce a functioning CM-OFET.

## 5.10 References

- [1] Banica, F. G. (2012). *Chemical sensors and biosensors: fundamentals and applications*. John Wiley & Sons
- [2] Martín-Yerga, D., Carrasco-Rodríguez, J., Alonso, F. J. G., & Costa-García, A. (2017). Competitive electrochemical biosensing of biotin using cadmium-modified titanium phosphate nanoparticles and 8-channel screen-printed disposable electrodes. *Analytical Methods*.
- [3] Nollet, L. M., & Toldrá, F. (Eds.). (2015). *Handbook of Food Analysis, -Two Volume Set*. CRC Press.
- [4] Zourob, M., Elwary, S., & Turner, A. P. (Eds.). (2008). *Principles of bacterial detection: biosensors, recognition receptors and microsystems*. Springer Science & Business Media.
- [5] Shils, M. E., & Shike, M. (Eds.). (2006). *Modern nutrition in health and disease*. Lippincott Williams & Wilkins.
- [6] Deng, T., Li, J. S., Huan, S. Y., Yang, H. F., Wang, H., Shen, G. L., & Yu, R. Q. (2006). Quartz crystal microbalance bioaffinity sensor for biotin based on mixed self-assembled monolayers and metastable molecular complex receptor. *Biosensors and Bioelectronics*, 21(8), 1545-1552.
- [7] Brehm, B. (2015). *Nutrition: Science, Issues, and Applications*. ABC-CLIO, Denver, Colorado.
- [8] Trindade, T., & da Silva, A. L. D. (Eds.). (2011). *Nanocomposite particles for bio-applications: materials and bio-interfaces*. CRC Press.
- [9] Huangxian, J.; Guosong, L.; and Feng, Y. (2017). *Immunosensing for Detection of Protein Biomarkers*. Elsevier.
- [10] Yang, V. C., & Ngo, T. T. (Eds.). (2012). *Biosensors and their Applications*. Springer Science & Business Media.
- [11] Anzai, J. I., Hoshi, T., & Osa, T. (2000). Avidin—Biotin Mediated Biosensors. In *Biosensors and Their Applications* (pp. 35-46). Springer, Boston, MA.
- [12] Pazy, Y., Kulik, T., Bayer, E. A., Wilchek, M., & Livnah, O. (2002). Ligand Exchange between Proteins EXCHANGE OF BIOTIN AND BIOTIN DERIVATIVES BETWEEN AVIDIN AND STREPTAVIDIN. *Journal of Biological Chemistry*, 277(34), 30892-30900.
- [13] Suspène, C., Piro, B., Reisberg, S., Pham, M. C., Toss, H., Berggren, M., ... & Horowitz, G. (2013). Copolythiophene-based water-gated organic field-effect transistors for biosensing. *Journal of Materials Chemistry B*, 1(15), 2090-2097.

- [14] Hood, E. E., & Howard, J. A. (2014). Commercial plant-produced recombinant avidin. In *Commercial Plant-Produced Recombinant Protein Products* (pp. 15-25). Springer Berlin Heidelberg.
- [15] Scientific, T. (2009). Avidin-Biotin Technical Handbook. Text available@ [http://www.piercenet.com/files/1601675\\_AvBi\\_HB\\_INTL.pdf](http://www.piercenet.com/files/1601675_AvBi_HB_INTL.pdf).
- [16] Zourob, M., Elwary, S., & Turner, A. P. (Eds.). (2008). *Principles of bacterial detection: biosensors, recognition receptors and microsystems*. Springer Science & Business Media.
- [17] Torchilin, V. P. (1995). *Handbook of targeted delivery of imaging agents* (Vol. 26). CRC Press.
- [18] Williams, E. H., Davydov, A. V., Motayed, A., Sundaresan, S. G., Bocchini, P., Richter, L. J., ... & Rao, M. V. (2012). Immobilization of streptavidin on 4H-SiC for biosensor development. *Applied surface science*, 258(16), 6056-6063.
- [19] Jeong, C. K., Jin, H. M., Ahn, J. H., Park, T. J., Yoo, H. G., Koo, M., ... & Lee, K. J. (2014). Electrical biomolecule detection using nanopatterned silicon via block copolymer lithography. *small*, 10(2), 337-343.
- [20] Brownlee, J. (2007). Antigen-antibody interaction. Melbourne, Australia: Complex Intelligent Systems Laboratory, Centre for Information Technology Research, Faculty of Information and Communication Technologies, Swinburne University of Technology.
- [21] Bongrand, P. (1999). Ligand-receptor interactions. *Reports on Progress in Physics*, 62(6), 921.
- [22] Zhang, H., Williams, P. S., Zborowski, M., & Chalmers, J. J. (2006). Binding affinities/avidities of antibody-antigen interactions: Quantification and scale-up implications. *Biotechnology and bioengineering*, 95(5), 812-829.
- [23] Landry, J. P., Fei, Y., & Zhu, X. (2012). Simultaneous measurement of 10,000 protein-ligand affinity constants using microarray-based kinetic constant assays. *Assay and drug development technologies*, 10(3), 250-259.
- [24] Malaspina, D. C., Longo, G., & Szleifer, I. (2017). Behavior of ligand binding assays with crowded surfaces: Molecular model of antigen capture by antibody-conjugated nanoparticles. *PloS one*, 12(9), e0185518.
- [25] Lloret, N., Frederiksen, R. S., Møller, T. C., Rieben, N. I., Upadhyay, S., De Vico, L., ... & Martinez, K. L. (2012). Effects of buffer composition and dilution on nanowire field-effect biosensors. *Nanotechnology*, 24(3), 035501.

- [26] Yogo, T., Urano, Y., Mizushima, A., Sunahara, H., Inoue, T., Hirose, K., ... & Nagano, T. (2008). Selective photoinactivation of protein function through environment-sensitive switching of singlet oxygen generation by photosensitizer. *Proceedings of the National Academy of Sciences*, 105(1), 28-32.
- [27] Nicu, L. and Leichlé, T. (2014) *Micro-and Nanoelectromechanical Biosensors*. John Wiley & Sons. USA
- [28] Dixon, M. C. (2008). Quartz crystal microbalance with dissipation monitoring: enabling real-time characterization of biological materials and their interactions. *Journal of biomolecular techniques: JBT*, 19(3), 151.
- [29] Höök, F., Rodahl, M., Brzezinski, P., & Kasemo, B. (1998). Energy dissipation kinetics for protein and antibody- antigen adsorption under shear oscillation on a quartz crystal microbalance. *Langmuir*, 14(4), 729-734.
- [30] Lehner, C. (2015). Quartz Crystal Microbalance Studies on Friction Modifiers for Lubricant Applications.
- [31] Sauerbrey, G. (1959). Verwendung von Schwingquarzen zur Wägung dünner Schichten und zur Mikrowägung. *Zeitschrift für Physik A Hadrons and Nuclei*, 155(2), 206-222.
- [32] Nomura, T., & Okuhara, M. (1982). Frequency shifts of piezoelectric quartz crystals immersed in organic liquids. *Analytica Chimica Acta*, 142, 281-284.
- [33] Kanazawa, K. K., & Gordon, J. G. (1985). Frequency of a quartz microbalance in contact with liquid. *Analytical Chemistry*, 57(8), 1770-1771.
- [34] Hook, F., Rodahl, M., Keller, C., Glasmaster, K., Fredriksson, C., Dahqvist, P., & Kasemo, B. (1999). The dissipative QCM-D technique: interfacial phenomena and sensor applications for proteins, biomembranes, living cells and polymers. In *Frequency and Time Forum, 1999 and the IEEE International Frequency Control Symposium, 1999., Proceedings of the 1999 Joint Meeting of the European* (Vol. 2, pp. 966-972). IEEE.
- [35] Jordan, J. L., & Fernandez, E. J. (2008). QCM-D sensitivity to protein adsorption reversibility. *Biotechnology and bioengineering*, 101(4), 837-842.
- [36] BiolinScientific.com (2017) *QCM-D Measurements*, URL: <http://www.biolinscientific.com/measurements/qcm-d> [Last access 24 Dec. 17]
- [37] Liu, S. X., & Kim, J. T. (2009). Application of Kelvin—Voigt model in quantifying whey protein adsorption on polyethersulfone using QCM-D. *JALA: Journal of the Association for Laboratory Automation*, 14(4), 213-220.

- [38] Voinova, M. V., Rodahl, M., Jonson, M., & Kasemo, B. (1999). Viscoelastic acoustic response of layered polymer films at fluid-solid interfaces: continuum mechanics approach. *Physica Scripta*, 59(5), 391.
- [39] Höök, F., Kasemo, B., Nylander, T., Fant, C., Sott, K., & Elwing, H. (2001). Variations in coupled water, viscoelastic properties, and film thickness of a Mefp-1 protein film during adsorption and cross-linking: a quartz crystal microbalance with dissipation monitoring, ellipsometry, and surface plasmon resonance study. *Analytical chemistry*, 73(24), 5796-5804.
- [40] Koutsoumpeli, E., Murray, J., Langford, D., Bon, R. S., & Johnson, S. (2015). Probing molecular interactions with methylene blue derivatized self-assembled monolayers. *Sensing and bio-sensing research*, 6, 1-6.
- [41] Takahashi, S., Sato, K., & Anzai, J. I. (2012). Layer-by-layer construction of protein architectures through avidin–biotin and lectin–sugar interactions for biosensor applications. *Analytical and bioanalytical chemistry*, 402(5), 1749-1758.
- [42] Knoglinger, C., Zich, A., Traxler, L., Poslední, K., Friedl, G., Ruttmann, B., ... & Gruber, H. J. (2018). Regenerative biosensor for use with biotinylated bait molecules. *Biosensors and Bioelectronics*, 99, 684-690.
- [43] Lai, S., Demelas, M., Casula, G., Cosseddu, P., Barbaro, M., & Bonfiglio, A. (2013). Ultralow voltage, OTFT-based sensor for label-free DNA detection. *Advanced Materials*, 25(1), 103-107.
- [44] Cosseddu, P., Lai, S., Barbaro, M., & Bonfiglio, A. (2012). Ultra-low voltage, organic thin film transistors fabricated on plastic substrates by a highly reproducible process. *Applied Physics Letters*, 100(9), 61.
- [45] Viola, F. A., Spanu, A., Ricci, P. C., Bonfiglio, A., & Cosseddu, P. (2018). Ultrathin, flexible and multimodal tactile sensors based on organic field-effect transistors. *Scientific reports*, 8(1), 8073.
- [46] Lai, S., Barbaro, M., & Bonfiglio, A. (2016). Tailoring the sensing performances of an OFET-based biosensor. *Sensors and Actuators B: Chemical*, 233, 314-319.
- [47] Veres, J., Ogier, S., Lloyd, G., & De Leeuw, D. (2004). Gate insulators in organic field-effect transistors. *Chemistry of Materials*, 16(23), 4543-4555.
- [48] Veres, J., Ogier, S. D., Leeming, S. W., Cupertino, D. C., & Mohialdin Khaffaf, S. (2003). Low-k insulators as the choice of dielectrics in organic field-effect transistors. *Advanced Functional Materials*, 13(3), 199-204.

[49] Majewski, L. A., Schroeder, R., & Grell, M. (2003). Flexible high capacitance gate insulators for organic field effect transistors. *Journal of Physics D: Applied Physics*, 37(1), 21.

[50] Fumagalli, L., Natali, D., Sampietro, M., Peron, E., Perissinotti, F., Tallarida, G., & Ferrari, S. (2008). Al<sub>2</sub>O<sub>3</sub> as gate dielectric for organic transistors: Charge transport phenomena in poly-(3-hexylthiophene) based devices. *Organic Electronics*, 9(2), 198-208.

# Chapter 6

## Conclusions and Future Works

### 6.1 Conclusions

Despite the scale of research and potential opportunities for innovative biosensors, the majority of these technologies have had very limited market success. This is partly due to the challenges associated with translating innovative technology, particularly when developed for applications in healthcare. Furthermore, many of the novel technologies discussed in the academic literature are often too expensive to use or manufacture, limiting their widespread use, or require laboratories and trained people to operate. This reality will continue to motivate researchers to innovate and develop new biosensor technologies that are inexpensive, easy to fabricate and use-friendly alternatives.

A potential candidate for such new technologies are biosensors based on organic electronic devices. These devices are easy to fabricate, employing the mass fabrication technologies established within the microelectronics industry, employ inexpensive organic materials, amenable for miniaturization, opening up the possibility of portable analysis, and compatible with microfluidic system integration.

This thesis has presented a study into the fabrication, characterisation and application of such an organic biosensing device based on the recently developed charge-modulated organic field effect transistor (CM-OFET). This device architecture is very much in its infancy; to the best of our knowledge this concept has been investigated by a single group from the Department of Electrical and Electronic Engineering (DIEE), University of Cagliari. This device has two key features that make it an attractive option for the fabrication of biosensors. 1) the biosensing activity occurs in a region that is spatially separated from the organic FET. This enables the use of a wide variety of organic semiconductor layers that otherwise could degrade in contact with an aqueous sample. 2) the device is biased through a capacitively coupled control gate which again is spatially separated from aqueous electrolyte. This removes the need for an external reference electrode which are difficult to microfabricate reliably. Academic literature on the CM-OFET is to date very limited and

the concept has yet to be widely explored, particularly alternative approaches for fabrication and application of the technology for protein sensing.

The thesis has primarily investigated the characteristics of a CM-OFET biosensor that was based on widely available Si/SiO<sub>2</sub> substrate. Here, the degenerately doped silicon substrate forms the gate electrode while the silica layer acts as the gate dielectric on which the organic semiconductor layer is assembled between metallic electrodes. This fabrication approach was adopted due to its simplicity, requiring minimal fabrication steps, and compatibility with conventional microfabrication technology. Despite the simplicity, limitations associated with the geometrical layout and high voltage operation associated with the thickness of the dielectric layer led to a modified design. This second design employed Al/Al<sub>2</sub>O<sub>3</sub> as gate and gate dielectric layers and was designed to comply with the geometrical considerations for optimum operation of the charge-modulated device.

Chapter 3 presented rigorous electrical characterisation of the CM-OFET operating as a transistor biased using both the Si gate and the capacitively coupled control gate electrode. The chapter also investigate how environmental effects, such as electrical noise, temperature and light, influence the CM-OFET and thus how they are controlled so they do not influence the interpretation of the measured results. This detailed characterisation confirmed the possibility of a fabricating a functioning Si/SiO<sub>2</sub> CM-OFET. Critically, the yield for working devices showing transistor-like behaviour with maximum source drain current > 10nA was more than 90%.

In chapter 4, the application of the CM-OFET device based on Si/SiO<sub>2</sub> as a sensor for monitoring pH was explored. In the chapter, the sensing mechanism was thoroughly explained, including how to render the surface of the floating gate within the sensing region sensitive to local pH by functionalizing the sensing region of the device with 3-aminopropyltrimethoxy-silane (APTES) SAM. This functionalization was confirmed using standard surface analytical technique, namely XPS. Finally, electrical measurements of the CM-OFET devices were presented and discussed. Measured results demonstrated that the response of the CM-OFETs to pH change was inconsistent. In particular, the response of the device to change in local pH was found to show no trend across all devices and the

percentage of source drain current change (apart from very limited cases) was comparable to the fluctuation in source drain current change due to inherent behaviour of the device.

Chapter 5 focussed on the application of the Si/SiO<sub>2</sub> CM-OFET device for protein detection, here the model biotin-avidin system. The same APTES coated surface used for pH detection was also used here to provide a chemical reactive amine group for immobilization of biotin modified with a reactive NHS ester. The biotinylation protocol was verified using QCM-D measurements which confirmed biotinylation of the silanized QCMD crystal and specific binding between avidin and biotinylated sensor surface. The chapter then moved on to discuss the sensing mechanism by which the avidin binding can be detected in the fabricated CM-OFET device. Here, sensing exploits the charge sensitivity of the CM-OFET to detect the change in surface charge between biotin and avidin. Specifically, the local increase in positive surface charge upon avidin binding to the biotinylated surface of the CM-OFET sensing region, should lead to a reduction in the source drain current. Again, experimental results for avidin detection were inconsistent and comparable to the inherent device noise.

Reflecting on the performance of the CM-OFET device both for pH sensing and avidin binding detection, an alternative design was presented to account for the effects of device geometry on the CM-OFET biosensor sensitivity. This alternative design was based on an Al/Al<sub>2</sub>O<sub>3</sub> material system. The change from Si/SiO<sub>2</sub> to Al/Al<sub>2</sub>O<sub>3</sub> addresses two major shortcomings in the Si/SiO<sub>2</sub> device. Firstly, the high operating voltage required for Si/SiO<sub>2</sub> due to the low dielectric constant of SiO<sub>2</sub> and the large oxide thickness. Al<sub>2</sub>O<sub>3</sub> has nearly 2.5 times higher dielectric constant which enabled a significant reduction in the operating voltage. The second limitation of the Si/SiO<sub>2</sub> CM-OFET was the device geometry. Optimum performance for the CM-OFET device requires careful consideration of the electrode geometry, and in particular the overlap between source and drain electrodes with the control gate. The alternative Al/Al<sub>2</sub>O<sub>3</sub> CM-OFET presented in chapter 5 was designed to account for these geometrical effects. Finally, the Al/Al<sub>2</sub>O<sub>3</sub> CM-OFET was tested and was shown to exhibit behaviour typical of an organic transistor. Furthermore, modification to the electrode geometry was shown to improve the device characteristics, specifically minimising the unwanted gating effects of the drain electrodes. However, the source drain current in this device was rather low due to a low carrier mobility attributed to the high

surface energy of the  $\text{Al}_2\text{O}_3$  gate dielectric layer. A potential solution was given to this problem in the form of SAM modification to  $\text{Al}_2\text{O}_3$  gate dielectric layer.

## 6.2 Future Works

Evidently the main priority for further work regarding this research project is the experimental investigation of the modified  $\text{Al}/\text{Al}_2\text{O}_3$  CM-OFET for sensing applications. A single experiment to test the  $\text{Al}/\text{Al}_2\text{O}_3$  CM-OFET for pH sensing showed encouraging signs of the device's response to pH as shown in figure 6.1. Here, the change in source drain current was seen to increase consistently with increasing pH; something that could not be observed in the  $\text{Si}/\text{SiO}_2$  CM-OFET. It must be noted that, this has only been shown for a single device and for three different pH levels and this characteristic needs to be confirmed. Also, the percentage of source drain current change decreased over time due to the reduction of the device's current. This ageing behaviour needs further investigation.

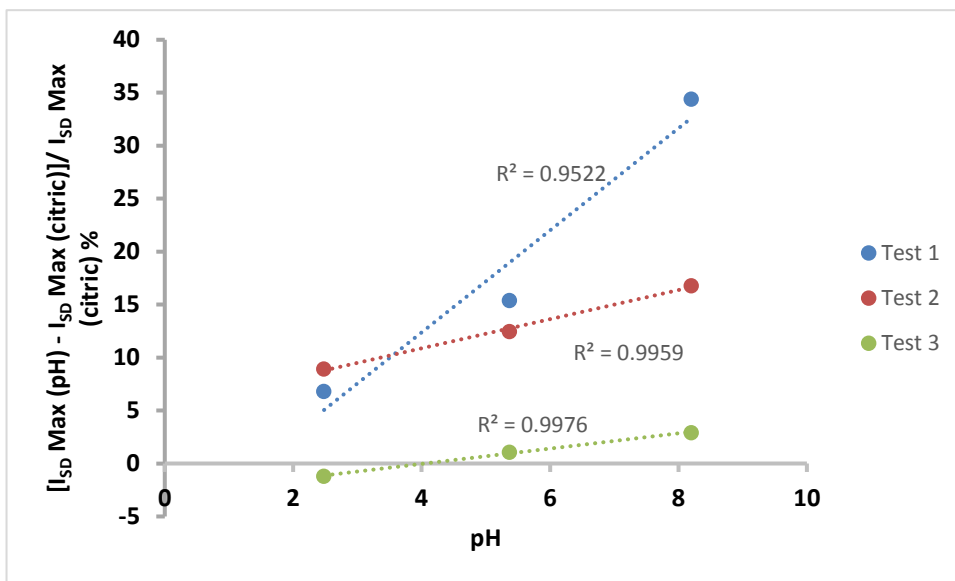


**Figure 6.1:** Experimental results of pH sensing using an  $\text{Al}/\text{Al}_2\text{O}_3$  CM-OFET device, the figure shows the percentage change in  $I_{\text{SDMax}}$  for three independent measurements (at 3 different pH levels). Here, the transfer characteristics of the device were measured 25 mins after introduction of the test pH solution.

As discussed in chapter 5, as a starting point to achieve a more satisfactory performance, the charge carrier mobility in the OSC of the  $\text{Al}/\text{Al}_2\text{O}_3$  CM-OFET needs to be improved. One possible solution is the use of a SAM at the OSC-gate dielectric interface. The use of n-

octadecyltrichlorosilane (OTS) SAM has been reported to improve the mobility in OFET devices with  $\text{Al}_2\text{O}_3$  as the dielectric layer. The use of a SAM intermediate layer can also help regulate molecular ordering of the OSC layer which could lead to a more reproducible OSC leading to a reduction in the device to device source drain current variability.

Enhanced mobility may also be advantageous for sensing applications. This is because the source drain current is directly proportional to the OSC mobility. Thus, as can be seen in figure 6.2, improving the mobility can theoretically result in higher source drain current change per unit gate voltage shift, this in turn should increase sensitivity.

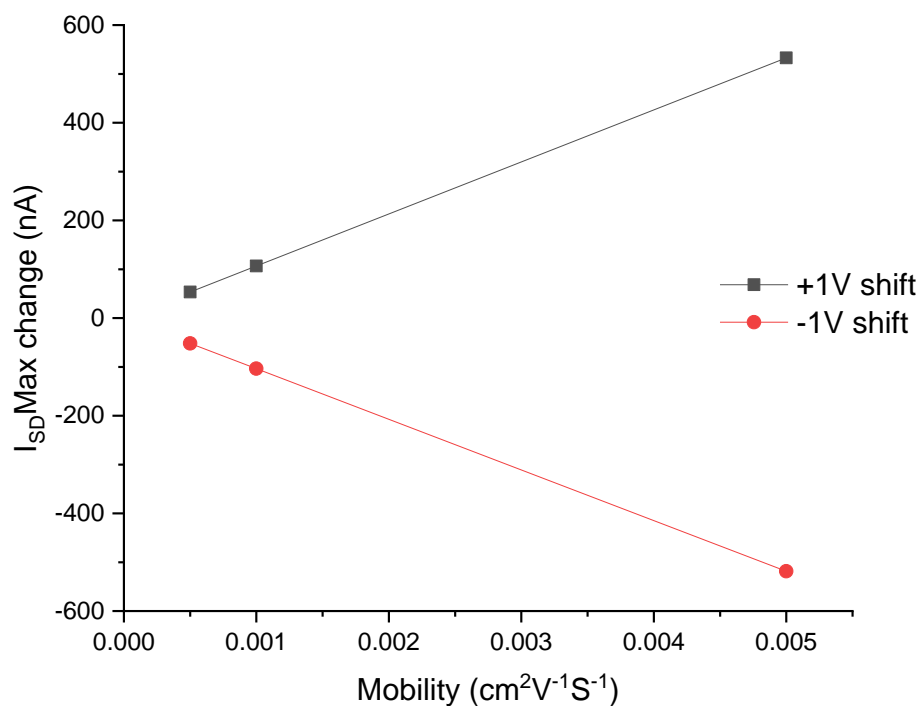


**Figure 6.2:** Theoretical effect of mobility on maximum source drain current change per unit gate voltage shift for Al/ $\text{Al}_2\text{O}_3$  CM-OFET ( $\text{Al}_2\text{O}_3$  40nm).

The OSC solution deposition method needs to be also be investigated and optimized. The simple drop casting method chosen for this work, although potentially known to provide high crystallization (and thus high mobility), also increases randomness and the potential for multilayer formation which contribute to a lack of reproducibility between fabricated devices. A combination of a controlled deposition method and SAM treatment may potentially help reduce device to device variation as well as minimize the noise in the

fabricated devices (source drain current fluctuations due to randomness in crystallization of the OSC).

Addressing the OSC solution deposition method is very important as it is very likely that only the combination of reducing the inherent current fluctuation (by an optimized deposition method) and the improved geometrical layout design can produce a functioning CM-OFET.

From a technological point of view, for the Al/Al<sub>2</sub>O<sub>3</sub> based device, anodization of the Al layer, rather than deposition via ALD, is a concept worth revisiting. Such a process greatly simplifies device fabrication and reduces fabrication cost. The use of substrates with a high surface roughness, such as Mylar plastic sheet could be a good starting choice.

A final suggestion regards the time domain measurement,  $I_{SD}$  vs time. Results presented in chapter 4 showed that the response of the CM-OFET in this type of measurement was largely dominated by noise and bias stress effect, which affected the interpretation of the data. Bias stress can be reduced if continuous biasing is replaced by biasing using voltage pulsing. Reducing the bias stress effect could enable measurements and quantification of the time dependent variations in the source drain current.

# Appendix A: Si/SiO<sub>2</sub> CM-OFET device fabrication steps

## A.1. Si/SiO<sub>2</sub> Substrate Preparation and Cleaning

- 1- Cut Si/SiO<sub>2</sub> wafer to appropriate samples sizes, approximately (1.2X3cm).
- 2- Blow samples with nitrogen gun to blow of debris.
- 3- Put samples in Acetone Beaker and sonicate in an ultra-sonication bath for 3 minutes.
- 4- Transfer to a beaker of isopropanol IPA and sonicated for another 3 minutes.
- 5- Blow dry with nitrogen gun.



**Figure A.1:** Clean Si/SiO<sub>2</sub> substrate.

## A.2. Sensing area realization

- 1- Cover one end of the sample with an insulating tape.
- 2- Place the sample on the spinner chuck.
- 3- Dispense photoresist (S1813) on the sample.
- 4- Spin for 1 minute at 4000 rpm.
- 5- Remove the insulating tape.
- 6- Bake the sample on 150C° hotplate for 5 minutes.
- 7- Prepare 7ml of buffer oxide etch BOE solution (HF 1:6 NH<sub>4</sub>F) in a small beaker.
- 8- Dip the region uncovered by photoresist of the sample in the BOE solution for 4 minutes.

- 9- Dip the whole sample in a large beaker of DI water to remove the majority of the etchant residue.
- 10- Immerse the sample in a second beaker of DI water for 3 minutes, and then rinse the samples by refilling the beaker with DI water for 30 seconds.
- 11- Dry the sample with nitrogen gun.
- 12- Soak a cotton bud in acetone and use it to remove the bulk of the hard-baked photoresist.
- 13- Soak the sample in Acetone beaker for several hours.
- 14- Transfer sample to IPA beaker and sonicate for 3 minutes.



**Figure A.2:** Si/SiO<sub>2</sub> substrate covered with photoresist with one end exposed.

### **A.3 Contacts formation**

#### **a- Photolithography and metal deposition**

##### ***Photolithography***

- 1- Clean sample in Piranha solution (H<sub>2</sub>SO<sub>4</sub> 7:3 H<sub>2</sub>O<sub>2</sub>) for 5 minutes.
- 2- Dip the sample in a large beaker of DI water to remove the majority of the Piranha residue.
- 3- Immerse the sample in a second beaker of DI water for 3 minutes, and then rinse the samples by refilling the beaker with DI water for 30 seconds.
- 4- Blow dry sample with nitrogen gun.
- 5- Heat the sample on 110C° hotplate for 1 minute.
- 6- Place the sample on the spinner chuck.
- 7- Dispense Primer solution (Hexamethyldisilazane HMDS) on the sample.

- 8- Spin for 30 seconds at 4000 rpm.
- 9- Bake the sample on 190C° hotplate for 1 minute.
- 10- Place the sample back on the spinner chuck.
- 11- Dispense photoresist (S1813) on the sample.
- 12- Spin for 1 minute at 5000 rpm.
- 13- Bake the sample on 110C° hotplate for 3 minutes.
- 14- Transfer and load the sample to the chuck of the Mask-Aligner machine.
- 15- Load the sample against the desire region in the photomask.
- 16- Expose the sample through the photomask to UV light (Dose 22mW/cm<sup>2</sup>) for 5 seconds.
- 17- Unload the sample and transfer it to a beaker of photoresist developer (351 microposit).
- 18- Develop the sample for one minute while shaking the developer solution.
- 19- Quickly take the sample to a beaker of DI water to stop the developing process.
- 20- Dry with nitrogen gun.
- 21- Check the sample under the optical microscope and return to developer solution if features are underdeveloped.

**Table A.1:** Photolithography recipe

	Spin Speed	Time	Temperature	Notes
Primer (HMDS)	4000 rpm	30 sec	Room temperature	
Primer bake		1 min	190 C°	
Photoresist (S1813)	5000 rpm	1 min	Room temperature	
Soft bake		3 min	110 C°	
Exposure		5 sec		Dose (22mW/cm <sup>2</sup> )
Developer (351 microposit)		1 min	Room temperature	shake

### ***Metal deposition***

- 1- Mount two Tungsten Evaporation boats in place in the evaporation machine.
- 2- Load one Ti pellet in one boat and one Au pellet in the second boat.
- 3- Lay the samples on a holder 10-15cm above the Ti/Au evaporation sources (facing down towards evaporation sources).
- 4- Seal the evaporation chamber and pump it down for 2+ hours.
- 5- Once the evaporation chamber pressure is below  $1 \times 10^{-5}$  mbar start evaporation process.
- 6- Using a manual Dial start heating the Ti source by feeding a high current across the resistive evaporation boat of the Ti source (keep the Ti source shuttered).
- 7- Slowly increase current until Ti pellet start to melt.
- 8- Open shutter until 6nm is deposited (thickness monitor reading) and then close the shutter, turn off the current supply and let boat cool down.
- 9- After 5-10 minutes (when pressure is back to  $1 \times 10^{-5}$  mbar) turn on heating on the Au source.
- 10- Slowly increase current until Au pellet start to melt.
- 11- Open shutter and adjust deposition rate to be approximately  $1 \text{ \AA}/\text{sec}$ .
- 12- Leave shutter open until 30nm is deposited (thickness monitor reading) and then close the shutter, turn off the current supply and let boat cool down.
- 13- After 20+ minutes vent the vacuum chamber and collect the samples.

### ***Lift-off***

- 1- Soak the sample in Acetone for 15 minutes.
- 2- Sonicate for 5-30 seconds (until majority of photoresist is removed).
- 3- Transfer to fresh Acetone beaker and leave for 15 minutes.
- 4- Sonicate for 0.5 to 5 minutes (depending on the cleanness of the channel between S and D electrodes).
- 5- Transfer sample to IPA beaker.
- 6- Sonicate for 30-90 seconds (depending on the adhesion of Au).
- 7- Dry with Nitrogen.

***b- Metal deposition via shadow mask***

- 1- Mount two Tungsten Evaporation boats in place in the evaporation machine.
- 2- Load one Ti pellet in one boat and one Au pellet in the second boat.
- 3- Lay the shadow mask on a holder 10-15cm above the Ti/Au evaporation sources.
- 4- Position the samples against the mask (each sample against a set of transistors' contacts).
- 5- Seal the evaporation chamber and pump it down for 2+ hours.
- 6- Once the evaporation chamber pressure is below  $1 \times 10^{-5}$  mbar start evaporation process.
- 7- Using a manual Dial start heating the Ti source by feeding a high current across the resistive evaporation boat of the Ti source (keep the Ti source shuttered).
- 8- Slowly increase current until Ti pellet start to melt.
- 9- Open shutter until 6nm is deposited (thickness monitor reading) and then close the shutter, turn off the current supply and let boat cool down.
- 10- After 5-10 minutes (when pressure is back to  $1 \times 10^{-5}$  mbar) turn on heating on the Au source.
- 11- Slowly increase current until Au pellet start to melt.
- 12- Open shutter and adjust deposition rate to be approximately  $1 \text{ \AA}/\text{sec}$ .
- 13- Leave shutter open until 30nm is deposited (thickness monitor reading) and then close the shutter, turn off the current supply and let boat cool down.
- 14- After 20+ minutes vent the vacuum chamber and collect the samples.

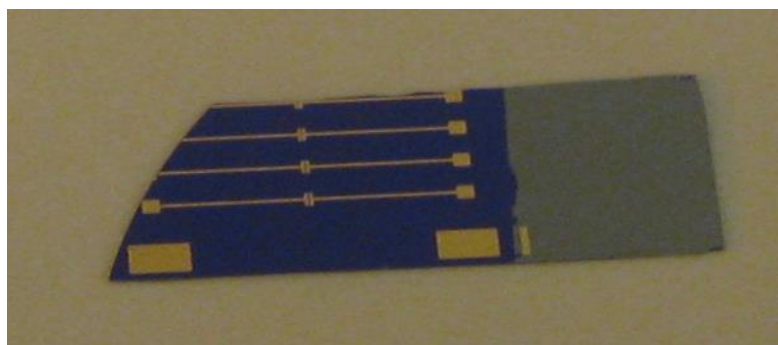


**Figure A.3:** Si/SiO<sub>2</sub> substrate with Si exposed at one end and S/D and control Gate contacts patterned at the other end.

#### **A.4 OSC (Tips-Pentacene) Preparation and Deposition**

##### **Preparation**

- 1- Tips-Pentacene as received from (University of Leeds Biology Lab or Sigma Aldrich) is dissolved in Toluene in 10 mg/ml.
- 2- Poly( $\alpha$ -methylstyrene) (P $\alpha$ MS) as received from (Sigma Aldrich) is dissolved in Toluene in 10 mg/ml.
- 3- Using an analytical weighing balance the two prepared solutions are mixed in Tips-Pentacene 7:3 P $\alpha$ MS weight ratio wt%.

##### **Deposition**

- 1- Clean Samples in Piranha solution for 5 minutes.
- 2- Wash with DI water for 1+ minute.
- 3- Blow sample with nitrogen.
- 4- Dry the samples on hot plate for few seconds.
- 5- Using a Micro-pipette apply a droplet of Tips-Pentacene/P $\alpha$ MS mixture onto the S/D region of the fabricated sample.
- 6- Cover the sample and leave for slow solvent evaporation for 20-30 minutes.
- 7- Check under optical microscope for crystals formation.
- 8- If crystals have not satisfyingly formed, a second droplet is applied.
- 9- Check again under optical microscope for crystals formation, if crystals still not satisfyingly formed, strip the layer by dissolving in Toluene and start the process from step 1 again.
- 10- Anneal the sample on a hotplate at 80C° for 20 minutes in ambient condition.

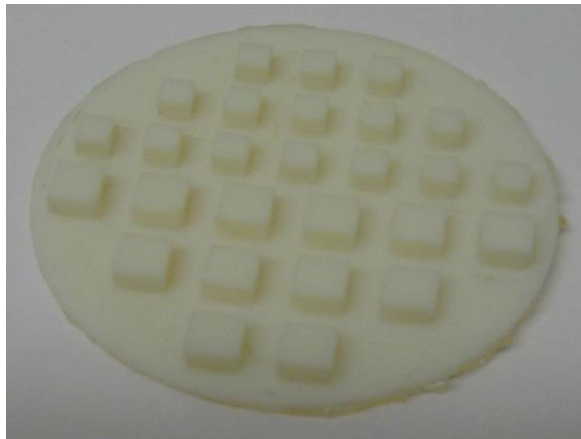
Depositing the Tips-Pentacene on top of the patterned S and D completes the fabrication of a **bottom contact** OFET.



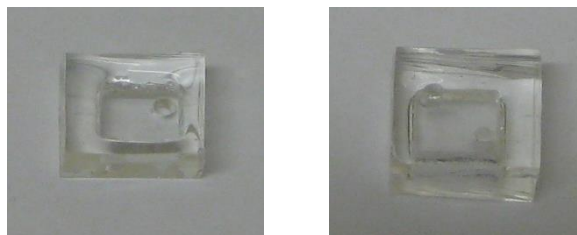
**Figure A.4:** A complete Si/SiO<sub>2</sub> OFET including deposited OSC (Tips-Pentacene/ P $\alpha$ MS).

### A.5 Microfluidic chamber making

- 1- Measure a 50ml of PDMS (pre-polymer) precursor in a plastic cup.
- 2- Add 5ml of the curing agent (Sylgard 184 kit) to the cup.
- 3- Mix Thoroughly for 2 minutes.
- 4- Use a vacuum desiccator to remove bubbles from the mixing.
- 5- Place 3D master mold in a thermal plastic petri dish.
- 6- Cast the PDMS mixture over the 3D master mold.
- 7- Place in a 60C° oven for minimum of 6 hours.
- 8- Gently peel the replica PDMS mold from the master mold.
- 9- Dissect into individual microfluidic chambers using a knife.
- 10- Punch two opening holes at opposite sides for inlet and outlet.



(a)



(b)

**Figure A.5:** (a) 3D Master mold for PDMS microfluidic Chamber making (b) PDMS microfluidic chamber.

## A.6 Gate sensing region functionalization and fluidic chamber integration

If performed before OSC deposition

- 1- Clean sample in Piranha solution ( $\text{H}_2\text{SO}_4$  7:3  $\text{H}_2\text{O}_2$ ) for 5 minutes.
- 2- Dip the sample in a large beaker of DI water to remove the majority of the Piranha residue.
- 3- Immerse the sample in a second beaker of DI water for 3 minutes, and then rinse the samples by refilling the beaker with DI water for 30 seconds.
- 4- Blow dry sample with nitrogen gun.
- 5- Heat the sample on  $110^\circ\text{C}$  hotplate for 1 minute.
- 6- Load the sample in a UV-Ozone cleaner for 5 minutes treatment.
- 7- Prepare 5ml of 5% APTES solution in IPA by volume in a 50ml centrifuge tube.
- 8- Immerse the cleaned sample uprightly in the 5%APTES solution, covering only the sensing region.
- 9- Leave the sample immersed in the functionalizing solution overnight (approximately 18 hours).
- 10- Remove the sample from the functionalizing solution and immersed in a beaker of IPA and shake for 1-2 minutes.
- 11- Remove the sample from the IPA beaker and give it a quick rinse with IPA.
- 12- Dry with nitrogen gun.
- 13- Put a pre-prepared PDMS chamber in an IPA beaker and sonicate for 3 minutes.
- 14- Remove PDMS chamber from IPA and dry with nitrogen gun.
- 15- Load the PDMS chamber to the UV-Ozone cleaner and turn on the UV light source for 5 minutes to activate the silanol groups on the PDMS surface.
- 16- Mount the PDMS chamber to the sensing region of the sample.
- 17- Transfer the sample to a  $90^\circ\text{C}$  hotplate.
- 18- Pour liquid PDMS around the corner of the PDMS chamber.
- 19- Leave PDMS to cure for 20 minutes.

If performed after OSC deposition

- 1- Cover the contacts and OSC region with para-film.
- 2- Dip the sensing region (exposed Si) of the sample in Piranha solution ( $\text{H}_2\text{SO}_4$  7:3  $\text{H}_2\text{O}_2$ ) for 3-5 minutes.

- 3- Dip the sensing region (exposed Si) of the sample in a large beaker of DI water to remove the majority of the Piranha residue.
- 4- Dip the sensing region (exposed Si) of the sample in a second beaker of DI water for a minute.
- 5- Blow dry sample with nitrogen gun.
- 6- Put a pre-prepared PDMS chamber in an IPA beaker and sonicate for 3 minutes.
- 7- Remove PDMS chamber from IPA and dry with nitrogen gun.
- 8- Load the PDMS chamber to the UV-Ozone cleaner and turn on the UV light source for 5 minutes to activate the silanol groups on the PDMS surface.
- 9- Mount the PDMS chamber to the sensing region of the sample.
- 10- Transfer the sample to a 90C° hotplate.
- 11- Pour liquid PDMS around the corner of the PDMS chamber.
- 12- Leave PDMS to cure for 20 minutes.
- 13- Prepare 1ml of 5% APTES solution in IPA by volume in a micro-centrifuge tube.
- 14- Connect tubing to the inlet and output of the PDMS chamber.
- 15- Using a micro-pump draw a 100-200µl of the functionalizing APTES solution to the sensing region inside the PDMS chamber.
- 16- Leave the functionalizing APTES solution resting on the sensing region inside the PDMS chamber overnight (approximately 18 hours).
- 17- Using the micro-pump flow IPA through the PDMS chamber for 5 minutes to wash away the un-attached APTES molecules.
- 18- Disconnect tubes and leave sample to dry before use.



**Figure A.6:** A complete Si/SiO<sub>2</sub> CM-OFET-sensor with functionalized sensing region and integrated PDMS microfluidic chamber.

# Appendix B: Masks

## B.1 Photo-Mask Design

Using L-Edit software provided for drawing ICs layout designs a photo-mask was designed to perform the photolithography stages necessary for the fabrication of the OFET/Sensor.

The photo-mask depicted in figure B.1a is of a 3" diameter and is divided to three main regions, the sides of the 3" diameter photo-mask are packed with multiple source and drain contacts structure (see b figure B.1). These were used in preliminary device investigations as they have high density of devices per area allowing for less consumption of substrates and materials.

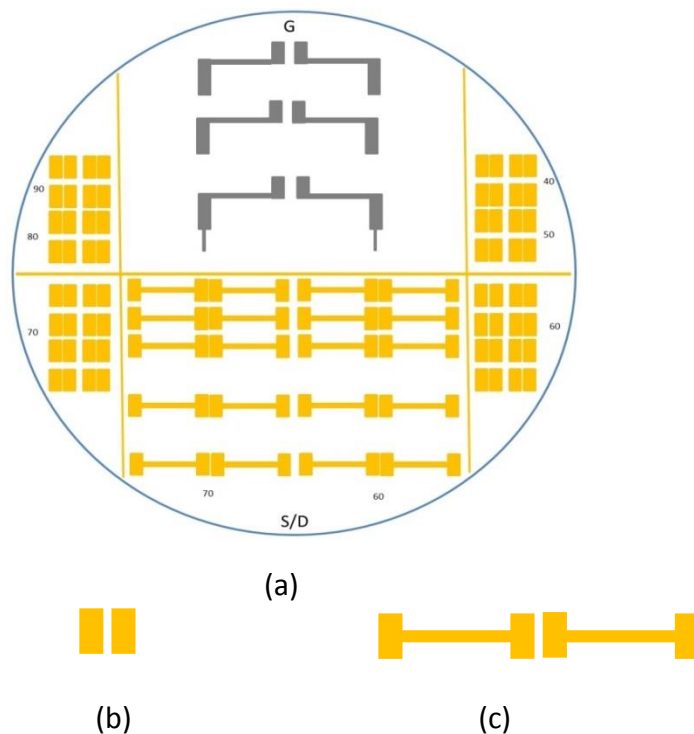


**Figure B.1:** (a) A depiction for our designed Photo-Mask, (b) S/D first geometry and (c) S/D second geometry.

The middle part of the photo-mask was divided into two regions. The upper half contains the gate contact patterns for the first photolithography stage in a bottom contact transistor design. The lower half contains a second geometry of source and drain contacts. When rotated by 180°, the lower half aligns with the upper half for the second photolithography

stage. The second geometry for S and D contacts (figure B.1c) was designed to be used for a sensor architecture. The mask geometry was designed to ensure sufficient space for microfluidic channel integration and that the contact pads are located a sufficient distance from the sensing region to avoid contact with solution

## B.2 Shadow Masking

### B.2.1 Au deposition

shadow masking was selected as an alternative approach for the fabrication of metal contacts. In the shadow masking technique, selective deposition is accomplished by directly depositing material of choice through a stencil mask patterned with the desired features. As a result, the electrical contacts for the fabricated device are formed in a single processing step.

Two shadow masks were used in the fabrication of the CM-OFET device, the first mask was ordered from Ossila Ltd specialist in organic electronic devices. The mask is designed to accommodate 12 sets of S/D contacts structure. Each set contain S/D contacts for 5 transistors (see figure B.2). Rectangular disks in the design separating S/D sets were utilized as control gate contacts. This mask was used to make S/D and control gate contacts for both designs of the CM-OFET devices ( $\text{Si/SiO}_2$  and  $\text{Al/Al}_2\text{O}_3$ ).

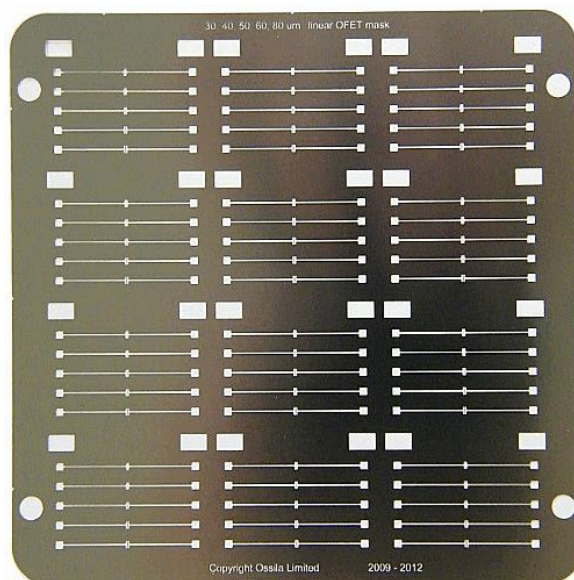


**Figure B.2:** A picture of the shadow mask ordered from Ossila Ltd for source, drain and control gate patterning.

### B.2.2 Al gate patterning

In the second CM-OFET design based on Al/Al<sub>2</sub>O<sub>3</sub>, a second shadow mask was in-house made in the electronic engineering laboratories and used for depositing the Al gate layer as can be seen in figure B.3

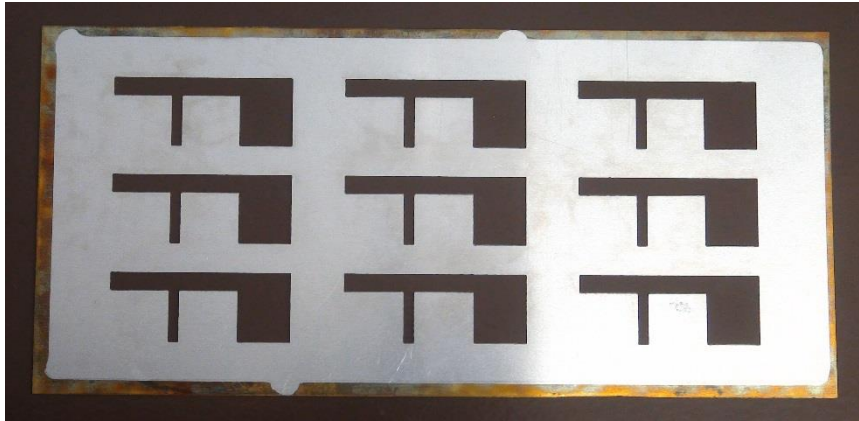


**Figure B.3:** A picture of the shadow mask made in-house for Al patterning.

# Appendix C: Al/Al<sub>2</sub>O<sub>3</sub> CM-OFET devices fabrication steps

## C.1. Si/SiO<sub>2</sub> Substrate Preparation and Cleaning

- 1- Cut Si/SiO<sub>2</sub> wafer to appropriate samples sizes.
- 6- Blow samples with nitrogen gun to blow of debris.
- 7- Put samples in Acetone Beaker and sonicate in an ultra-sonication bath for 3 minutes.
- 8- Transfer to a beaker of isopropanol IPA and sonicated for another 3 minutes.
- 9- Blow dry with nitrogen gun.



**Figure C.1:** Clean Si/SiO<sub>2</sub> substrate.

## C.2. Al metal deposition via shadow mask

- 1- Prepare a tungsten evaporation wire with Al rings around it.
- 2- Mount tungsten evaporation wire in place in the evaporation machine.
- 3- Lay the shadow mask on a holder 10-15cm above the Al evaporation sources.
- 4- Position the samples against the mask (each sample against a gate pattern).
- 5- Seal the evaporation chamber and pump it down for 2+ hours.
- 6- Once the evaporation chamber pressure is below  $1 \times 10^{-5}$  mbar start evaporation process.
- 7- Using a manual Dial start heating the Al source by feeding a high current across the resistive evaporation wire with the Al source (keep the Al source shuttered).
- 8- Slowly increase current until Al rings start to melt.

- 9- Open shutter until 50nm is deposited (thickness monitor reading) and then close the shutter, turn off current supply and let boat cool down.
- 10- After 20+ minutes vent the vacuum chamber and collect the samples.

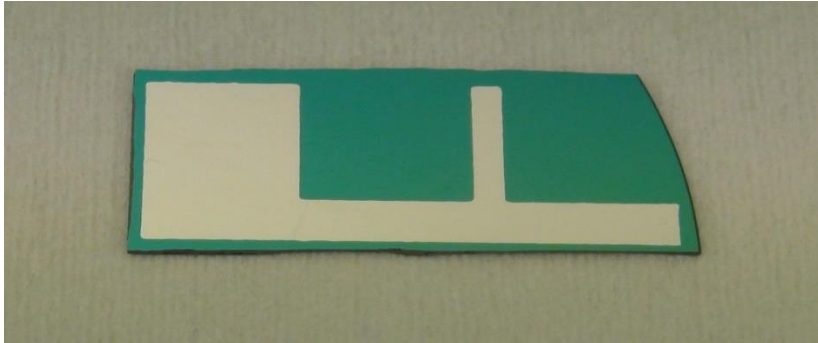


**Figure C.2:** Pattern Al on Si/SiO<sub>2</sub> substrate

### C.3. Al<sub>2</sub>O<sub>3</sub> deposition (ALD)

- 1- Rinse samples with DI-water for 20 seconds.
- 2- Put samples in Acetone beaker and sonicate in an ultra-sonication bath for 5 minutes.
- 3- Transfer to a beaker of isopropanol IPA and sonicated for another 2 minutes.
- 4- Blow dry with nitrogen gun.
- 5- Insert samples to the ALD reaction chamber through a load-lock system.
- 6- Apply in-situ O<sub>2</sub> plasma for 1 minutes at 200C° 300W.
- 7- For first half-cycle apply TMA and then purge the system (200C° 300W).
- 8- For second half-cycle O<sub>2</sub> plasma then purge the system (200C° 300W).
- 9- Repeat deposition cycle for 351 times at (0.114nm/cycle) to deposit 40nm.

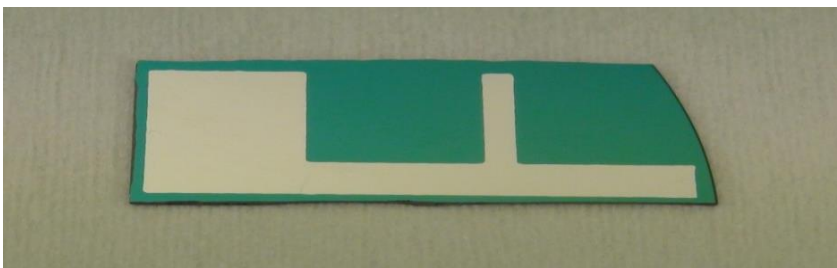


**Figure C.3:** Si/SiO<sub>2</sub> substrate with patterned Al gate and Al<sub>2</sub>O<sub>3</sub> gate dielectric on top (Al<sub>2</sub>O<sub>3</sub> transparent).

#### C.4. Au metal deposition via shadow mask

- 1- Mount two Tungsten Evaporation boats in place in the evaporation machine.
- 2- Load one Ti pellet in one boat and one Au pellet in the second boat.
- 3- Lay the shadow mask on a holder 10-15cm above the Ti/Au evaporation sources.
- 4- Position the samples against the mask (each sample against a set of transistors' contacts).
- 5- Seal the evaporation chamber and pump it down for 2+ hours.
- 6- Once the evaporation chamber pressure is below  $1 \times 10^{-5}$  mbar start evaporation process.
- 7- Using a manual Dial start heating the Ti source by feeding a high current across the resistive evaporation boat of the Ti source (keep the Ti source shuttered).
- 8- Slowly increase current until Ti pellet start to melt.
- 9- Open shutter until 6nm is deposited (Thickness monitor reading) and then close the shutter, turn off current supply and let boat cool down.
- 10- After 5-10 minutes (when pressure is back to  $1 \times 10^{-5}$  mbar) turn on heating on the Au source.
- 11- Slowly increase current until Au pellet start to melt.
- 12- Open shutter and adjust deposition rate to be approximately  $1 \text{ \AA}/\text{sec}$ .
- 13- Leave shutter open until 30nm is deposited (Thickness monitor reading) and then close the shutter and let boat cool down.
- 14- After 20+ minutes vent the vacuum chamber and collect the samples.

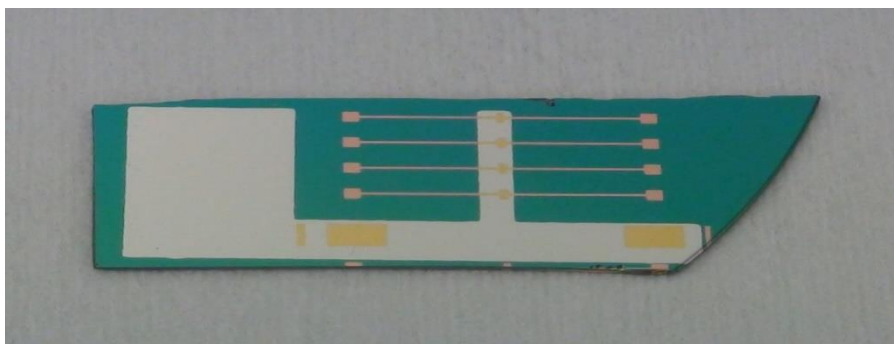


**Figure C.4:** Al/Al<sub>2</sub>O<sub>3</sub> sample with S/D and control Gate contacts patterned at one end.

### C.5 Sensing area realization

- 1- Prepare diluted 319 microposit developer solution 1:3 water.
- 2- Dip the designated sensing region in the diluted developer solution for 30 seconds.
- 3- Remove the sample swiftly from the developer solution and dip a beaker of DI water for 30 seconds.
- 4- Immerse the sample in a second beaker of DI water for 2 minutes.
- 5- Dry the sample with nitrogen gun.

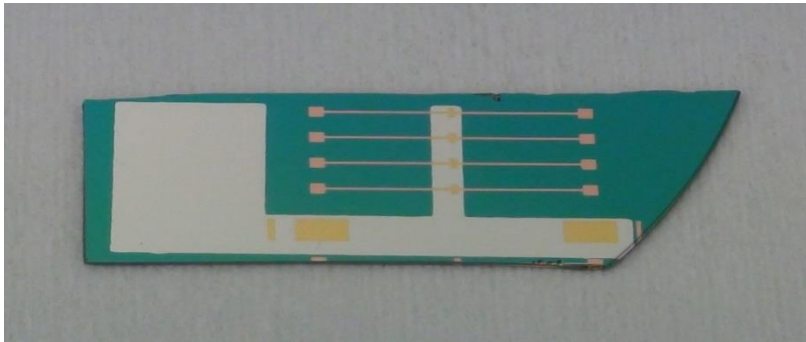


**Figure C.5:** Al/Al<sub>2</sub>O<sub>3</sub> sample with S/D and control gate contacts patterned at one end and Al exposed at the other end.

### C.6. OSC (Tips-Pentacene) Preparation and Deposition

#### **Preparation**

- 1- Tips-Pentacene as received from (University of Leeds Biology Lab or Sigma Aldrich) is dissolved in Toluene in 10 mg/ml.
- 2- Poly( $\alpha$ -methylstyrene) (P $\alpha$ MS) as received from (Sigma Aldrich) is dissolved in Toluene in 10 mg/ml.
- 3- Using an analytical weighing balance the two prepared solutions are mixed in Tips-Pentacene 7:3 P $\alpha$ MS weight ratio wt%.

#### **Deposition**

- 1- Blow sample with nitrogen gun.
- 2- Load the sample in a UV-Ozone cleaner for 5 minutes treatment.

- 3- Using a Micro-pipette apply a droplet of Tips-Pentacene/PαMS mixture onto the S/D region of the fabricated sample.
- 4- Cover the sample and leave for slow solvent evaporation for 20-30 minutes.
- 5- Check under optical microscope for crystals formation.
- 6- If crystals have not satisfyingly formed a second droplet is applied.
- 7- Check again under optical microscope for crystals formation, if crystals still not satisfyingly formed strip the layer by dissolving in Toluene and start the process from step 1 again.
- 8- Anneal the sample on a hotplate at 80C° for 20 minutes in ambient condition.

Depositing the Tips-Pentacene on top of the patterned S and D completes the fabrication of a **bottom contact** OFET.

### **C.7 Microfluidic chamber making**

See A.5 (Appendix A)

### **C.8 Gate sensing region functionalization and fluidic chamber integration**

If performed before OSC deposition

- 1- Place samples in Acetone Beaker and sonicate in an ultra-sonication bath for 1 minutes.
- 2- Transfer to a beaker of isopropanol IPA and sonicated for another 1 minutes.
- 3- Blow sample with nitrogen gun.
- 4- Load the sample in a UV-Ozone cleaner for 5 minutes treatment.
- 5- Prepare 5ml of 5% APTES solution in IPA by volume in a 50ml centrifuge tube.
- 6- Immerse the cleaned sample uprightly in the 5%APTES solution, covering only the sensing region.
- 7- Leave the sample immersed in the functionalizing solution overnight (approximately 18 hours).
- 8- Remove the sample from the functionalizing solution and immersed in a beaker of IPA and shake for 1-2 minutes.
- 9- Remove the sample from the IPA beaker and give it a quick rinse with IPA.
- 10- Dry with nitrogen gun.
- 11- Put a pre-prepared PDMS chamber in an IPA beaker and sonicate for 3 minutes.

- 12- Remove PDMS chamber from IPA and dry with nitrogen gun.
- 13- Load the PDMS chamber to the UV-Ozone cleaner and turn on the UV light source for 5 minutes to activate the silanol groups on the PDMS surface.
- 14- Mount the PDMS chamber to the sensing region of the sample.
- 15- Transfer the sample to a 90C° hotplate.
- 16- Pour liquid PDMS around the corner of the PDMS chamber.
- 17- Leave PDMS to cure for 20 minutes.

If performed after OSC deposition

- 1- Clean sensing region with DI water by dipping the sensing region only
- 2- Dry with nitrogen gun.
- 3- Put a pre-prepared PDMS chamber in an IPA beaker and sonicate for 3 minutes.
- 4- Remove PDMS chamber from IPA and dry with nitrogen gun.
- 5- Load the PDMS chamber to the UV-Ozone cleaner and turn on the UV light source for 5 minutes to activate the silanol groups on the PDMS surface.
- 6- Mount the PDMS chamber to the sensing region of the sample.
- 7- Transfer the sample to a 90C° hotplate.
- 8- Pour liquid PDMS around the corner of the PDMS chamber.
- 9- Leave PDMS to cure for 20 minutes.
- 10- Prepare 1ml of 5% APTES solution in IPA by volume in a micro-centrifuge tube.
- 11- Connect tubing to the inlet and output of the PDMS chamber.
- 12- Using a micro-pump draw a 100-200µl of the functionalizing APTES solution to the sensing region inside the PDMS chamber.
- 13- Leave the functionalizing APTES solution resting on the sensing region inside the PDMS chamber overnight (approximately 18 hours).
- 14- Using the micro-pump flow IPA through the PDMS chamber for 5 minutes to wash away the un-attached APTES molecules.
- 15- Disconnect Tubes and leave sample to dry before use.

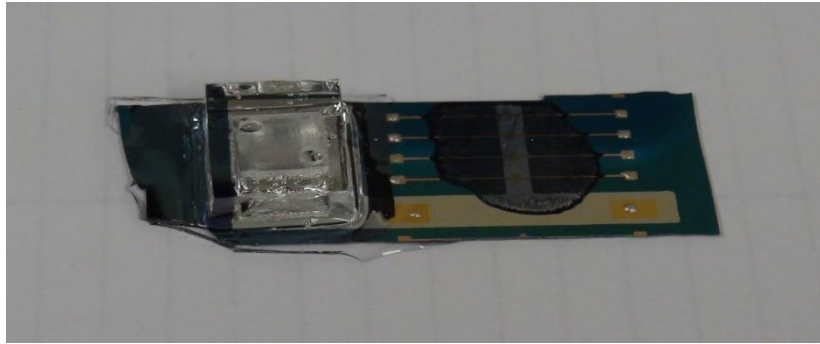


**Figure C.6:** A complete Al/Al<sub>2</sub>O<sub>3</sub> CM-OFET-sensor with functionalized sensing region and integrated PDMS microfluidic chamber.

# Appendix D: How to extract the figures of merits

Utilizing the transfer and output characteristics the following parameters which evaluate the performance of the fabricated Si/SiO<sub>2</sub> OFET devices can be extracted:

Mobility $\mu_{\text{FET}}$	ON/OFF ratio $I_{\text{ON}}/I_{\text{OFF}}$	Onset Voltage $V_{\text{SO}}$	Threshold Voltage $V_{\text{TH}}$	Sub-threshold Swing $S$
--------------------------------	--	----------------------------------	--------------------------------------	----------------------------

All the transfer characteristics measurements were collected at saturation. The mobility and the threshold voltage  $V_{\text{TH}}$  are extracted by exploiting equation (D.1). Plotting of the square root of  $I_{\text{SD}}$  against the gate voltage, the slope of the line =  $(WC_i\mu/2L)^{1/2}$  and from the line equation  $y=a+bx$  at  $y = 0$  i.e.  $I_{\text{SD}}^{1/2} = 0$ ,  $V_{\text{TH}} = -a/b$ .

$$I_{\text{DS}} = \frac{W\mu C_i}{2L} (V_G - V_T)^2 \quad (\text{D.1})$$

$C_i$  is the capacitance per unit area of the gate insulator =  $\epsilon_r \epsilon_0 / t$

Where  $\epsilon_0$  is the free space permittivity and  $\epsilon_r$  is the relative permittivity of the silicon dioxide (gate insulator) and  $t$  is the oxide thickness.

$$C_i = (3.9 \times 8.854 \times 10^{-14} \text{ F/cm}) / (300 \times 10^{-7} \text{ cm}) = 11.51 \text{ nF/cm}^2$$

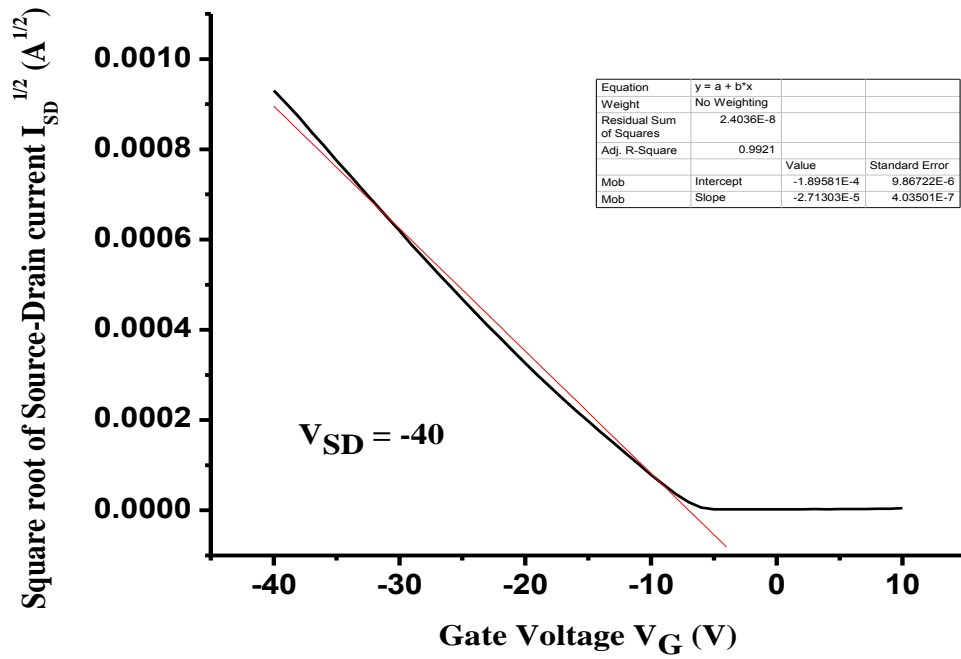


**Figure D.1:** Plot of  $I_{SD}^{1/2}$  vs  $V_G$  at saturation for one of the fabricated OFETs.

Slope =  $(WC_i\mu/2L)^{1/2} \rightarrow \mu = (\text{slope})^2 \cdot 2L / WC_i = (2.71 \times 10^{-5})^2 \cdot 2 \cdot 50 \times 10^{-4} / (2000 \times 10^{-4} \times 11.51 \times 10^{-9})$ ,  $\mu = 3.2 \times 10^{-3} \text{ cm}^2 \text{ V}^{-1} \text{ S}^{-1}$ .

The table in figure D.1 shows that the intercept  $a = -1.9 \times 10^{-4}$ , the slope  $b = -2.71 \times 10^{-5}$

$$V_{TH} = -a/b = 1.9 \times 10^{-4} / -2.71 \times 10^{-5} = -7 \text{ V}$$

The Onset Voltage  $V_{SO}$ , the ON/OFF current ratio ( $I_{ON}/I_{OFF}$ ) and the sub-threshold swing  $S$  were extracted from the  $\text{Log}_{10}$  plotting of the transfer characteristic as in figure D.2.

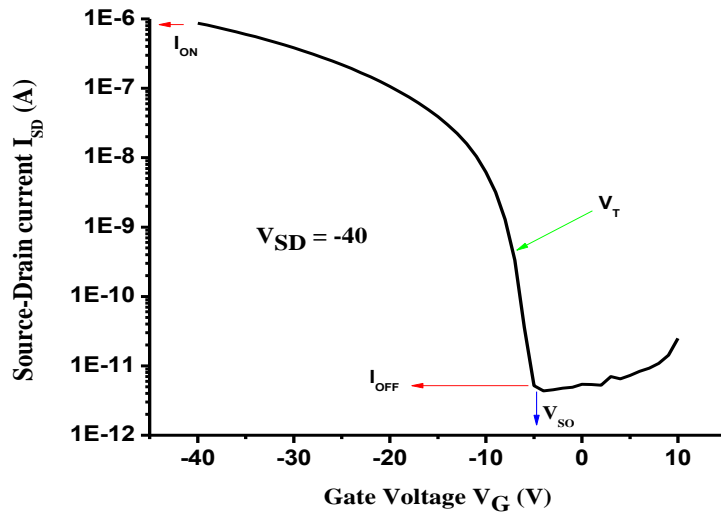


**Figure D.2:** Transfer characteristic at saturation ( $\text{Log}_{10} I_{SD}$  vs  $V_G$ ) for one of the fabricated OFETs.

The Onset Voltage  $V_{SO}$  is the voltage at which the current starts to rise ( $V_{SO} = -4$  V in figure ap4.2),  $I_{OFF}$  is  $I_{SD}$  just before the rise ( $I_{OFF} = 4.37 \times 10^{-12}$  A) and  $I_{ON}$  is  $I_{SD}$  at  $V_G = -40$  (i.e. at the highest gate voltage  $I_{ON} = 8.7 \times 10^{-7}$  A) giving  $I_{ON}/I_{OFF} \approx 2 \times 10^5$ , for the sub-threshold swing  $S$  it was estimated as the number of volts per current decades between the Onset Voltage and Threshold Voltage

$$S = (V_{TH} - V_{SO}) / [\text{Log}_{10} I_{SD}(V_{TH}) - \text{Log}_{10} I_{SD}(V_{SO})] \text{ which equal to } 1.6\text{V/dec for this device.}$$

# Appendix E: Fitting a stretched exponential function to $I_{SD}$ decay curve

The stretched exponential function for source drain current decay is:

$$I_{SD}(t) = I_{SD}(0) \exp\left[-\left(\frac{t}{\tau}\right)^\beta\right] \quad (E.1)$$

$$\frac{I_{SD}(t)}{I_{SD}(0)} = \exp\left[-\left(\frac{t}{\tau}\right)^\beta\right] \quad (E.1a)$$

Taking the Log for both sides

$$\text{Log}\left[\frac{I_{SD}(t)}{I_{SD}(0)}\right] = -\left(\frac{t}{\tau}\right)^\beta \quad (E.2)$$

Fitting a  $y = a \cdot x^b$  to the curve as shown in figure E.1. Here  $y = \text{Log}[I_{SD}(t)/I_{SD}(0)]$ ,  $a = -(1/\tau)^\beta$  and  $\beta = b$ .

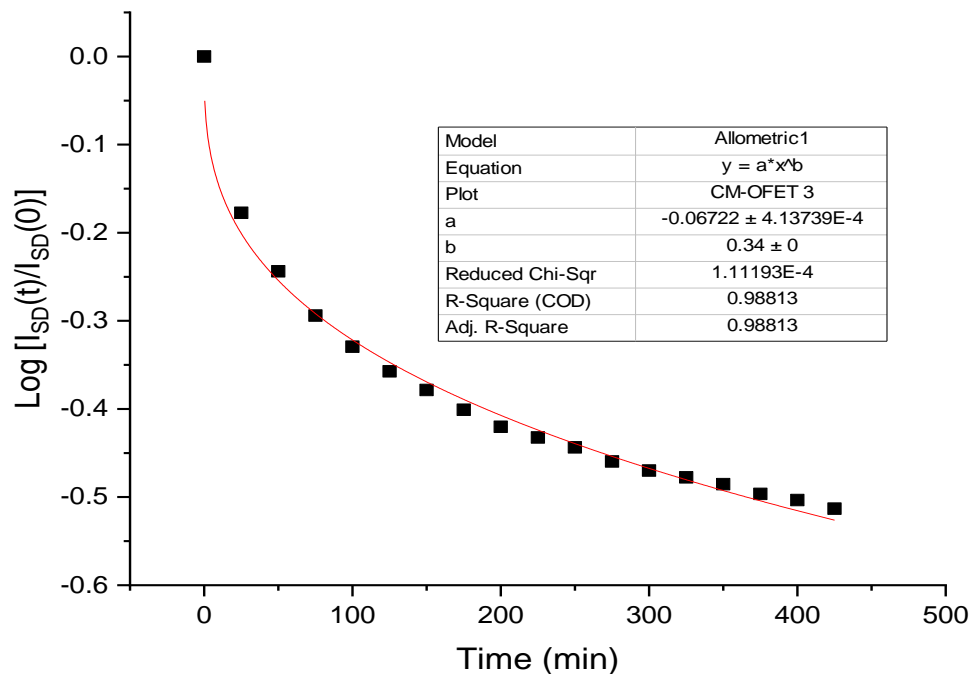


**Figure E.1:** Fitting of stretched exponential function to source drain current decay in dark for one CM-OFET.



